Development of validation techniques for super-resolution ultrasound imaging with microbubble contrast agents

Brown, Jemma

Awarding institution:
King's College London

Development of validation techniques for super-resolution ultrasound imaging with microbubble contrast agents

by

Jemma Brown

Submitted to the School of Biomedical Engineering & Imaging Sciences in fulfillment of the requirements for the degree of

PhD in Biomedical Engineering

at

King's College London

December 2019

Supervised by: Dr Robert J. Eckersley and Professor Meng-Xing Tang

Acknowledgements

The most rewarding part of my PhD thesis has been the time spent working with fantastic colleagues and friends. Primary thanks go to my first supervisor, Dr Robert Eckersley. I am hugely grateful for his unselfish sharing of his time and expertise. His supervision was perfectly balanced so that his door was always open for support and advice, whilst still giving me freedom to pursue my own research ideas and interests. I am extremely grateful to my second supervisor Professor Meng-Xing Tang and co-supervisor Professor Chris Dunsby who were also a great support and source of guidance throughout this project. In addition to my supervisors I would also like to thank all the members of our SRUS group; Dr Sevan Harput, Dr Kirsten Christensen-Jeffries, Dr Ge Zhang and Jiaqi Zhu for our helpful meetings.

I am extremely grateful to Dr Kirsten Christensen-Jeffries for her help and advice throughout this project. Above all, I could not be more appreciative of her unselfish time and effort in reading many drafts of the work in this thesis.

I am especially grateful for all the opportunities to learn from colleagues and gain feedback from all at the Ultrasound Lab for Imaging and Sensing at Imperial College London. I am especially grateful to Professor Enrico Grisan for always taking an interest in my work and for our helpful discussions. I also hugely enjoyed collaborating with fellow students Jiaqi Zhu and Kai Riemer. Together we worked on investigating a signal processing technique which will be presented later in this thesis.

I would also like to acknowledge Shu Wang, a fellow PhD student at King's College London, for sharing her 3D printing expertise during an interesting and fun collaboration. Thanks also go to Dr Michael Reinwald for kindly sharing his digital probe model.

I would also like to acknowledge my Thesis Progression Committee Members; Professor Andrew Reader, Dr Martin Bishop and Dr Richard Southworth. Your interest in my work and probing questions from new perspectives really helped to drive the work forward.

A highlight of my time at KCL has been the co-supervision of several under-

graduate students, Samradnyee Kolas, Alex Skondras, Christine Salib, and Cahil de Menezes who helped me explore and test new ideas. I also had the fantastic experience of leading an outreach project with 3 A-level students, Sabah Ally, Nimah Ashraf and Senthooran Ramesh. These students helped with the final chapter of this thesis and their enthusiasm really kept me going. This outreach project would not have been possible without the help of Dr Matt Allinson who handled all the logistics.

Thanks also go to Ceri Matthews and Judith Coghlan who facilitated the patent submission for a portion of the work in this thesis. Your probing questions helped me to think about my work completely in a completely different context and even exposed me to a future career path as a patent attorney.

Huge thanks also go to Rob Miles and Soba Akinwunmi, supposedly for admin and IT support, but mostly for great chats, laughter, snacks and pep talks.

On a more personal note, I would also like to thank my wonderful friends from near and far for filling my life with so much joy and perspective. In particular I would like to thank my new CDT friends; Aditi, G(J)ames, Rainbow, Max and Sam, who all helped make the PhD experience a lot of fun.

I would also like to thank my parents for their unconditional love and support. I am so appreciative of the emphasis you placed on the importance of education whilst never putting any pressure on me. Without you I would have achieved nothing.

My PhD stipend and consumables were funded by the King's College London Imperial College London EPSRC Centre for Doctoral Training in Medical Imaging (EP/L015226/1). This work was also supported in part by the EPSRC under Grant EP/N015487/1 and Grant EP/N014855/1.

Abstract

Non-invasive, longitudinal imaging of microvasculature at depth is not possible with existing medical imaging techniques. Previous work has demonstrated the potential of super-resolution ultrasound imaging (SRUS) with microbubbles (MBs) to visualise microvasculature. However, to ensure reliable representation of the vasculature for useful clinical translation, the factors which affect the super resolution image must be better understood. In this work, simulation and phantom tools to validate acoustic SRUS imaging have been developed and applied.

MBs are ultrasound (US) contrast agents that scatter strongly such that individual MBs can be detected when low concentrations of the contrast agent are imaged. The MB positions can be determined by localising their isolated point spread functions. By building up a map of localisations over time a representation of the vasculature can be generated. Both simulated and *in vitro* ground truth investigation are required to validate and improve upon super-resolution (SR) protocols.

A simulation environment combining the Marmottant model to simulate MB dynamics and k-Wave to incorporate tissue and model wave propagation has been developed. This has allowed the comparison and investigation of methods of extracting the MB signal from the surrounding tissue signal. A simultaneous optical and acoustic test rig was constructed to provide an experimental ground truth. To reduce artefacts produced using current vessel phantoms, a novel acquisition and signal processing method was invented to counter the limited dynamic range of the ultrasound transducer. Finally, microvascular phantoms have been developed to provide targets that better allow the capabilities of SRUS to be investigated compared to previous phantoms used in the literature.

In short, this work involved the development of simulation and experimental tools to begin to address the challenges surrounding clinical translation of SRUS.

Contents

List of Figures

List of Tables

Acronyms and Abbreviations

ADC	Analogue to digital converters
AM	Amplitude modulation
AWSALM	Acoustic wave sparsely activated localisation microscopy
BP	Boiling point
CAD	Computer aided design
CANR	Contrast acoustic noise ratio
CCD	Charge-coupled device
CEUS	Contrast enhanced ultrasound
CFL	Courant-Friedrichs-Lewy
CPS	Contrast pulse sequence
CT	Computed tomography
CTR	Contrast tissue ratio
DAS	Delay and sum
DI	Differential imaging
DOF	Depth of field
DSPC	1,2-distearoyl-sn-glycero-3-phosphocholine
DSPG.NA	1,2-distearoyl-sn-glycero-3-phospho-rac-(1-glycerol) sodium salt
FDM	Fused deposition modelling
FN	False negative
FOV	Field of view
FP	False positive
FPALM	Fluorescent photoactivated localisation microscopy
FWHM	Full width at half maximum
GFP	Green fluorescent protein
GPU	Graphics processing unit
HDR	High dynamic range
HFR	High frame rate
IMHC	Immunohistochemical
IQ	In-phase and quadrature
LDPE	Low-density polyethylene
MB	Microbubble
MCMCDA	Markov chain Monte Carlo data association
MI	Mechanical index
MIOT	Maximum intensity over time

MRI	Magnetic resonance imaging
mULM	Motion model ultrasound localisation microscopy
NA	Numerical aperture
ND	Nanodroplet
OCT	Optical coherence tomography
PAI	Photoacoustic imaging
PALM	Photoactivated localisation microscopy
PBCA	Poly(butylcyanoacrylate)
PDMS	Polydimethylsiloxane
PDLGA	Poly DLlactide-co-glycolide
PI	Pulse inversion
PET	Positron emission tomography
PMMA	Polymethacrylate
PNP	Peak negative pressure
PPW	Points per wavelength
PRF	Pulse repetition frequency
PSF	Point spread function
PVA	Polyvinyl acetate
PW	Plane wave
rBV	Relative blood volume
RF	Radiofrequency
ROI	Region of interest
RMS	Root mean square
R-P	Rayleigh-Plesset
SDS	Sodium dodecyl sulfate
SLA	Stereolithography
SNR	Signal to noise ratio
SOFI	Super-resolution optical fluctuation imaging
SPECT	Single photon emission computed tomography
SPL	Spatial pulse length
SR	Super-resolution
SRUS	Super-resolution ultrasound
STD	Standard deviation
SVD	Singular value decomposition
TGC	Time gain compensation
TI	Thermal index
TMM	Tissue mimicking material
TN	True positive
TP	True negative
US	Ultrasound
UV	Ultraviolet

Chapter 1

Background

1.1 Clinical need

A key clinical challenge within the field of medical imaging is the resolution of microvasculature at depths on the order of centimetres within the human body. Microvascular changes can be an important marker of disease or indicate a response to therapy. This introductory section will explain the clinical motivation for visualising microvasculature.

1.1.1 Microvasculature

The cardiovascular system (the heart and vasculature) is responsible for supplying the requirements of the tissues in the body [2]. A schematic of the cardiovascular system is shown in Figure 1-1. Blood leaves the left side of the heart from the aorta and through the arterial branches. These then branch into narrower vessels called arterioles which further branch to capillaries. The structure of capillaries is simply a unicellular wall of endothelial cells which is surrounded by an outer basement membrane [3]. These endothelial cells have actin and myosin which change their shape depending on their chemical environment [2]. Diffusion of oxygen, glucose, and other nutrients leave the blood through the thin capillary walls and the carbon dioxide and other waste products enter the blood stream. The venous system then

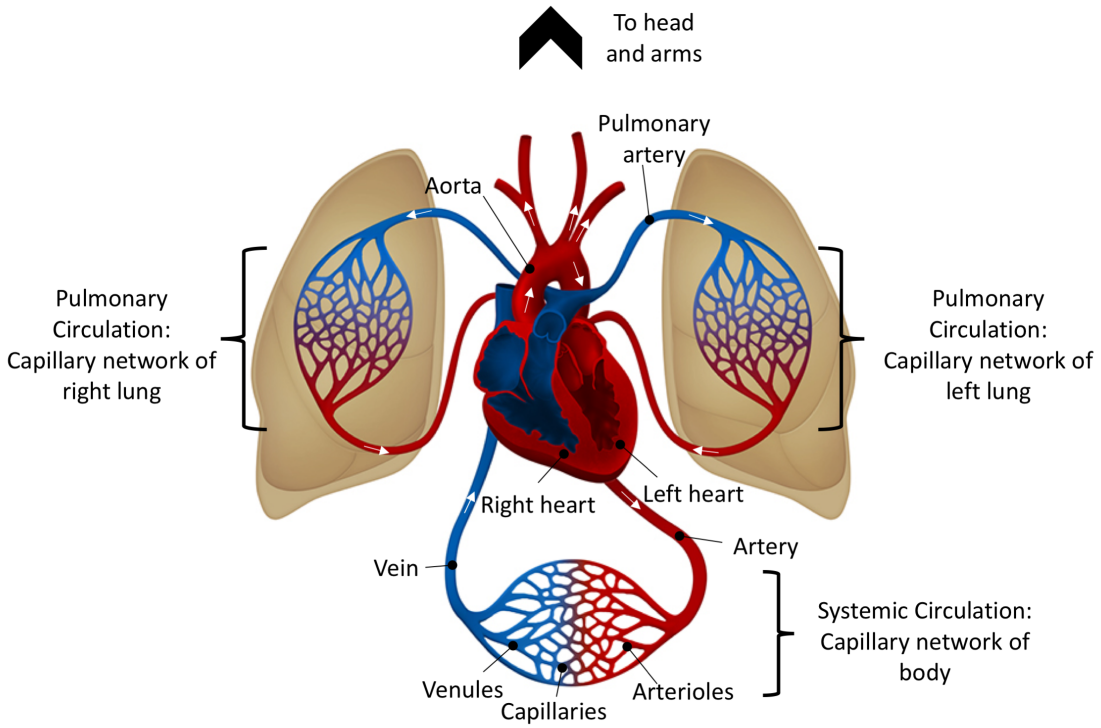

Figure 1-1: Cardiovascular system. Red vessels show oxygenated blood in arterial circulation and blue vessels show deoxygenated blood in arterial circulation. The systemic circulation and pulmonary circulation work together to supply oxygen to the tissues. Adapted from "The Circulatory System" by Andre R Almeida, which is licensed under CC BY-NC-ND 4.0.

returns the blood to the heart through a structure which is effectively a mirror image of the arterial systems; draining from the organ via narrow venules, into veins and returning to the right side of the heart. This is known as the systemic circulation. The pulmonary circulation is then responsible for re-oxygenating the blood. Blood leaves the right heart through the pulmonary artery which branches into the capillary network of the lungs. Here, carbon dioxide is released and oxygen enters the blood stream via the capillary networks before being fed back to the right heart [4]. Almost every cell will be located within 50-100 μm of a capillary [5].

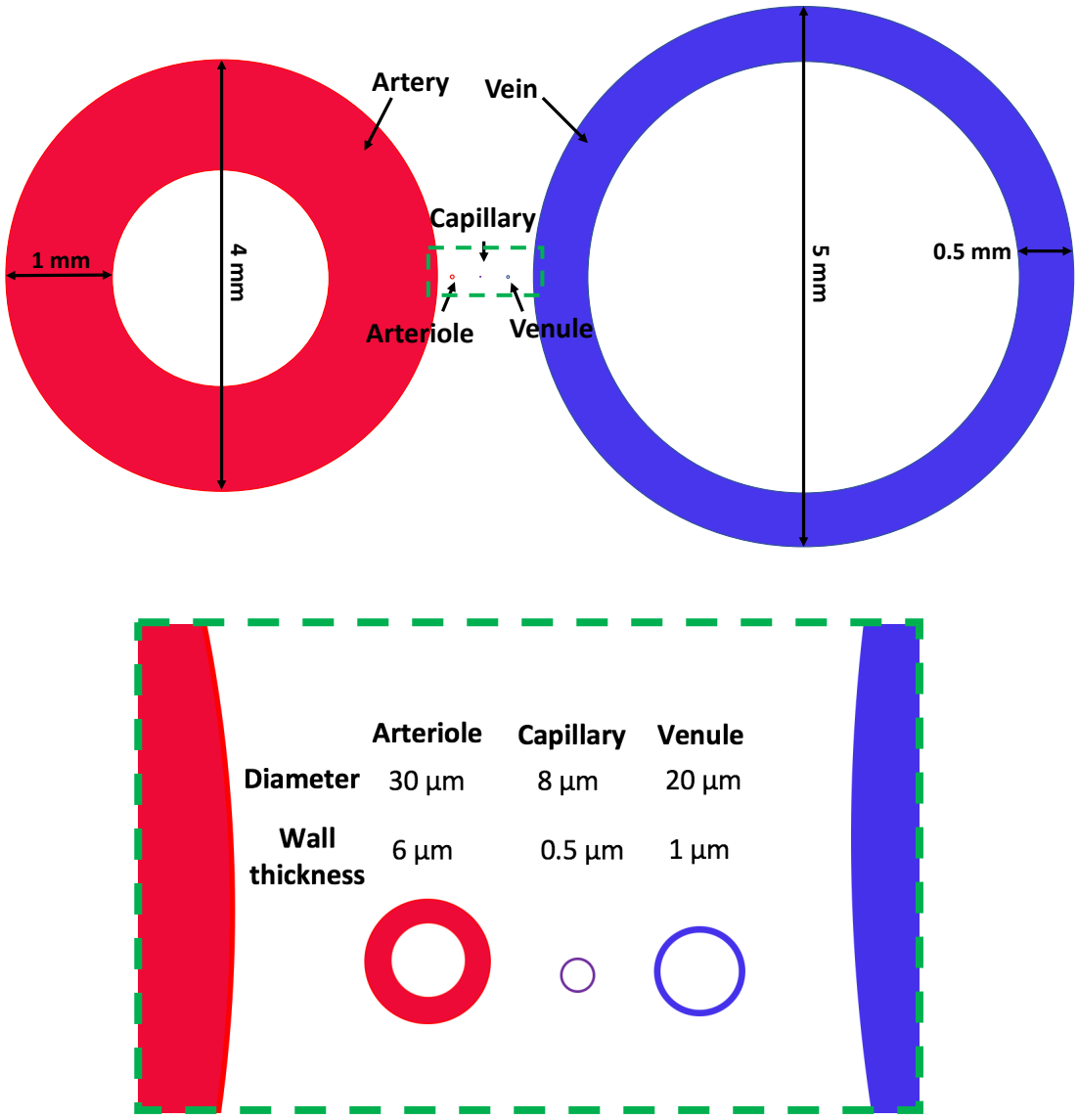

Figure 1-2: Scale of vessels. Cross sectional vessels within circulatory system. Image drawn to scale and the values for average outer diameter and wall thickness taken from Koeppen et al., (2009) [2].

There is a huge variation in scale, on the order of 10^3, between the vessels in the human body. With the largest artery, the aorta, being approximately 25 mm in diameter compared to the average capillary being $\approx$ 8 µm in diameter [2]. When considering SR we are particularly interested in the set of microvessels. Microves-

sels include arterioles (≈ 30 μm), capillaries (≈ 8 μm) and venules (≈ 20 μm) [2]. The mean diameters and wall thickness of these vessels are presented in Figure 1-2 (diagram to scale).

The microvasculature is a system which can dynamically respond to the tissue needs. The blood flow primarily depends on the tissue metabolic activity [3]. For example, active tissue can require up to 20-30 times more blood flow than resting tissue. The flow is controlled by the arterioles whose muscular walls enable them to contract and expand. Every arteriole branches into multiple capillaries. Because the same volume of blood flow needs to travel through each segment of the system each second, the total cross-sectional area of the vessels is at a maximum for the capillary bed, and the average blood velocity is at a minimum [3]. Moreover, the pulsatile flow due to the pumping heart is damped to a steady flow due to the resistance of the smaller vessels and distensibility of the large arteries. Mean velocities and areas are given in Figure 1-3, where the data is taken from [3].

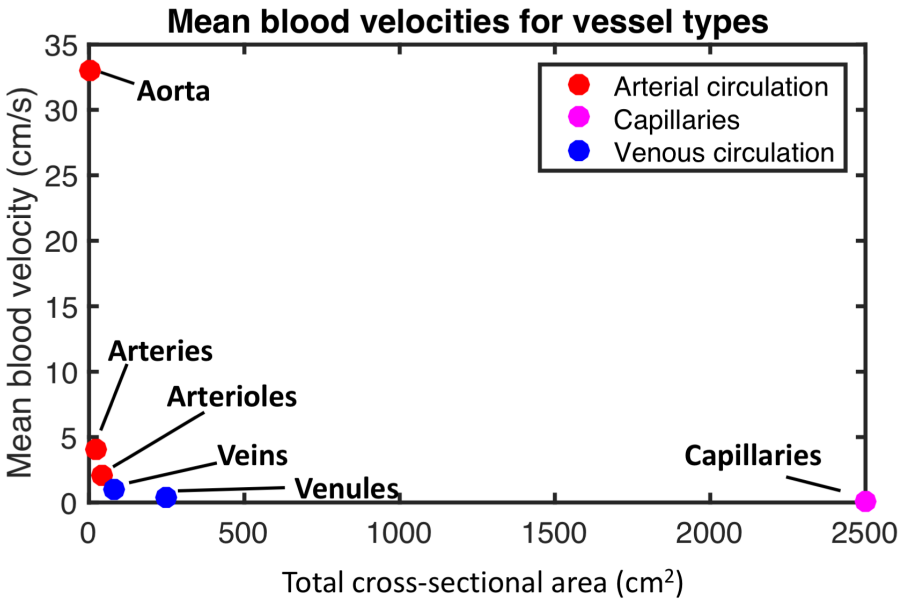

Figure 1-3: Mean blood velocities with respect to total cross sectional area for main vessel types. Data taken from Hall, (2015) [3].

For long straight vessels, the blood flow is generally assumed to be laminar. That

is, the blood flows in streamlines with each layer of blood being the same distance from the wall. The flow velocity profile over the vessel is assumed to be parabolic [3]. The liquid nearest the wall moves most slowly and the central streamline is the fastest. The smallest capillaries have diameters on the same scale as red blood cells. This means that the flow dynamics are not applicable, and instead the cells move through in single file [6].

Microvascular structure and function is implicated in a breadth of diseases and conditions. Some examples include, many cancers [7, 8, 9], diabetes [10, 11], coronary artery disease [12] and neurovascular brain disease such as Alzheimer's and vascular dementia [13]. As will be described in the following literature review, the majority of the previous literature investigating SR has focused on imaging tumour microvasculature.

1.1.2 Angiogenesis

Angiogenesis is when new blood vessels are formed from already existing vessels [14]. This is a normal, healthy process which occurs throughout our lives. However, angiogenesis can also be a biomarker for diseases such as cancer [9]. Tumours cannot grow beyond 100 - 200 μm without forming new blood vessels to supply their metabolic needs. Thus, vessel growth is triggered to support the growth of tumours and also their spread. In comparison to normal vasculature, tumour vessels are disorganised, tortuous, non-constant in diameter with more branching and shunts than normal vasculature. Functionally, this all results in a chaotic and changeable blood flow [9].

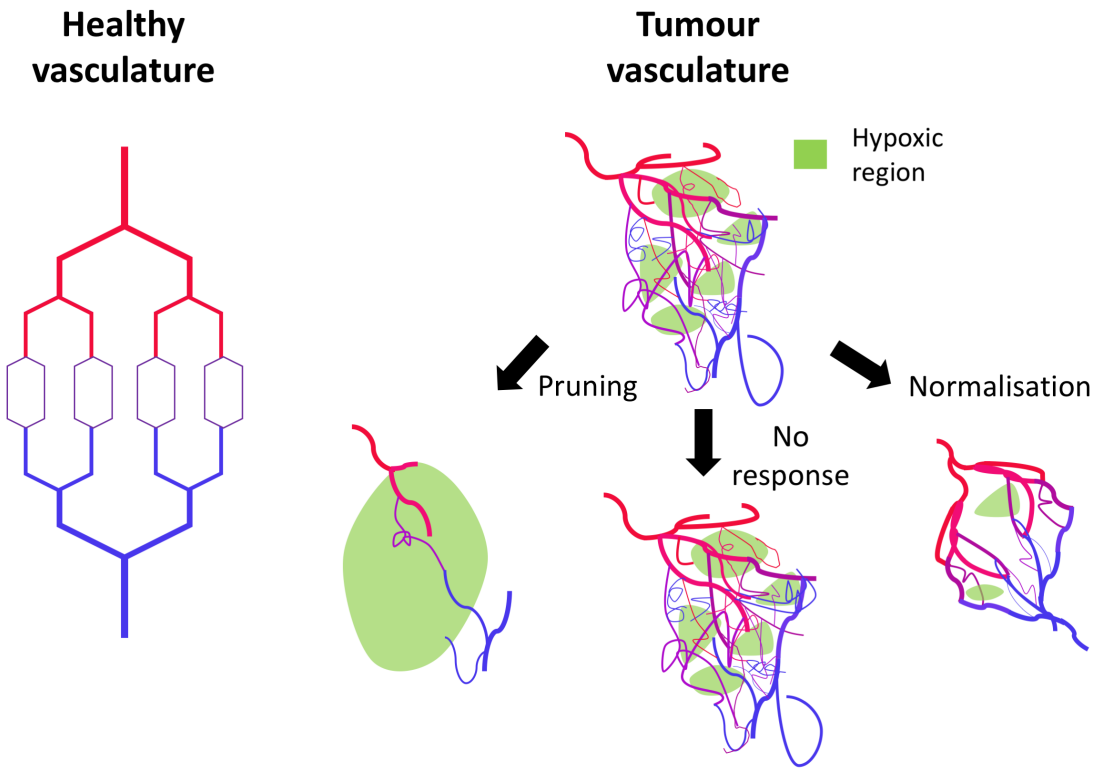

Figure 1-4: Healthy vs tumour microvasculature and treatment response.The ordered structure of the arterial vessels (red), capillaries (purple) and venous vessels (blue) is shown on the left. The more complex tumour vasculature and hypoxic regions (green) is shown on the right. The right image shows three potential responses to anti-angiogenic treatment. This image was inspired from; Carmeliet & Jain, (2011) and Jain, (2014) ([15, 16]).

Tumour vasculature is also generally denser than healthy vasculature [17], so one method of distinguishing tumour vasculature from healthy tissue is the relative blood volume (rBV). This is the fraction of tumour vessels to total tumour area and is commonly used to assess US images of tumours [18, 19, 20]. However, despite the higher density, the poor quality of tumour vessels means that they cannot always supply enough oxygen to the cells (hypoxia) [16]. Figure 1-4 shows a comparison between the ordered structure of healthy vasculature and the more complex tumour vasculature. Regions of hypoxia are shown in green. This has important implications for therapy, as hypoxic tumours have been shown to be more resistant to treatments such as chemotherapy, immunotherapy and radiotherapy [16]. In addition, the vasculature heavily influences metastasis [7]. Blood vessels not only provide the main transport

route for cancer cells, but their design is also a main factor in how efficient metastasis can be [7].

Angiogenesis can work for and against cancer treatment. Some drug delivery techniques take advantage of the leaky vessel walls to selectively deliver drugs to the tumour site and avoid systemic side effects [21]. Conversely, anti-angiogenic therapy can be used to destroy the tumour vasculature, and consequently blood supply, in a process known as pruning [9]. However, it is uncertain whether this will damage normal vasculature and tumours do not consistently shrink during the treatment. The lack of understanding regarding the action of anti-angiogenic therapies led Carmeliet and Jain (2000) to highlight the need for new imaging methods which can monitor treatment response. More recently, there is increasing evidence that, in some cases, anti-angiogenic therapies can work to make the tumour vasculature more ordered for a period of time. This is called normalisation [15]. By administering anti-cancer therapies during this window of normalisation there is a potential to improve treatment efficacy [15]. Figure 1-4 also shows three possible scenarios following treatment of tumour angiogenesis; pruning, normalisation, or no response to treatment. However, there is much that is unknown about the function of these agents and more research is required. Thus, a non-invasive, longitudinal technique would be useful in a research capacity to understand the action of anti-angiogenic agents and eventually to monitor treatment response.

The drastic changes to microvasculature during the formation of tumours, and also during anti-angiogenic treatment, makes the imaging of tumour microvasculature an excellent clinical application for SRUS. There is currently no non-invasive modality capable of visualising the structure and function of tumour microvasculature at depths greater than a few millimetres.

1.2 Other modalities

Imaging a point source will produce a point spread function. The width of which will be dependent on the imaging modality and acquisition parameters. The following sec-

tion will summarise the fundamental and practical factors which limit the resolution of the main medical imaging modalities.

1.2.1 Magnetic resonance imaging

Magnetic resonance imaging (MRI) uses the interaction of the water molecules in the body with applied magnetic fields to image deep within tissue (full body imaging is possible) [22]. The hydrogen atoms in the water molecules act like magnetic dipoles, of which a subset can be polarised using a magnetic field. The resonant frequencies of the polarised nuclear spins of the water molecules have a linear dependence on magnetic field strength. By transmitting a RF pulse tuned to this frequency these spins can be excited. Upon relaxation, a signal is emitted which can be detected by a receiver coil. The position of these spins can be encoded by applying a gradient magnetic field along a particular axis, in addition to the static field. Thus, the resonance frequency of a spin will depend on its position and thereby the spins can be excited slice by slice. This frequency space (k-space) is sampled over time to reconstruct a full image. Contrast between different tissue is obtained due to different tissue having different amounts of water.

One factor which determines the resolution of MRI depends on the maximum gradients that can be applied in order for different planes within the body to be distinguished from each other. However, this maximum gradient is generally set at an upper limit (regardless of field strength) to prevent physiological effects like peripheral nerve stimulation [23]. High resolution images require a larger portion of this space to be sampled compared to low resolutions. Thus, the resolution also depends on the acquisition time. For a given time there is also a trade-off between resolution and SNR [24]. Thermal noise of electrolytes in the patient and electrons in the signal receivers mean that MRI data is inherently noisy. Thus, for a feasible acquisition time, either resolution can be improved by acquiring more of k-space, or SNR can be improved by taking averages of lower resolution images.

Most scanners in routine clinical use operate at field strengths of 1.5 T or 3 T and allow resolutions on the order of 1 mm [25]. Increasing the field strength is a

way of approaching the trade-off between time, resolution and SNR. This is because increasing the field strength increases the spin polarization of the tissue and thus the obtainable SNR. 7T scanners are becoming clinically available, and one model has been approved for clinical use in both Europe and the US [26]. Using a 7 T research scanner, vessel imaging in the brain have been acquired with isotropic resolutions of 200 μm. Each image took between 20-30 minutes to acquire. However, two images were acquired to provide sufficient SNR, giving a minimum scan time of 40-60 minutes [27]. Including positioning and pre-scans, the volunteers had to be scanned for a total time of 90 minutes. These long scan times increase the sensitivity to motion, and ultimately the resolution will be limited without the ability to correct for involuntary motion like the movement of the brain due to blood pulsatility, eye movements and muscle relaxation [27]. Regardless, staying still for up to 90 minutes is generally not feasible for unwell patients.

1.2.2 X-Ray/CT

X-ray imaging involves transmitting X-rays through the patient and receiving at a detector on the opposite side of the emitter. The amount of photons absorbed depends on the electron density of the tissue [28]. Computed Tomography (CT) combines X-rays taken at multiple angles to generate a 3D representation of the body. However, both CT and X-ray have poor soft tissue contrast. For the visualisation of vessels, an iodinated contrast agent can be injected [29]. The high atomic number of iodine means that it strongly absorbs X-rays, increasing vessel contrast with respect to the surroundings [30].

Compared to other non-invasive modalities, CT generally has high spatial resolution of approximately 0.5-0.625 mm along each axis [29]. This is in addition to a reasonable temporal resolution of 83-135 ms. This value for spatial resolution comes from the size of the detector elements. The majority of CT detectors are made from arrays of detector elements of dimensions 0.5-0.625 mm^2 [31]. The detectors are separated with a small gap to prevent crosstalk (signals at one element affecting adjacent elements). However, any photons that hit this gap do not contribute to the image,

which reduce the efficiency of radiation use. Therefore, there is a limit to how small these can be made due to the need to limit patient exposure to ionising X-rays. The other factor which limits resolution is the focal spot size of the source. Larger spot sizes will increase image blurring on the detector elements.

CT can only reach the necessary resolution in animal studies with micro-CT imaging, where resolutions of 1 μm are possible [32]. In particular, *ex vivo* studies can provide superior resolution by filling the vessels with a polymer such as microfill before imaging. This approach has been used for monitoring therapy during *in vivo* testing [33]. However, due to the high doses required, there are concerns that the radiation exposure may affect the results of *in vivo* studies during micro-CT imaging [34].

1.2.3 SPECT/PET

Single photon emission computed tomography (SPECT) and positron emission tomography (PET) are nuclear imaging techniques which detect gamma radiation emitted from radioactive tracers injected inside the patient. SPECT tracers directly emit gamma rays whereas PET tracers emit positrons which annihilate with an electron to produce a pair of gamma photons emitted in opposite directions.

SPECT detectors are generally made of a continuous scintillator crystal, coupled to an array of photomultiplier tubes [35]. In order to determine the direction of travel of a photon a collimator is positioned over the crystal. Collimators are made from a material such as lead that will absorb the photons. Narrow channels are made through the material so that only photons travelling over a small range of directions can travel through a specific channel to reach the detector [36]. As in CT imaging there is a trade-off between resolution and sensitivity to the ionising radiation. The design of these holes are varied according to desired image magnification, sensitivity and resolution [36]. Sub-millimetre resolutions are possible using a pinhole detector. However, high magnifications and therefore a small FOV make this detector choice most suitable for small animal imaging. The detectors also have an intrinsic resolution depending on the crystal and positioning electronics [37]. The two primary factors

are; photons undergoing multiple scattering in the crystal which produces an error in the position recorded, and statistical fluctuations in the number of photons produced by the scintillation crystal for a different event from the same position cause variation in the calculated position. This statistical variation is generally the limiting factor and results in a PSF with FWHM of 2.9-4.5 mm. However, research is ongoing in developing new detector materials and resolutions of approximately 0.5 mm have been measured [38]. There are no fundamental limitations on the resolution of SPECT, but detector limitations mean that currently resolving vasculature is not feasible.

PET no longer needs collimators; if two photons can be detected approximately simultaneously, and at approximately 180^o to each other, they are assumed to be from the same event. Thereby, the line where the event occurred can be determined. Timing differences between the two signals mean that the position of the event along the line can be determined. For PET, resolution is now limited two physical factors. The photons may not be truly collinear due to some net momentum of the positron/electron system. This factor can lead to a PSF blurring of approximately 1.5 mm FWHM [39]. Another limiting factor is that emitted positrons can travel away from the radioisotope before annihilating. This can occur in any direction and thereby further increases uncertainty in the calculated position. This depends on the isotope used and is 0.54 mm FWHM for F^{18} [40]. In the clinic, the dominant factor limiting resolution is normally the detector element size. These normally have an area of 4 mm x 4 mm. Decreasing this size can be unfeasible due to increased expense and decreased sensitivity [40]. The positron range and collinearity are the only factors that fundamentally limit the resolution of PET [40]. Moses (2011) predicts their combined effects (for F^{18} imaging) to be 1.83 mm FWHM and 0.67 mm FWHM for clinical and pre-clinical imaging respectively. In the field of tumour imaging, PET is instead valuable for functional imaging rather than structural, for example measuring the microvascular tumour uptake of agents [41, 42].

1.2.4 Optical imaging

The resolution of optical imaging is limited by the diffraction of light. Diffraction is the spreading of light when it encounters an obstacle (generally the microscope objective). The Abbe limit was the first description of how the spreading of the light depended on the wavelength. In his first work, E. Abbe (1873) stated that the separation between two point sources could never be less than $\lambda/2$ if they were to be resolved [43]. This was later refined to describe the effect of the numerical aperture (NA) [44]. Where the NA is a measure of the range of angles which an optical system can accept light [45]. The limit was derived to be:

$$D_{\mathrm{xy}} = 0.5\frac{\lambda}{\mathrm{NA}} \tag{1.1}$$

$$D_{\mathrm{z}} = \frac{2\lambda}{\mathrm{NA}^2} \tag{1.2}$$

where D_{xy} is the smallest detectable lateral feature (in the image plane) and D_z is the smallest detectable axial feature. This limit comes from considering the diffraction pattern of an optical point source being imaged through a circular aperture. The diffraction pattern of such a point source is an Airy disk. Figure 1-5 shows the diffraction pattern for two nearby optical scatterers. A more commonly used measure of resolution is the Rayleigh criteria, which states that for two points to be resolved they must be separated by the distance between the disk maxima and first minima.

This corresponds to lateral resolution of:

$$D_{\mathrm{xy}} = 0.61\frac{\lambda}{\mathrm{NA}} \tag{1.3}$$

Below the resolution limit, the point spread functions of two points overlap such that they cannot be distinguished as shown in Figure 1-5.

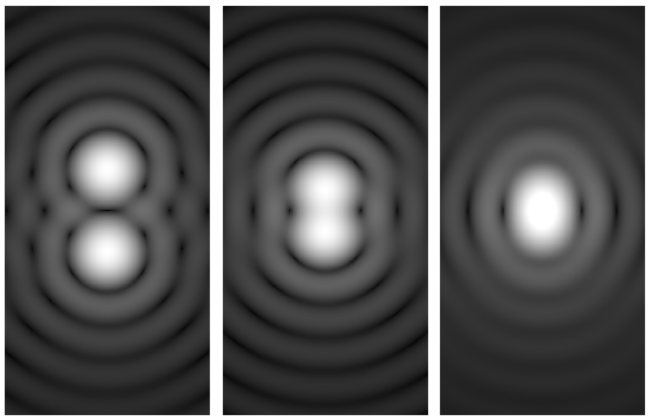

Figure 1-5: The Rayleigh diffraction criteria for two nearby optical scatterers. The two scatterers are spaced further than the Rayleigh criteria (left), at the Rayleigh limit (middle) and closer than the diffraction limit (right). This image "Airy disk spacing near Rayleigh criterion" by S. Bliven has been fully released to the public domain so can be used freely.

Due to the high frequencies of optical radiation, optical resolution is limited laterally to distances on the order of 200-250 nm [45]. Therefore, optical methods are currently the primary option for non-invasive imaging of microvasculature [46]. However, tissue attenuation increases with increasing frequency due to increased scattering [47]. Thus, optical techniques can only be used for superficial imaging. Optical coherence tomography (OCT) uses low wavelength laser light to maximise this depth [48]. This can generate images with resolutions of 5-10 μm but is only suitable for depths of 1-3 mm due to scattering [46].

Optical imaging can still be useful *ex vivo* as a ground truth to test other methods. For example, immunohistochemical (IHC) analysis involves the tumours being set in paraffin and stained to allow measures of the vasculature to be extracted optically. Then average measures of vessel parameters like rBV can be extracted.

1.3 Ultrasound imaging

Ultrasound (US) is defined as longitudinal waves with frequencies higher than the range of human hearing $>$ 20 kHz. Clinical US imaging generally uses frequencies in the range of 2-10 MHz [22]. The formation of an US image generally involves the

transmission of an US pulse into the tissue and receiving the returning signal which has been reflected from tissue boundaries. Given an estimate for the average speed of sound in the subject, and the time taken for the pulse to be reflected, the distance to a particular boundary can be very simply calculated. Repeating this across the FOV enables a map of the tissue structures to be reconstructed in a process known as beam forming.

Described by Wells (2005) as an example of one of the most disruptive applications of science and engineering to medicine [49], US is a desirable modality to optimise for SR. This is due to US being affordable, portable and without the need for ionising radiation. This section will outline the basic physics of US. This will contain the necessary background to understand the motivation for the design of the simulation used in the next chapter. Particular attention will be given to the factors which affect the resolution of conventional US.

1.3.1 Transducers

Transducers are used to transmit and receive the sound signal and can take many forms. Sound is generated using a piezoelectric material. Piezoelectric materials can transform electrical energy to mechanical energy and vice versa. The first transducers were a single element which vibrated at a resonant frequency (depending on its width) in response to an electrical delta pulse [22]. Modern transducers have an array of several elements and also can operate over a range of frequencies. The frequency can be controlled by the input electrical signal [22], and the range of frequencies a transducer is sensitive to is known as its bandwidth.

1.3.2 Phased arrays vs linear arrays

The two types of multi element probes used for the work throughout this thesis are linear arrays and phased arrays. Linear arrays have a line of elements and typically uses a subset of elements to produce a narrow US beam. Phased arrays can electronically focus and steer the beam whilst using all the elements [22]. This is done by

exciting the elements so that they emit signals with phase differences relative to each other.

1.3.3 Image formation

Transmission

Conventional B-mode US involves building up an image line by line [50]. Using a linear array, this is achieved by firing a small group of elements to acquire one line, and then on the next pulse a new subset of active elements is defined. This new subset has normally just shifted along the array by one element. This continues for each line.

Phased arrays can build up each line by adjusting the electronic delays over the active elements. The focal depth of the beam is determined by the transducer width, any extra lenses coupled to the transducer face and any electronic phase delays.

This work primarily uses linear arrays, where each pulse uses 64 active elements. These elements use phase differences across the 64 elements to focus the beam. Instead of additional steering, as would be possible with a true phased array, the image is built up line by line by shifting the subset of active elements over the full transducer face, as shown in Figure 1-6.

The rate at which a transmitter sends a pulse is known as the pulse repetition frequency (PRF). Between pulses the wave needs enough time to propagate to the required depth and back. Thus, temporal resolution is primarily limited by imaging depth. For B-mode imaging, the total frame rate is lowered by a factor of the number of image lines.

This work also uses plane wave (PW) imaging, which is limited by the time it takes for the pulse to propagate through the tissue depth. PWs are generated by firing all active elements of the probe simultaneously [51]. This means that the full FOV is sampled in one pulse. The high frame rates achievable with this approach make it possible to image transient events which require a high temporal resolution [51, 52]. The two techniques are represented schematically in Figure 1-6.

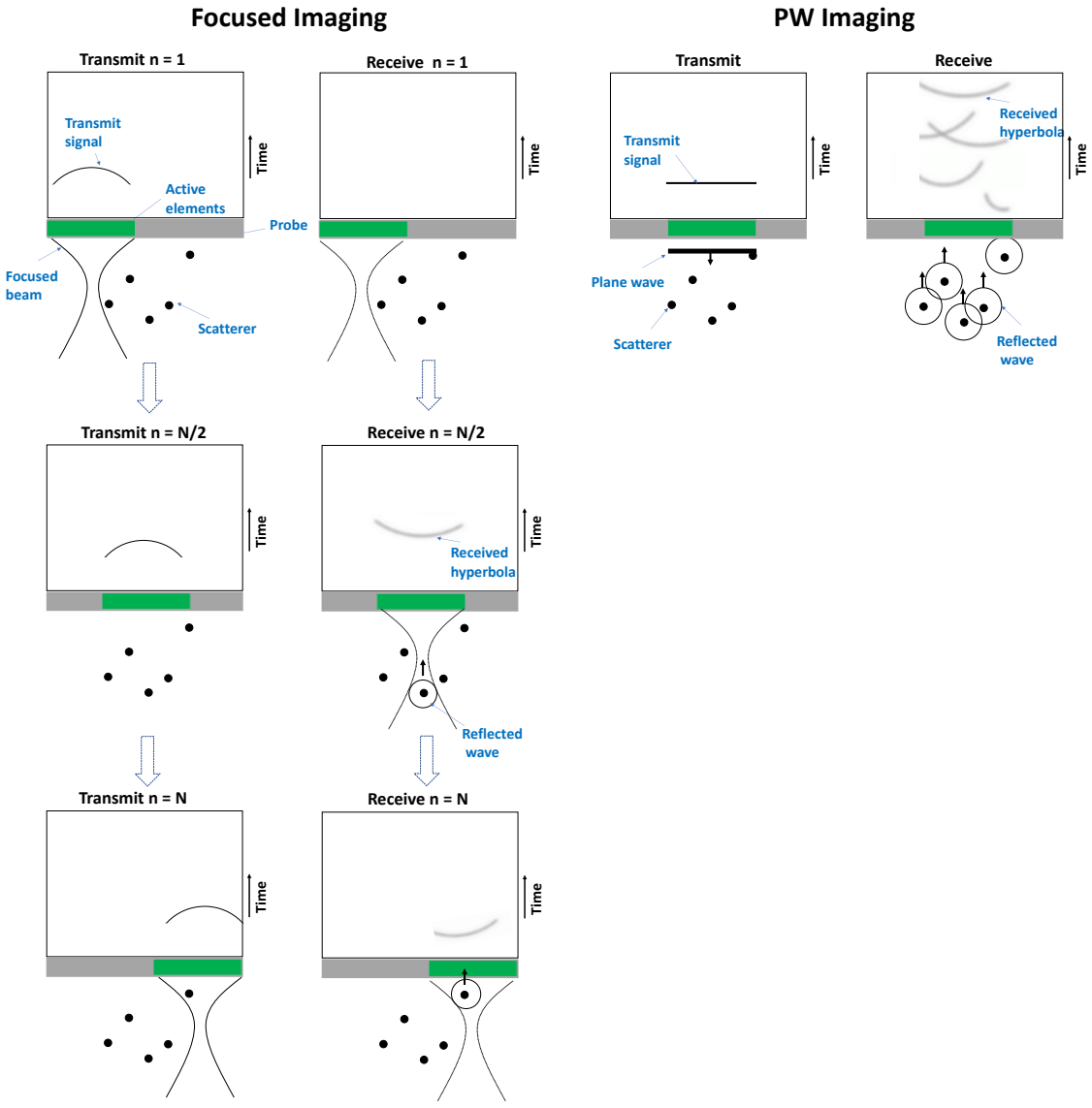

Figure 1-6: Image acquisition schematic. Focussed imaging (left) creates an image of the scatterers line by line, whereas plane wave imaging (right) can acquire the full FOV in a single shot. The green elements are the active elements.

Reflected signal

The transmitted beam is then reflected from boundaries/inhomogeneities in the medium. The strength of this signal depends on the impedance difference between the mediums either side of the boundary. Tissue impedance is the product of the tissue density and speed of sound in tissue. Larger differences in impedance are associated with

stronger reflected signals.

Reception

Between the transmit pulses the transducer must switch to receiving mode, so that the piezoelectric material can record vibrations from reflected signals. These are typically weak compared to the transmit pressures, thus have to be amplified using pre-amplifiers. At this stage, the signals can also be amplified according to the depth that the signals have travelled from in a process known as time gain compensation (TGC). This compensates for exponential signal attenuation with depth, which will be discussed in more detail in subsection 1.3.7. These analogue signals can then be sampled to a digital representation using analogue to digital converters (ADC).

Beamforming

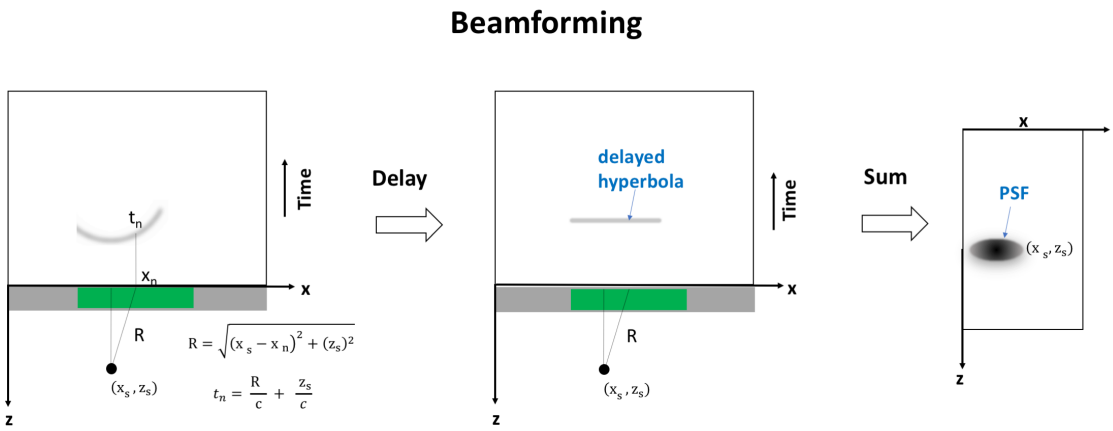

Figure 1-7: Delay and sum beamforming for plane wave imaging. The equation of the signal parabola with respect to time is calculated (left) for each pixel, the hyperbola is delayed (centre) and summed to produce an image (right).

Now the signal can be electronically beamformed. This beamforming is performed based on the relative spacing of the elements. The signal from a point scatterer is a spherical wave. Thus, it will not reach each element simultaneously, instead it will follow a hyperbola pattern over the aperture extent.

For beamforming, the signal at each element is delayed according to how far a signal must have travelled from a particular position. This delay process is simply the reverse of the focusing procedure. The signals for all elements can now be coherently summed to give an overall signal. This is known as delay and sum beamforming (DAS). Dynamic beamforming can be achieved by adjusting the delays according to depth, this is because deeper targets will have less variation in arrival times over the probe elements than shallower targets.

For PW imaging, the only focusing is in receive. For each pixel in the FOV, the signal over the parabola associated with it can be delayed and summed. Thus, a full image can be formed from just one transmission. This is shown in Figure 1-7. The equation of the signal hyperbola with respect to time is t_n for an element x_n, and a position in the FOV (x_s,z_s). The method for focussed imaging is very similar, just that x_s is the lateral focus position and z_s can be fixed or vary with depth (dynamic focusing).

1.3.4 Array geometry

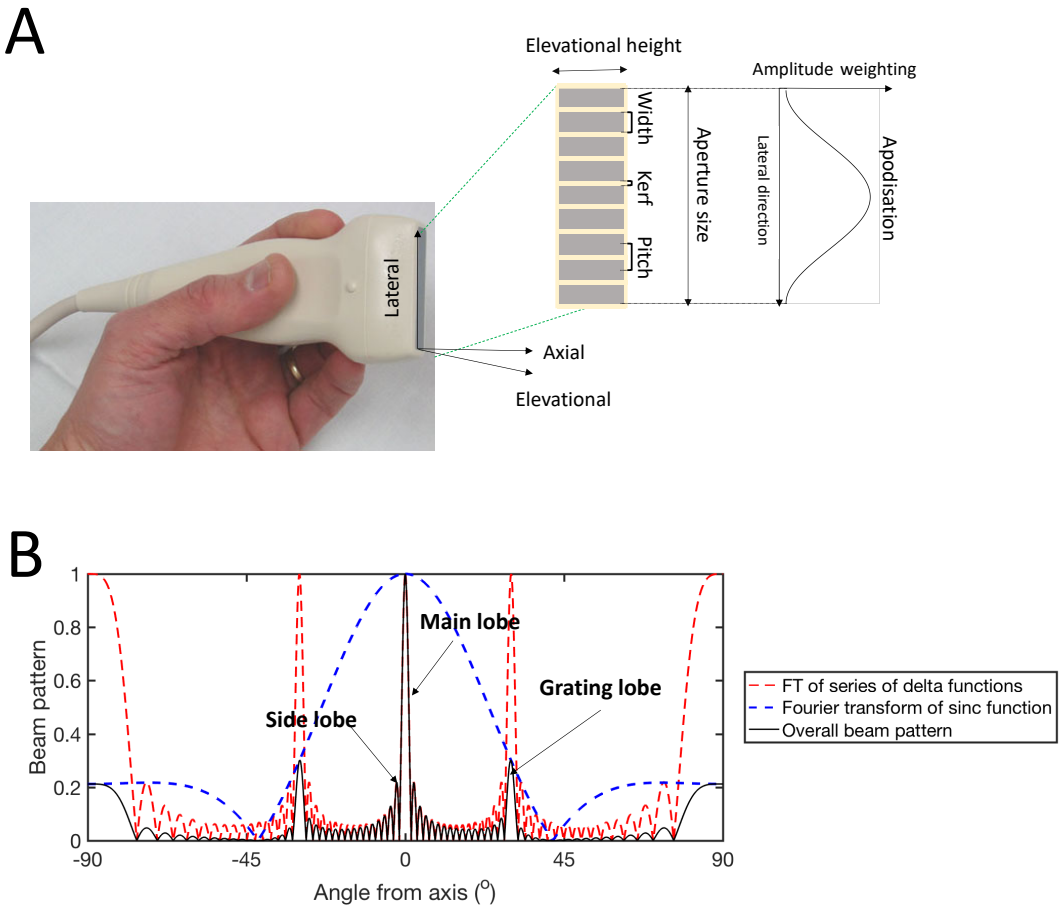

Figure 1-8: Probe geometry and artifacts. (A) shows an example linear array probe with a schematic of the array face geometry. A possible apodisation function is also shown. The probe image on the left is adapted from "Medical Ultrasound linear array Probe/scan head/transducer", by Daniel W. Rickey 2006, which is licensed under the Creative Commons Attribution-Share Alike 2.5 Generic license. (B) shows the overall normalised beam pattern (black) with side lobes and grating lobes due to contributions from a finite aperture and element size respectively.

Figure 1-8(A) introduces some of the terminology used when discussing arrays. The spacing between element centres is known as the pitch. The distance between the elements is the kerf, and the lateral extent of the element is width. Emitting energy from a finite aperture can generate artifacts. Grating lobes and side lobes are parts of the US beam that are not emitted along the axis of the intended beam direction [53]. However, their reflections are strong enough to interfere with the image reconstructed

assuming reflections from the main lobe only.

The beam pattern is shown in Figure 1-8(B). Side lobes arise from the generation of an US beam using a finite aperture. The diffraction pattern of a wave propagating through an aperture is the Fourier transform of the aperture (assuming Fraunhofer diffraction). Therefore, the far field pattern is a sinc function for a rectangular aperture. These first side lobes are substantial relative to the main lobe [54]. Smoothing the sharp edges of the rectangular aperture reduces this high frequency signal. Thus, the emitted signals are normally tapered for the outer elements using a function such as Hamming, Henning, Gaussian, etc. in a process known as apodisation.

Grating lobes are due to splitting the aperture into a line of elements. Mathematically, the aperture can be represented as a sum of delta functions convolved with a finite aperture of width equal to the element width. The Fourier transform of a grating is periodic, with a frequency that depends on the element pitch relative to the wavelength [55]. If the width is $\geq \lambda$ then grating lobes will occur. To avoid grating lobes completely (even when the beam is steered) the element spacing should be chosen to be smaller than $\lambda/2$.

1.3.5 Data types

The multiple types of data collected and visualised throughout this thesis will be briefly explained here. Radiofrequency (RF) data refers to frames which still have the phase information. This can be pre-beamformed, that is the hyperbolas incident on the aperture before delay and summing, or post-beamformed. The oscillatory nature of this data can make structures difficult to visualise. Thus, this is often presented as Bmode data. Bmode data is where the phase information is removed by just representing the envelope of the signal. The envelope of a signal is the magnitude of the analytical signal. The analytic signal is a complex number, which is made from combining the original signal with its Hilbert transform as below:

$$X_{\text{analytical}} = X_{\text{real}} + iX_{\text{hilb}} \tag{1.4}$$

The Hilbert transform gives every Fourier component of the original sequence a 90^o phase shift. By combining the original signal with its Hilbert transform, the negative frequency components are removed and instead the signal is represented with a real (I) and quadrature (Q) part. Data represented in this way is known as IQ data. IQ data can be collected from the research scanner used in this work. Figure 1-9 shows some of these different data types.

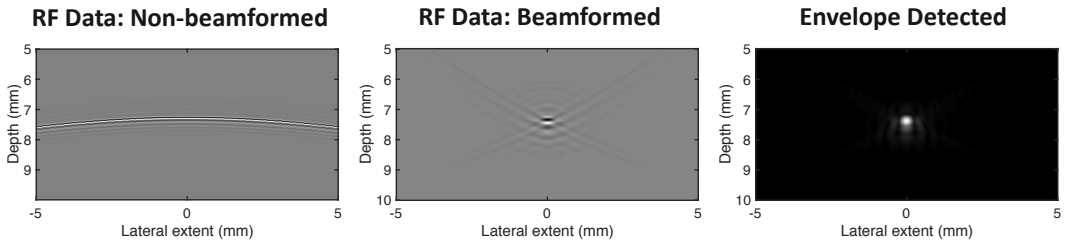

Figure 1-9: Types of US data. Each frame shows signal from the same scatterer. Phase information can be shown in non-beamformed RF data (left) or beam-formed RF data (centre). It can be easier to visualise envelope detected data (right).

1.3.6 Spatial resolution

Axial resolution

The axial resolution is the minimum distance which two objects can be separated along the direction of beam propagation. This is determined by the spatial pulse length, which is determined by the pulse wavelength (λ) in the medium and number of cycles (n) of each pulse.

$$\mathrm{SPL} = \lambda n \tag{1.5}$$

This can also be expressed in terms of temporal pulse length (t_p):

$$\mathrm{SPL} = t_{\mathrm{p}} c \tag{1.6}$$

where c is the speed of sound.

Axial points are said to be resolvable if they are separated by > 0.5 SPL [22]. The temporal pulse length should be low for the optimum axial resolution. However, this requires the transducer to have a wide bandwidth. The transducer bandwidth is determined by how well damped the piezoelectric crystal is to the electrical input. This requires careful choice of transducer material, and surrounding layers [56]. Generally $n = 1.5$ - 2 for clinical US transducers [56].

Axial resolution does not vary with depth and is the same for B-mode and PW imaging.

Lateral resolution

The lateral resolution is the minimum distance which two objects can be separated along the direction of the probe elements. This is depth dependent and depends on the beam diameter at that depth in tissue. Generally, in B-mode imaging, the focus is defined at a single depth. This means that the best lateral resolution will be at that specific depth and will worsen either side. Considering the maximum resolution at the focal depth, mathematically, the PSF in the lateral direction of B-Mode imaging is a sinc^2 function w.r.t. to the lateral direction (x) [56]. This is because the Fourier transform of a rectangular aperture is a sinc function and the PSF is a result of transmitting and receiving through this aperture. The received signal *U(x)* is given by:

$$U(x) \propto \text{sinc}(\frac{xD}{f\lambda})^2 \tag{1.7}$$

where D is the aperture width and f is the focal length.

As in optics, the Rayleigh criteria is normally used to express the diffraction limited resolution. Applying the Rayleigh criterion that the points are well resolved if separated by a distance between the maximum and the minimum, the sinc can be set to 0, giving a minimum separable distance of [56]:

$$\Delta x = \frac{f\lambda}{D} \tag{1.8}$$

Other authors prefer to consider the resolution in terms of the FWHM [57] where

$$\text{FWHM} = constant \cdot (\frac{f\lambda}{D}) \tag{1.9}$$

and the constant depends on the transducer apodisation.

For PW imaging, the spatial resolution has been empirically determined to be:

$$\Delta x = constant \cdot (\frac{L\lambda}{D}) \tag{1.10}$$

where L is depth and the constant was determined to be 1.521 [58].

Due to the lack of transmit focusing, PW imaging has worse lateral resolution than focussed. Using coherent compounding, which involves combining PWs of different orientations, the resolution can be improved [51].

Elevational resolution

This is the resolution perpendicular to the imaging plane and is defined by the transducer width [22]. The signal in the 2D imaging plane is a projection over the extent of the elevational direction that the probe is sensitive to. Again, this is the same for focussed and PW imaging. It should be noted that 3D imaging can be achieved using 2D matrix array probes. In this case, the conventional resolution in the elevational direction equals that in the lateral direction.

1.3.7 Depth vs resolution

It can be noted that increasing the frequency of the transmit pulse will improve lateral and axial resolution. However, as in optical imaging, there is a trade-off between frequency and depth penetration. Acoustic attenuation is primarily due to scattering and thermal absorption. The US wave is exponentially attenuated with depth [54]:

$$I = I_o e^{-2\mu x} \tag{1.11}$$

where x is the distance travelled (2 times the depth), I_o is the initial intensity and μ

is the attenuation coefficient in dB/cm.

In soft tissues μ is proportional to wave frequency (f) to the power of m:

$$\mu \propto f^m \tag{1.12}$$

For most applications in diagnostic US, $m \approx 1$ [56]. Increasing frequency will limit the depth penetration of the US beam through tissue. In conventional imaging, this makes it harder to reconstruct high resolution images at depth.

1.3.8 Safety

An investigation on safety is not a focus of this thesis. However, previous authors have cautioned that although US is often considered safe it does have bioeffects which should be understood [59].

There are two main safety hazards normally discussed when considering diagnostic imaging, thermal effects and cavitation. Thermal heating is due to energy deposited in the tissue due to attenuation [60]. Cavitation can arise from the gas nuclei in liquid parts of the medium expanding into a bubble. This bubble may then oscillate in response to the US pulse (stable cavitation). Or, in the compression phase the bubble may violently collapse (inertial cavitation) [59]. Less well understood is also the effects from radiation pressure, this can cause movements of particles in the medium, in particular in liquids (known as acoustic streaming) [60].

The thermal energy deposited can be monitored using the thermal index (TI):

$$\mathrm{TI} = \frac{W_{\mathrm{out}}}{W_{\mathrm{deg}}} \tag{1.13}$$

where W_{out} is the acoustic power for the imaging conditions and W_{deg} is the power required to raise the temperature by 1^oC. Most clinical scanners estimate the TI value based on whether the US is incident on soft tissue, fluid or bone. This is because these mediums have very different attenuations, bone being the highest so most at risk for thermal effects [60]. Imaging for longer times increases the risk of damage from heating. Thus, there have been guidelines published on the time and TI value

that should be used for specific applications explaining that TI values greater than 0.3 should be avoided [59].

Cavitation has been shown to cause microvasculature damage in animal models [59]. In particular, inertial cavitation poses the most risk. Inertial cavitation has been associated with light emission, shock waves and the generation of free radicals. This was estimated to occur at temperature > 5000 K, and this led to the definition of mechanical index (MI) as a measure of the likelihood of cavitation:

$$\mathrm{MI} = \frac{\mathrm{PNP}}{\sqrt{f}} \tag{1.14}$$

where PNP is the peak negative pressure (maximum rarefaction pressure) and f is the transmit centre frequency [54]. Without MBs, the likelihood of bubble formation is low for MI < 1 [61].

There is some concern over the sheer stress on cells due to acoustic streaming [59]. However, Duck (2008) expresses that as the bioeffects causes by radiation pressure is not well understood it is difficult to assess the risk, and there are no official safety measures such as the TI and MI values. Duck (2008) also writes that the highest risks associated with diagnostic US come with the use of contrast agents [60]. Thus, this will also be considered in section 1.3.10, after MBs have been introduced.

1.3.9 Research systems

Research systems allow much more control of the image acquisition process compared to clinical scanners. Another key benefit is access to the raw data, so that images are not changed by unknown image processing and compression procedures. This work uses the ULA-OP research platform which has 64 independent channels, each with an independent arbitrary waveform generator [62]. Thus, the system can be programmed to transmit and receive over a wide range of parameters. For example, transmit frequency, PRF, apodisation, focusing, beam steering angle, aperture size and receive gain can all be customised [62]. The system has a sample rate of 50 MHz for 12 bit data. During a single acquisition the system can store up to 1 GB of RF data

and 512 MB of image data/IQ data. The data can be extracted in pre-beamformed RF data, post-beamformed RF data or IQ data.

1.3.10 Microbubble contrast agents

The blood itself is a weak scatterer of US. The contrast of blood vessels can be increased by introducing MB contrast agents [63]. MBs are blood pool agents which consist of gas cores encapsulated in a shell, and are generally 1-10 μm in diameter [64]. The high compressibility and low density of the MB core compared to tissue make them strong scatterers of US. Historically, the efficacy of gas bubbles to amplify the blood signal was used before the introduction of commercial agents. For example, bubbles in injected saline were used to increase contrast for imaging of aorta function. These bubbles were assumed to either occur during the injection process or already exist in the saline [65]. Their lifetime could be enhanced by pre-combining with the patient's blood, where the surfactants acted as a type of shell [66]. Indeed, this method is still in use clinically by mechanically agitating saline (with or without patients' blood) prior to injecting. These bubbles are unstable and unlikely to survive the pulmonary circulation, thus the only way they can enter the left side of the heart is if there is a deviation in normal circulatory flow (a cardiac shunt) [67]. However, these homemade bubbles are still unstable [68]. Engineered bubbles have a shell and core which are designed to have good persistence in the blood stream and a predictable response to an US pulse.

As of 2015, Paefgen et al. (2015) reported that there were 4 commercially available, approved, contrast agents in clinical use worldwide [69]. They are principally used for adults [70]. Although, in the US, they were recently FDA approved for paediatric liver examination in 2016 [71].

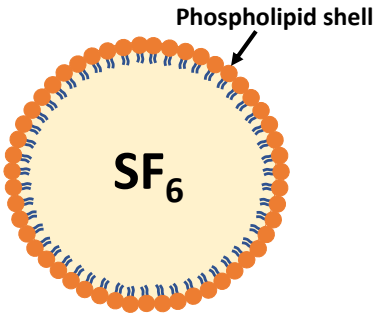

Figure 1-10: Schematic of a Sonovue MB.

Gas core

Bubbles are unstable because of the surface tension between the gas core and surrounding liquid; thus, the gas wants to diffuse into the liquid. Changing an air core to an alternative gas which has a lower solubility and lower diffusivity than air makes the MBs more stable. For example, perfluorocarbons have been used for several brands [68]. Sonovue uses sulphur hexa fluoride [72]. In a standard dose of 2 ml only 16 µl of sulphur hexafluoride (SF_6) is given. This dissolves in the blood and is exhaled (after 15 minutes almost 100% of the gas was recovered in tests). A schematic of a Sonovue MB is shown in Figure 1-10.

Shell types

The MB shell helps to stabilise the MB. The three main types of shell are polymer coating, proteins and lipid [73]. The properties of the shell affect the MB response to acoustic radiation. For example, protein shells are relatively rigid [73], whereas phospholipids create a flexible shell which will allow the MB to strongly oscillate in response to acoustic pulses without breaking [68].

The Sonovue shell uses two types of phospholipids (DSPC and DSPG.Na), and palmitic acid to form the shell [74]. To make Sonovue, saline is injected into a vial of lyophilisate containing the phospholipids and the gas. Agitation of the two parts causes the phospholipids to self-assemble around the gas bubbles. The phospholipids

are weakly held together by Van der Waals forces [73].

Behaviour of MBs in an acoustic field

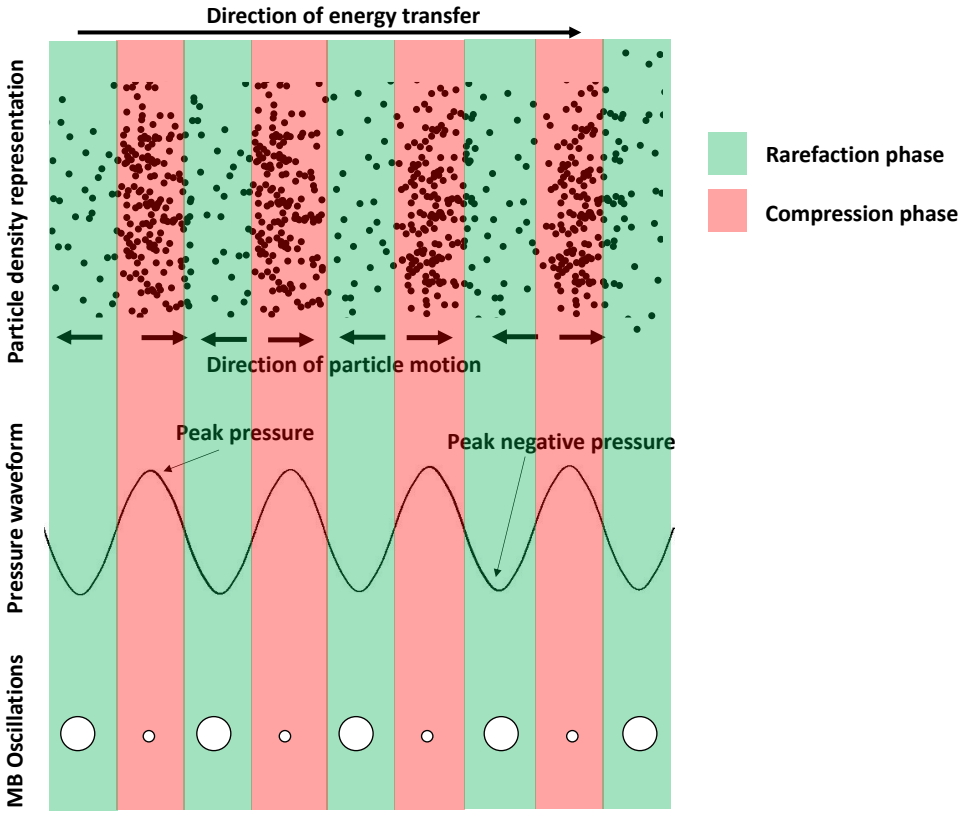

Figure 1-11: MB interaction with an acoustic field. Sound waves propagate by particle motion in the medium (top). The pressure wave can be described as a periodic variation in density, where individual particles oscillate about their resting position. This can also be represented as a pressure waveform (middle) where peak pressures correspond to compression of the medium and peak negative pressures correspond to rarefaction. A MB will be compressed in the compressive phase and expand in the rarefaction phase (bottom).

MBs will volumetrically oscillate in response to the acoustic field as shown in Figure 1-11 [75]. The high compressibility of the MBs mean that they are highly echogenic, so much so that individual MBs can be detected. The simplest linear model of the MB is of a damped simple harmonic oscillator. This system has a resonant frequency inversely proportional to the MB radius [75]. More commonly in the literature, MBs have been described by models that capture the effect of shell properties, core gas

and surrounding liquid properties [68]. Using US pulses at the bubble resonance frequency will produce a stronger bubble response signal [73]. Conveniently, the resonance frequency of micrometre sized bubbles lies in the range of commonly used medical US frequencies (1-10 MHz) [73].

Optical observations of MBs under acoustic pulses have been an important method of understanding their behaviour in an acoustic field [76, 77, 78]. This has uncovered other physical phenomena such as the translation of MBs due to the acoustic radiation and the coalescence of nearby oscillating MBs [79]. By examining the response of MBs to a known pulse, the properties of MBs have been determined and different models compared [80, 81]. Optics have also shown how US can cause MB destruction through several different mechanisms - slow diffusion, damage to shell, fragmentation into smaller MBs or rapid expulsion of shell from the MB core [82]. Now optical systems are even developed enough to optically observe the interaction of a MB and cell in response to an US pulse [83]. The optical literature specifically relating to SRUS will be discussed in Chapter 3.

Non-linear imaging

As the incident amplitude of the US increases, and the frequency approaches that of resonance depending on the MB size, MBs can generate a non-linear response. This means that the radial oscillations will not have an amplitude linearly proportional to the incidence pulse and the frequency composition will have components other than the transmit frequency. Instead the MBs will emit harmonics, subharmonics and super harmonics of the incident frequency [68].

Figure 1-12: CEUS liver imaging. Example of CEUS scan (right) compared to linear mode (left). This image taken from "Contrast-enhanced ultrasound of an abscess in the liver" by R. Badea and S. Ioanitescu (2012). "Ultrasound Imaging of Liver Tumors - Current Clinical Applications". DOI: 10.5772/31137., which is licensed under CC BY 3.0.

Since sound backscattered from tissue is largely linear, the MB signals can be discriminated from the tissue using their nonlinear response. By combining rescaled responses to pulses of different amplitudes (amplitude modulation) [84] or combining responses to out of phase pulses (pulse inversion) [85, 86], the non-linear signal can be extracted. Amplitude modulation (AM) and pulse inversion (PI) are examples of multipulse techniques. Combining AM and PI can generate more non-linear signal [87]. Figure 1-12 provides an example CEUS image of the liver and Figure 1-13 schematically demonstrates how AM and PI work.

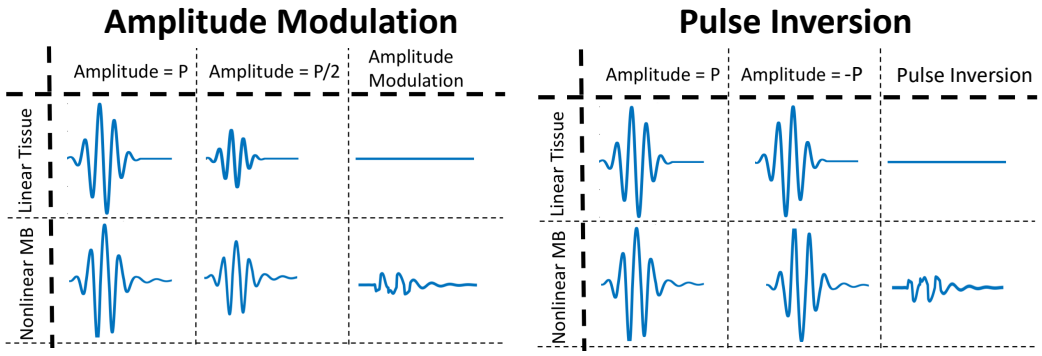

Figure 1-13: Multi-pulse non-linear modes. Schematic of non-linear modes, amplitude modulation (left) and pulse inversion (right). Where AM transmits a pulse of amplitude P, and a second pulse of amplitude P/2. Pulse inversion uses opposite phases for successive pulses. Algebraically combining the responses from tissue (top) and MB signal (bottom) allow MBs to be distinguished from linear tissue.

In this work, a general contrast sequence [1, -1, 0.5] was normally used to allow post processing using amplitude modulation or pulse inversion. This notation means that the second pulse of the contrast sequence has the same amplitude but opposite phase as the first pulse. The third pulse has the same phase but half the amplitude of the first pulse.

Although MBs are generally useful for increasing the contrast of microvasculature, resolution is still limited by diffraction.

MB non-linearity vs nonlinear propagation

Another related interaction worth mentioning here is non-linear propagation of a US wave in tissue. This has a different mechanism from the non-linear signal generated by MBs. Sound waves can be described as pressure waves with dense areas (compressive phase) and less dense areas (rarefaction). Sound propagates by the compression of the tissue particles within the tissue in response to the mechanical movement of the transducer elements. For some applications it is appropriate to use linear physics to describe the subsequent propagation. However, the relationship between changes in pressure and changes in density is not linear, instead there is a quadratic component [54]. At high pressures, this component becomes more prominent and

the linear approximation between the two breaks down. Sound speed depends on the tissue density; thus the compressive phase of the wave has a higher speed than the rarefactional phase [56]. This leads to a distortion of the pulse, such that a sinusoidal pulse become more sawtooth like. This is equivalent to producing more higher frequency signal components. Thus this signal can also be extracted when performing non-linear imaging and lead to non-linear artefacts which reduce contrast of MB signal [88].

Safety

Confidence in the use of Sonovue was dented in Europe after three deaths appeared to be temporally related to the use of contrast agents. It was temporarily withdrawn, but then reinstated with new restrictions against its use in patients with recent acute coronary syndrome or clinically unstable cardiac disease conditions [70]. It is currently advised that extreme care and risk assessment is required for use in such patients and its use is contradicted for some specific cardio-vasculature and respiratory diseases [89]. In 2007 the FDA contraindicated the use of contrast agents in warnings on the labelling to contradict the use of the agent due to risk of cardiac events in high risk patients following four fatalities temporally related to CEUS [90]. Following this, there were several large-scale studies that investigated the safety of MBs and showed that: serious "allergic like" reactions occurred in $\sim$ 1:10,000 patient doses and there was no increased risk of mortality for CEUS imaging of cardiac patients compared to US imaging alone. Therefore, these contraindications were changed to warnings. Clinicians should be prepared for the chance of a rare allergic reaction, as is also the case for contrast agents used in MRI and CT imaging [70, 90].

There has been previous concern over the increased risks from inertial cavitation when using MBs. This is because there is no longer the need to create the MBs from the tissue [59]. Without MBs, the likelihood of bubble formation is low for MI $<$ 1, with UCAs a lower MI should be used to avoid bioeffects (MI $<$ 0.4) [61]. These bioeffects include microvasculature rupture, which could be particularly hazardous for applications such as brain imaging, ocular imaging and neonatal imaging [59].

However, as long as the guidelines are followed, and the necessary precautions taken, the safety profile of MBs is excellent [70]. The most common side effects, reported in around 2% of patients during large clinical trials, have been headache and unusual sensation around the injection area [70]. These are generally brief and do not require treatment.

1.4 Current US microvascular imaging techniques

1.4.1 High frequency

Simply working at high transmit frequencies ($>$ 20 MHz) can decrease the point spread function sufficiently to visualise superficial microvasculature. For example, Goertz et al. (2000) used a 50 MHz centre frequency to detect flow in a mouse ear vessel that was below 20 μm in diameter [91]. However, attenuation in tissue increases at these frequencies, limiting this technique to superficial imaging. One disadvantage of working at high frequencies is low microbubble sensitivity because the bubble resonance is at 1-3 MHz [92].

1.4.2 Doppler

Doppler methods are used to image blood flow [93]. Doppler techniques use the frequency shift between received signals to provide contrast, either through colour doppler where colour maps show the blood velocity and direction or the more sensitive power doppler where only the strength of the signal is visualised [94]. They can be made more sensitive through the introduction of contrast agents [95] or signal processing which takes advantage of the high coherence of blood signal relative to noise [96]. However, these techniques are still subject to the resolution limit.

1.4.3 Acoustic angiography

Acoustic angiography is a contrast technique which uses low frequency transmission and MBs but only receives the high frequency signal components [97, 98, 99]. Thus,

the super harmonic bubble response allow the vasculature to be distinguished from the tissue. Gessner et al. (2013) showed that resolutions of $\approx$ 150 µm axially and $\approx$ 200 µm laterally at depths of 5 mm can be achieved [97]. However, resolutions achieved using these techniques are still limited by the fundamental diffraction limit.

1.4.4 Photoacoustics

In photoacoustic imaging (PAI), optical energy is absorbed by the tissue or optically absorbing dyes/nanoparticles. Thermal energy is then transformed into acoustic radiation due to thermal expansion/relaxation which can be detected using an US transducer [100].

The axial resolution depends on the same factors as the US imaging. However, photoacoustic signals have very high frequencies of several hundreds of MHz, thus the achievable resolution is primarily dependent on the sensitivity of the transducer [101]. For most systems, the lateral resolution depends on the focusing of the optical energy and thus the resolution is limited by the light wavelength, numerical aperture and any optical aberrations [101]. If weakly focusing light energy is used instead, then the lateral resolution depends on the PSF of the US system [101]. One particular benefit of PAI over US alone is the natural contrast of the optical absorption of haemoglobin, which makes PAI particularly useful for microvasculature imaging [102].

However, as in US imaging, there is a depth/resolution trade-off for PAI resolution. It is possible to detect photoacoustic signal at depths up to 5 cm with the help of dye contrast [103, 104]. When the lateral resolution depends on optical focus, resolution of a few micrometres are possible (small enough to visualise capillaries [105]) but the depth resolution is limited to $<$ 1 mm [102].

1.4.5 Microvascular assessment metrics

Here two metrics often used for the quantification of perfusion in US are described.

Maximum intensity over time (MIOT) images show the maximum value of each pixel over the full acquisition time. This can be used to extract rBV values. How-

ever, measurements made from MIOT images may be prone to overestimation due to diffraction [20].

Mean blood flow velocities can be calculated by fitting the slope of the replenishment curve when doing destruction replenishment imaging. This involves a bolus injection, using a destruction pulse to clear the FOV of MBs, then calculating the intensity over time in a ROI. This curve can then be fitted to a model to extract the mean flow speed [106].

1.5 Optical SR

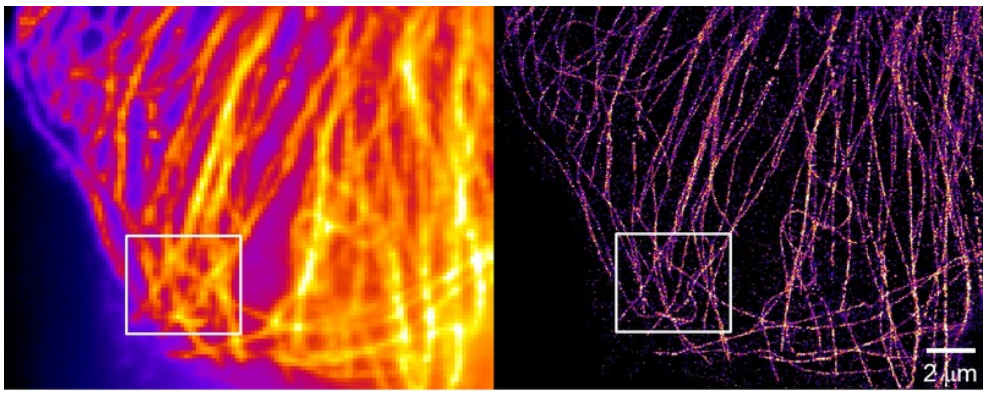

Figure 1-14: Example of optical SR. A diffraction limited image of microtubules in a cell (left) and the SR image (right). This image is by Matthew D. Lew and Steffen J. Sahl, Moerner Laboratory. (2012) This file is licensed under the Creative Commons Attribution-Share Alike 4.0 International license.

The 2014 Nobel Prize for Chemistry was awarded to Eric Betzig, Stefan W. Hell and William E. Moerner for their work developing techniques which allowed visualisation on a intercellular scale using optical microscopy [107]. As in US, the resolution of optical microscopy is fundamentally limited by the wavelength. Conventional resolution allows visualisation of structures on the order of cells. However, there was interest in resolving structures on the subcellular level to learn more about structures and processes on the nanoscale. Figure 1-14 shows an impressive example of subcellular imaging. The three winners of the Nobel Prize developed the tools for several differ-

ent types of SR. The type most relevant to this work is localisation microscopy. It is important to understand some of the ideas in optical SR because authors in the acoustic literature have developed these techniques for US SR.

Fluorescence is the absorption of light energy in the form of photons, and subsequent emission of photons of equal or greater wavelength [108]. Fluorophores are molecules which exhibit fluorescence strongly enough for individual molecules to be imaged above any background signal [109]. These fluorophores can be bound to proteins within cells in order to further understand cellular processes [110]. They can also exhibit interesting temporal behaviour. For example, individual fluorophores can be observed to blink on and off on the time scale of seconds [109]. They can also undergo photobleaching, where the repeated stimulation damages the molecules such that they can no longer fluoresce [107]. Green fluorescent protein (GFP), and variants of it, is a particularly widely used fluorophore. Dickson et al. (1997) made the important discovery that single molecules of GFP could be turned on an off like a switch. They could be imaged using a fluorescent exciting wavelength, and after a period they would turn off. However, this bleaching was reversible, as they could be reactivated using a different wavelength, and fluorescent imaging resumed [109].

The position of an isolated fluorophore can be localised to a much higher precision than the diffraction limited resolution. This can be achieved by using an algorithm to estimate the centre of each fluorophore emission by fitting the signal to a Gaussian [111]. This precision (σ) fundamentally depends on the standard deviation (STD) of the photon distribution from the fluorophore (s) and the number of photons collected (N) [111].

$$\sigma = \frac{s}{\sqrt{N}} \tag{1.15}$$

Since s is of the order of $\lambda/2$, and over 10^4 photons can be detected per fluorophore, the resolution can be on the order of a few nanometres. Thereby, if these localisations can be recorded over the extent of a structure of interest, an image beyond the diffraction limit can be achieved.

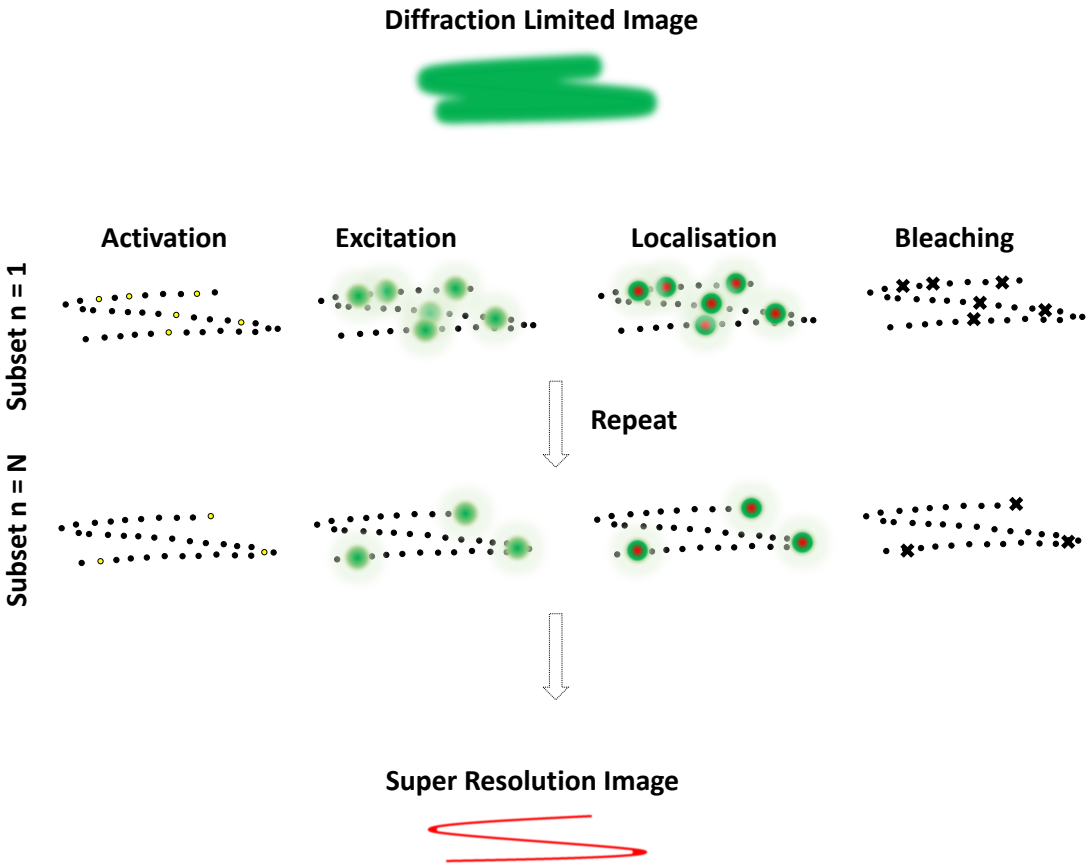

Figure 1-15: Schematic of FPALM. The diffracted limited image does not show the S-shaped structure (top). The image is formed by stochastically activating and imaging N subsets of the fluorophores in the sample. Isolated signals can be localised and the fluorophores in the sample. Isolated signals can be localised and the fluorophores in that sub-set bleached. Combining the localisations from all sub-sets will give an SR image (bottom).

The primary challenge is obtaining a sparse population of fluorophores whilst still being able to image the full structures. The main method from localisation microscopy techniques which has been translated to SRUS, is photoactivated localisation microscopy (PALM) [111] or fluorescent photoactivated localisation microscopy (FPALM) [112]. These are very similar techniques, developed by different groups, which rely on the switchable nature of GFP variants. They activate a subset of the GFP molecules across the FOV using a brief laser pulse. This subset is now imaged using illumination from the excitation wavelength for fluorescent imaging (dif-

ferent from the activation pulse). These should be sparse enough to be isolated point sources. After a significant portion of these have been bleached (either reversibly or irreversibly), a new subset of sources is activated using the brief laser pulse. The number of activated fluorophores can be controlled by the length and amplitude of the activation laser pulse. And the rate of photobleaching can be controlled using the excitation intensity. This process is shown schematically in Figure 1-15.

1.6 Literature review of SRUS

1.6.1 Basic principles

MBs are the acoustic analogue of fluorophores. In particular, they scatter US strongly enough such that individual MBs can be imaged. If isolated signals can be generated from the MBs, then individual scatterers can be localised beyond the diffraction limit. Then the fundamental limitation on the maximum resolution is not limited by the signal wavelength but on how accurately and precisely the localisation can be made.

Figure 1-16 outlines the steps of SRUS. The first step is signal acquisition. The literature review will outline the breadth of acquisition parameters and techniques which have been used in SRUS research. US imaging also has the added complication of signal from the surrounding tissue. Fluorophores normally just need to be extracted from any background fluorescence, which can generally be done by thresholding. Thus, the detection method is a particularly important step for SRUS. One difference between fluorophores and MBs is that MBs move with the blood flow, whereas fluorophores are generally bound to a target. Thus, an optional step of SRUS is velocity tracking of the MBs. Depending on the imaging target, motion correction is another optional step. An essential step of any SRUS using isolated signals is the localisation of the signals, where the scatterer positions are determined. Finally, the visualisation step involves combining all the localisations/tracks to form a representation of the vasculature.

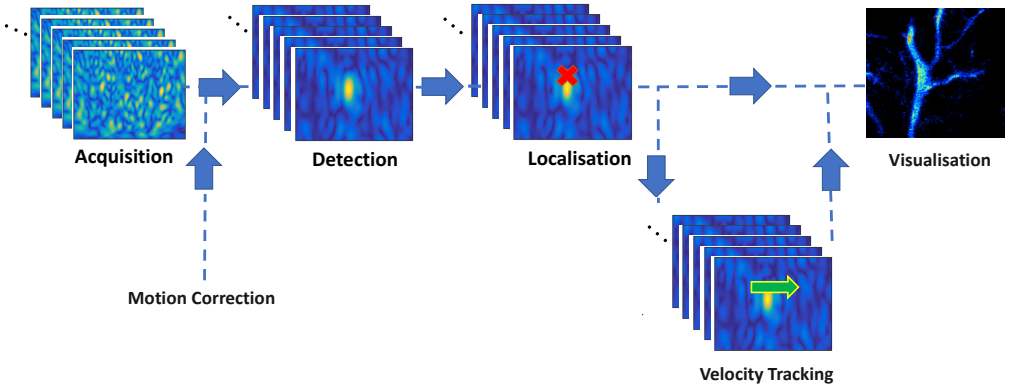

Figure 1-16: Stages of SRUS. Motion correction and velocity tracking can be used if required.

Proof of principle studies *in vitro* and *in vivo* were first published by 4 main groups between 2011 and 2013 [18, 113, 114, 115]. From the initial few publications, interest in SRUS has grown exponentially. This literature review will outline the key pieces of literature within the field and main discussion points to give a full review of the field of SRUS. Special attention will be drawn to areas where there is a need for validation. One of the first points of interest is the potential clinical targets. For clinical applicability, it is also especially important to understand how long acquisition will take. Limiting the acquisition time has also motivated a different formulation of SRUS using statistical measures rather than localisation microscopy; or using nanodroplets instead of MBs. Finally, movement towards 3D SRUS will be briefly discussed.

1.6.2 Clinical targets and directions

Much of the research in SRUS will be applicable to microvasculature imaging in general, rather than a specific disease. The majority of studies in the literature, and discussed here, are pre-clinical but demonstrate a potential clinical direction.

Several examples of healthy tissue have been imaged [116, 117, 118, 119, 120]. Errico et al. (2015) and Christensen-Jeffries et al. (2015) both showed impressive reconstructions of relatively 2D structures (planes of a rat brain and a mouse ear

respectively). Due to it having an interesting branching structure, and well characterised structure and function, the kidney has also been used as a target to test SRUS techniques [117, 118, 119]. Zhu et al. (2019) performed mechanical scanning of healthy lymph nodes in order to visualise the microvasculature in 3D. This was the first step in using SRUS to image lymph node vasculature with a view to detect metastasis [120]. There has been particular motivation to consider angiogenesis as a target [18, 19, 20, 121, 122].

Siepmann and Schmitz (2011) were one of the first groups to demonstrate principles of the SRUS technique [18]. They mainly aimed to show that it was possible to detect and visualise single MBs within tumour microvasculature. The authors provided a comparison between SRUS and MIOT. They demonstrated that SRUS is less likely to overestimate the vasculature area of the tumour. Where SRUS calculated a rBV of 7.7 %, compared to a rBV of 46.3 % using MIOT. This was a very small study of only one sample but showed promise for finer imaging of tumour vasculature. Lin et al. (2017) took the next step in determining if vasculature markers of angiogenesis could be extracted from SR images [121]. The authors show that by processing vessels extracted using SRUS using a distance metric to measure tortuosity, they could show a significant difference between a tumour and healthy tissue. This work compared SRUS to acoustic angiography (transmitting at 4 MHz, receiving at 25 MHz). Although, the imaging time was much longer (one slice requiring 26 s) the results showed that SRUS provided better resolution both *in vitro* and *in vivo*. The authors point to a need to refine the technique in order to increase the efficiency of localisations to improve acquisition time.

It is necessary to consider whether, although existing US techniques do not meet the required resolution, they can still distinguish between tumour types or differentiate between healthy and malignant tissue. A recent work by Opacic et al. (2018) used SRUS to differentiate between three tumour types. The existing techniques compared to SRUS in this work were rBV from MIOT images and the mean velocity determined from destruction replenishment curves [20]. A further aim of this work was to use the SRUS images to generate new biomarkers which could be used to discriminate

between tumours. Surprisingly, velocity measures could not be used to discriminate the tumour type. However, the authors did note that fitting the intensity-time curve was not always possible due to noise, while SRUS was more robust. The rBV could be used to distinguish between the three tumour types using MIOT and SRUS. The most successful marker for discriminating between 3 tumour types using SRUS was the maximum distance between the nearest vessels. This is a metric which definitely does need resolution beyond the diffraction limit. Thus, this study gives motivation for refinement of the SRUS technique. The rBV measures agreed with the measurements from Siepmann and Schmitz (2011) which showed that SRUS was less likely to overestimate rBV than MIOT [18]. Avoiding overestimation will mean that smaller differences in rBV between tumours will be more accurately measured. Preliminary clinical data presented here showed that SRUS could be used to visualise vasculature changes over the course of chemotherapy treatment. After one cycle of chemotherapy, tumours of two patients were observed to become more homogeneously vascularised. This clinical work was extended in later work which reported that SRUS was beneficial over MIOT for visualising inhomogeneity, for example hypervascularity around the tumour borders [19]. And also provided much higher resolution velocity information than possible with MIOT. This visualisation of inhomogeneity has also been pointed out by Ghosh et al., (2017)[122], however this demonstration was weaker - without comparison to another CEUS method. This hypervascularity in the outer borders of the tumours and a necrotic core is an established marker of tumour angiogenesis, and a feature that can be missed by biopsies [17].

SRUS has the potential to become an important tool for many microvasculature applications. The literature has shown particular potential for obtaining structural measurements of tumours namely tortuosity, distance between vessels and inhomogeneity. It has also shown potential for more accurate calculations of rBV. These have been shown to be better measured using SRUS than any other non-invasive technique. However, the ground truth measures (when taken) were generally bulk measurements from Micro-CT and IHC analysis. These allow average measures of vessel distance/rBV to be extracted from a sample of the tissue. These do not allow

validation of how well represented the individual structures were.

1.6.3 Acquisition strategies

One thing to note is that SRUS is possible over a wide range of parameters. Table 1.1 is included to help summarise the acquisition choices made in some of the key literature dealing with *in vivo* imaging. Transmit frequencies from 6.5 MHz - 40 MHz have been used, frame rates from 15 Hz - 500 Hz, various MB types, dilutions and infusion rates have also been used. There has been SRUS demonstrated with focussed imaging and PW imaging (with and without compounding). Following the demonstration by Errico et al. 2015 using PW imaging, there has been a shift to high frame rate (HFR) acquisition [116, 118, 119, 120, 121]. Moreover, there have been an extensive range of detection, tracking, motion correction and localisation methods used across the multiple groups which will be explained in more depth later.

Date	First Author & Ref.	Ref.	Target	Imaging Mode	Focussing	Transmit Frequency (MHz)	Framerate (Hz)	MB type	Injection Rate/Volume	Concentration
2011	M. Siepmann	[18]	Mouse tumour	Linear	Focused	40	33	BR38 (Bracco)	Bolus (50 µl)	$1x10^9$ MB/ml
2015	K. Christensen-Jeffries	[124]	Mouse ear	CPS contrast	Focussed PW, 3 angle compounding	6.5	25	Sonovue	Infusion (0.2-5.0 µl/min, <200µl)	2.5 × original concentration*
2015	C. Errico	[116]	Rat brain	Linear		15	500	Bracco (no details)	Bolus (150 µl)	2×10^8 MB/ml
2016	K. B. Hansen	[139]	Rat kidney	Contrast	Focused	Unknown	50	Sonovue	Infusion (no rate details)	0.1 × original concentration*
2017	D. Ghosh	[122]	Mouse tumour	Harmonic imaging	Focused	7	15	Definity	'Slowly injected'	$2.5x10^7$ MBs injected in total
2017	F. Lin	[121]	Rat tumour	Linear	PW	4.5	500	Synquest labs (lipid shelled)	Infusion (10 µl/min)	$1x10^{10}$MB/ml
2017	J. Foiret	[118]	Rat kidney	Contrast	PW	6.9	300	House-made (lipid shelled)	Bolus (150 µl)	$5x\ 10^7$ MB/ml
2017	S. Dencks	[125]	Mouse tumour	Linear - destruction/replenishment	Focused PW, 5 angle compounding	40	50	Hard shell PBCA	Bolus (50 µl)	$2x10^8$ MB/ml
2018	P. Song	[119]	Rabbit kidney	Linear		8	500	Optison	Bolus (100 µl)	$5\text{-}8x10^8$ MB/ml
2018	Y. Opacic	[20]	Mouse tumour	Linear - destruction/replenishment	Focused	40	50	Hard shell PBCA	Bolus (50 µl)	$2x10^8$ MB/ml
2019	S. Dencks	[19]	In human breast cancer	Contrast	Focused PW, 15 angle compounding	10	15	Sonovue	Slow Bolus (500 µl over 10 s)	Original concentration*
2019	J. Zhu	[120]	Rabbit lymph node	Linear		18	500	House-made (lipid shelled)	Bolus (100 µl)	$5x10^9$ MB/ml

Table 1.1: Acquisition choices. Acquisition parameters from main pieces of literature with an *in vivo* component. * the original concentration of Sonovue is reported as 1-5 x 10^8 MB/ml [123]

One piece of work worthy of a particular mention, although not included in Table 1.1 as this was not an *in vivo* demonstration, is O'Reilly and Hynynen (2013). *In vitro* SR in 3D was achieved using a particularly low transmit frequency of 0.3 MHz (harmonic imaging), and low frame rate of 10 Hz.

It is encouraging that SRUS appears robust across a large parameter space. Now it is essential that these methods can be refined for clinical translation. A key challenge highlighted in the assessment of the different SRUS protocols and new techniques is the lack of a reliable ground truth which can realistically approximate both the *in vivo* environment and US acquisition.

1.6.4 Acquisition time

The time required to produce an SR image is of key concern, and something which should be minimised for easier clinical uptake. The mouse ear images produced by Christensen-Jeffries et al. (2015) required an acquisition time of around 8 minutes [124] and Errico et al., (2015) generated slices of a the rat brain cortex in 150 s [116]. The difference in acquisition time was attributed by the authors of [116] to the use of ultrafast imaging compared to the low frame rates available on the clinical scanner used by [124]. However, it should also be noted that other factors such as the relative depths imaged (1.5 cm in [124] and 3.5 mm in [116]) and relative transmit frequencies (6.5 MHz in [124] and 15 MHz in [116]) may have been more important.

There have been three main pieces of previous literature which have specifically explored the factors affecting the acquisition time [125, 126, 127]. By simulating the MB events using Poisson statistics, Christensen-Jeffries et al. (2019) explored how the acquisition time depended on acquisition frequency, frame rate, tissue blood volume fraction, desired SR pixel size, MB signal density (including a comparison between bolus and infusion injections), and flow speed [126]. There are limitations in interpreting the exact times rather than the trends reported in this work. This is because it assumes a perfect SR procedure. Moreover, for Poisson statistics to be used the MB events should be independent. This may not be true as, in the case of flowing MBs, events may not truly be independent as a single MB is likely to

be detected along its flow profile. Nonetheless there were some key points that are useful to highlight as they provide insight in to the SRUS process. Although the SRUS resolution is no longer limited by the diffraction limit, transmit frequency is still important. Higher transmit frequencies allow more isolated MBs to be detected in a single FOV due to the smaller PSFs, thus frequency effects acquisition time. Potentially the most important finding was that the acquisition time is limited by flow speed for the vessels with the slowest flow. This work agreed with Hingot et al. 2019, who approached the question using experimental *in vivo* data rather than a numerical model [127].

There are two slightly different, but related, factors which affect why the smaller vessels take longer to visualise. Christensen-Jeffries et al. (2019) discusses how acquisition time is restricted at low speeds due to the fact that MBs must flow beyond the precision of the SR measurement between imaging frames in order to acquire new information. Thus, the flow speed rather than the frame rate sets the limit on how quickly vasculature can be visualised. Hingot et al. (2019) focuses on the fact that low flow rate in the capillaries makes it less likely for a MB to enter in the first place. The authors make the argument that since the number of MBs is dominated by the number of red blood cells, $1{:}10^5$, it is very rare for a MB to enter a particular capillary during an acquisition. The number of MBs appearing over different sizes of vessels were counted for experimental rat brain data. Typically, a vessel of size 100 μm sees dozens of MBs every second, whilst one of 20 μm only sees 1 every 10 s. This work predicts that it would take around 10 minutes to map the entire network to 5 μm pixels. In Opacic et al. (2018) their methods section writes that the resolution limit of their SRUS method was characterised using vessels where at least 5 MBs had passed over the 40 s acquisition [20]. The FWHM of the smallest vessel was measured to be 10 μm. The aim of this condition was to ensure that the achievable resolution measured was not set simply using 1 MB track. However, considering this in the light of the work by Hingot et al., (2019), it is unlikely that these vessels were truly < 10 μm in diameter. Care must be taken in reporting the smallest vessels that can be resolved using SR, as a vessel can easily look much smaller than reality. This

underlines the need for a ground truth where the true vessel size is known.

Another option is to consider what information can be extracted in a shorter time than takes to fully reconstruct the vasculature. This is the focus of the third group working in this domain. The actual values of the work by Dencks et al. (2017) are potentially not so useful in the context of this thesis, since they are working at very high acquisition frequencies of 40 MHz [125]. However, their approach of modelling the SR imaging process using a saturation model is interesting. One factor that was investigated in particular was a measure equivalent to the rBV. This work highlighted that, using their saturation model, although 45 -170 s may be required to reconstruct 90 % of the microvessels, estimation of the rBV can be done in much less time. It was predicted in a later study that approximately 25 % of the vasculature needs to be reconstructed in order to provide a reasonable estimate of the rBV [19]. A reliable phantom containing the structures required for this to be tested is required for validation of these percentages.

1.6.5 Statistical methods and sparsity

There is an alternative approach to SRUS which uses a higher MB density than suitable for single MB localisation. The first example of this was the translation of SR optical fluctuation imaging (SOFI) [128] to CEUS [129]. This technique is not used throughout the thesis; however, it is necessary to consider it for a thorough review of the field. Moreover, the developments in this thesis could also be applied to this method in the future.

Statistical methods can apply higher order statistics to generate SR images from higher order moments and cumulants [129, 130]. Moments and cumulants are quantities which statistically describe a distribution. For example, the first order cumulant and moment is simply the mean, the second order the variance, and the third order the skewness. Beyond the third order, cumulants and moments describe different features. This method is based on the assumptions that; the signal statistics are constant with respect to time (for the short time scales processed in a single ensemble), no tissue motion is present such that the vessels change position relative to the SR

grid, and that signals from MBs in the same vessel are correlated whereas those in different vessels are uncorrelated. By applying this method *in vivo*, Bar Zion et al. (2017) showed that SOFI can achieve very short scan times of < 1 s [129]. However, the authors showed only a modest improvement in spatial resolution by reducing the point spread function by up to 50 %. The main limitations of this method were poor SNR and inconvenient dynamic range of the images formed using higher statistics. In later works, the spatial resolution of this method was improved by the incorporation of the prior information that the distribution of emitters is sparse on the high-resolution SRUS image grid [130]. This technique known as SUSHI, produced an improvement in spatial resolution up to 10-fold compared to that of a temporal mean image. This improvement in resolution was achieved at an impressive temporal resolution of approximately 25 Hz. SUSHI outperforms localisation microscopy at higher concentrations of MBs than appropriate for localisation methods and is reported to have similar resolutions at sparse concentrations. However, using *in vivo* data, these have generally been compared using the same data set which is not necessarily fair as they operate best under different conditions.

There is a strong motivation to achieve SR with high temporal resolution. For example, the visualisation of rapid changes in blood flow would be useful both for tumour imaging and neural activity [129]. More generally, this also limits the distortion of the image caused by patient motion and could mean that motion correction is not required. However, van Sloun et al. 2017 also argues that given that the majority of clinical data is acquired at low frames rates, it is useful to be able to work at these low rates [131]

The assumption of sparsity is appropriate for SR and can be used to reconstruct SR images without the incorporation of higher order statistics. van Sloun et al. (2017) introduced the method of applying a sparse reconstruction on individual frames, without the incorporation of temporal information achieved using ultrafast imaging. The SR image process can then be treated as a simple inverse problem with a regularisation sparsity condition:

$$y = Ax \tag{1.16}$$

where y is the received CEUS data, x is the distribution of MBs, and A is an operator describing the imaging process. A can be estimated using the PSFs from isolated MBs. This method assumes a shift invariant system so is only applied to a fraction of the image at any one time. Then x can be found using a minimisation process:

$$\hat{x} = argmin \tag{1.17}$$

$$||y - Ax||_2{}^2 + \lambda||x||_1 \tag{1.18}$$

where λ determines the penalty for non-sparsity [131]. van Sloun et al (2017) shows how by combining this sparse reconstruction of higher density MB frames, with a motion correction algorithm to account for movement over these longer timescales, sparse reconstruction can be performed at the lower frame rates used more routinely in clinics at present. As well as easier clinical translation, this is also important because statistical techniques are also limited in their ability to resolve the smallest vessels due to the low likelihood of a MB entering the vessels as discussed in subsection 1.6.4. Most recently, it has been proposed that flow dynamics of the MBs can also be incorporated into the reconstruction as prior information [132].

It should be acknowledged that it will be very difficult to compare these techniques to localisation microscopy *in vivo* or even *in vitro*. This is because the statistical and sparse techniques operate at a much higher concentration than localisation methods. And, in the case of statistical vs localisation microscopy, on very different time scales. A fair comparison of these methods is a potential topic for future work.

1.6.6 Detection methods

Detection methods are required to distinguish MB signals from tissue. The three primary methods used in the literature are differential imaging (DI), singular value

decomposition (SVD) and contrast imaging. These three methods are compared in the first chapter of this thesis, where PI is chosen as the contrast method, and published in Brown et al. (2019) [133].

DI is the extracting of changing MB signals between frames by subtraction. Initially DI was used to generate the variation between frames by using pulses strong enough to destroy a number of MBs [113]. A following publication described how fast moving MBs will also be extracted [134]. When movement is involved, the signal appearing in the processed frame is not an actual bubble signal, but a difference between two MB signals. However, motion will also affect non-linear techniques using multiple pulses [135]. Thus, future work was needed to investigate how blood flow and frame rate affects both these methods.

The SVD filter introduced by Errico et al., (2015) has been extensively used in following literature [121, 122, 125, 127, 136, 137, 138]. Errico et al., (2015) argued that acquiring at a high temporal resolution enabled the extraction of transient changes to the MBs, even allowing extraction of isolated MB signals within a high concentration cloud of MBs. This is due to the use of a singular value decomposition (SVD) filter being able to discriminate between the unique signature of individual MBs and tissue. These transient changes were attributed to be due to motion, dissolution and disruption (although in this work the MI was set to minimise MB dissolution and disruption). The SVD extracted these transient changes of the MBs and was said to cause individual MBs to "blink" over the processed stack of images, providing temporally and spatially isolated sources to be localised. The use of the SVD filter on ultrafast imaging sequences was presented as being a distinct technique, disparate from the imaging of a low concentration of contrast agents at a low frame rate, and "the first" *in vivo* technique for having the potential to achieve high resolutions, deep within organs and with reasonable acquisition times. This is an assertion which has been carried though following literature [121, 129]. However, more research was required to understand the function of the SVD filter for MB imaging. The investigation of whether performing contrast sequences, such as PI, at ultrafast frame rates would allow these temporal fluctuations to be extracted is needed. This will be explored in

more depth in the next chapter of this thesis.

1.6.7 Velocity tracking

Beyond structural information, SR also has the potential to provide important functional parameters such as blood velocity. One particular benefit of reliable MB tracking is the separation of adjacent arteries and veins - effectively increasing resolution of these vessels [124]. Measures of velocity generally require some form of tracking. Thus, in this section, tracking and velocimetry are considered equivalent.

There has been a range of techniques developed and implemented in the literature such as intensity based cross correlation of nearby signals [124], matching the peak intensity of MB signals around a search region [139], a nearest neighbour approach [116, 119] or a more robust probabilistic approach [20, 140]. It should be noted that the approach by Song et al. (2018) is not the simplest nearest neighbour approach [119]. Instead a "bipartite graph-based" method is used to optimise the tracking so that the total distance between associated MBs is minimised. The velocity and density maps of the cross-correlation were observed to be similar to the bipartite pairing. However, it should be noted that cross-correlation is significantly more computationally expensive, thus perhaps the pairing algorithm is a good alternative. The authors note that both methods may break down in the case of higher concentrations of MBs, in which case the more mathematically involved tracking by Ackermmann et al., (2016) may be more appropriate. This work introduced the modified Markov chain Monte Carlo data association (MCMCDA) algorithm. This was able to associate MB localisations with specific tracks and could handle false alarms (perhaps due to noise), the initiation and termination of tracks. This was validated *in vitro*, comparing the measured speeds with those expected given the infusion pump settings and tube diameter. The averaged values correlated well.

As discussed previously, although the use of HFR will not always improve acquisition time, it is generally accepted that the extra temporal resolution will help tracking methods make the correct associations when imaging a FOV with a range of flow speeds. In situations where HFR is not feasible, it has been argued that a high

performing tracking algorithm will be robust to low frame rates. The combination of MCMCDA tracking, and the saturation model [125], and SR localisations using low frame rate imaging, was termed Motion model ultrasound localisation microscopy (mULM) [20]. The same group had previously shown that the tracking method was expected to show improved visualisation of tumour morphology than nearest neighbour approaches, in particular due to better assignment near bifurcations [141]. It is predicted that this probabilistic approach will have benefit for clinical applications where elevational thickness means that there are overlapping vessels [19]. For the imaging of dense vasculature or higher MB concentrations the challenge of tracking MBs becomes greater. A group focusing on higher concentration of MBs for SRUS applied multiple hypothesis tracking and Kalman filtering to assign localisations to tracks [132]. This work is particularly interesting because the history of MB localisations can be used to predict the future trajectory of the MBs and thus future localisations. Moreover, velocity estimates from optical flow tracking was also fed into the Kalman filtering to improve the estimation.

Tracking does not have to be used for SRUS images; however, work is showing that it can improve the completeness of SRUS images. That is, plotting tracks can make it much easier to visualise the vasculature structure from sparse localisation information. Although, conversely, erroneous tracks due to false alarms affect the image more. Thus, it is doubly important to provide strong validation of these tracking techniques.

1.6.8 Motion correction

Given the micrometre scale accuracy and precision of SRUS, the technique is particularly sensitive to motion artefacts. These can arise, for example, from probe motion, the patient changing position, muscle spasms, respiration and vessel pulsatility. There is a need for motion correction of images in a wide range of modalities, and techniques which can be fairly trivially translated to SRUS. Thus, there have been multiple different methods applied to SRUS image acquisition. Most simply, motion can be limited experimentally by using a stereotactic frame [116] or rejection of frames with significant movement [121]. Multiple works combine the rejection of frames with

significant movement (due to the concern that they contain non-rigid or out of plane motion) with another technique for correcting smaller motions [20, 117, 118, 125]. Gating of data to account for both respiratory [118] and cardiac cycles [117] have been applied, before correcting similar segments using a least squares approach to account for rigid motion. Several works have also taken advantage of the higher resolution phase information by correcting on the RF data, this was achieved using cross correlation techniques [127, 139]. However, not all of these techniques are always directly applicable to clinical use of SRUS. For example, Hansen et al. (2016) present "Robust microbubble tracking" by combining motion correction with the MB tracking. As the focus was on correcting the motion of a mechanical ventilation system, B-mode and contrast mode images were collected in sequential acquisitions. Then it was assumed that the motion corrected on the B-mode images could be directly applied to the CEUS image assuming a constant periodic motion. This method will not be applicable in more complex, realistic scenarios where the patient or probe will move unpredictably.

Surprisingly, there have been few works which have exclusively dealt with motion correction. The efficacy of SVD over solely temporal filters has recently gained traction in the field for filtering tissue motion [142]. Harput et al. (2018) applied a two-stage motion correction approach for non-rigid and affine motion to improve SR imaging [136]. Here motion estimation was performed on B-mode images and then used to remove the motion from SVD filtered contrast enhanced images before the localisation of isolated MBs. In later work this was translated to 3D and tested *in silico* [143]. The accuracy of these methods were estimated to be 12.2 µm (worst case studied) and 18 µm in 2D and 3D respectively using simulation. Hingot et al. (2017) used SVD twice; first to separate the strongest tissue components which can be used to make an estimation of the motion, and second (with different thresholding) to detect MBs [144]. The localisations were corrected following the MB detection using the tissue motion estimate. This work corrected for tissue motions on the order of 40 µm, however this was performed on *in vivo* data without a ground truth so the accuracy of the method could not be determined. The order in which MB detection

techniques and motion correction methods should be applied is a topic for future research. Hingot et al. (2017) showed that doing motion correction on data with MBs can generate significant error, so the correction should be performed after the MBs have been removed.

It should be noted that many of the errors measured for these techniques are on the order of tens of microns. These may limit visualisation of the smallest vessel for *in vivo* applications, and in the future, it will be important to reliably compare these. A comparison would require a model which could realistically represent MBs, tissue and movement. This is ambitious, and something which may be more feasible *in silico* rather than *in vitro*.

1.6.9 Localisation methods

There has been fairly little work on comparing localisation techniques. The main piece of literature was Christensen-Jeffries et al. (2017) comparing commonly used methods in the literature and a few new approaches [145]. The majority of work has used either the centroid or Gaussian PSF technique. Christensen-Jeffries et al. (2017) showed that using the onset of the PSF was more accurate than centroid, Gaussian fitting and peak detection. The axial onset localisation is found by taking the first value over the 3 standard deviations of the noise level. This will be the method largely used in this work.

From the beginning of their work in SR, O'Reilly et al. (2013) have worked in 3D. Initially localisation was achieved by fitting of a 3D gaussian to the PSFs [114]. However more recent work compared this approach with a deconvolution approach which improved the resolution by 3-fold [146]. This work simulated 3D SR acquisition by simply taking MB PSFs from experimental data and translating them along different paths before testing localisation methods. However, this required the assumption that the observed signals were truly isolated MB signals. And did not allow the exploration of other factors which could affect the localisation such as size/surroundings. The modelling methods used throughout the field will be discussed more in the next chapter.

Some work has looked at localising by fitting to the RF hyperbolas. The MB position then corresponds to the hyperbola maximum. There is motivation to use this method to benefit from the higher resolution phase information, however it has not been applied very broadly across the literature because it requires access to the RF data.

1.6.10 Visualisation

This seems like a trivial step, as there is little engineering required. However, it is important to consider briefly as there are a breadth of options used in the literature, they can convey different information, and in some instances may affect interpretation of results.

The most common visualisation of structural information is using a localisation density map [115, 116, 118, 124]. This means that the pixel values are incremented if a MB is detected and given different colours/shades for different cumulative frequencies of localisations. The pixel size chosen makes a significant difference to the image. Hingot et al. (2019) shows how larger pixels lead to the image becoming saturated much faster, but at the expense of resolution [127]. Using larger pixels can make the structures less sparse, and thus easier to visualise. Another method of making localisation map easier to visualise is by taking a weighted average of the surrounding pixel values, or by compressing the dynamic range [119]. However, it should be noted that some of these techniques may degrade the high-resolution information. In general, pixel size has been chosen to be greater than the predicted precision of SRUS [116, 121]. These pixels can either be filled solidly [20], according to the nearest match to the localisation. Alternatively, a Gaussian can be plotted to more accurately represent how there is some uncertainty in the localisation value [114, 124]. Generally, the standard deviation of the Gaussian is chosen to equal the precision. However, the less intense outer regions of the Gaussians can decrease the overall signal in the SR image. For purely visualising the structures it may be acceptable to use the filled pixels of arbitrary size. However, for making measurements, such as the FWHM of vessels, it is more accurate to use either pixel sizes relating to the precision or a

weighted approach such as a Gaussian representation. Thus, this work will generally use a Gaussian representation with standard deviation given by the precision values.

Often velocity information is also extracted [20, 116, 124]. Generally, this is presented using separate images with colour maps responding to speed and direction separately. Here, more than in structural maps, any discontinuities can be visually distracting. Thus some authors colour the pixels according to a weighted algorithm to take into account the values of surrounding pixels [119, 124]. Christensen-Jeffries et al., 2015 uses the weighted Gaussian approach to represent the velocity maps. More generally tracks representing the MB paths are drawn. These can be straight lines drawn between the localisations [116, 140] or using more complex line algorithms [20]. The images become less sparse by filling in all the pixels between the localisations.

Plotted tracks are often subject to a persistence control. That is, for a persistence control of 5, the same MB must be detected in 5 adjacent frames. On applying this method to *in vivo* imaging of a rabbit kidney, this method was observed to remove "unreliable" signals, which visibly reduced the reconstruction of the vasculature structure imaged [119]. However, without a ground truth, it is difficult to know if the removal of these signals was really justified - as they may have come from a true vessel. Thus, this visualisation choice can affect the interpretation of the data.

One particularly interesting example of visualisation was in the *in vivo* rabbit experiment by Foiret et al. (2017) of kidney vasculature [118]. In this work, only localisations associated with a flow speed $\leq$ 2mm/s were shown. This allowed extraction of the microvasculature, without image domination from the larger vessels. This may be one of the reasons why the results in this paper were much clearer than the previous proceedings where this filtering was not used [117].

1.6.11 3D imaging

The application of SR to 3D has clear motivation. Primarily, 3D tortuous structures associated with pathologies such as tumours could not be resolved in all 3 directions using 2D SRUS. Without the relatively large elevational extent which exists in 2D imaging, the technique would also no longer suffer from errors due to projection

of the signal onto a 2D plane. For example, velocity tracking would no longer be limited by this projection error which can cause velocities to be underestimated. There have been several works which have produced a 3D representation of a target by mechanically scanning in the elevational plane [116, 120, 121]. However, there is a trade-off between the step size used in the translation and the time taken to reconstruct the organ. Larger step sizes will be unable to resolve some of the 3D vasculature features; however short step sizes may take unfeasibly long to image a volume with respect to the MB flow. True 3D imaging, such as that with a matrix array probe, will enable a larger volume to be imaged at once. This may allow a reduction of acquisition time over 2D as the visualisation of vasculature markers of disease will be extracted more quickly.

The hardware for 3D imaging is currently limited and expensive. Christensen Jeffries et al. (2017) used two linear arrays simultaneously to provide 3D visualisation of an *in vitro* cellulose tube phantom [147]. The two probes were aligned perpendicularly to each other such as the elevational direction of one probe was collinear with the axial direction of the other to compensate for the poor elevational resolution. By synchronising these probes so that one transmitted and both simultaneously received, MBs could be localised in 3D without the use of state of the art 2D arrays. This approach can provide a starting step for developing 3D SRUS, however it has limited application in the clinic. This approach suffers from a very small FOV (15.4 x 1.188 x 1.188 mm) due to 3D imaging only being possible in the overlapping FOV of both probes. Moreover, perpendicular arrays are not likely useful for clinical targets and this set-up required the assumption that MBs scatter spherically symmetrically (which may not always be true [148]).

One field which is more suited to 3D imaging is that of transcranial imaging, where hemispherical arrays can achieve 3D imaging [114]. In the infancy of SRUS, O'Reilly et al all (2013) provided very impressive results of 3D SRUS of a spiral tube phantom shielded by an *ex vivo* human skull. This work was particularly impressive due to having the additional challenge of correcting for aberration of the skull. One drawback of this work was the long acquisition time required due to the use of focused

transmit and the requirement that there was a single MB in the focal region. Most work for more general imaging in the literature has moved towards using bespoke matrix arrays.

An early example simply used two parallel rows of a 2D matrix array probe [134]. However, there was no quantification of the resolution in the elevational direction or discussion of the reconstruction process. Thus, it is difficult to assess how successful this approach was. More recently the same group has demonstrated 3D SR using a 32 x 32 matrix array *in vitro* [137]. This work successfully visualised an *in vitro* branching phantom, and was particularly valuable in discussing some of the challenges associated with imaging in 3D. Although high frame rates could be acquired, 1 s of acquisition time required 89 s of data transfer time. The data then required 45 s to beam-form. The data storage requirements and computational power make 3D imaging very challenging. Another challenge is the lower sensitivity of the probe compared to linear arrays due to the element size. In non-contrast imaging, this can be improved by increasing the pulse amplitude. However, for SRUS, MB destruction is generally to be avoided. Alternatively, compounding can be used to increase SNR but this will increase the data burden. Harput et al. (2019) generated similar results with lower computations/data storage requirements by using a 2D sparse array [138]. Following a density tapered spiral layout (so that the highest density of active elements was in the central region) 512 elements were randomly assigned on a 35 x 32 element grid. This reduced the number of electronic channels required, whilst not sacrificing on aperture size compared to 2D array probes. Data requirements were also reduced in a more simplistic way by having intervals (on the scale of several ms) between HFR imaging (PRF = 2500Hz). This can reduce data redundancy for sufficiently slowly moving MBs.

An important step towards 3D is the generalisation of SR techniques and steps which have been developed in 2D for 3D. It is hoped that much of the research in 2D should be able to be fairly trivially translated to 3D. For example, Harput et al. (2018) expanded the use of a motion correction method initially used for 2D SRUS and developed it to be suitable for 3D SRUS [143]. Throughout this thesis, attention

will be drawn to how the work would translate to 3D.

1.6.12 Nanodroplets

Nanodroplets (NDs) are an alternative method of US contrast to MBs [149]. These are sub-micron particles, which can undergo a phase change to MBs upon activation. By incorporating optically absorbing dye into their shell or core, these can be optically triggered using laser light. Alternatively, an incident US pulse can also provide the energy to trigger a phase change. SR using NDs was first shown by Luke et al. (2016). Here, laser light was used to vaporise NDs to MBs where they briefly scattered before condensing back to NDs. One of the factors influencing the vaporisation of these ND is the boiling point (BP) of the liquid material at its core. Luke et al. (2016) used a perfluorohexane core which has a BP of 56 ^{o}C [150]. A laser was used to rapidly vaporise the NDs, these then re-condensed back to NDs since their core had a BP above that of body temperature. Using differential imaging, isolated re-condensation events could be extracted, and then super-localisation performed on these signals. This method works on the assumption that the recondensation events are stochastic. Results have shown that, on the time scale of ultrafast imaging, subsets of the NDs recondense at different times. Previous authors suggest that this stochasticity is driven by a combination of laser fluence, particle size distribution, nearby MBs, quantities of optical dye, and local temperatures, pressures and viscosity [150, 151]. However, in the future, it will be necessary to prove the validity of this stochasticity assumption and how it might relate to acquisition parameters. This work was later expanded to consider the use of compounding, which was shown to improve the lateral and axial resolutions by 54 % and 68 % respectively [152]. However, the success of this approach depends on multiple frames either side of the event being captured. This will be a challenging condition to keep consistent across a FOV with a relatively high concentration of events, and the localisation process will have to be robust to varying signal SNRs. A drawback of this work is the use of optical triggering, which will limit the depth possible using these droplets. Thus, our group has focused on NDs which can be acoustically triggered.

Zhang et al. (2018) developed acoustic wave sparsely activated localisation microscopy (AWSALM) which used acoustically triggered NDs for SR acquisition [151]. The BP of the droplets was much lower in this work (-2 ^{o}C) which enabled focused US to vaporise a subset of NDs. In this work the stochastic component was during the activation. Where the subsequent activation pulse could be used to destroy the previously created MBs. The MBs were imaged using HFR imaging. This work was expanded using an even lower BP core (-37 ^{o}C) [153]. These NDs could be activated using pulse pressures achievable with PW imaging. Thus, the PWs could be used to simultaneously activate, image and destroy subsets of the ND population. This method enabled the impressive image formation of a 200 µm cellulose tube in just 200 ms. This was possible because a higher concentration of NDs can be used relative to MBs, and a full reconstruction does not rely on flow. Conversely, this does mean that this technique will provide the structural information but not the functional flow information of MB SRUS. This is an exciting direction of SRUS, and could rapidly increase acquisition speeds and could have different applications compared to MB SR. One key application is that NDs will allow extravasation into the extra-vasculature space due to their sub-micrometre size, which could enable leaky vasculature to be detected. Alternatively, they could be targeted to visualise specific pathologies. More work needs to be done to understand any differences between the process with SRUS and NDs. One key drawback of NDs compared to MBs is that they have not yet been clinically approved. Much of the following work in this thesis could be adapted to consider NDs, in the final discussion any adaptations will be outlined.

1.7 Thesis outline

The general concepts of SRUS by localisation of individual MBs is superficially very simple. However, as highlighted by the literature review, multiple steps are required for the SRUS process and there is little consensus between different groups working on SRUS regarding the best approach. For example, SRUS has been demonstrated over a large range of acquisition parameters, but there has been little research investigating

how these choices may affect SRUS images. Moreover, as a CEUS technique, SR images are also subject to the variation in MB behaviour and physiological conditions [154]. For clinical translation of the technique it is important that the factors which affect SRUS are understood and that the most reliable protocols for accurate and precise imaging *in vivo* are developed.

Some general challenges highlighted by the literature review are:

- Using SRUS to reliably extract clinically relevant measures (such as tortuosity and distance between vessels).
- Generating useful images at reasonable acquisition times, and potentially achieving real time implementation.
- The comparison of low MB concentration localisation techniques with statistical/sparse reconstruction methods.
- Development and comparison of acquisition, detection, localisation, MB tracking, motion correction and visualisation methods.
- Implementation of 3D SRUS.
- Investigating the potential of NDs for SRUS.

One important part of confronting all these challenges is the development of validation tools for SRUS.

1.7.1 Aims and objectives of thesis

Several specific objectives were formulated to develop validation tools for SRUS.

- Development of a simulation environment to test SRUS.
- Development of an optical ground truth of for SRUS.
- Development of realistic and practical microvascular phantoms for *in vitro* studies.
- Exploration of some of the factors which affect the efficacy of SRUS.

1.7.2 Summary of thesis

This thesis comprises 5 further chapters. Chapter 2 develops a simulation environment for SRUS and uses it to compare detection methods. Chapter 3 develops a simultaneous optical and acoustic set-up for SRUS. Following observations of a non-linear artifact in Chapter 3, Chapter 4 outlines the development of a high dynamic range imaging technique for CEUS imaging more generally. The work of Chapter 4 is currently patent pending. Finally, Chapter 5 investigates various novel methods for fabrication of microvascular phantoms for SRUS. Chapter 6 is the final conclusion of the thesis, where the results will be discussed as a whole and future work proposed.

Chapter 2

Development of Simulation Toolbox for Investigating Detection of Microbubbles for Super-Resolution Ultrasound

2.1 Abstract

This chapter introduces a new simulation platform developed to simulate SRUS, and more specifically, compare MB detection methods. Detection methods such as pulse inversion (PI), differential imaging (DI) and singular value decomposition (SVD) filtering are used to separate the MB and tissue acoustic responses. Finally, this chapter also explores three artifacts associated with filtering data using SVD.

The simulation developed within this work simulates the MB response based on the properties of Sonovue^{TM} and using the Marmottant model. Non-linear propagation through tissue was modelled using the k-Wave software package. The three main detection methods (PI, DI and SVD) were compared in terms of the localisation accuracy, precision and contrast to tissue ratio (CTR). During this work an artifact, which presented as a variation in intensity over time, was observed when

applying the SVD filter. This artifact was termed "flashing". Two other artifacts, termed "smearing" and "splitting" were also observed. "Smearing" presented as a spatial blurring of the MB signal over the path of moving MBs and "splitting" was a change in shape of MB signals. In collaboration with J. Zhu and K. Riemer, these artifacts were investigated using simulation, *in vitro* experiments and clinical data. I investigated the artifacts *in silico* using the simulation presented in this chapter. J. Zhu investigated the artifacts *in vitro* and using clinical data. Some of J. Zhu's work is included in the discussion of this chapter at section 2.6.3, where it is discussed in relation to the simulation. K. Riemer also investigated the flashing artifact using an *in vivo* model (although his experiments were less relevant to the work in this thesis so have not been included here).

The results for the comparison of the detection techniques showed that, for the parameters studied, that PI is most appropriate for low frequency applications, but also most dependent on transducer bandwidth. SVD is preferable for high frequency excitation where localisation precision on the orders of a few microns is possible. PI is largely independent of flow direction and speed compared to SVD and DI, so is appropriate for visualising the slowest flows and tortuous vasculature. SVD is unsuitable for stationary MBs and can introduce a localisation error on the order of hundreds of microns over the speed range 0-2 mm/s and flow directions from lateral (parallel to probe) to axial (perpendicular to probe). DI is only suitable for flow rates > 0.5 mm/s or as flow becomes more axial. The amplitude of the SVD artifacts are increased by decreasing the filtered stack size, decreased MB flow speed and increased initial CTR. The SVD artifacts are due to the decomposition failing to adequately separate tissue and MB signal.

Overall, this work develops a MB and tissue non-linear simulation platform to improve understanding of how different MB detection techniques can impact the SR process and explores some of the factors influencing the suitability of each. The work in this chapter shows that SR protocols cannot be blindly applied without careful considering of the acquisition and processing choices made with respect to different applications.

2.2 Introduction

2.2.1 Detection methods

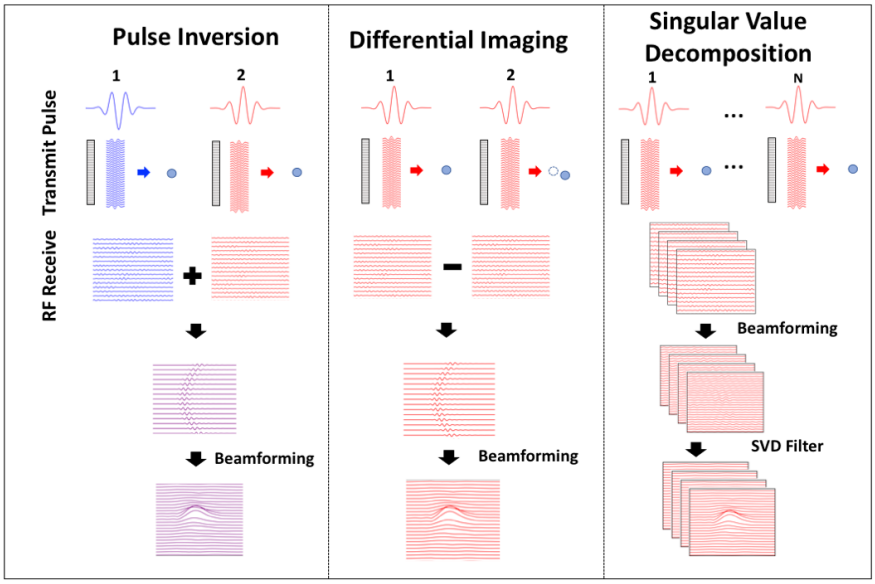

Figure 2-1: Schematic of MB detection methods. Pulse inversion and differential imaging both combine two frames of data. Where red is associated with a positive pulse and blue is 180 degrees out of phase. SVD requires a stack of N images. In this work the SVD filter is applied to beamformed RF data before envelope detection.

Detection algorithms are used to extract the MB response from the surrounding tissue signal. The three detection methods shown in Figure 2-1 have been investigated in this chapter using simulation. PI isolates the non-linear components of the received signal [85]. The second harmonic content of MBs allows this non-linear method to extract isolated MB signals from linear background signal [115]. Linear methods that detect MBs using movement due to flow have also been used. DI extracts the variation of MB signals between frames by subtracting adjacent frames. Initially DI was used to generate the variation between frames by using pulses strong enough to destroy a number of MBs [113]. A following publication described how fast moving MBs will also be extracted [134]. Errico et al. (2015) later introduced SVD as a method to discriminate between MB and tissue signals, discussing that the SVD processing will generate strong signals for sub wavelength movements [116]. Their work explains

that the SVD filter separates MB and tissue signal based on the spatial and temporal characteristics of their acoustic response.

One motivation for the work in this chapter is the hypothesis that the signals resulting from the DI and SVD must depend heavily on the MB velocity and imaging parameters such as the PRF. Likewise, multi-pulse non-linear techniques are also affected by factors such as flow speed as the linear components will not cancel as effectively if the MB has a significant flow speed relative to the PRF. Therefore, more work is required to investigate the dependence of detection methods on MB velocity and PRF.

2.2.2 Blinking MBs

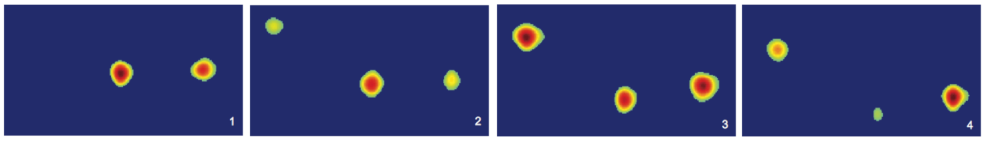

Figure 2-2: Beamformed SVD filtered MB signals. Each frame is separated by 44ms. (adapted from Errico et al., (2015) [116], with permission from Springer Nature under license number 4697061254519.

Previous literature has suggested that using SVD or DI, in combination with HFR imaging, is a distinct technique compared to performing SRUS at the low frame rates more commonly available on clinical scanners [113, 116]. The SVD is described as being able to extract transient changes over the field of view. This is termed MB "blinking". The authors argue that, by using ultrafast imaging, the "blinking" and "flickering" of the MBs can be used in a similar way as blinking flurophores are used in optical FPALM. It is claimed that the DI and SVD filtering techniques can extract these signal changes. More work is required to understand the "blinking" of MBs described in Errico et al. (2015), since significant blinking is not expected unless the MB properties are significantly changing over the imaging time or the MB is moving in and out of the FOV. This experimental temporal blinking is shown in Figure 2-2.

More work is required to understand the blinking associated with SVD and whether a similar phenomenon can be observed using non-linear techniques at a HFR.

2.2.3 Simulation of US

There are many existing simulation environments for US modelling [155]. However, currently these are not flexible enough to investigate many of the factors affecting SR. Field II uses a convolution approach to describe the US field using a spatially dependent impulse response [156, 157, 158]. Previous authors have extended Field II to simulate the flow of MBs [159] and more recent work has used Field II to simulate SR [160]. Pipenbrock et al. (2018) presented the use of Field II to compare different methods of extracting pixels corresponding to MB signals, however this work avoided including any MB behaviour by modelling the MBs as linear scatterers. A key limitation of Field II is the assumption of linear acoustics. k-Wave is a simulation platform which solves coupled non-linear differential equations which describe the non-linear wave propagation through media [161]. k-Wave models have been shown to closely replicate experiment [162]. k-Wave has not previously been combined with MB simulation.

2.2.4 Simulation of MBs

The MB response can be simulated using existing models which describe MB dynamics [68, 163]. Although uncoated MBs can be completely described, the behaviour of coated MBs remains an open problem [68]. The majority of present MB models are derived from the Rayleigh-Plesset (R-P) equation [163]. For this work the Marmottant model has been used [80] due to its ability to predict the highly non-linear response which can be experimentally observed [78]. The Marmottant model is unique in that it describes the MB surface tension in terms of three regimes; the buckled state, the elastic state and the ruptured state. These states are dependent on the MB radius. The following theory section, subsection 2.3.1, will discuss MB modelling in more depth.

2.2.5 Simulation of SRUS

There are multiple factors which may affect CEUS imaging *in vivo* such as acquisition settings, patient physiology and MB behaviour [154]. It can be practically challenging to control and investigate how these sources of variation individually and jointly affect the efficacy of SRUS using an *in vivo* model. However, the lack of realistic phantoms and simulation platforms can mean that *in vivo* models are the only way to realistically test and investigate SRUS protocols, and CEUS protocols in general. For example, Song et al. (2018) cite the lack of realistic phantoms and simulations as their motivation for testing their SRUS protocol *in vivo* [119]. Fabricating a microvascular phantom is not trivial, and it may not be possible to test the full range of acquisition parameters (such as transmit frequency and bandwidth) using limited laboratory equipment. Thus, there is particular motivation to develop a realistic simulation to provide a ground truth validation. There is a gap in the field of CEUS imaging for a realistic simulation that models MB behaviour within an US simulation platform.

For comparing linear and non-linear detection methods, a simulation must include the linear and nonlinear behaviour of MBs and the tissue, as well as how the MB signal may change as it propagates through the tissue. Modelling the flow of MBs and tissue movement is also important. There has only been one comparison of detection methods *in silico* in the literature [160]. This work compared three linear techniques, including SVD, using a linear simulation in Field II and modelling the MBs as point scatters. Simulation has been used more widely to investigate other research questions within SRUS and will be reviewed here.

Previous work has considered using simulation to determine the best-case theoretical resolutions for SRUS [164]. This simulation used a simple model of the spherical wave formed from an ideal point scatterer propagating in a homogeneous medium. The random temporal error of the time at which the MB signal was detected at the probe was modelled based on experimental measurements, and the error propagated through to the corresponding spatial localisation error. This work explored different transducer geometries, transmit frequencies, imaging depths and sampling frequen-

cies. This model predicted that resolution below 10 μm, using a centre transmit frequency of 3 MHz, was feasible. However, considering that a realistic MB response will be significantly different compared to a linear scatterer and this work only considered homogeneous media, this model is too simplistic to estimate the resolution in realistic scenarios.

Other authors have also used a purely linear model to describe the MB response [140, 160]. Ackermann and Schmitz (2016) used moving linear scatterers in a Field II simulation to test a probabilistic tracking algorithm. Perhaps this approach was a good approximation of their experimental protocol using hard-shelled PBCA MBs, which do not show strong nonlinearity at the high transmit frequencies investigated. However, this approach is likely to be less appropriate for imaging lipid-shelled MBs. One attempt to include a more realistic MB response was presented by Christensen-Jeffries et al., (2017). This work investigated different localisation methods using a MB response modelled using the Marmottant model and a level of Gaussian noise [145]. However, no tissue response was incorporated, and the propagation of the MB signal was not considered.

An alternative approach to capture realistic MB behaviour is to extract MB signals from experimental data. Foroozan, O'Reilly and Hynynen, (2018) simulated 3D SR acquisition by simply taking a few MB signals from experimental data and translating them along different paths before testing localisation methods [146]. However, this required the assumption that the signals observed were truly isolated MB signals and did not allow a wide range of factors to be investigated. Other groups have measured the experimental variation expected in the signals of isolated MBs and model the SRUS data as a summation RF modulated bivariate PSFs which are summed at each MB location [132, 165]. An RF modulation at the second harmonic can be used to simulate the nonlinear frequency. However, neither of these simulation approaches modelled tissue or wave propagation.

Overall, there is a gap in the field for a simulation realistic enough to compare nonlinear and linear detection methods and the multitude of factors which may affect them. This chapter aims to explore the parameter space, through simulation, in a

way that would not be feasible otherwise.

2.2.6 Factors affecting efficacy of detection methods

Frequency

There has been a growth in literature applying SR techniques. In particular, there has been a focus towards high frequency excitation, with SVD filtering and demonstrating the SRUS in various *in vivo* models [116, 121, 125]. Song et al., 2018, also recently showed the use of DI for the visualisation of rabbit kidney vasculature at an excitation frequency of 8 MHz [119]. In this chapter high frequency is defined as transmit frequencies above the Sonovue^{TM} MB resonance (1- 3 MHz). Accordingly, in this chapter low frequency is defined as $\leq$ 3 MHz and high frequency is defined as $\geq$ 4 MHz. It should be noted that this definition differs from the conventional definition of high frequency US which is generally understood to mean using a transmit centre frequency of 30 - 100 MHz [166]. Transmit frequencies of $>$ 30 MHz are only suitable for applications where penetration depths on the order of only a few centimetres are required, such as clinical imaging of superficial structures and preclinical imaging of small animals.

The influence of frequency in SR imaging is multifaceted. Increasing frequency will limit the depth penetration of the US beam through tissue. In conventional imaging, this makes it harder to reconstruct high resolution images at depth. Additionally, the behaviour of contrast agents is frequency dependent [92]. The low resonance frequency of MBs mean that SR should not be limited by depth. However, non-linear propagation of the beam through tissue and MBs can reduce the CTR [88]. This is especially problematic as the harmonic signal is already a fraction of the intensity of the linear MB signal. The bandwidth limitations of transducers are also an important consideration when comparing techniques. The influence of transmit frequency with and without including the effect of the transducer bandwidth in the model is explored in this work. Investigations without inclusion of the transducer bandpass allows a more general investigation of how properties such as frequency

dependent attenuation and nonlinear propagation may affect the different methods. Including the bandpass filtering then highlights the importance of probe sensitivity for each method.

Physiology

The influences of physiological factors are especially important to understand as they cannot be controlled. The visualisation of tumour microvasculature is a particularly challenging environment to image and a potential application for SR [121, 167]. Blood flow in the tumour microvasculature can be an order of magnitude less than healthy vessels - with speeds less than 1 mm/s for vessels up to 60 μm in diameter [168]. Tumour microvascular flow is changeable, even briefly stopping or reversing direction [169]. Structurally, tumour vessels are tortuous and form a complex 3D structure [170]. Nonetheless, accurate longitudinal and non-invasive imaging is essential for the development of therapeutic agents [171]. Thus this work investigates the dependence of each detection method due to MB speeds between 0 mm/s and 2 mm/s, and studies the effect of flow direction bound between lateral flow (parallel to the transducer) and axial flow (perpendicular to the transducer).

SVD filtering choices

The mathematics of SVD filtering will be discussed in more detail in subsection 2.3.3. However, it is important to underline here that, compared to DI and PI, there are more choices to make for SVD filtering. As with all signal processing techniques, care must be taken to ensure that any associated artifacts are understood to avoid clinical misinterpretation. One such choice is determining the singular value thresholds. These can be determined empirically [142]; or by choosing cut-offs based either on Doppler frequencies of the singular vectors or the singular value curve turning points [172]. Stack size has been shown to affect CTR of the filtered images [172, 173, 174]. There is no universally agreed stack size: much of the recent literature does not clearly state the size being processed. A better understanding of how SVD processing parameters might affect SR is required. In this work, stack size and eigenvalue cut-off

choices are considered.

2.2.7 Chapter outline

This chapter outlines the development and use of a simulation tool which can explore the available MB detection techniques. A novelty of this work is the introduction of a simulation environment where nonlinear and linear detection methods for SRUS can be quantitatively compared. The methods section details how k-Wave and the Marmottant model are combined and the the exact implementation of the detection methods and processing steps such as sampling, noise addition and beamforming used to mimic a realistic experiment. The simulation has been designed with the intention of quantifying how factors such as MB size, frequency and blood velocity will affect how accurately and precisely the extracted MB signals can be localised using the different detection techniques. Results are presented on the impact of various key parameters. Although many of the results will be applicable more generally, physiological parameters relevant to the specific clinical example of visualisation of tumour microvasculature have been chosen here. A series of simulations will investigate how the choice of detection technique may blur or distort the SR images. Following a more general comparison between the techniques, focus has been given to several artifacts that SVD filtering can introduce. The chapter concludes with discussion on how the results can inform on the application of each detection method depending on the application, and suggestions for avoiding common artifacts.

2.3 Theory

2.3.1 MB modelling

This section gives a brief outline of the origin of the terms that make up the Marmottant model. A more comprehensive discussion of various MB models can be found in reviews [68, 163, 175].

The Marmottant equations is:

$$p_{\mathrm{l}}(R\ddot{R}+\frac{3}{2}\dot{R}^2) = (P_0+\frac{2\sigma(R_0)}{R_0})(\frac{R}{R_0})^{-3\gamma}(1-\frac{3\gamma}{c}\dot{R}) - P_0 - \frac{2\sigma(R)}{R} - \frac{4\mu\dot{R}}{R} - \frac{4\kappa_{\mathrm{s}}}{R^2} - P(t) \tag{2.1}$$

with parameters defined as water density (p_{l}), ambient pressure (P_0), MB surface tension (σ), gas exponent (γ), dynamic liquid viscosity (μ), shell viscosity (κ_{s}), speed of sound (c), MB resting radius (R_0) and input pulse $P(t)$.

The equation models how the shell properties change during oscillation by incorporating a radii dependent surface tension term:

$$\sigma(R) = \begin{cases} 0 \text{ if } R \leq R_{\mathrm{buckling}} \\ \chi(\frac{R^2}{R^2{}_{\mathrm{buckling}}} - 1) \text{ if } R_{\mathrm{buckling}} \leq R < R_{\mathrm{ruptured}} \\ \sigma_{\mathrm{water}} \text{ if } R \geq R_{\mathrm{ruptured}} \end{cases}$$

where $R_{buckling}$ describes the regime where the radii decreases such that the surface tension is 0, and shell elasticity is represented by χ. The shell is elastic for small oscillations. At $R_{ruptured}$ the shell has expanded to the extent that it may break, and the surface tension becomes that of water. $R_{buckling}$ and $R_{ruptured}$ are calculated as below [80]:

$$R_{\mathrm{ruptured}} = R_{\mathrm{buckling}}(1+\frac{\sigma_{\mathrm{water}}}{\chi})^{\frac{1}{2}} \tag{2.2}$$

$$R_{\mathrm{buckling}} = constant \cdot R_0 \tag{2.3}$$

Origin of MB model terms

To understand the terms of the Marmottant equation, it is useful to start from the most basic description of a bubble. For an air bubble surrounded by water, having only one interface, the difference between the gas pressure P_{g} in addition to the

vapour pressure P_{v} compared to the liquid pressure P_{l} is sustained by surface tension σ:

$$P_{\mathrm{g}} + P_{\mathrm{v}} - P_{\mathrm{l}} = \frac{2\sigma}{R} \tag{2.4}$$

P_{v} can be neglected as it is negligible for small bubbles [163] so that:

$$P_{\mathrm{g}} - P_{\mathrm{l}} = \frac{2\sigma}{R} \tag{2.5}$$

For a bubble in equilibrium, P_{l} is the atmospheric pressure (P_0), and R is the bubble resting radius R_0 [176]. This gives an equation for the gas equilibrium of P_{ge}:

$$P_{\mathrm{ge}} = \frac{2\sigma}{R_0} + P_0 \tag{2.6}$$

For the R-P and Marmottant models, the assumption that the gas obeys a polytropic gas law is made,

$$P_{\mathrm{g}} = P_{\mathrm{ge}}(\frac{R}{R_0})^{-3n} \tag{2.7}$$

where n is the polytropic index. It is assumed that this is an adiabatic process such that $n = \gamma$ (ratio of specific heats for encapsulated gas). Thus, the gas pressure at a different radius will be:

$$P_{\mathrm{g}} = (P_0 + \frac{2\sigma}{R_0})(\frac{R}{R_0})^{-3\gamma} \tag{2.8}$$

We are interested in the response of the bubble to an acoustic field *P(t)*. For an incompressible liquid, the equation of motion can be derived by equating the kinetic energy gained by the liquid to the difference between the work done at the bubble wall and at infinity to give [176]:

$$\frac{P_{\mathrm{l}} - P_{\mathrm{inf}}}{\rho_{\mathrm{l}}} = \frac{3\dot{R}^2}{2} + R\ddot{R} \tag{2.9}$$

where

$$P_{\mathrm{inf}} = P_0 + P(t) \tag{2.10}$$

Combining equations 2.5, 2.8, 2.9, and 2.10 gives:

$$p_{\mathrm{l}}(R\ddot{R} + \frac{3}{2}\dot{R}^2) = (P_0 + \frac{2\sigma}{R_0})(\frac{R}{R_0})^{-3\gamma} - P_0 - \frac{2\sigma}{R} - P(t) \tag{2.11}$$

Poritsky (1951), later incorporated the effect of the liquid viscosity by adding the term $\frac{4\mu\dot{R}}{R}$ to give the final R-P equation [177]:

$$p_{\mathrm{l}}(R\ddot{R} + \frac{3}{2}\dot{R}^2) = (P_0 + \frac{2\sigma}{R_0})(\frac{R}{R_0})^{-3\gamma} - P_0 - \frac{2\sigma}{R} - \frac{4\mu\dot{R}}{R} - P(t) \tag{2.12}$$

There are three contributions to the damping of the bubble oscillations [163].

$$TotalDamping = viscous + thermal + radiation \tag{2.13}$$

The term due to liquid viscosity term can be combined with the thermal damping by doubling the value of dynamic liquid viscosity (μ) to be double that of water [178].

For an incompressible fluid the radiation damping of bubble oscillation is neglected [163]. However when the bubble shell velocity is not negligible compared to the speed of sound, this assumption breaks down. Several authors worked to accommodate the effect of an incompressible fluid. Brenner et al. (2002) describes how these formulations can be written as a general equation [179].

$$(1-(\lambda+1)\frac{\dot{R}}{c})p_{\mathrm{l}}R\ddot{R}+\frac{3}{2}\dot{R}^2\rho(1-(\lambda+\frac{1}{3})\frac{\dot{R}}{c}) = (1+(1-\lambda)\frac{\dot{R}}{c})(P_{\mathrm{g}}-P_0-P(t))+\frac{R}{c}\dot{P}_{\mathrm{g}}-4\mu\frac{\dot{R}}{R}-\frac{2\sigma}{R} \tag{2.14}$$

When $\frac{\dot{R}}{c} = 1$, singularities occur. A popular choice is to set the prefactors of these terms to 0 to obtain:

$$p_{\mathrm{l}}(R\ddot{R}+\frac{3}{2}\dot{R}^2\rho)=(P_{\mathrm{g}}-P_0-P(t))+\frac{R}{c}\dot{P}_{\mathrm{g}}-4\mu\frac{\dot{R}}{R}-\frac{2\sigma}{R} \tag{2.15}$$

with P_g as in Equation 2.8, so that $\dot{P}_{\mathrm{g}}$ is:

$$\dot{P}_{\mathrm{g}}=(P_0+\frac{2\sigma}{R_0})(\frac{R}{R_0})^{-3\gamma}(-\frac{3\gamma}{c}\dot{R}) \tag{2.16}$$

Marmottant et al. (2005) also incorporates a term to include the shell viscosity of $\frac{4\kappa_{\mathrm{S}}}{R^2}$, as in [180]:

$$p_{\mathrm{l}}(R\ddot{R}+\frac{3}{2}\dot{R}^2)=(P_0+\frac{2\sigma}{R_0})(\frac{R}{R_0})^{-3\gamma}(1-\frac{3\gamma}{c}\dot{R})-P_0-\frac{2\sigma(R)}{R}-\frac{4\mu\dot{R}}{R}-\frac{4\kappa_{\mathrm{s}}}{R^2}-P(t) \tag{2.17}$$

The novel contribution of the Marmottant model is the incorporation of the dynamic behaviour of the shell by describing the variation of the shell surface tension with bubble radius $\sigma(R)$.

The radial changes of the bubble oscillations can then be converted to pressure using the equation [176]:

$$P=\frac{\rho_{\mathrm{l}}}{R_{\mathrm{p}}}(R^2\ddot{R}+2R\dot{R}^2)-(\frac{R}{R_{\mathrm{p}}})^4(\frac{\rho_{\mathrm{l}}\dot{R}^2}{2})$$

(2.18)

where R_{p} is the bubble position.

2.3.2 k-Wave toolbox

k-Wave solves the energy, momentum and mass conservation equations at each point in space and time to model the wave propagation

Momentum Conservation:

$$\frac{\partial u}{\partial t}=-\frac{1}{\rho_0}\nabla p \tag{2.19}$$

Mass Conservation:

$$\frac{\partial \rho}{\partial t} = -\rho_0 \nabla \cdot u \tag{2.20}$$

Energy Conservation:

$$p = {c_0}^2 \rho \tag{2.21}$$

Where u is the acoustic particle velocity, p is the acoustic pressure and ρ is the density, ρ_0 is the bulk equilibrium density and c_0 is the sound speed. For the simulation of non-linear propagation through inhomogeneous media extra terms are added:

$$\frac{\partial u}{\partial t} = -\frac{1}{\rho_0} \nabla p \tag{2.22}$$

$$\frac{\partial \rho}{\partial t} = -(2\rho + \rho_0) \nabla \cdot u - u \cdot \nabla \rho_0 \tag{2.23}$$

$$p = {c_0}^2 (\rho + d \cdot \nabla \rho_0 + \frac{B}{2A} \frac{\rho^2}{\rho_0} - \mathrm{L}\rho) \tag{2.24}$$

where d is the acoustic particle displacement and the operator L describes the absorption and dispersion.

$$\mathrm{L} = -(2\alpha_0 {c_0}^{y-1}) \frac{\partial}{\partial t} (-\nabla^2)^{\frac{y}{2}-1} + (2\alpha_0 {c_0}^y) \tan(\frac{\pi y}{2}) (-\nabla^2)^{\frac{y+1}{2}-1} \tag{2.25}$$

The parameters α_0 and y relate to the frequency (f) dependent absorption:

$$\alpha = \alpha_0 f^y \tag{2.26}$$

B/A is the second-order nonlinearity parameter which characterises the non-linearity of the tissue. The B/A value quantifies how easily harmonic components will be generated as the pulse propagates [181].

The distinguishing feature of k-Wave is how the differential terms are calculated.

Instead of using a finite difference or finite element approach, which is computationally unfeasible for the required degree of accuracy, the global Fourier spectral method is used. This method involves treating the 2D field of view as a continuous domain and rewriting the equations in terms of Fourier transforms using the identity:

$$\mathcal{F}\frac{\partial}{\partial x}f(x) = ik_{\mathrm{x}}\mathcal{F}\{f(x)\} \tag{2.27}$$

For example, the momentum conservation equation for 1D homogeneous, nonlinear propagation, can be rewritten from:

$$\frac{\partial \mathbf{u}}{\partial t} = -\frac{1}{\rho_0}\nabla p \tag{2.28}$$

to

$$\frac{\partial \mathbf{u}}{\partial t} = -\frac{1}{\rho_0}\mathcal{F}^{-1}\{ik_{\mathrm{x}}\mathcal{F}(p)\} \tag{2.29}$$

A

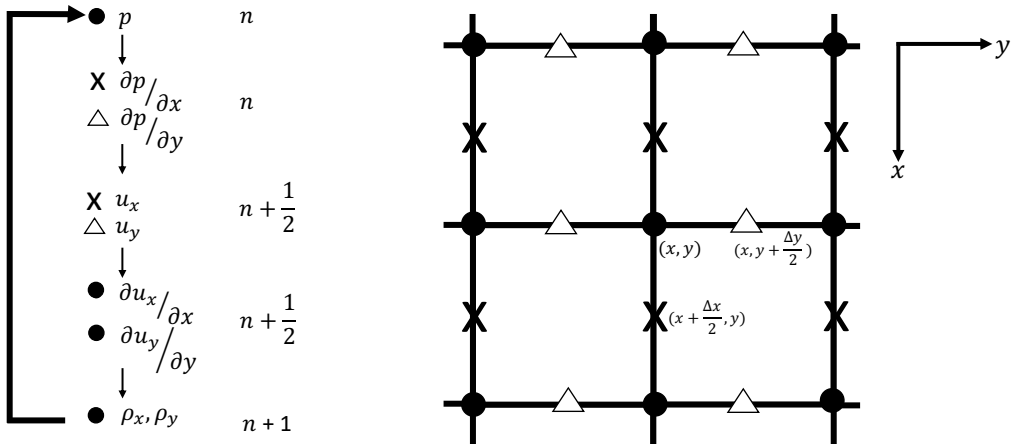

B

Parameter	Position	Time
Axial velocity input	x + Δx/2,y	t
Axial velocity output	x + Δx/2,y	t + Δt/2
Pressure input	x ,y	t + Δt/2
Pressure output	x ,y	t + Δt

Figure 2-3: Simulation staggered grid. (A) Image inspired from ′k-Wave: A MATLAB toolbox for the time domain simulation of acoustic wave fields.User Manual′, by Treeby et al. (2012), pg13 [182]. This shows the staggered spatial and temporal grid in 2D where p is the acoustic pressure, ρ is the particle density, and u is the particle velocity. The particle velocities and first spatial derivatives of the pressure are calculated on the staggered grid points given by x and Δ, and other variables calculated at regular grid points (dots). (B) Table showing how the input and output pressures and velocities should be interpreted relative to each other.

This involves spatially discretising the field of view by representing the space as a grid, as shown in Figure 2-3. Temporally the simulation is discretised by defining a time step associated with this grid. Mass and velocity sources can be defined on the grid and the resulting acoustic field can be sampled across the field of view by defining sensor positions. A spatially and temporally staggered grid is used because this enables more accurate simulation of the acoustic wave propagation on a larger grid size compared to using an un-staggered grid by reducing the sampling error [183]. One practical disadvantage of this are the phase offsets introduced between the inputs

and outputs, the adjustments which are relevant to this work are given for reference in Figure 2-3. Further details of how the k-Wave package models wave propagation is provided in Treeby et al. (2012) [182].

It is obvious that the grid spacing must be sufficiently fine to capture the highest frequencies allowed by Nyquist theorem. However, discretisation choices also impacts the numerical error. The spatial discretisation is generally reported in terms of points per wavelength (ppw) [182]. Stability is ensured by an appropriate choice of time step. The Courant-Friedrichs-Lewy (CFL) number is introduced to ensure the temporal and spatial discretisation are appropriately related. This dimensionless number (N_{CFL}):

$$N_{\mathrm{CFL}} = c_{\max}\frac{\Delta t}{\Delta x} \tag{2.30}$$

would be 1 for a stable solution to the homogeneous, linear case where $c_{\max}$ is the maximum acoustic sound speed, Δt and Δx are the temporal and spatial discretisation respectively. In practice, for the more complicated cases, this number is determined by convergence testing [184]. It should be noted that the smaller the temporal and spatial discretisation, the longer the simulation time. Therefore, there is a trade-off between the required simulation accuracy/stability and the simulation speed. For the convergence testing performed for this work please see Appendix A.

2.3.3 SVD filter

SVD is a powerful method of matrix factorisation which has generally been applied across US research to separate blood signal from noise and/or clutter [142, 185, 186, 187]. In particular, of most relevance to this work, is the recent literature showing that SVD filtering can also be used to extract MB signals [116, 121, 125]. Demené et al., (2015) describe the method of SVD for CEUS in detail. The technique is outlined briefly here.

Generally, US flow imaging data $s(x, z, t)$ can be described by three signal com-

ponents consisting of: clutter $c(x, z, t)$, blood scatterers $b(x, z, t)$ and noise $n(x, z, t)$, where t is the time of acquisition and x and z are the lateral and axial coordinates, respectively. In this case, the signal $s(x, z, t)$ is reorganised into a two dimensional spatiotemporal Casorati matrix $S(N_{\mathrm{x}} * N_{\mathrm{z}}, n_{\mathrm{t}})$. This is where each frame is vectorised and added as a column as shown in Figure 2-4. This work uses beamformed RF data (before Hilbert transform).

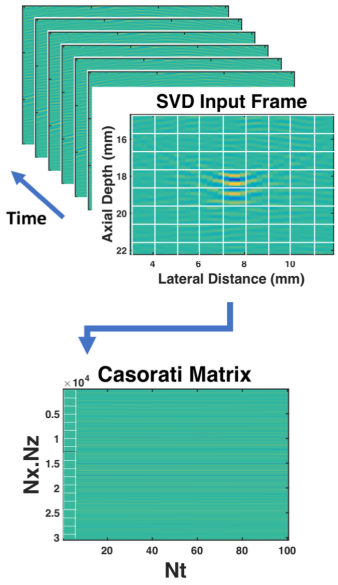

Figure 2-4: Generation of Casorati matrix for SVD. Each frame of spatial information is reformed as a column vector of the Casorati matrix.

SVD is then used to factorise the Casorati matrix to:

$$S = UDV^* \tag{2.31}$$

where columns of U are spatial singular vectors and corresponding columns of V are the associated temporal vectors. U and V are orthonormal. D is a diagonal matrix, where the elements are the singular values which decrease as the column number increases. They illustrate the relative contribution to the overall signal of each singular vector pair. A spatial singular vector re-ordered back to N_{z} rows by

N_x columns can be thought of as a virtual image extracted from the data. The corresponding temporal singular vector controls how each of the pixel amplitudes vary together over time. For MB detection a lower singular value threshold is set (l), below which the spatial and temporal signal contributions of the singular vectors are discarded as unwanted tissue signal and an upper threshold is set (u) beyond which the information is discarded as unwanted noise. The filtered signal is given by:

$$S_{\text{filtered}} = \sum_{i=l}^{i=u} U_i D_i V^*_i$$

(2.32)

Mathematically, the decomposition corresponds to finding the eigenvectors and eigenvalues of the covariance matrices SS^* and S^*S:

$$SS^* = UDD^*U^* \tag{2.33}$$

$$S^*S = VD^*DV^* \tag{2.34}$$

The eigenvectors form an orthogonal basis which describes variation in the data. In other words, the SVD filter identifies similar characteristics over space and time for individual pixels. The eigenvectors can be thought of as a least square fit along the direction of increasing variance or decreasing spatiotemporal coherence. The eigenvalues give a weighting to how large a contribution each signal component makes to the whole data set. SVD filtering relies on the assumption that tissue, blood and noise signal are represented by different singular vectors. Namely, that tissue regions will consistently move together over time and thus exhibit high spatiotemporal coherence. Conversely, noise will be more random and thus have low spatiotemporal

coherence. By combining only the desired singular vectors a new filtered data set can be achieved.

2.4 Methods

2.4.1 Tissue properties

The simulation was designed to be flexible enough to simulate a range of tissue environments. Using k-Wave, each grid point can be be allocated a value of sound speed, density, non-linearity and attenuation. Tissue was modelled based on the soft tissue acoustic properties provided by [188], see Table 2.1. Inhomogeneity to model boundaries between tissue and blood was introduced by assigning regions across the frame to equal the acoustic properties of blood (see Table 2.2 for values used). Heterogeneity on the sub-resolution scale was introduced by defining a number of scatterer positions. The acoustic properties of these scatterers were normally distributed with a mean of the bulk tissue values and a standard deviation of 0.8% of the mean. The number of scatterers per resolution cell was 10 for each centre transmit frequency to ensure a fully developed speckle pattern [189]. The tissue geometry used throughout this chapter is shown in Figure 2-5.

Tissue Parameters	Values
Speed of Sound(c)	1570 ms^{-1}
Density (p)	1050 kgm^{-3}
Power Law Prefactor (α)	1 db$(\text{MHz cm})^{-1}$
Power Law Prefactor (y)	1.05
B/A Non-linear Exponent (B/A)	7.4

Table 2.1: Example soft tissue acoustic properties, Azhari, H. (2010)

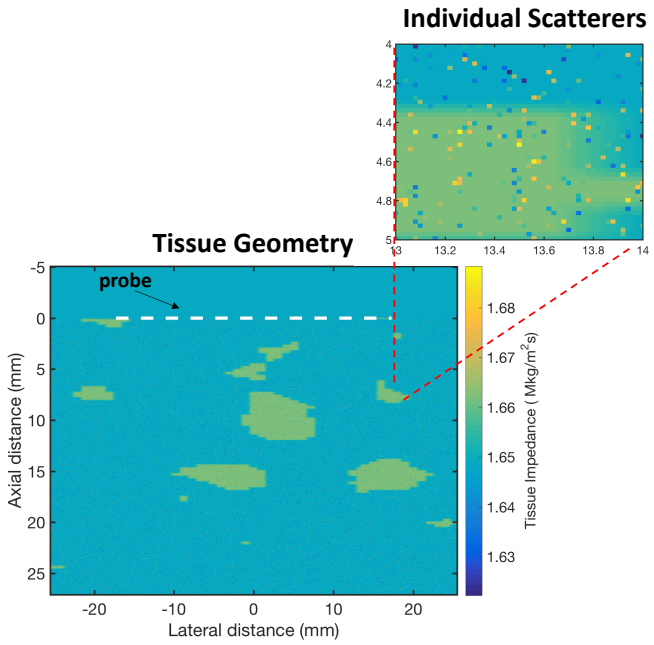

Figure 2-5: Tissue geometry.

2.4.2 MB properties

This work focussed on modelling Sonovue MBs described in Chapter 1. The properties and size distribution of Sonovue have been characterised and estimated in previous literature [81, 178]. In addition, a value for the ambient pressure has also been taken from literature [190]. The parameters used in the following simulations are provided in Table 2.2.

The MB size distribution provided in Gorce et al. (2000) has been provided in Figure 2-6 [191]. Unless otherwise indicated, the simulations were repeated for MBs of resting radii 0.5, 1, 2, 3, 4 and 5 μm. The results are then generally presented as weighted averages by scaling the result for each MB size according to the expected distribution shown in Figure 2-6 before summing together.

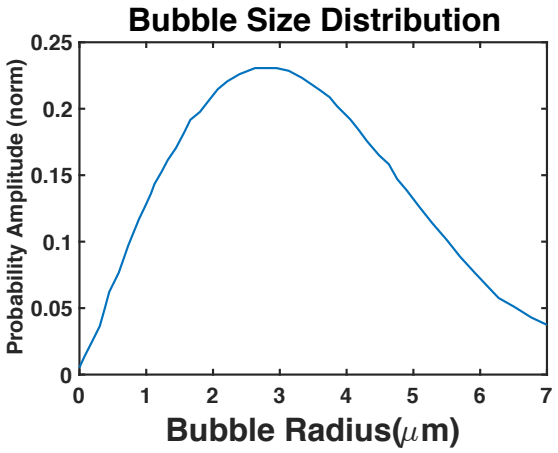

Figure 2-6: Sonovue size distribution. Expected size distribution of Sonovue extracted from Gorce et al. (2000). [191]

Model Parameter	Value	Reference
Bubble surface tension (σ)	$\sigma(R_0) = 0.072$ Nm^{-1}	[178]
Gas exponent(γ)	1.07	[178]
Dynamic viscosity(μ)	2x10^{-3} Nsm^{-2}	[178]
Shell elasticity (χ)	0.3 Nm^{-2}	[81]
Shell viscosity(κ_s)	3.2x10^{-9} kgs^{-1}	[81]
Blood speed of sound(c)	1575 ms^{-1}	[188]
Blood density (p_l)	1055 kgm^{-3}	[188]
Ambient pressure (P_0)	101325 kgm^{-3}	[190]
Buckling radius (R_{buckling})	$0.99 \cdot R_0$	[80]

Table 2.2: MB properties used in simulation

2.4.3 Pulse and probe design

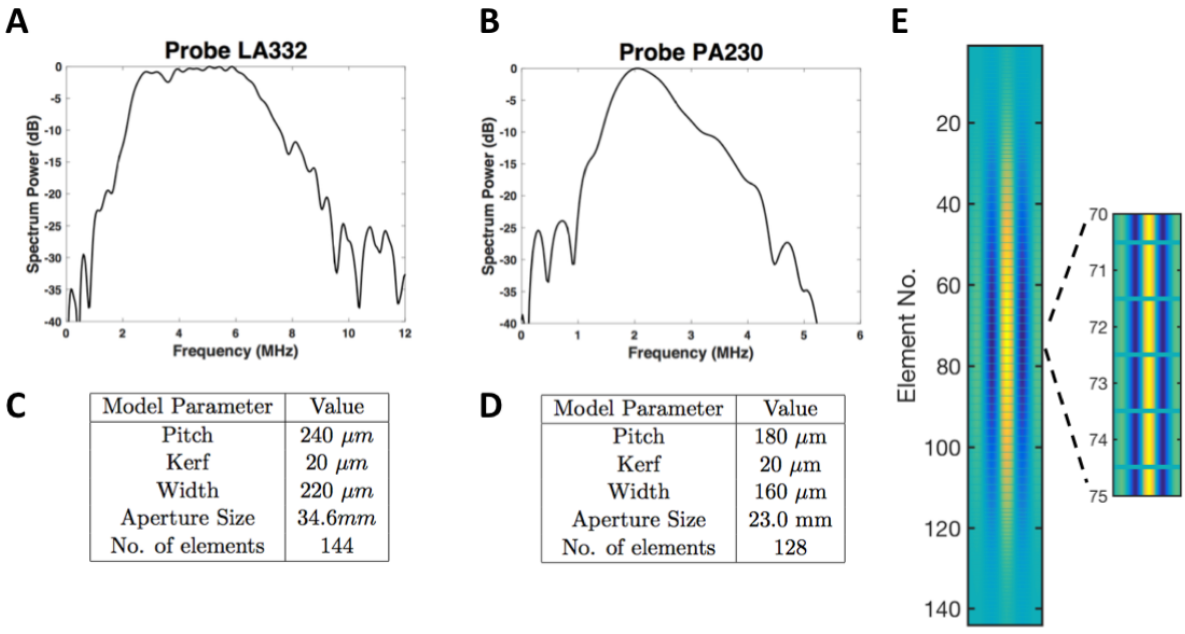

C

Model Parameter	Value
Pitch	240 μm
Kerf	20 μm
Width	220 μm
Aperture Size	34.6mm
No. of elements	144

D

Model Parameter	Value
Pitch	180 μm
Kerf	20 μm
Width	160 μm
Aperture Size	23.0 mm
No. of elements	128

Figure 2-7: Probe and pulse design. Bandpass filter associated with LA332 probe (A) and PA230 probe (B) and associated geometry values for LA332 (C) and PA230 (D). Example of simulated pulse across the probe (E).

k-Wave does have an in-built transducer class, but it was decided to simulate the transducers independently for increased flexibility and control. The active elements of a linear transducer were modelled as time varying velocity sources. Each source pixel introduced a dipole field which mimicked the directivity of the transducer field [182]. Grid points corresponding to transducer elements contained velocity sources and grid points corresponding to kerf regions were left empty as shown in Figure 2-7(E). For this work, probe geometry was based on the ESAOTE probes available in our laboratory. The motivation for modelling these probes was so that the simulation could be more easily used alongside *in vitro* experiments in future work. In addition, these probes operate over a frequency range that is appropriate for clinical applications of SRUS. However, there were some practical problems with simulating these probes on the computational grid as sources must be defined on grid points. For example, the reported pitch of the LA332 probe is 245 µm. Due to the challenges

of simulating this on the grid, the pitch was approximated to be 240 μm and the kerf 20 μm.

The axial grid spacing was set to be 6 ppw of the second harmonic of the transmit frequency, see Appendix A for more detail. The lateral grid spacing was set to 20 μm. This value was chosen because it was below the 6 ppw limit for the SVD and DI simulations performed using the higher frequency LA332 probe, could reasonably approximate the kerf size, and be a factor of the element size. The last two points meant that the transducer face could easily be defined on the computational grid.

For each source a Gaussian pulse of n cycles could be simulated. The amplitude of each signal was then modulated by the apodisation. The following simulations used a Hamming filter. Plane wave transmission of a single angle could be modelled by ensuring a constant phase across the aperture.

Finally, the receive transducer was modelled by positioning sensors at the element centres. The received signals were band-passed filtered using realistic transducer sensitivities, again modelling the available ESAOTE probes. The frames were down-sampled so that the time discretisation matched the 50 MHz sampling rate of the experimental ULA-OP system [192].

2.4.4 Simulation steps

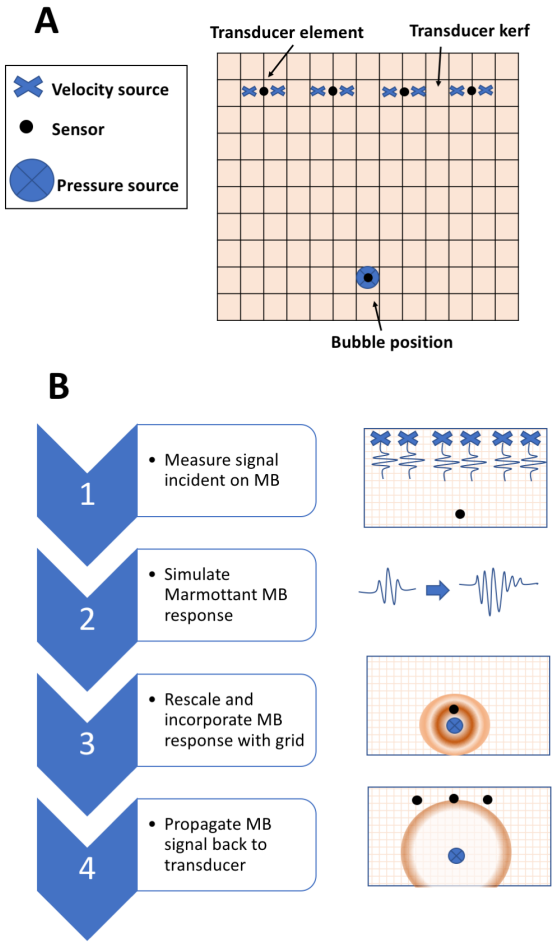

Figure 2-8: Simulation geometry. (A) Schematic of simulation geometry showing the sensors and sources on the grid. (B) Flow diagram of MB simulation steps (using same key as (A)). (1) A plane wave was generated by a line of mass sources. The resulting pressure was measured at the MB position. (2) The Marmottant response was determined. (3) This response was rescaled for incorporation with the grid. (4) The MB signal was propagated back to the sensor positions.

Figure 2-8 outlines the four steps used to incorporate the Marmottant model and k-Wave simulation.

1. Prior to the transmit wave reaching the bubble, the pulse will have experienced frequency dependent attenuation and non-linear propagation through the tissue. This was included by simulating the transmit pulse and recording the waveform

at each MB position using a k-Wave sensor.

2. The MB response was modelled by using the signal received from step 1 as the input to the Marmottant model.

3. The Marmottant pressure response was then added as a mass source to the mass conservation equation at the MB position. This generated a monopole field as if from a radially oscillating volume [182]. The MB size is not negligible compared to the grid dimensions. This meant the MB pressure response could not be accurately represented by a mass source at a single point on the grid. Rescaling of the pulse was required so that the amplitude matched that expected from Equation 2.18 at a given distance from the MB position. This was done by determining P from Equation 2.18 using $R_p = 50$ μm. This specific value of R_p was chosen arbitrarily as a value which was an order of magnitude greater than any variations between MB sizes, whilst still being small enough to enable k-Wave simulations to be performed in a reasonable time. The MB response at $R_p = R_0$ was added as a point source in the grid and propagated a distance of 50 μm from the MB position. The pulse was then compared to the theoretical amplitude given by Equation 2.18 when $R_p = 50$ μm. The input was rescaled to ensure the simulated value at 50 μm matched the theoretical value.

4. The nonlinear propagation of the rescaled MB response to the receive transducer was then modelled using k-Wave. The receive transducer was modelled using sensors at the element centres.

Each step was repeated separately for each MB resting radius.

2.4.5 Movement

Scatterer and source positions can only be defined at grid points in k-Wave. Sensors can be defined at any position in the simulation plane. Using ultrafast imaging, both tissue and MB motion may be less than 1 μm between frames. With grid dimensions generally on the order of tens of microns (smaller grids require much longer simulation

time) movement must be simulated by shifting the sensor positions and source phase rather than scatterer or source positions.

For MB movement, in a homogenous medium, the sensor used in step 1 and the receive sensors in step 4 can be shifted appropriately depending on the MB displacement.

For tissue movement, simulation is simpler. The scatterer positions can be kept constant. In transmit, for axial tissue movement the phase of the transmitted pulse can be shifted and the sampling of the apodisation shifted for lateral motion. In receive, the sensors modelling the receive probe can also be shifted appropriately.

Using this method to generate motion means that, in order to model relative tissue and MB movement, the responses must be simulated separately and then coherently combined.

2.4.6 Noise

Previous literature has focused on understanding and correcting speckle as the major noise component of US [193, 194]. This coloured noise was introduced to the simulation via the incorporation of tissue inhomogeneity. Random noise is introduced from the electrical circuitry of the transducer. This has been modelled as white Gaussian noise as suggested in Demené et al., (2015).

An arbitrary level of white Gaussian noise was generated using a built in MATLAB function (awgn()). This noise was added onto an example frame of simulated data. The power of the useful signal (P_{signal}) and arbitrary noise ($P_{\text{noise}\prime}$) was determined by averaging the square of their respective signal amplitudes, (A_{signal}) and (A_{noise}) .

$$P_{\text{signal}} = \langle {A_{\text{signal}}}^2 \rangle \tag{2.35}$$

$$P_{\text{noise}\prime} = \langle {A_{\text{noise}}}^2 \rangle \tag{2.36}$$

Rearranging:

$$SNR = 10\log_{10}(\frac{P_{\text{signal}}}{P_{\text{noise}}}) \tag{2.37}$$

the desired ratio for the powers of signal and noise can be expressed:

$$\frac{P_{\text{signal}}}{P_{\text{noise}}} = 10^{\frac{SNR}{10}} \tag{2.38}$$

The extracted noise can be rescaled according to the chosen SNR via a scaling parameter (g).

$$P_{\text{noise}} = gP_{\text{noise}}\prime \tag{2.39}$$

Where g is calculated from:

$$g = \frac{P_{\text{signal}}}{10^{\frac{SNR}{10}}P_{\text{noise}}\prime} \tag{2.40}$$

The noise amplitude can be rescaled before being added to the signal frame.

$$A_{\text{noise}} = \sqrt{g}A_{\text{noise}}\prime \tag{2.41}$$

The SNR used for the simulations in this chapter was chosen based on a reference experiment. The reference experiment used a suspension of 0.3 ml of Sonovue^{TM} MBs (Bracco Imaging SpA, Milan, Italy) diluted using 50 ml of ultrapure water (Milli-Q$^{\text{TM}}$, MilliporeSigma, Massachusetts, United States) and drawn through a 200 μm cellulose tube (Hemophan®, Membrana, Wuppertal, Germany) at a flow rate of 15 μl/min. The flow phantom was imaged at a transmit centre frequency of 4 MHz using the LA332 probe (Esaote,Genoa, Italy) and ULA- OP (Univ. degli Studi di Firenze, Florence, Italy). Single plane waves of phase +1 were acquired and regions of interest corresponding to tube and MB (signal) and noise defined on the RF data. The SNR for this experiment was calculated to be 26.3 dB. In order to compare the different MB sizes and parameter sets the noise level was kept constant (the SNR was allowed to vary). The amplitude of the noise was determined by fixing the SNR of the modelled RF image of a 2 μm MB in tissue at 4 MHz to be 26.3 dB.

2.4.7 Comparing the detection methods

Pulse inversion

Pulse inversion involved the summation of temporally adjacent positive and negative frames of simulated RF data before beamforming and envelope detection. This extracted any non-linear signal and changes due to movement [85].

Differential imaging

Differential images were produced by the subtraction of temporally adjacent positive frames as in Desailly et al. (2013) [134]. Simulated RF frames were processed before beamforming and envelope detection. Signal was generated by movement between frames.

SVD

Computationally SVD was performed using the MATLAB economy-size SVD function (svd()). In this work the SVD filter is applied to beamformed RF data before envelope detection and the cut-off thresholds were chosen so as to achieve the maximum CTR.

Contrast to tissue ratio

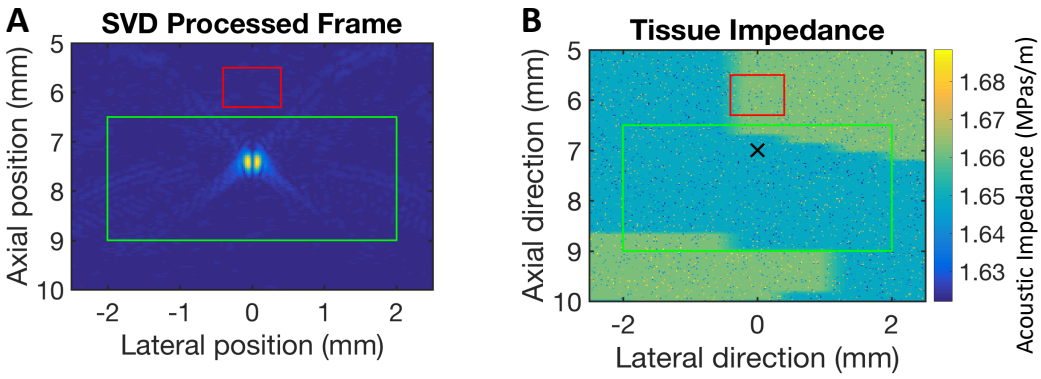

Figure 2-9: Signal quantification in terms of CTR. (A) These are shown on an example SVD processed frame, with the tissue region of interest and MB region of interest represented by the red box and green box respectively. (B) The ROIs are shown on the map of the tissue impedance, with the MB position shown by a cross. These regions were chosen to ensure MB lobe signal was not included across the parameter range.

Figure 2-9 show the regions of interest used to determine the CTR. The regions of interest for MB and tissue signal have different axial positions due to reduced lateral resolution causing MB lobes to mask tissue breakthrough for some parameter sets. Thus, it was simpler to define the regions as shown in Figure 2-9 and compare maximum pressure values for the tissue V_{tissue} and MB signal V_{bubble} [195]:

$$\mathrm{CTR} = 20\log_{10}\frac{V_{\mathrm{bubble}}}{V_{\mathrm{tissue}}} \tag{2.42}$$

The noise and localisation process were repeated twenty times. Twenty repetitions were empirically chosen as this generated a small spread of CTR values about the mean for the chosen noise level. The accuracy was determined as the mean of the bias between the localised and known MB positions and the precision by the standard deviation. This quantification was performed for the first output frame of each detection method so that the MB position in the FOV was constant. It was also em-

pirically observed that SVD filtering can cause the image intensity to fluctuate over the stack. This fluctuation causes the signal to drop from a maximum at t = 0 to a minimum corresponding to the centre of the stack size, and then back to a maximum at the final frame of the stack. This temporal fluctuation will be investigated later in this chapter, see section 2.5.3. Thus, unless otherwise specified, the first frame was chosen to compare PI and DI with the best case CTR for SVD.

Localisation

The extracted signals were envelope detected using a Hilbert transform and localised using the onset method [145] as introduced in subsection 1.6.9. Normally the axial position is found using an onset threshold of the noise mean plus 3 standard deviations. However, for this work, a threshold of 4 standard deviations was chosen. This was because the onset method was developed at a specific set of parameters, using a higher threshold here enabled fairer comparison across these three detection techniques and wider parameter space.

Specific simulations

- **SVD stack size and filter order**:

  To determine a stack size which generates the best CTR for the SVD experiments, 1000 frames for a MB moving laterally at 0.5 mm/s were simulated using a centre transmit frequency of 6 MHz. These were filtered using varying stack sizes and eigenvalue cut-offs.

- **Frequency dependence: Transmit Centre Frequency**

  Several different commercially available transducers will be able to image at the same transmit centre frequency. However, differences in geometry and sensitivity of these transducers will mean that the resulting images are different for different probes. To achieve the most general comparison of the detection methods over different transmit frequencies a linear array was designed for each

centre frequency (1.5 MHz, 2 MHz, 3 MHz, 4 MHz, 5 MHz, 6 MHz and 7 MHz). For each frequency, a Gaussian pulse three cycles in length and MI of 0.1 was used as the input to the Marmottant model. The same MI value and number of cycles was used throughout this chapter. The ratio of pitch size to transmit wavelength was set to a constant value of 0.61 to avoid the generation of side lobes. The aperture size was also set to a constant value due to its impact on lateral resolution. Keeping the pitch to kerf ratio constant meant that the number of elements of each transducer ranges from 16 at 1 MHz to 112 at 7 MHz. These values were chosen to correspond to experimental work using 64 elements of the LA332 probe (Esaote, Italy) with the ULA-OP (Universit degli Studi di Firenze, Italy) system at 4 MHz. The influence of frequency was then determined for each processing method for a MB flowing laterally at 0.5 mm/s.

- **Frequency dependence: Probe Bandwidth**

  To simulate the more practical situation of using commercially available transducers of a particular geometry and frequency sensitivity the following simulations were performed using the properties of the PA230 (1-4 MHz) and LA332 (1-4 MHz) probes. This enabled investigation of how transducer sensitivity, and position of transmit centre frequency within the probe bandpass, have different implications for different detection methods.

- **Tumour Physiological environment**

  Following the frequency investigations, transmit frequency and the probe simulated could be fixed to one determined appropriate for each technique. The dependence of CTR and localisation accuracy and precision on speed were determined for a range of speeds < 2 mm/s for lateral motion, and the dependence on direction was investigated at a flow speed of 0.5 mm/s.

- **Investigating Artifacts Introduced by SVD Filtering**

  Following the observation that the SVD filter introduced a variation of the frame

intensity over the stack length, further work was done to investigate potential artifacts introduced by SVD. A single MB of 2 μm in radius, flowing at a velocity between 0.5 and 5 mm/s, and surrounded by tissue was modelled. To investigate the underlying causes of the flashing artifact bubble speed, initial CTR and stack size were varied.

2.5 Results

2.5.1 MB response

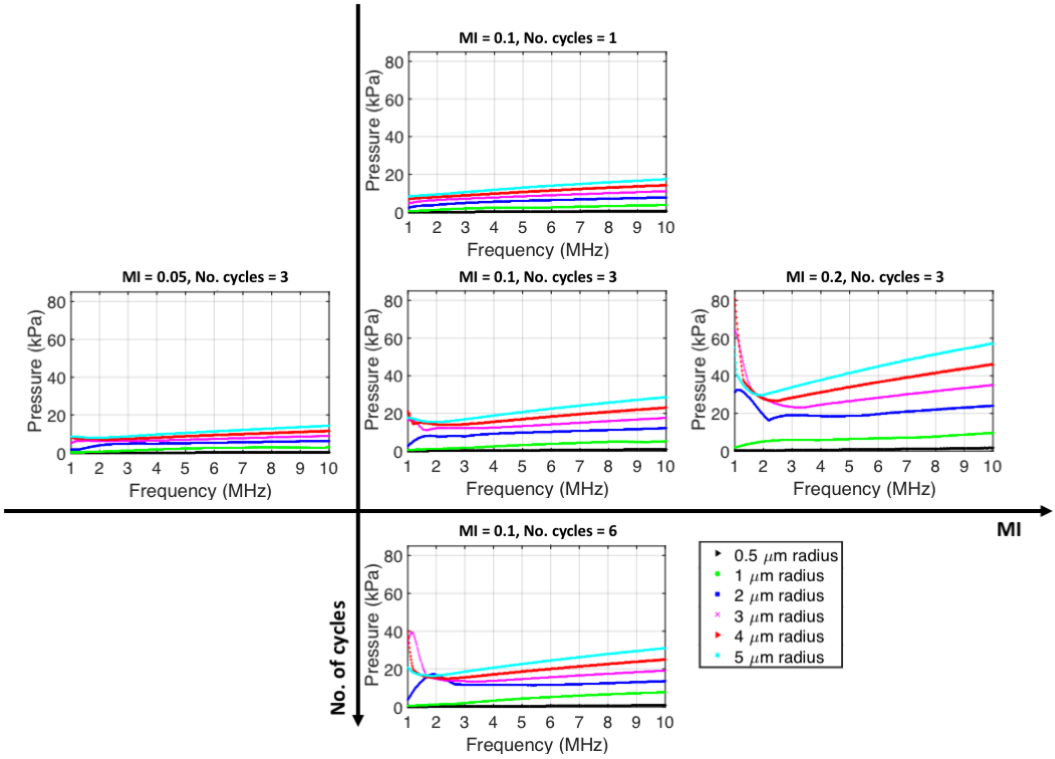

Figure 2-10: Dependence of MB response with respect to the number of cycles and MI value for a range of MB radii.

Before incorporation with k-Wave the MB response was calculated to enable easier interpretation of later results. Figure 2-10 shows the predicted behaviour of each MB size over the frequency range 1-10 MHz, where the MI was kept constant over the

frequency range. The maximum absolute pressure was measured at a distance 50 μm from the MB centre for each frequency and repeated for five MB radius values (0.5, 1, 2, 3, 4 and 5 μm). As expected, the scattering generally increases in amplitude as frequency increases due to the increased scattering cross-section. MB resonance behaviour can be observed at low frequencies for some parameters. In particular, increasing the pulse length and MI increases the resonant behaviour.

2.5.2 Detection methods

SVD stack size:

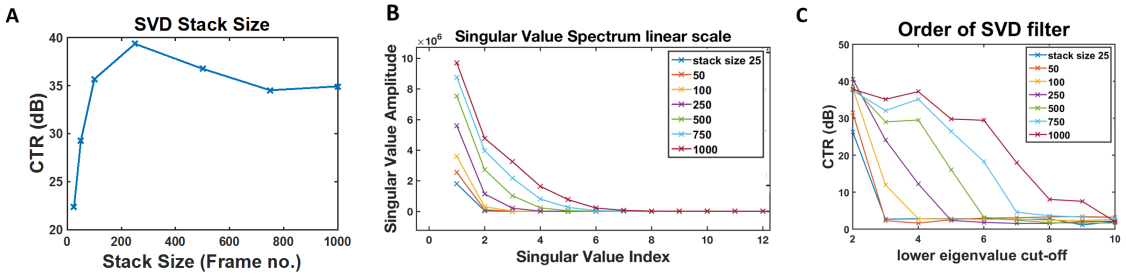

Figure 2-11: Effect of SVD stack size. (A) Effect of stack size on CTR when filtering a 2 μm MB moving laterally at 0.5 mm/s where the lower singular value cutoff is 2. This shows that large stack sizes are not always beneficial. (B) Singular value spectrum at each stack size. As stack size increases the weightings of each component become more evenly shared. (C) CTR for each stack size as lower SVD eigenvalue cut-off is adjusted.

Figure 2-11 investigates the influence of stack size on a 2 μm radius MB moving at 0.5 mm/s laterally using a pulse with centre transmit frequency of 6 MHz. The CTR rises until a stack size of 250 frames is reached. For this set of parameters, the CTR began to fall at stack sizes beyond 250 frames. Figure 2-11(B) shows that a larger stack size allows the signal to spread over a wider range of eigenvalues. Figure 2-11(C) shows that the CTR cannot be improved by adjusting the lower singular value cut-off for each stack size. To achieve the best CTR for SVD with the lowest acquisition time, the following SVD demonstrations were performed using 250 frames and removing

the signal associated with the first singular value and those values >14 which were associated with noise.

Effect of frequency:

Figures 2-12 - 2.5.2 show the effect of centre transmit frequency and bandpass filtering on SR in terms of CTR and localisation precision. Figure 2-12 shows the results without transmit or receive bandpass filtering to enable generalisation of the results to different probes. This was to ensure that any trends due to varying centre transmit frequency alone were not obscured by the introduction of filtering. Figure 2-12(A-C) shows the trends of each individual bubble size due to the growing interest in how MB size will affect SR [196]. These results are then presented as weighted averages in Figure 2-12(D), to show any overall frequency dependence of the detection techniques. The weighted average was calculated by scaling the result for each MB size according to the expected Sonovue^{TM} size distribution as reported in Gorce et al. (2000) before summing together.

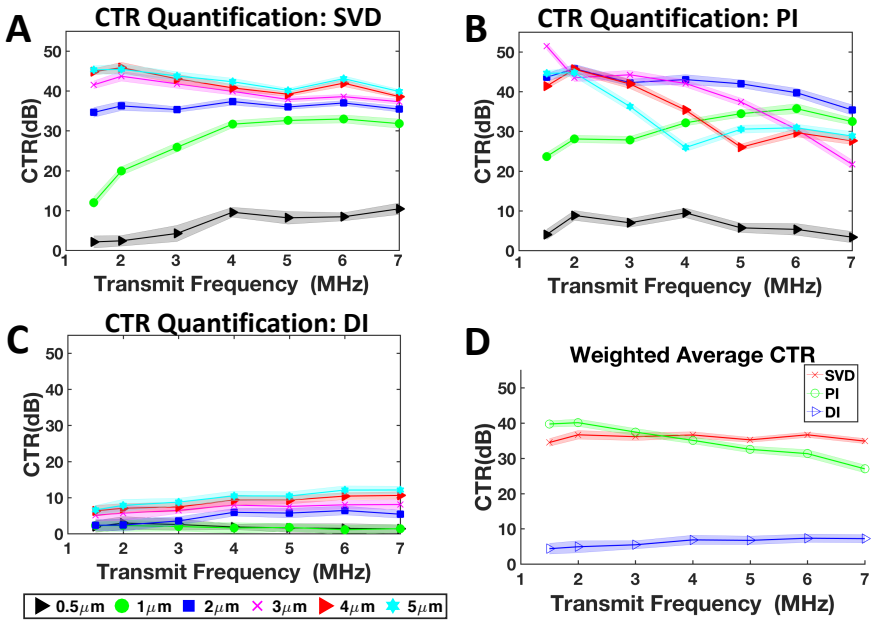

Figure 2-12: CTR dependence on centre transmit frequency. The CTR dependence of each MB radii on acquisition centre frequency for MBs flowing laterally at 0.5 mm/s for SVD (A), PI (B) and DI (C). (D) presents the CTR weighted average over the MB distribution for all three detection methods.

Figure 2-13 shows how the localisation precision depends on frequency due to the changing CTR and size of initial point spread function.

Finally, Figure 2.5.2 introduces bandpass filtering that matches the sensitivity from commercially available probes. This is to explore whether some techniques are more affected than others by the probe sensitivity and position of centre frequency in the bandwidth.

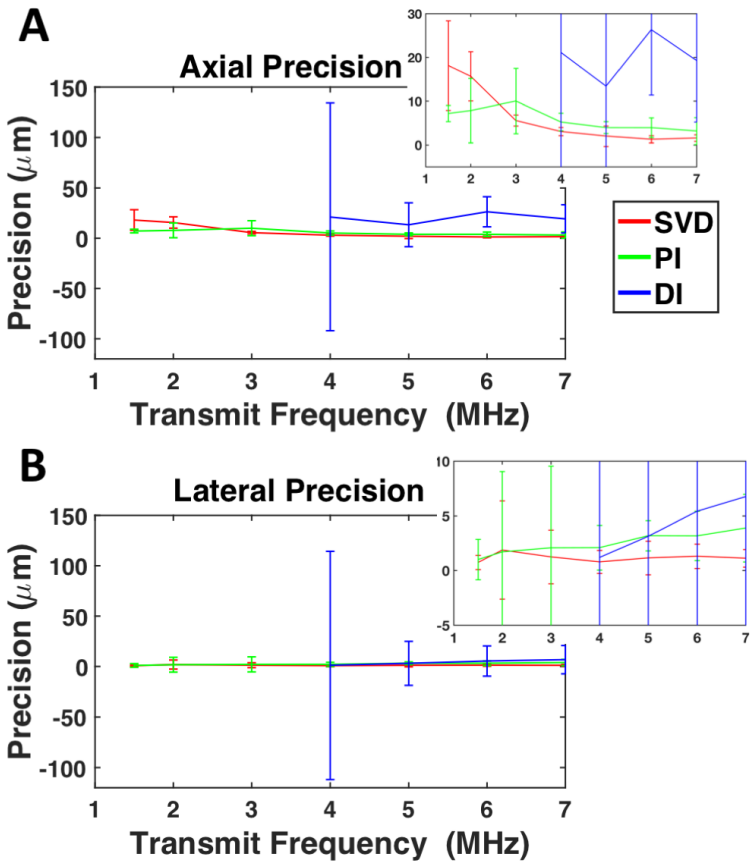

Figure 2-13: Dependence of localisation precision on centre transmit frequency. (A) shows the average axial localisation precision at each transmit centre frequency for each of the MB detection methods. This is the standard deviation of the axial position measured over repeated simulations. The error bars represent the standard deviation of the weighted average, i.e. variation due to contributions from different MB radii. Missing points (for DI only) correspond to simulations where the MB signal was not sufficiently greater than the tissue/noise for the localisation to be made. (B) shows the average lateral localisation precision for each MB detection method, where the inset is to visualise data points that have error bars that are much smaller than for DI.

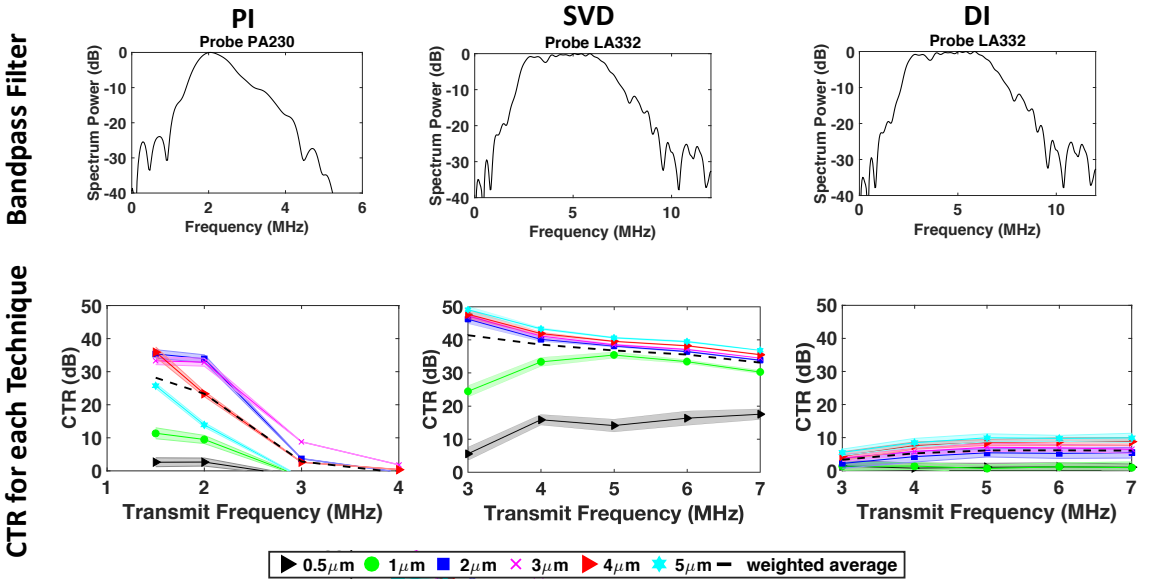

Figure 2-14: Effect of transducer bandpass filter. (Top) The bandpass of the modelled transducer based on PA230 (left) and LA332 (middle and right). (Bottom) Frequency dependence on CTR for PI (left), SVD (middle) and DI (right) when probe sensitivities are introduced.

Low frequency excitation:

Figure 2-12 shows that PI has the greatest CTR at the lowest frequencies. Individual bubbles contribute differently to the total CTR for each processing technique. CTR increases with increasing radii for SVD and DI, see Figure 2-12 (A and C). Due to resonance behaviour this trend is not true for PI, also shown in Figure 2-12(B). Figure 2-12(D) shows that the weighted average CTR of PI decreases as the MBs exhibit less non-linear behaviour at higher frequencies. PI generated a CTR improvement of 3.4 dB at a transmit frequency of 2 MHz over SVD and 36.2 dB over DI.

Figure 2-13 shows the high axial and lateral precision of PI at low frequencies. The average axial and lateral precision at 2 MHz, for example, is 7.8 μm and 1.7 μm respectively for PI imaging. Missing points on Figure 10 correspond to simulations where the MB signal was not sufficiently greater than the tissue/noise for the onset method to detect a MB. The results show that DI is not appropriate at frequencies

$\leq$ 4 MHz for the velocities used in this simulation.

Figure 2.5.2 shows the incorporation of a bandpass filter over the frequency range 1.5 - 4 MHz for PI. This technique suffers as the second harmonic frequency rises above the transducer sensitivity range. For most commercially available low frequency transducers, ensuring that transmit frequencies are at the lower end of the transducer sensitivity, to ensure sufficient sensitivity at the 2nd harmonic, is crucial for PI. DI and SVD are less limited by a narrower band-pass filter.

High frequency excitation:

Figure 2-12(A) shows an upwards trend in CTR for SVD with frequency for the MB sizes $<$ 2 μm in radius. For larger MB radii, the CTR of the SVD processing is fairly constant over the frequency range. And Figure 2-12(D) shows that, overall, SVD does not significantly vary with frequency. As shown in Figure 2-12(D), DI showed improved CTR with increasing frequency with an increase of 2.98 dB at 6 MHz compared to 1.5 MHz. However, it is clear that for these flow rates, SVD is preferable to DI across the frequency range.

Figure 2-13 shows that DI localisation was only possible for frequencies $\geq$ 4 MHz. The localisation precision plots for individual bubble sizes have not been presented here. Instead, Figure 2-13 shows the weighted average. Some MB radii did not generate sufficient CTR to enable localisation, so did not contribute to the weighted average presented in Figure 2-13. Only MBs $\geq$ 3 μm in radii generated sufficient CTR to enable localisation for DI at centre transmit frequencies $\geq$ 4 MHz. SVD and PI could localise all but the smallest MBs, 0.5 μm radii, over the frequency range studied here.

Figure 2.5.2 shows that introduction of the bandpass filter has less effect on CTR for the linear techniques over the frequency range compared to PI. For SVD, although average CTR is fairly constant over the frequency range, the improved axial and lateral precisions at higher frequencies motivates the use of SVD for high frequency applications, see Figure 2-13. The axial precision improves from 18.1 μm at 1.5 MHz to 1.6 μm at 7 MHz.

Velocity dependence:

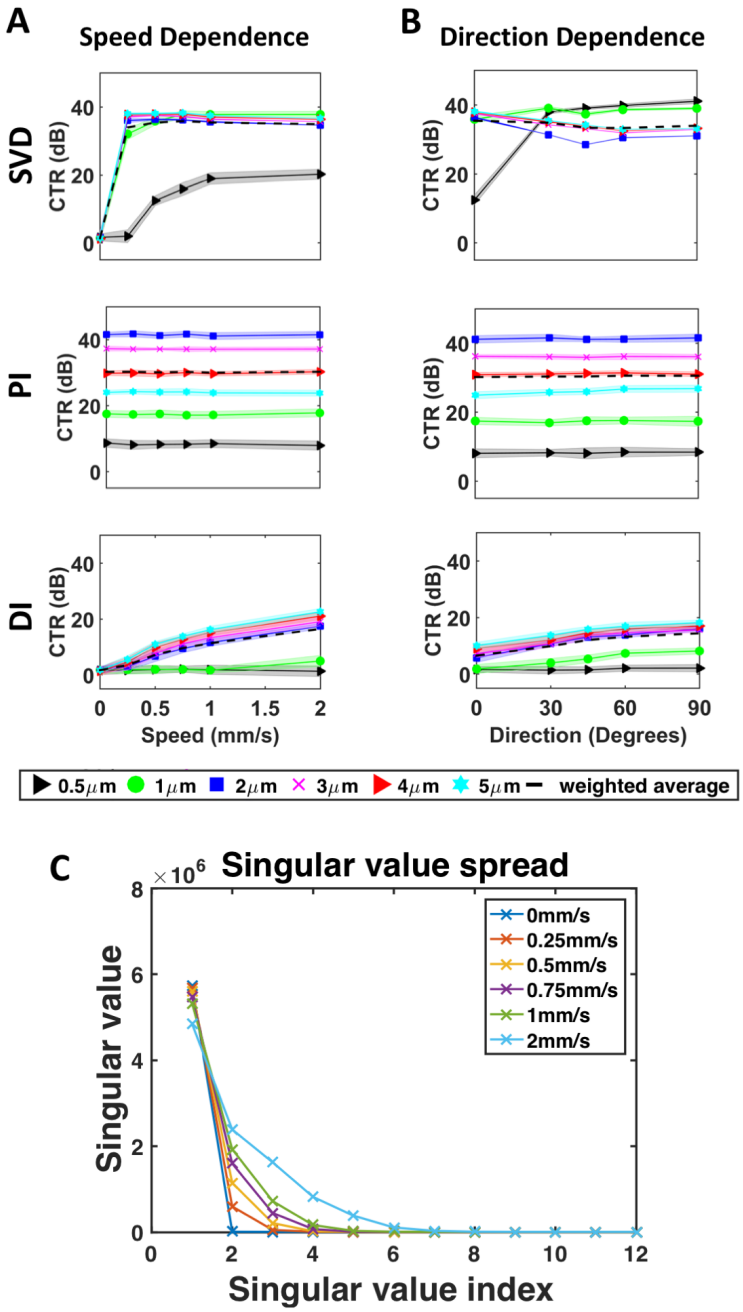

Figure 2-15: CTR dependence on velocity. (A) shows the CTR dependence of each MB radii and the weighted average on flow speed for MBs flowing laterally. (B) shows the CTR dependence on flow direction at a speed of 0.5 mm/s. (C) Spreading of data across singular vectors for varying lateral speed.

For the following simulations, PI was performed at a frequency of 2 MHz using the bandpass filter associated with the PA230 probe. DI and SVD were performed at a higher frequency of 6 MHz using the bandpass filter associated with the LA332 probe. These centre frequencies and probes were chosen for each technique considering the best average CTR and precision values determined in the previous section.

Figure 2-15 shows how CTR varies with MB flow speed and direction. Figure 2-16(A) and (C) are graphical visualisations of how the accuracy and precision values determined from the simulation results will affect SR images for different MB speeds and directions respectively. For each processing technique an example ground truth vessel is shown, where each 30 x 30 μm segment corresponds to a different velocity. Using the values for the weighted average of localisation and precision the simulated SR image is overlaid on the ground truth image. The simulated SR segments are shifted with respect to the ground truth by their axial and lateral bias. The height and width of the simulated SR image of these ground truths are increased by the axial and lateral localisation precision respectively, with larger rectangles representing poorer precision. These same results for localisation precision and accuracy are presented graphically in Figures 2-16(B) and (D), where the error bars represent the standard deviation from the weighted average over the different bubble radii.

Applications with slowest/stationary MBs, varying flow rates or flow in different direction:

Figures 2-15 and 2-16. both show that PI is less dependent on MB velocity compared to DI and SVD. Figure 2-15 shows that CTR is constant over the 0 - 2 mm/s MB speed range and all flow directions for PI. In comparison, SVD and DI are not appropriate for stationary MBs. At 0 mm/s the CTR drops to 0 dB for SVD and DI. This is also shown by the missing segments (represented by a cross) and data points in Figure 2-16 (B). Figure 2-15 also shows that DI and SVD have lower CTR values for lateral motion. The DI localisations are limited by noise. The results show that DI is only appropriate for MB speeds > 0.75 mm/s or as flow becomes more axial. Figure 2-16

shows that SVD can introduce bias on the order of hundreds of micrometres over a range of speeds and directions. PI is more suitable for applications with varying flow velocities as any bias is constant over the range of velocities investigated here.

Applications with faster flow, with an axial component of flow velocity:

Figure 2-15 shows that the highest CTR for faster flow can be achieved using SVD processing. However, CTR values begin to plateau and even decrease by a few decibels for MBs with radii > 1 μm. This effect is due to the signal spreading more evenly over the singular value components with increasing speed as shown in Figure 2-15(C). Figure 2-15 also shows that DI and SVD have higher CTR as the flow becomes more axial (90 degrees). For DI, at 0.5 mm/s, the localisations are only possible when there is some axial component of velocity. Although DI has a significantly lower CTR compared to PI and DI, the localisation accuracy and precision are comparable. Thus, DI will still be a useful technique for faster blood flow or flow with some axial component. Figure 2-15 (A and B) show that there is more variation in CTR for PI across the different MB sizes compared to SVD and DI. This is shown by the relatively larger error bars for PI in Figure 2-16. A degree of axial movement enables SVD to detect even the smallest MBs of 0.5 μm radii. Axial precision falls to sub-micron for SVD localisation of axial flow compared to 11.3 μm for DI and 12.1 μm for PI, see Figures 2-16 (D).

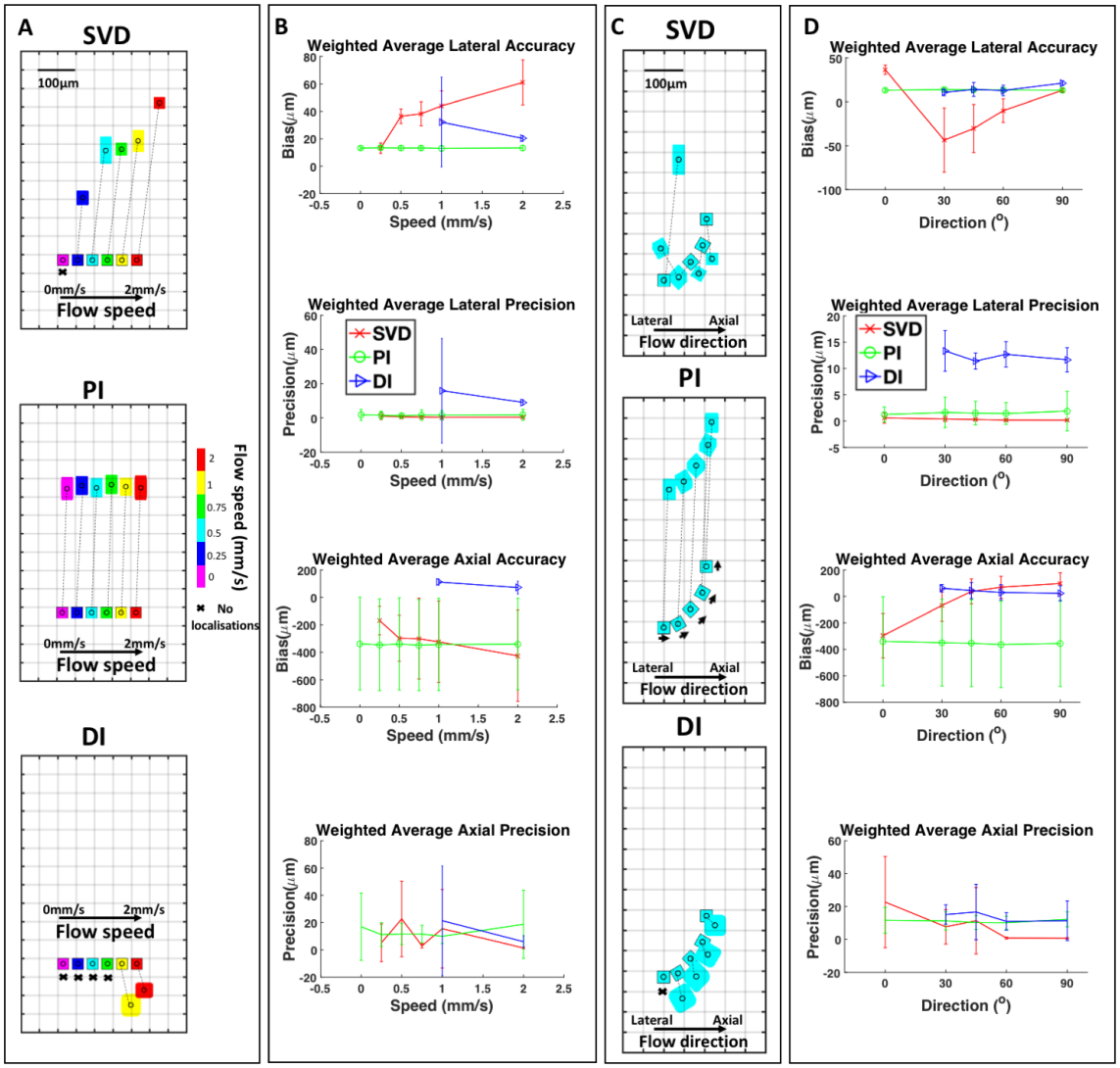

Figure 2-16: Localisation dependence on velocity. (A) Visualisation of localisation results over speed range 0-2 mm/s for SVD (top), PI (middle) and DI (bottom). Scale is represented by a background grid (50 x 50 µm). The same ground truth vessel is presented at a depth of 7 mm, with each vessel segment being represented by a square of size (30 x 30 µm). Each segment corresponds to a different MB flow speed. When CTR values are sufficient to generate localisations, the SR image is modelled by shifting each vessel segment by the localisation accuracy determined from the simulation. If MB signal does not exceed the noise threshold a cross is shown to represent missing data. Localisation precisions in lateral and axial directions are represented by increasing the width and height of the rectangle by the lateral and axial precision respectively, i.e. so that larger rectangles represent poorer precision. The centre points of the corresponding ground truth and simulated segments are joined to highlight the translation. (B) Shows the same accuracy and precision values determined from the simulation graphically. (C) Visualisation of localisation results over direction range (0-90°). The same ground truth vessel (of segment dimensions 30 x 30 µm) is presented at a maximum depth of 7 mm. Each segment corresponds to a different MB flow direction at a MB flow speed of 0.5 mm/s. When CTR values are sufficient to generate localisations the SR image is modelled by shifting each vessel segment by the localisation accuracy determined from the simulation. The vertical extent of the rotated rectangle is increased by the axial precision and horizontal extent increased by the lateral localisation precision. The centre points of the corresponding ground truth and simulated segments are joined to highlight the translation. (D) Shows the same accuracy and precision values determined from the simulation.

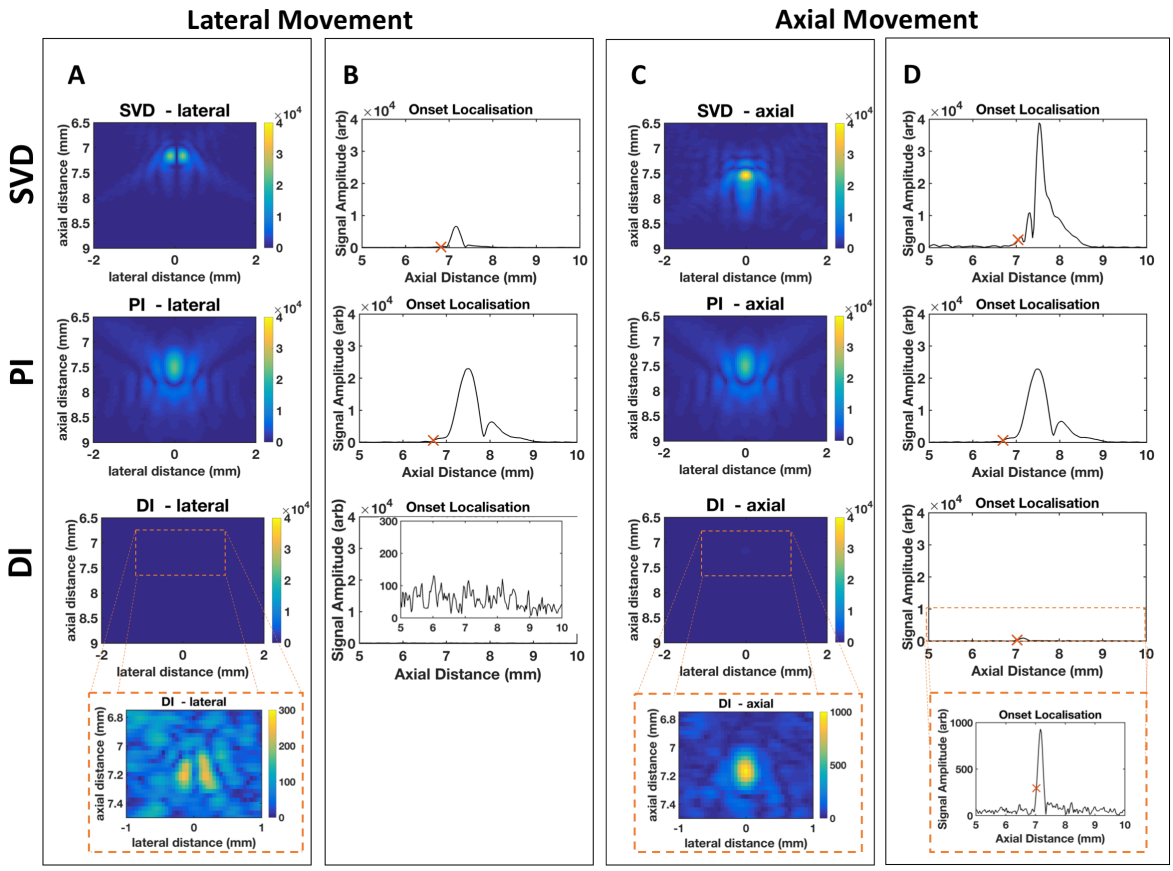

Figure 2-17: Visualisation of variation of MB point spread function. Shape of bubble signals for 0.5 mm/s lateral (left) and axial (right) movement. PI was performed at a transmit frequency of 2 MHz for PI (middle). A centre transmit frequency of 6 MHz was used for DI (bottom) and SVD (top). (A) The beamformed and envelope detected processed frames for SVD (top), PI (middle) and DI (bottom) for lateral flow. (B) The axial profile used for determining the MB axial position during the onset localisation. The cross shows the localisation position where possible. (C) Beamformed frames for axial flow. (D) Onset localisation for axial movement. Insets are used for DI (provided within orange dashed boxes) due to dynamic range used for overall comparison of the methods being too large.

PSF shape changes:

Figure 2-17 shows how drastically different MB signals can appear using different methods. DI and SVD have signal loss in the centre of the point spread functions. This signal loss is manifested in the bias introduced for lateral and axial accuracy shown in Figure 2-16(D) for SVD at 0 degrees. This only occurs for lateral motion. It is hypothesised that this is due to less variation between adjacent frames for a

MB moving laterally compared to axially. Lower curvature at the centre of the MB hyperbola means that this signal is simply removed in DI filtering and decreased for SVD filtering. This is even more striking in Figure 2-18 where the same frequency parameters are also used so that the filtering was applied on the same MB signals (note the different colour scales). Figure 2-18(A) for PI filtering shows significant ringing, whereas DI and SVD again have signal loss in the centre of the point spread function. This was one factor which motivated future investigation of the artifacts introduced during SVD filtering.

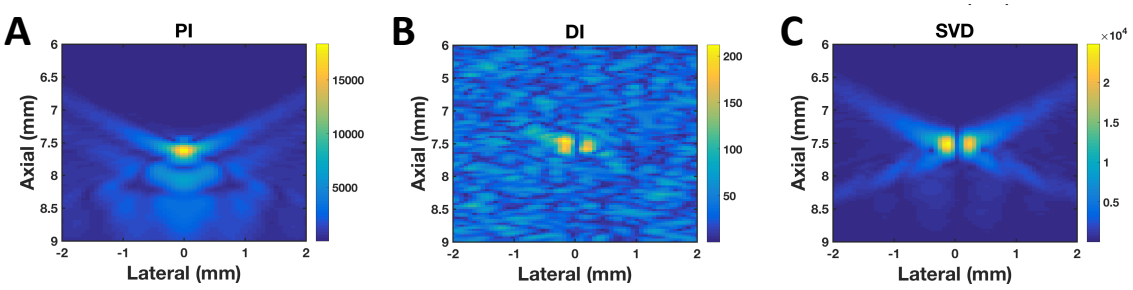

Figure 2-18: Same data; different detection methods. Shape of MB signals for 0.5 mm/s lateral flow at a centre transmit frequency of 4 MHz for PI (A), DI (B) and SVD (C). These images are from the same simulated data.

2.5.3 SVD artifacts

Flashing

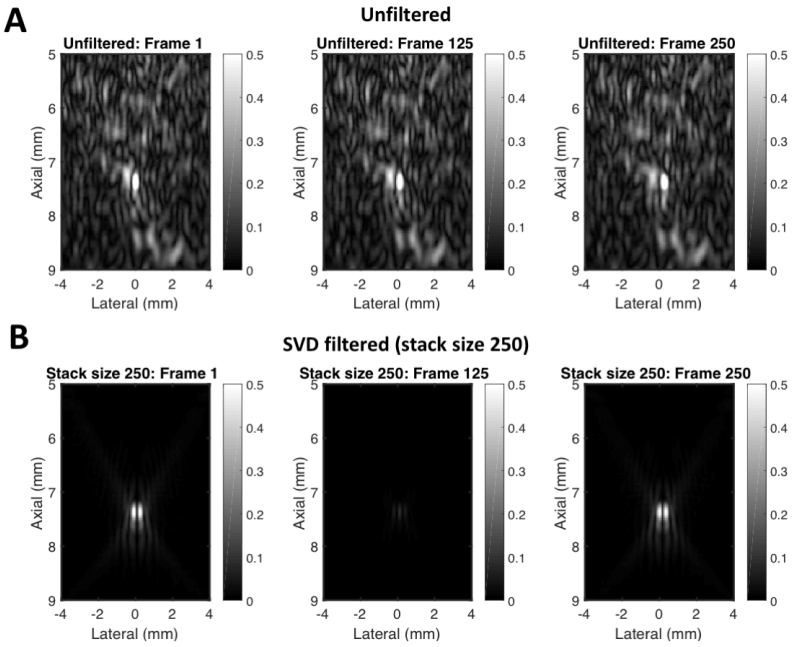

Figure 2-19: SVD flashing artifact. Flashing artifact introduced by SVD for a MB moving laterally at 1 mm/s. (A) Unfiltered image data for the first, middle and final frame of the 250 stack. (B) SVD filtered data for the first, middle and final frame of the 250 stack.

Figure 2-19 shows the variation in intensity introduced over time after SVD filtering of 250 frames for a MB moving at 1 mm/s and acquired at a frame rate of 1000 Hz. No flashing can be observed in the unfiltered data as shown in Figure 2-19(A). However, after application of the SVD filter, Figure 2-19(B) shows a 5 dB decrease between the first and middle frame for a stack size of 250 frames.

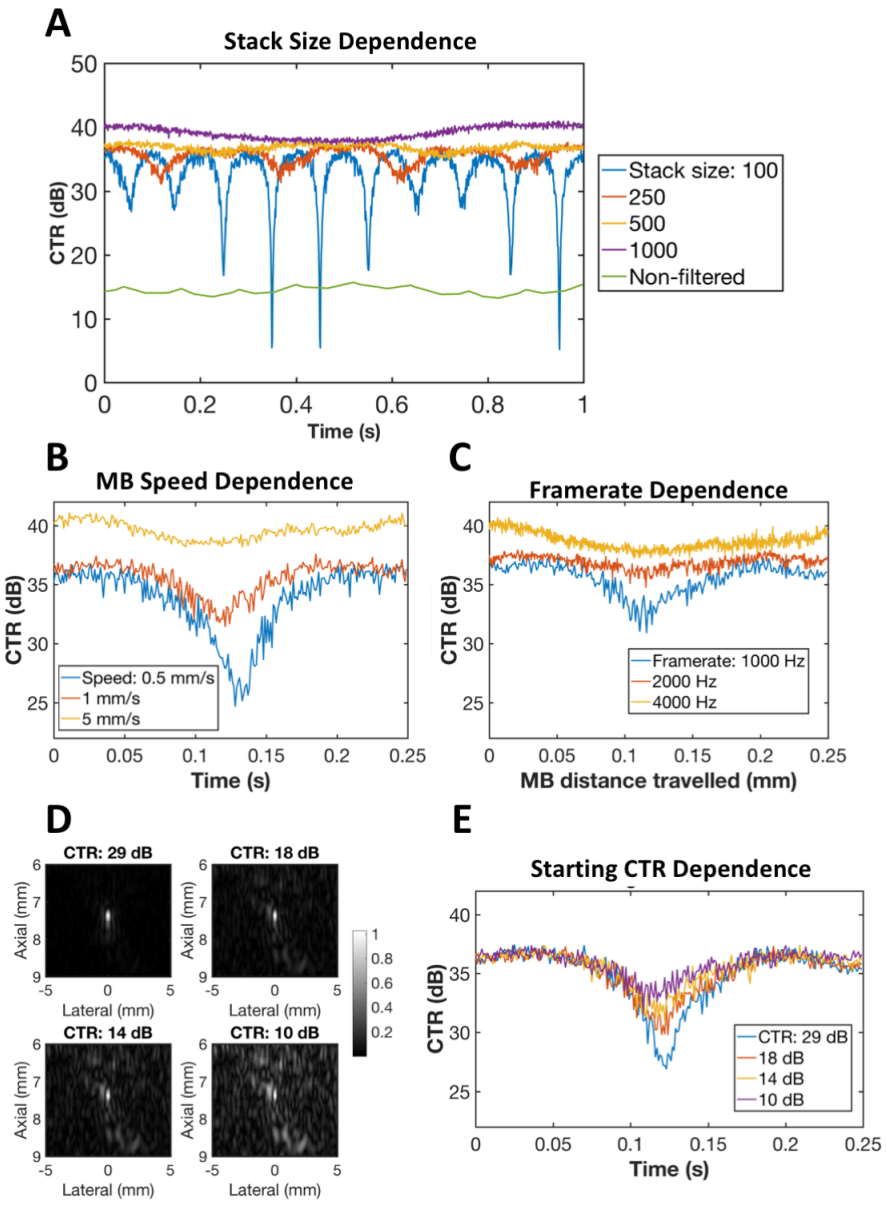

Figure 2-20: Quantification of flashing artifact *in silico*. (A) Quantification of flashing artifact in terms of contrast to tissue ratio for the unfiltered data and for SVD filtering with a stack sizes of 100, 250, 500 and 1000 frames for a MB moving laterally at 1mm/s. (B) Quantification of flashing artifact in terms of contrast to tissue ratio for MB flowing laterally at 0.5mm/s, 1mm/s and 5mm/s (stack size of 250 frames). (C) Flashing artifact dependence on framerate for a MB moving laterally at 1mm/s. (D) Unfiltered data for initial CTR of 29 dB, 18 dB, 14 dB and 10 dB. (E) CTR over stack size of 250 frames for each initial CTR.

Figure 2-20 reveals a dependence of the flashing on stack size (A), MB flow speed (B), frame rate (C) and initial CTR of unfiltered data (D-E). Overall, the results in

Figure 2-20 show that the flashing occurs with a frequency of one flash per stack. Variation in MB speed/framerate and starting CTR and stack size all affect the amplitude of the flashing artifact.

Figure 2-20(A) shows how the flashing is dependent on stack size. For 1 mm/s lateral MB flow, increasing stack size reduces the amplitude of the flashing. Figure 2-20(B) shows the dependence of the flashing on MB speed. The amplitude of the intensity fluctuation increases with decreasing MB flow speeds. Figure 2-20(C) shows that increasing the frame rate, whilst keeping the distance and time acquired for constant, will decrease the flashing artifact amplitude. Figure 2-20(E) shows that the flashing amplitude also depends on the initial CTR of unfiltered data. The variation in intensity decreases with decreasing initial CTR. Nonetheless, even when the initial CTR is only 10 dB, an artificial variation in intensity of 4.7 dB is still present. Figure 2-20(D) is included to help visualise the different CTR values of the unfiltered data.

Smearing

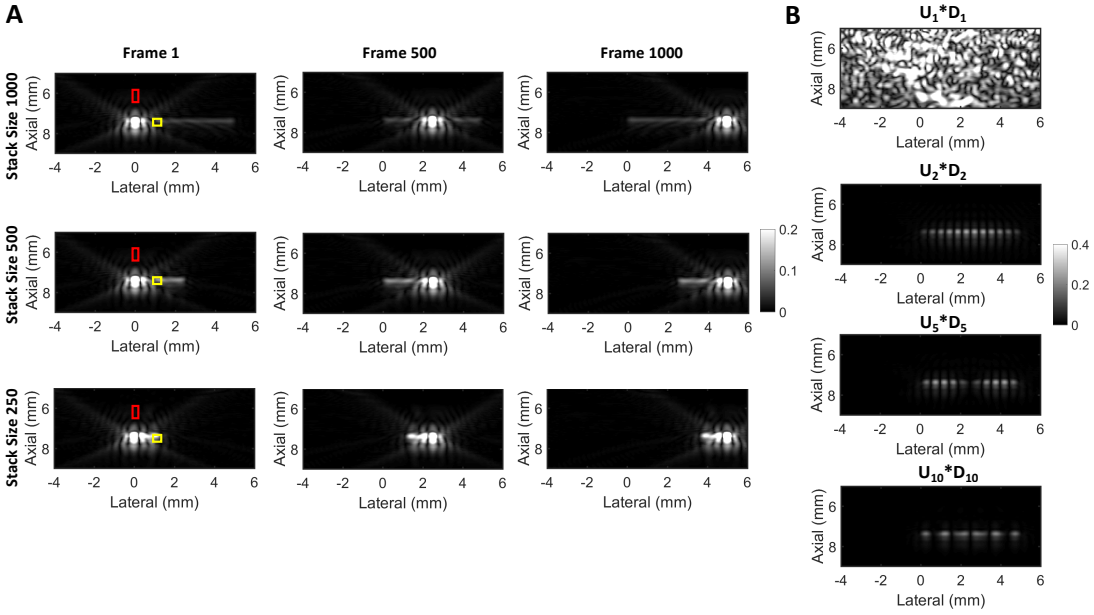

Figure 2-21: SVD smearing artifact. SVD filtered frames of MB moving laterally at 5 mm/s and at a frame rate of 1000 Hz. The frame intensity has been normalized with respect to the top left frame for easier visulaization. (A) shows the first frame (left), middle frame (centre) and final frame (right) are shown for stacks sizes 1000 frames (top), 500 frames (centre) and 250 frames (bottom). The yellow box shows the region where the mean smear signal was calculated, and the red box shows the region where the mean noise was calculated. (B) shows some example spatial singular vectors (U_x) weighted by the corresponding singular value (D_x) for a stack size of 1000 frames. The first frame is associated with the largest singular value and is rejected as tissue. The following frames, associated with singular values 2, 5 and 10, are examples of those frames combined to give the filtered images.

Figure 2-21(A) shows the possibility of a smearing artifact, where a weak signal is observed over all the positions of the moving MB over the stack size. The length of this smearing corresponds to the distance the MB travels during a single stack. It is only obvious when the MB flow is fast enough such that the MB moves beyond the extent of its PSF. For the first frame of each stack size the SNR of the streak was calculated using the mean of the signal over a region of interest centred 1.15 mm laterally from the MB position and 0.2 mm in width (the maximum distance possible using the stack size of 250 frames) and the mean of the same noise ROI as

before. Using a smaller ensemble length resulted in an increase in the amplitude of the smearing artifact. The SNR was 13.4 dB, 18.4 dB and 21.1 dB for a stack size of 1000, 500 and 250 respectively.

Figure 2-21(B) shows the spatial singular vectors, Hilbert transformed and weighted by the associated singular value. The signal associated with the first singular value is rejected as tissue. The signal associated with singular value 2 is the most energetic component associated with the filtered data. The second spatial singular vector (U_2) contains MB signal smeared over the path of the moving MB. Ideally, at each time point the signal from the other singular vectors would cancel out this smearing. However, as in the blinking example, the presence of some MB signal in the rejected singular vector component prevents proper cancellation.

Splitting

Figures 2-17 and 2-18 introduced that when filtering with SVD or DI, a single point spread function can resemble two adjacent signals. Figure 2-22 shows the difference between the unfiltered and filtered data. The SVD filter introduces a gap in the centre of MB response.

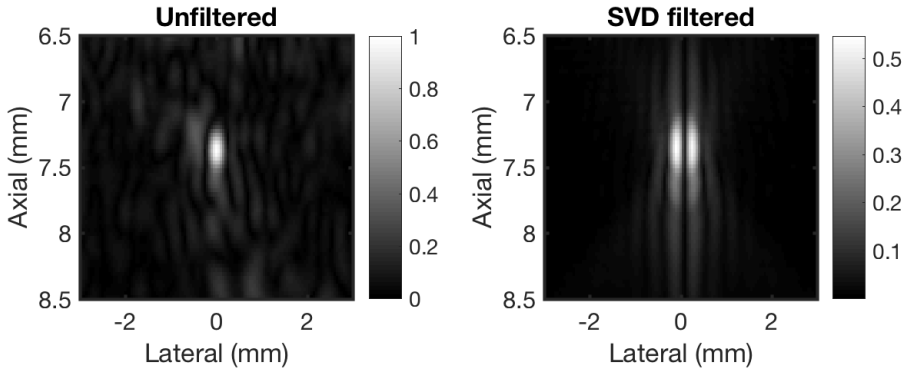

Figure 2-22: SVD splitting artifact. The unfiltered data (left) of a single MB in tissue flowing laterally at 1 mm/s compared to the SVD filtered result (right).

2.6 Discussion

2.6.1 Summary and implications of simulation development:

One contribution of the work in this chapter is the introduction of a simulation that incorporates the MB response modelled using the Marmottant model in addition to wave propagation and tissue response from k-Wave. The use of k-Wave allows modelling of complex wave phenomena, such as non-linear behaviour, which can be especially important when including MBs. Other authors simulating SRUS have generally performed linear simulations [140, 160, 164]).

Non-linear acquisition has previously been modelled simply by modulating gaussian PSFs by a RF component at a frequency corresponding to the second harmonic of the excitation frequency [132, 165]. Christensen-Jeffries et al., (2017) also used the Marmottant model to simulate the MB response to compare localisation techniques [145]. However, none of these works included the tissue response or modelled the non-linear propagation of the MB signal.

At the MI value used in this work, the effect of non-linear propagation on the detection techniques is expected to be minimal. Nonetheless, even without significant non-linear propagation, using k-Wave can still be beneficial compared to other simulation platforms such as Field-II. The k-Wave code is completely open source and editable. For the work in this thesis, this control made it easier to integrate the MB behaviour with wave propagation through tissue (linear or non-linear), whilst also having full control over the US probe, excitation pulse and tissue properties. For example, the effect of frequency dependent attenuation of the excitation pulse before reaching the MB position could be modelled. Likewise, any attenuation of the MB response when propagating back to the transducer was also included. It is not clear how (or if) this scenario could be modelled using a platform like Field-II.

Contrast agents have not previously been incorporated with k-Wave. It is hoped that the approach introduced in this chapter could be useful for research questions in the field of SRUS, and potentially CEUS more generally.

2.6.2 Comparison of MB detection techniques

The second contribution of this chapter was a comparison of the three main detection methods (PI, DI and SVD) and the factors which affect them. Song et al. (2018) recently highlighted the need for a systematic review of MB extraction techniques, when discussing their use of DI. Due to the challenges of creating a microvascular phantom for experimental validation, this simulation has been developed to compare non-linear and linear detection techniques. This work has used the simulation as a ground truth for investigating some of the factors affecting which detection method is most appropriate to extract the MB signal for SRUS.

Effect of SVD processing parameters:

The results have shown that stack size in SVD influences the CTR of MB signals by changing the spread of the signal across the singular values. Thus, larger stack sizes do not always correspond to larger CTR values even when the eigenvalue cut-offs are adjusted. This is because some MB signal can be removed with tissue. SVD splits the signal into orthogonal components which cannot be simply split into tissue, MB and noise signal. Previous work with low frame rates has observed the overlap between MB and tissue signal [197]. This is especially problematic if the contrast in the unfiltered images is originally strong because SVD requires the assumption that tissue is significantly more energetic than noise and MB signal [186].

Effect of transmit frequency:

The results show that PI is more effective at lower frequencies. This is due to the resonant behaviour of MBs. For frequencies less than 3 MHz, using a probe with sufficiently wide bandwidth, it has the highest CTR. SVD CTR is less affected by frequency. This is true both for the investigations with and without incorporation of bandpass filtering. When incorporating the probe bandpass the detection techniques are affected both by the MB dependence on frequency, attenuation and nonlinear propagation in tissue, and the sensitivity of the available probes. The LA332 probe

has a flatter frequency response than that of the PA230 probe. Thus SVD, already relatively robust to varying frequency without bandpass filtering, is a feasible choice over a wider range of frequencies for the LA332 probe modelled here. In comparison, transmit frequency choice for PI is more affected by the dependence of the MB response on frequency and by the narrower sensitivity of the PA230 probe. Although two specific probe examples have been simulated here, we suggest that these findings are also generally applicable when choices of detection method are being made based on available equipment. At the MI and pulse length used here, only a slight resonance behaviour can be observed in the results. As pulse MI increases, the MB signal will contain increased subharmonic and ultraharmonic components [198]. The non-linear behaviour of the MBs also depends on pulse length. Short pulses, more traditionally used for imaging studies, have been used here. However, longer pulses generate stronger resonance behaviour as shown in Figure 2-10. Future work could investigate how varying MI and pulse length affect each detection method. In such work, it would also be important to simulate how these parameters might affect MB destruction/dissolution and thus the CTR of each technique.

Effect of blood velocity:

The results have shown that SVD and DI are more affected by speed and direction of MB flow than PI. SVD and DI do not work for stationary MBs and are less effective for lateral flow compared to axial. Variation in accuracy (bias) introduced over a physiological variable will cause the morphology of the imaged vessel to be distorted relative to the ground truth. Although PI does introduce an axial bias, this depends on the threshold chosen for the onset localisation method. Constant bias over blood flow speed and direction will not affect the structural or functional information acquired. Opacic et al., (2018) showed that the distance between adjacent vessels could be used to distinguish between tumour types [20]. This chapter has shown that detection methods can distort the shape of vessels if speed changes. That is, a vessel position may may be erroneously shifted relative to vessels which have different blood velocities. Moreover, since blood flow can range from 0 mm/s to several mm/s in a

single vessel [2], DI and SVD may even distort the shape of individual vessels.

Speed dependence will be influenced by choice of PRF. The CTR of slower MBs could be increased by decreasing the frame rate for the linear techniques. However, it is important to understand how this may affect the localisations of the faster MBs. Without a ground truth measurement of the MB speed it will be challenging to correct for any localisation bias introduced. It is unnecessary to obtain a zero bias, but the bias should be constant over the flow directions and MB sizes, so the image is not blurred but only shifted. However, for fast axial flow, SVD is associated with high precision compared to PI. Thus, for some applications the improved precision may be considered more beneficial than a constant bias.

Computational cost:

The computational cost of the three techniques is a further consideration that deserves discussion. SVD processing is significantly computationally more expensive than the simple techniques of PI and DI. This will have implications on the real-time applications of the techniques. Demené et al. (2015) reports that the computation times are of the order of a few seconds for typical data sizes and computational resources [142]. By minimising the stack size, Desailly et al. (2016) reports acceptable CTR for a stack size of 30 frames, requiring a processing time of < 30 ms [173]. To the best of our knowledge, achieving the highest CTR possible with SVD in real time using larger stack sizes has not yet been demonstrated. In comparison, contrast pulse sequences have been widely implemented in real time [199]. There is clear motivation to develop SRUS in real-time. Dencks et al., (2018) write how they visualised their clinical acquisition using a non-linear mode in real time to ensure that the MB concentration was appropriate for SR [19]. The authors would have preferred to only image linearly to maximise framerate, however the MBs were not visible with only linear imaging in this case.

Limitations:

There are limitations to the investigation of detection methods using this simulation. This work has attempted to give both a physically fair comparison of the techniques at different frequencies before moving to more practical scenarios with realistic transducer models. However, this is still an incomplete exploration of the huge parameter space, and so will not be applicable to every scenario.

One limitation of this study is the scope of the detection methods investigated. For example, there are other non-linear detection methods which have not been considered here [87, 200]. Other authors use harmonic imaging instead of multi-pulse non-linear techniques [114, 146]. There is also the possibility of combining detection methods, for example, Harput et al. (2018) filters contrast enhanced US images with SVD [136]. However, it should be noted that results of this investigation would still be valid and combining these methods would result in an unknown combination of the errors associated with each technique.

In practice, each technique must be robust over a wide range of initial CTR and SNR levels. Tissue geometry, as shown in Figure 2-5, was kept constant across the simulations in this work. Physiologically relevant tissue acoustic properties and geometry were chosen to mimic a realistic tissue scenario. Simulations were performed at a relatively shallow depth of 7 mm to perform k-Wave simulations in a reasonable time. This meant that a significant proportion of MB signal could be contained in the first singular vectors of the SVD decomposition. Noise was also kept constant across the simulations. However, in practice, SNR affects the efficacy of each technique and additional signal processing techniques may be required to improve image quality. Modelling across a range of different tissue geometries, initial CTR values and SNR values is a topic for future investigation.

One benefit of modelling the ultrasound propagation in k-Wave is that non-linear propagation can also be simulated. Future work could involve using the simulation to investigate the influence of non-linear propagation on each detection technique by varying the tissue B/A value or the pulse MI.

2.6.3 Investigation of SVD artifacts

The work in this chapter has shown how the use of the SVD filter may introduce error into SR localisation. The simulation also revealed artifacts which could be caused by SVD filtering. Variation in intensity over the stack of filtered images which did not exist in the initial data could be observed (flashing artifact). In addition, smearing and splitting artifacts which have never been reported have been shown here. The results show that the stack size of data, the speed of flow, and initial CTR can have on the artifacts. This discussion section provides an understanding of the cause of these artifacts.

Comparison of simulation results with clinical and *in vitro* data, via collaboration

A PhD student at Imperial College London, J. Zhu, had also identified this flashing artifact in filtered data. Together with another student, K. Riemer, we collaborated to investigate the SVD artifacts more comprehensively and for contrast US in general rather than just SR. The *in vitro* data shown in Figure 2-23(A-C) was collected and processed by J. Zhu. The in-human data shown in Figure 2-23(D) was collected by F. Xu and P. Huang, and was processed by J. Zhu. The data has been included here to show the correspondence with the simulation results, but primary credit for this section of the work is attributed to J. Zhu. The only credit which can be attributed to this thesis is the interpretation and comparison of the experimental results in relation to the simulation. For reference, the methodology of these experiments can be found in Appendix B.

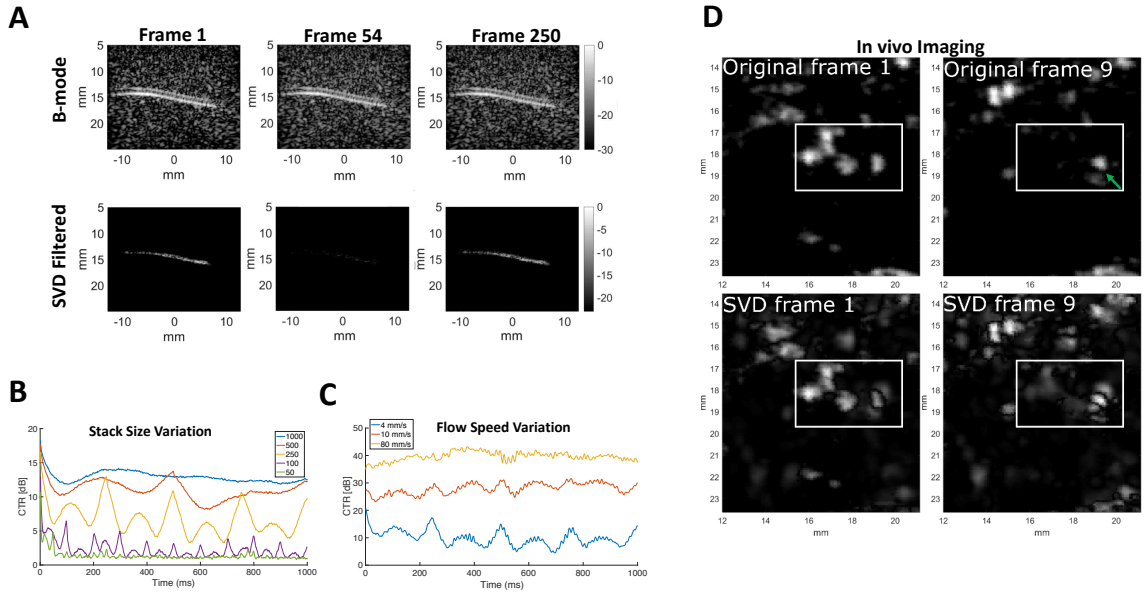

Figure 2-23: *In vitro* and *in vivo* demonstration of SVD artifacts. (A) shows the unfiltered image data for the first, an intermediate and the final frame of 4 mm/s MB flow in a cellulose tube (top). This was then SVD filtered using a stack size of 250 frames (bottom). (B) shows how the CTR varies for changing stack size and (C) shows the dependence on MB flow speed. (D) shows a smearing artifact in clinical dataset. Weak signal in SVD filtered image (frame 9) is observed over the previous spatial positions (frame 1) of the moving MBs. The green arrow highlights MB signal which has been changed by the SVD filter.

Figures 2-23(A) provides visual evidence of how the SVD filtered signal can fluctuate over the stack size when it has not changed in the B-Mode data. This is quantified in 2-23(B) we can see how this fluctuates over each stack size. This fluctuation has a different pattern compared to the simulation. In the simulation, the signal generally dipped to a minimum around the centre point of the stack and at a maximum at the first and final frames. For the *in vitro* data, the signal peaked during the first and final frames but also had a smaller local maximum around the centre point of the stack. This could be due to the difference in the distribution of the signal over the frame for a tube with a high concentration of MBs compared to a single MB. As corroborated by the simulation results presented in Figure 2-20(B), Figure 2-23(C) shows that an increase in flow velocity also reduces the amplitude of the CTR fluctuations. Increasing the flow speed is also associated with an increased SVD CTR,

as also shown during the detection investigations (particularly Figure 2-15(A)).

Figure 2-23(D) provides an example of the smearing artifact occurring during SR clinical imaging. Signal from MBs which appear in original frame 1, but do not appear in frame 9, can be observed in frame 9 of the SVD filtered data. Likewise the PSF of the single MB (indicated by a green arrow) which can be clearly observed in the unfiltered frame 9 has been changed in the SVD filtered image to a signal which appears more like several closely spaced MBs than a single isolated MB. This is corroborated by the simulation results shown in Figure 2-21 which showed that MB signals could appear in the SVD filtered data without being in the unfiltered data at the same time and position.

Origin of SVD artifacts

Figure 2-24 shows why the decomposition of the flowing MB data using SVD can result in the flashing artifact. The first singular vector, which is rejected as tissue, contains significant MB signal. Ideally, U_1 would contain only tissue signal and V_1 would be constant with respect to time. Instead, the changing amplitude of the first temporal vector over the stack size causes a changing amplitude of the MB signal contained in U_1 to be subtracted from the filtered data - resulting in the flashing artifact.

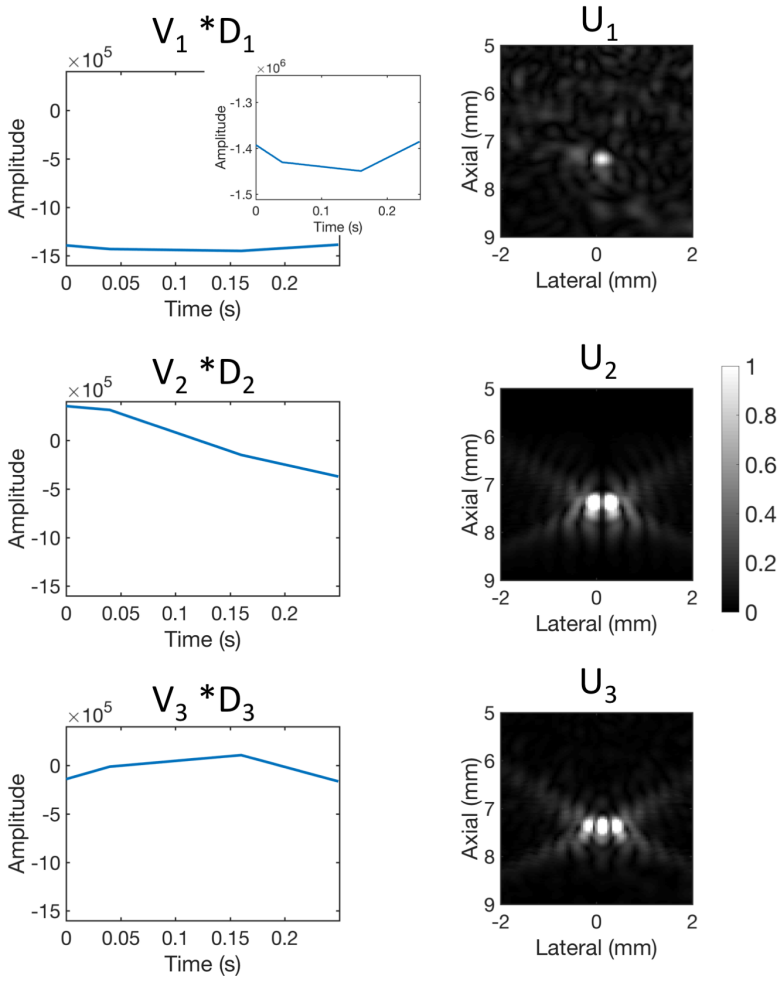

Figure 2-24: Individual vectors of the decomposition. First three singular vectors for the decomposition of a MB flowing laterally at 1 mm/s and a stack size of 250 frames. The temporal singular vectors scaled by the singular value (left) are used to scale the pixel values given by the spatial singular vectors (right) at each point in time.

There is a similar explanation for the incidence of the smearing artifact. Figure 2-21(B) shows how, for this simulation, the most energetic component associated with the filtered data (U_2) contains MB signal smeared over the path of the moving MB. Ideally, at each time point the signal from the other singular vectors would cancel out this smearing. However, as in the flashing example, the presence of some MB signal in the rejected singular vector component prevents proper cancellation.

The splitting artifact occurs because the centre of the PSF has the highest energy signal over the stack of filtered images. Thus, this signal is sorted into the first singular value and thereby removed during SVD filtering.

These three artifacts arise due to failure of the assumption that SVD filtering can always adequately separate the tissue, MB and noise from each other. SVD can decompose the total signal into a series of oscillatory components (see Figure 2-24), which together interfere to represent the unfiltered data with no flashing, smearing or splitting. However, when a singular value containing significant MB information is removed these three artifacts are the result.

Steps to limit the effect of SVD artifacts

The results have shown that there are some choices which can mitigate these artifacts. Figure 2-15(C) shows that for higher relative speeds between the MB and tissue, the signal is shared more evenly across the singular vectors. This explains the result provided in Figure 2-20(B) and Figure 2-23(C) where the flashing artifact is smaller in amplitude for higher MB flow speeds. Likewise, increasing the stack size also increases the number of singular values which can be used to assign signal components to. Less of the moving MB signal exists in the first singular value, so increasing the stack size can result in reduced flashing as shown in Figure 2-20(A) and Figure 2-23(B). However, countering the SVD artifacts by increasing the stack size has implications for practical data storage/transfer and computational times, and thus real-time imaging. The amplitude of the flashing artifact also depends on the initial CTR of the data. The strong tissue signal is now better represented by the first singular value and less flow signal is contained in the subtracted oscillatory component. This suggest that SVD will be more useful in instances where clutter signal is obscuring the MB signal, which may be more likely in certain clinical applications.

Potential impact of SVD artifacts

The artifacts introduced by SVD may lead to erroneous results and clinical misinterpretation. In terms of SRUS, the flashing artifact could lead to an erroneous shift in the localisation of a single PSF over the stack of frames due to changing intensity of the signal. This would be especially true for localisation methods which rely on making the localisation above an intensity threshold - such as the onset method.

Moreover, when the CTR drops to a minimum during the stack size the MB may no longer be detected and hence no localisation made. This could also mean that acquisition time is increased because the MBs signals are not being efficiently used. Beyond SR, the quantification of blood flow and perfusion can be a biomarker for disease. For example, intensity changes observed for perfusion protocols are used to distinguish benign and malignant masses [201]. It would be important to check that the SVD filter did not interfere with the interpretation of these intensity changes.

Given the results of this chapter, it is likely that the "blinking" of the MBs observed in Errico et al. (2015) was actually the flashing artifact due to the application of the SVD filter. Bar Zion et al. (2017) suggests that a physical cause of this blinking could be movement in and out of the plane of view [129]. However, on the timescales relevant to ultrafast imaging, this is unlikely to result in a blinking artefact unless there is sufficiently fast blood flow and a tortuous 3D structure (unlikely in the planar rat brain vasculature). Misinterpretation of the temporal "blinking" could result in the misunderstanding that MBs behave similarly to flurophores. That is, their "blinking" behaviour means that a sparse sparse distribution of isolated scatterers can be extracted from a high concentration of scatterers.

Perhaps of particular concern for SR is when filtering choices can change the shape of individual point spread functions. As observed in Figure 2-23(C), the smearing artifact can lead to distortion of the MB signal. This could cause shifts in the localisation positions. In addition, if either the smearing or splitting artifacts result in adding MB signals to frames where they did not originally exist, this would lead to recording a higher density of MBs than really exist in that region. Christensen-Jeffries, (2015), used SRUS techniques to count MB in lower limb vasculature to quantify the degree of peripheral artery disease [202]. The smearing and splitting artifacts would have implications in such applications. Artifacts which affect the shape of the PSF may also result in localisations being made outside of the vessel wall, causing blurring.

SVD has also been used in other SR approaches to separate tissue and MB such as deep-ULM imaging [165]. It would be interesting to investigate the interaction of such artifacts on this method where the signal is learned. The work in this chapter

has shown that, if the training set only includes modelled Gaussian PSFs (as was performed by van Sloun et al., (2019)) there will be significant discrepancies between these signals and those after SVD filtering.

2.6.4 General limitations of the simulation:

Simplistic motion

The MB motion considered here has been very simplistic and the tissue has been kept stationary. A key limitation of this study is that the effect of tissue motion has not been investigated. Demené et al. (2015) emphasises the superior contrast to noise ratio achievable by SVD compared to traditional temporal filtering techniques [142]. However, a fair comparison of these techniques in the presence of motion is not trivial. In previous literature, motion has been limited experimentally by using a stereotactic frame [116] or rejection of frames with significant movement [121, 140]. Future work will investigate how small tissue movements likely to remain, for example due to vessel pulsatility, would affect each MB detection method. For performing SR on data with more significant movement post processing motion detection methods have been applied [136, 144]. Harput et al. (2018) recently applied a two-stage motion correction approach for non-rigid and affine motion to improve SR imaging. Here motion estimation was performed on B-mode images and then used to remove the motion from contrast enhanced images before the localisation of isolated MBs. Hingot et al. (2017) used SVD twice; first to separate the strongest tissue components which can be used to make an estimation of the motion, and second (with different thresholding) to detect MBs. The localisations were corrected following the MB detection using the tissue motion estimate. The order in which MB detection techniques and motion correction methods should be applied is a topic for future research. Simulations have suggested that motion correction techniques on B-mode data can be associated with errors on the order of tens of microns [136], which is comparable to the SR precisions reported in this work. Moreover, there are many types of motion to consider, from the periodic respiratory motion, to more unpredictable movements such as muscle

spasms and probe motion. To comprehensively compare how motion will influence the choice of detection method, different types of motion should be simulated followed by an appropriate motion correction technique with its associated error. This will need to be investigated in future work.

To investigate the effect of MB velocity without the results being affected by factors such as position in the FOV, simple linear movement in the centre of the FOV was modelled for each set of parameters. For other research questions, it may be more relevant to move the MBs along a path better representing a vasculature tree. For example, Dencks et al. (2016) simulated flowing MBs as events flowing along 3D random vessels trees with varying speeds [141]. The vasculature architecture was controlled by varying the number of branches and the number of bifurcations per branch. The MB velocity decreased with increasing branching to mimic the blood flow in real vasculature. This simulation helped to investigate the efficacy of tracking algorithms when the location of the MB was well known. Due to the MB signal only being simulated as a localised event, this simulation did not include the physics of US or MBs. It would be interesting to incorporate these random vessel trees into the more realistic simulation presented in this chapter.

The use of k-Wave means that the sources of signal must be defined on a grid. This imposes the restriction that movement on the micron level requires that tissue and MBs must be simulated separately if they are to move relative to each other since performing the simulation on a micron scale grid would be computationally unfeasible. Thus the simulation is a coherent combination of the tissue and MB responses. This means that reflections from impedance boundaries in the tissue of the MB signal will not be included.

Two-dimensional simulation

There are issues with simulating 3D phenomena using a 2D model. For example, movement in the elevational direction has not been incorporated. Acquiring 2D SR images of 3D structures can be of limited value due to the smearing of the information in the elevational direction. At present, this simulation will not be able to consider

this behaviour.

Ideally, these simulations should be performed in 3D. The time required to calculate a single MB signal was approximately 13 minutes in 2D. This then had to be repeated for the varying parameters like speed/direction, frequency and phase, all at the six different MB radii and over the stack sizes required for SVD processing. The long simulation time associated with k-Wave is the compromise for being able to realistically simulate wave propagation at each point in time and space. This was already performed using GPU optimised code which has been reported to have an order of magnitude increase in computational speed compared to a 4 core CPU [182], and for a relatively shallow MB depth of 7 mm. However, if this simulation was to be performed in 3D the simulation time would increase even further. For example, a single time step in 2D, with a grid size of 256^2 grid points, is 8 ms using a GPU. In 3D, using a grid size 256^3 grid points, is 500 ms. Thus, at present, it is much more feasible to use a 2D k-Wave simulation.

Missing physics

This simulation only modelled isolated MBs. Although this assumption is also used even for experimental work, more complex interactions may affect SR. The Secondary Bjerkes force [176] describes the coupling of the oscillations between neighbouring MBs. This force decays by the inverse square of the bubble separation. In addition, neither MB destruction/dissolution nor movement due to the primary Bjerkes force [203] have been included. Future work could look at integrating these into the simulation.

2.7 Conclusion

One outcome of this chapter has been the development of a MB and tissue non-linear simulation platform. This software could be used to answer research questions in CEUS which are not possible to realistically explore using existing software.

The primary research aim of this chapter was to improve understanding of how

different MB detection techniques can impact the SR process and explore some of the factors influencing the suitability of each. This work has shown that the choice of detection technique is not trivial. Instead, it can dramatically change the shape and intensity of extracted signals and the resulting localisation positions. Localisations using the signals extracted using SVD and DI are dependent on the speed and direction of the blood flow being imaged. Under slow flow physiological conditions DI has too low a CTR and localisation precision to be useful. This work suggests that PI is a more appropriate technique for accurately imaging the microvascular flow simulated here. PI is most effective at centre transmit frequencies ≤ 3 MHz - assuming a probe with sufficiently high bandwidth is available. SVD localisation had improved precisions at higher frequencies, where results showed that SVD performed on data acquired at a higher transmit frequency of 6 MHz would provide better overall CTR and precision than PI performed at 2 MHz. However, the variation in accuracy for SVD over the speed range studied here will cause distortion of the structural information. In particular this may affect the visualisation of regions where there are a range of difference vessel sizes and flow rates. For example, branching vasculature such as that from arterioles to capillaries may be misrepresented. Overall, this velocity dependence of DI and SVD mean that they are less suitable for visualisation of tumour microvasculature than PI.

The development of the simulation also enabled collaboration with other group members of the ULIS lab, J. Zhu and K. Riemer, to investigate artifacts which can be caused by SVD filtering. The flashing and smearing artifacts which could be observed in simulation were also observed in *in vitro* and clinical data. The simulation allowed the effect of stack size, frame rate, initial CTR and blood velocity on the SVD filtered data to be investigated using a well understood ground truth. The incidence of the same artifacts in *in vitro* and clinical data confirmed that the simulation was realistic enough to show real phenomena.

Overall, this work has developed a simulation platform suitable for investigating SRUS. The application of this simulation to the investigation of SRUS detection methods showed that care should be taken when making processing and acquisition

choices for SRUS. There has been much work in the literature showing that SRUS can generate images from a range of targets using various protocols. However, it is important for future research to consider and understand the effect any acquisition and processing choices may have on the final images.

Chapter 3

Development of Simultaneous Optical Imaging and Super-Resolution Ultrasound

3.1 Abstract

Currently, all detected MB signals are localised without consideration of their individual surroundings. However, the MB signal is not as easy to predict as the system PSF when imaging a linear scatterer. Despite accuracy on the order of microns being reported in SRUS, it is currently not possible to quantify error that may be introduced due to variation in the MB responses.

This work combines high frame rate plane wave ultrasound acquisition with a coincident optical microscope visualising the SR imaging of a 200 μm cellulose tube. An adjustable aperture has been introduced into the optical microscope to extend the optical depth of field (DOF) over the phantom.

The results showed that the introduction of the aperture enabled modest extension of DOF over 50 μm about the optical focus. Experimental verification found that, at flow rates of $\leq$ 15 μl/min, MBs are more likely to be detected over the top half of the tube phantom. Modelling of the parabolic flow suggested that buoyancy was

strong enough to cause the MBs to concentrate in the top portion of the tubing. The simultaneous optical and acoustic data suggested that obtaining SRUS images at flow rates most relevant to microvascular flow was more challenging than expected. At flow rates of ≤ 15 μl/min it is difficult to achieve a constant, active, concentration of MBs compared to the faster flow rate of 50 μl/min used in previous work. If the cellulose tube phantom used in this work is realistic, this may have implications for the applicability of SRUS for visualising the smallest vessels.

Investigations incorporating a ground truth, like this one, will allow different factors affecting the success of SRUS and sources of error to be identified, quantified and limited.

3.2 Introduction

SRUS methods which localise isolated MBs require an understanding of the relationship between MB response and position. However, it is well known that factors like MB size [92, 191, 204], nearby MBs [79, 82] and boundaries [77, 205, 206] will affect the individual MB signals. More work is required to determine how the environment of the MBs may affect their signal and thus the quality of super-resolution images. In this chapter optical microscopy performed simultaneously with the SRUS is developed in order to provide an experimental ground truth of SRUS.

3.2.1 Previous examples of optical microscopy in combination with US imaging

There have been multiple optical studies of MB dynamics [76, 77, 78, 82, 204, 206, 207, 208, 209, 210, 211, 212, 213], but none in the context of SRUS. Optical studies have enabled the effects of the first and second radiation forces to be observed [79, 82]. As the frame rate and data storage capabilities of optical cameras have increased, there has been more focus on imaging the oscillating MB wall in response to a pulse, using streak images [204, 211, 213] for example. The current most advanced imaging sys-

tems are the Brandaris 128 camera [214] and UPMC camera [215] which can achieve frame rates up to 25 Mfps using a rotating mirror system directing light to a series of CCD cameras. Even more recently, the Brandaris 128 camera has been combined with a confocal microscope to better image MBs interacting with cells [83]. Alternatively, light scattering can be used to measure the radial oscillations of MBs. This has the benefit of enabling higher throughput than high speed optical measurements [81, 216, 217]. A common challenge for the majority of approaches is the isolation and confinement of single MBs. This can be achieved by simply using a very low concentration and allowing MB to float against a wall [206], attaching to a surface [209], hydrodynamically focussed flow [217] or optical tweezers [77, 218]. Isolation and confinement are useful for studying some phenomena in a controlled manner, however there is concern that such confinement may affect the MB behaviour. For this work, confined MBs are not especially relevant to SRUS and instead it was preferable to image a flowing, dilute concentration of MBs as are used for SRUS. Additionally, the temporal resolution does not need to capture shell oscillation, only be able to match MBs appearing in the optical image with the acoustic image. Nonetheless, examining the previous literature from the optical imaging of MBs helps to inform on some of the factors which may affect the MB signal.

3.2.2 Motivation: MB size

Perhaps the simplest measure the optical setup can generate is that of the MB size. Of particular benefit is that MBs of the same size are expected to respond in the same way to the same incidence pulse. Therefore the signals and thus localisations should have less erroneous variation. Some groups have begun to investigate how MB size could be tuned for SRUS [122, 196]. However, there is evidence to suggest that MBs of the same size can have significantly different acoustic responses to the same pulse [208], perhaps due to varying shell composition [83]. Thus much is still uncertain about the role of MB size, and more specifically whether a monodisperse population would be beneficial for super-resolution. Having sufficient optical observations of SR localisations using a polydisperse MB population may allow the influence of having

a polydisperse population to be assessed.

3.2.3 Motivation: MB environment

The effect of the MB environment, such as boundaries and nearby MBs, have been investigated using optical observation. For example, Caskey et al., 2006, showed that a significantly increased expansion ratio using 25 μm PMMA tubing compared to 12 μm [205]. This was not because the MB was expanding beyond the diameter of the tube, for example, a 2.5 μm bubble did not significantly expand beyond its resting radius in 12 μm tubing. Similar results were found when comparing MB oscillation in *ex vivo* microvessels (which should have a realistic compliance which also affects MB response [148]) compared to oscillations in a 200 μm tube [219]. These were important studies as they were the first experimental demonstrations showing that MBs respond significantly different in small vessels compared to within a large volume of fluid. The MB response is also affected by other MBs in their proximity. Previous authors have used optics to show the coalescence of MBs due to the secondary Bjerkes force [79, 82]. Moreover, there are other less reported behaviour such as a "protective effect" of having nearby MBs which improves MB persistence [209]. The position in the FOV is also important. The PSF will vary spatially and can be estimated using calibration and simulation. An optical ground truth will enable assurance that the MB response changes as expected given different FOV position. More work needs to be done to understand the implications of these general factors which affect MB response on SRUS.

When imaging superficial structures, it can be possible to determine a ground truth using conventional microscopy [124]. Otherwise, *in vivo*, the improvement due to super-resolution techniques has widely been quantified by determining the full width half maximum (FWHM) of vessels [116, 121, 136]. However, these approaches only allow an overall assessment of the SR performance, and the latter has no confirmation of whether the vessels sizes are accurate. Ideally, it would be possible to allow the contributions of individual MBs to the SR image to be investigated. Generally, localisation of an isolated MB relies on knowledge of the system PSF and the

assumption that the MB response will be approximately similar. As introduced by Christensen-Jeffries (2016), characteristics of the MB signal such as eccentricity, area, power and axis length can be used to further differentiate isolated signals from multiple MB signals and noise [202]. However, perhaps the sensitivity and specificity of this threshold could be improved if the factors which affect the MB signals could be better understood. For example, given that the estimated SR precision is of the order of a few microns [115, 164], it is unexpected that many of the profiles of density maps have a Gaussian shape. Instead, a top-hat profile would be expected [115]. This could be due to differences in how the MBs respond depending on their environment. For example, Viessmann et al., (2013) suggests that perhaps more of the slowly moving MBs at the tube edge are destroyed compared to the faster centre MBs, or there is more damping due to the tube boundaries. There is motivation to use an optical ground truth to provide insight into what may be causing these unexpected profiles. Therefore, this chapter uses the same 200 μm diameter cellulose tubing used in the previous work by Viessmann et al., (2013).

3.2.4 Motivation: validation of MB tracking

One particularly important application for a simultaneous optical ground truth would be validation of MB tracking algorithms. There has been a range of techniques developed and implemented in the literature, as explained in subsection 1.6.7 of the introduction. Given that the potential to image microvasculature flow to aid diagnosis and monitoring of various diseases, notably diabetes [220] and cancer [168], there is increased motivation to quantify and compare the efficacy of such techniques. Having a ground truth of the MB tracking would allow the techniques to be refined, and the trade-offs between increasing accuracy but also increasing computational load to be better quantified. The previous chapter also discussed how the MB velocity can change the detected signal, depending on the detection method used. It would be interesting to experimentally validate these *in silico* results and explore how detection methods affect the performance of tracking methods.

3.2.5 Depth of field considerations

One problematic issue with simultaneous optical and acoustic imaging of a flowing MB population, which has not been addressed in previous literature, is the mismatch between the relative DOF of the acoustic and optical observation. The DOF is the distance over which the object being imaged can be resolved. Due to the significantly larger acoustic DOF, as shown in Figure 3-1(A), it is likely that a MB that appears isolated in the optical image will be affected by MBs visible in the larger acoustic FOV.

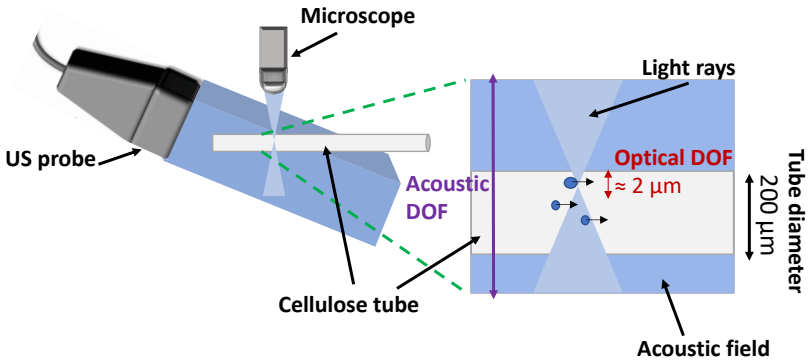

Figure 3-1: Comparing DOFs of plane wave US imaging and wide field optical microscopy for imaging 200 µm cellulose tubing.

Reducing the numerical aperture (NA) of a system can increase the DOF, but also reduce the resolution (Δr) as shown by Equations 3.1 and 3.2:

$$\Delta r = 0.51\frac{\lambda}{\mathrm{NA}} \tag{3.1}$$

$$\mathrm{DOF} = \frac{n \cdot \lambda}{\mathrm{NA}^2} + \frac{n \cdot e}{M \cdot \mathrm{NA}} \tag{3.2}$$

where λ is the wavelength, e is the pixel size, M is the magnification and n is the refractive index of the surrounding medium.

The NA is given by:

$$\text{NA} = n\sin\theta \approx n\frac{D}{2f} \tag{3.3}$$

where θ is the maximum half angle of the cone of light entering the lens (as shown in Figure 3-2 (A)), D is the aperture diameter and f is focal length of the objective.

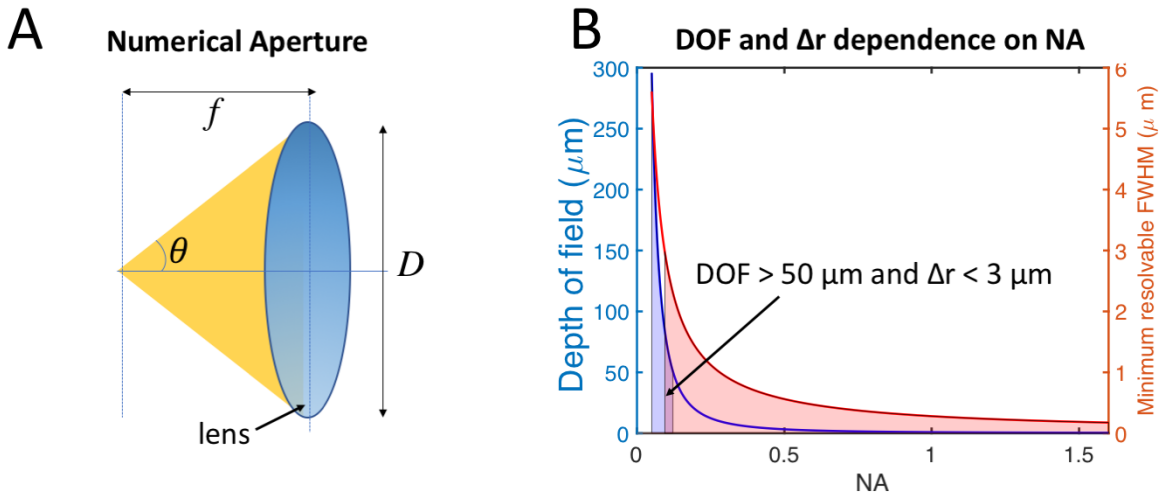

Figure 3-2: Importance of NA. (A) shows how the range of angles accepted by the lens depends on the lens focal length (f) and the physical diameter of the lens (D). (B) shows how the increasing NA leads to decreasing DOF but better resolution. There can be some (purple shading) overlap between the reasonable resolution and DOF values for imaging SRUS phantoms.

3.2.6 Chapter Outline

One aim of this chapter was to demonstrate the use of an adjustable optical aperture to extend the DOF. Plotting Equation 3.1 and 3.2, as in Figure 3-2 (A)) shows that it is possible to achieve an overlap between suitable resolution and DOF. A water immersive objective with suitable NA and magnification was not commercially

available. Thus an adjustable aperture was introduced to provide the flexibility of reducing the NA without changing the magnification.

This chapter describes the optical setup incorporated with the SRUS setup. Initially, improvement to the DOF using an adjustable aperture is characterised using an optical resolution target and then tested on MBs resting on the cellulose tubing. Trajectories of MB flow within the tube were modelled and experimentally verified using the optical setup. Simultaneous optical and acoustic data were collected with the aim of determining how MB environment will affect the localisations.

3.3 Methods

3.3.1 Initial optical setup

Initially the image formed by a water immersion x40 microscope (NA = 0.8, working distance = 3.3 mm) (LUMPLANFLN, Olympus, Tokyo, Japan) was recorded using a digital camera (Canon Powershot SX240 HS, Canon, Tokyo, Japan) which could record at a frame rate of 240 fps. This optical setup was focused on to a 200 μm cellulose tube (Hemophan®, Membrana, Wuppertal, Germany), secured near the surface of a gas equilibrated water tank, with a low concentration of flowing MBs (Sonovue^{TM}, Bracco Imaging SpA, Milan, Italy). A syringe pump (SP210 IWZ syringe pump, World Precision Instruments, Stevenage, UK) was used to control the flow speed. A light source was incorporated beneath the target using waterproof fibre optic tubing. The tubing was coupled to a XYZ stage made from three single axis stages (DTS25/M, Thorlabs, New Jersey, United States) and one angle bracket (DTSA03/M, Thorlabs, New Jersey, United States) and secured onto the optical bench. The camera and microscope were not attached to a micrometer stage. During initial experiments several issues with the simple setup were identified. The cellulose tube was subject to vibration with an amplitude on the order of micrometres. Due to the difficulty of coupling the bulky camera to the optomechanical support and lens tube, the camera/objective position could not be adjusted. It also became evident

that the DOF of the optics was very limited and would only be able to be focused in a narrow regions of the acoustic FOV. Visualisation was also hampered by the non-uniform illumination.

Thus several improvements were required:

- Damped posts (DP14A/M, Thorlabs) were used to make any contact with the optical bench. The posts supported the micrometer stages using mounting post brackets (C1515/M, Thorlabs). The optical bench was inflated, and any necessary electrical equipment, which may generate vibrations, were removed from the surface.

- A more suitable CMOS sensor (xiQ USB3, XIMEA) was incorporated to replace the previous camera. This was more compact and could be easily secured to the lens tube and also an XYZ stage.

- A diffuser (DG10-600, Thorlabs) was added above the optical fibre output to improve the light source uniformity.

- A higher resolution z-axis stage (SM1ZP/M, Thorlabs) was coupled to the objective to enable finer focusing (1 μm adjustments).

- An adjustable aperture (SM1D12C, Thorlabs) was introduced to improve the DOF.

3.3.2 Final optical setup

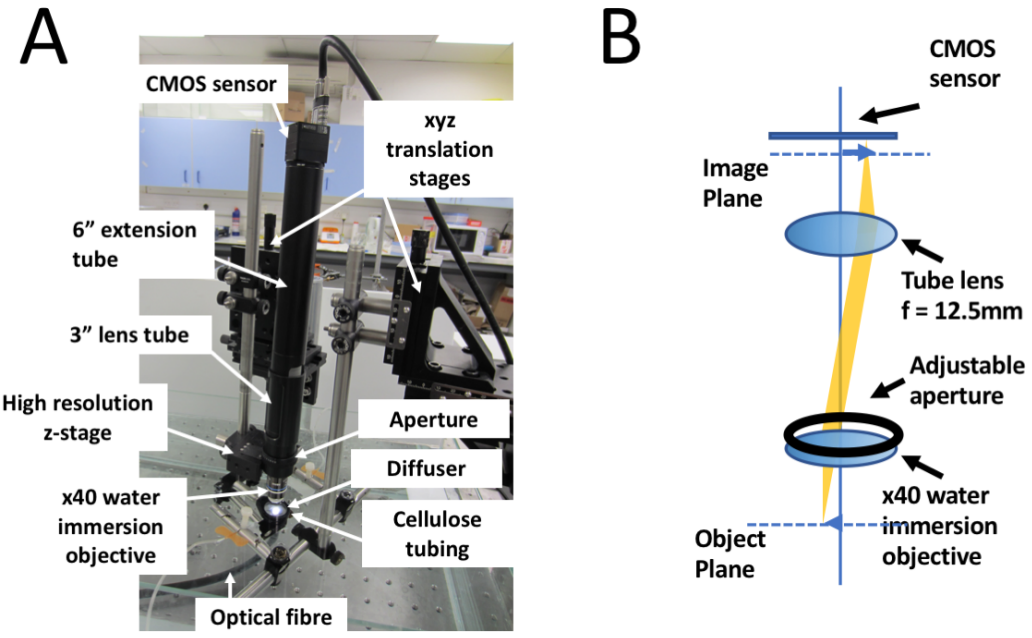

Figure 3-3: Optical setup. (A) shows a labelled diagram of the optical observation of MB flow in a cellulose tube and (B) is a schematic of the image formation within the optical tubes.

Figure 3-3(A) shows a labelled image of the optical setup. The left hand branch shows the CMOS sensor attached to the 6" extension tube (SM1E60, Thorlabs) attached to a 3" slotted lens tube (SM1L30C, Thorlabs) containing a tube lens of focal length 12.5 cm (AC254-125-A, Thorlabs) or 20 cm (AC254-200-A, Thorlabs) depending on the magnification required. The objective was designed to work with the 20 cm focal length lens and enable higher magnification images of the MBs, however the in plane FOV was smaller than the $\approx$ 200 µm tube width. Thus the 12.5 cm focal length lens was used when it was necessary to image the full extent of the tube. A diagram of the internal optics is proved in 3-3(B). The slotted lens tube was connected to the high resolution Z stage which supported the objective lens. Parallel to the lens, optomechanical posts were used to hold the fibre optic tubing below the diffuser. The camera was connected to a laptop (Latitude E6540, Dell, Texas, US) using a Micro-B

connector (Ximea).

The right hand branch supported the target to be imaged. Two optical posts (TR50/M, Thorlabs) with grooves cut to support the butterfly needles attached to the cellulose tubing were held by a perpendicular post which could be moved using a XYZ micrometer stage.

3.3.3 Resolution characterisation

The resolution over the DOF was characterised using a sector star resolution target (R1L1S3P, ThorLabs) as shown in Figure 3-4(A), where contrast between bright and dark bars provides a measure of resolution. The smallest resolution measurable was 115 lp/mm. This corresponded to a bar width of 4.3 μm. Resolution is generally quantified using these targets in terms of modulation period, which is the width over a dark and white bar. The highest resolution corresponded to a modulation period of 8.6 μm.

Using the tube lens with a focal length of 20 cm, profiles at the smallest possible radii were obtained at the focus and at 100 μm from the focus using the full aperture (12 mm in diameter) and 4 mm aperture. The aperture 4 mm in diameter was used as it was the smallest possible to avoid obscuring the image. A small degree of movement of the target occurred when adjusting the axial position, this was corrected for using a simple 2D cross-correlation motion correction using the MATLAB function (xcorr).

A more detailed characterisation was done with the lens of focal length 12.5 cm because this had the most suitable magnification to allow the full tube to be visualised in a single frame. Contrast was calculated by measuring the intensity profile over arcs at 4 μm intervals, a subset of these arcs are shown in Figure 3-4(B). The difference between the mean value of the maxima and minima of the profile is reported as the contrast. This was repeated over each aperture diameter and (1-12 mm) and 200 μm about the focal plane in 10 μm steps to assess the extent to which the DOF could be extended.

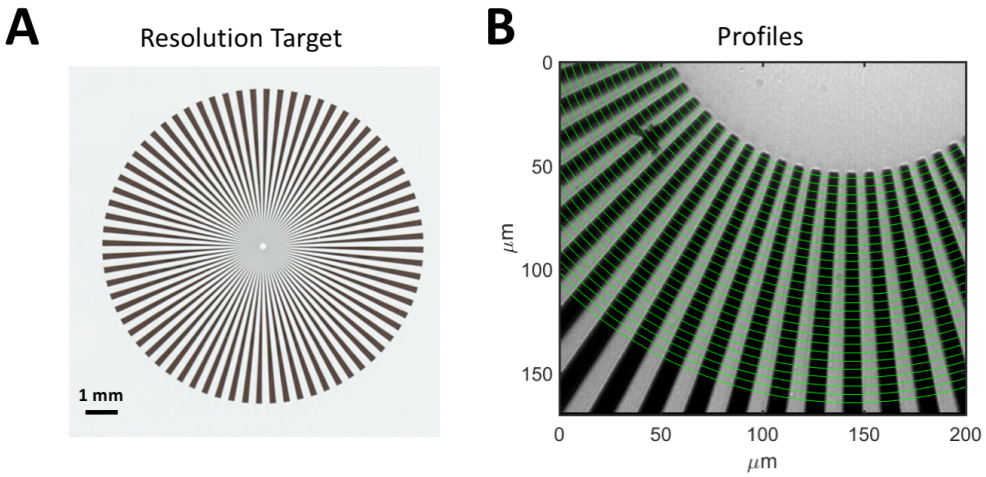

Figure 3-4: Quantification of optical resolution using a resolution target. (A) is an image of the optical target, adapted from (Thorlabs.com, 2019), where the scale bar corresponds to 1 mm. (B) shows an example image of optical target with the green lines indicating where intensity profiles were calculated.

It is more challenging to do a similar experiment using MBs because it is possible that they may move or dissolve, and thus it is difficult to compare the images of the same MBs over different distances from the focus and using different aperture sizes. However, it is necessary to check whether any improvements quantified using the target will make a meaningful difference when imaging MBs. Using both lenses, MBs resting on the tube of the cellulose tube were imaged at a range of apertures and distances from the focus.

Using the 20 cm lens, a MB of radius approximately 1 μm was imaged over a DOF of 100 μm moving the optical focus from 50 μm above the MB position to 50 μm below the MB position.

For the 12 cm lens, a distribution of MBs resting on top of the cellulose tube were imaged using 2 mm, 4 mm and full aperture and up to 50 μm from the focus. Thresholding was empirically applied and any 8-connected objects were extracted from the background using the MATLAB function "bwlabel()". This allowed qualitative assessment of how well MBs could be distinguished from the background under each set of microscope conditions.

3.3.4 *In vitro* optical flow characterisation

A dilute MB solution was drawn through a 200 μm cellulose tube using a syringe pump. The images from the optical setup were affected by flow speed, thus some preliminary data was collected at a range of speeds to assess the most appropriate flow rate to use in future experiments (5 μl/min,15 μl/min and 50 μl/min).

Flow rates 5 μl/min and 15 μl/min were appropriate for the frame rate of the camera but 50 μl/min was too fast to capture. Using the lower flow rates, it was empirically observed that MBs could only be optically detected over the upper half of the tube. To confirm this, using the widest possible aperture, the MB flow was characterised at 10 μm increments across the extent of the tube to map the MB flow distribution for 5 μl/min and 15 μl/min. The average number of MBs per frame were determined in MATLAB using the "imfindcircles()" function. These were characterised as MBs depending on their contrast compared to the background, size, and position (i.e. detections outside the tube walls and signals where there are marks on the lens were rejected). The algorithm was tested on an empty tube with no MBs to test to what extent the algorithm was affected by marks on the tube/dust on the lens.

3.3.5 *In silico* flow

The experimental results were compared with theory by modelling the MB parabolic flow. This simple model assumed that the parabolic flow was fully developed when exiting the needle. The maximum lateral velocity modelled corresponded to a flow rate of 50 μl/min as previously demonstrated to work for a similar setup [147]. Mean flow rates of 5 μl/min and 15 μl/min, used in the *in vitro* imaging of this chapter, were also simulated. The slowest simulated flow rate, corresponding to a maximum lateral velocity of 1 mm/s, was used to model flow in the smallest vessels. The initial axial velocity (v_0) was 0. The vertical equation of motion was formulated considering buoyancy, gravity and drag. The axial equation of motion was:

$$F_{\text{unbalanced}} = F_{\text{buoyancy}} - F_{\text{gravity}} - F_{\text{drag}} \tag{3.4}$$

$$m\frac{dv}{dt} = \rho g V - mg - 6\pi\eta R v \tag{3.5}$$

where force is given by F, m is MB mass, t is time, ρ is liquid density (1000 kgm^{-3}), g is acceleration due to gravity (9.8 ms^{-2}) and η is liquid dynamic viscosity (8.9x10^{-4} Pas).

The MB mass, for each MB size, was calculated assuming a sphere at atmospheric pressure and adding the estimated weights of the inner gas (molar mass of SF_6 = 146.1 g/mol) and shell lipids (molar mass of DSPC = 790.1 g/mol and molar mass of DPPG-Na = 801.01 g/mol, 1:1 mixture of both phospholipids. The area per lipid was estimated to be 0.4 nm^2 as used in Marmottant et al., (2005) [80].

The equation for the lateral speed was assumed to be parabolic flow, as shown in Figure 3-5:

$$u = u_0(1 - (\frac{y(t)}{d})^2) \tag{3.6}$$

where d is the tube radius (100 μm) and $y(t)$ is the axial MB position.

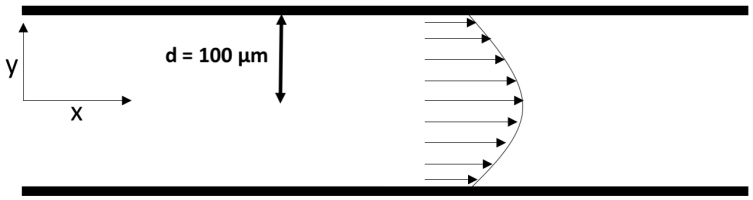

Figure 3-5: Schematic of parabolic flow in a 200 μm tube.

This model was used to estimate the trajectories of MBs across the tube extent.

3.3.6 Simultaneous imaging

Optical data was collected before and after the triggering of plane wave ultrasound using an ULA-OP system (MSD Lab, University of Florence). A LA332 (Esaote,

Genoa, Italy) probe was operated at a centre frequency of 4 MHz, with contrast sequence (1,-1, +0.5), as explained in the introduction section 1.3.10. The pulse repetition was chosen to be 400 Hz, as this had been shown to be successful for SRUS in previous work (Christensen-Jeffries et al., 2017). The contrast images were processed using amplitude modulation to give a frame rate of 133 Hz. Pulse amplitude was chosen such that MBs were not significantly diminished by destruction over the acquisition. The optical camera was used at a frame rate of approximately 99.0 ± 5.1 Hz. The US probe was aligned approximately parallel to the cellulose tube. The microscope was positioned above the cellulose tube and aligned along the vertical direction - approximately perpendicular to the direction of US propagation.

Alignment

Alignment of the modalities was achieved using the tip of a pipette which was threaded on to the cellulose tubes before connection to the butterfly needles as shown in Figure 3-6(A). Alignment was achieved when the pipette tip was in the FOV of the optical camera and could also be observed in the US image as shown in Figure 3-6(B).

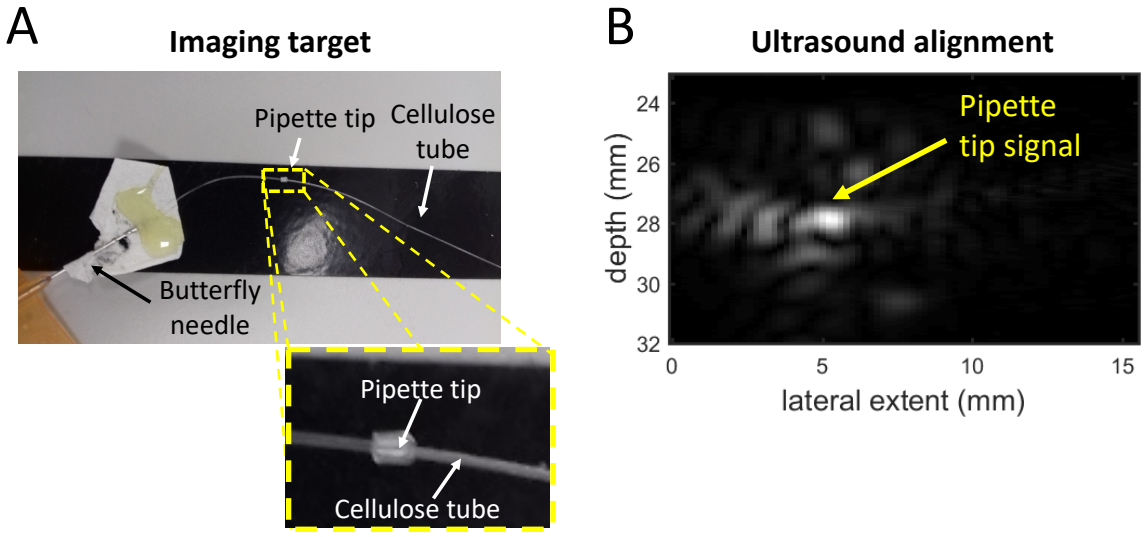

Figure 3-6: Alignment of simultaneous optical and US imaging. (A) shows how a pipette tip was threaded onto the cellulose tube phantom and was used to generate a strong signal in the US image as shown in (B).

Triggering

Both the camera and ULA-OP was controlled and triggered in MATLAB. Generally, 50 optical frames were collected, before the acoustic imaging was triggered and a further 200 optical frames collected.

Choice of flow rate

A flow rate of 15 μl/min was chosen as an appropriate speed for the optical imaging. Due to challenges acquiring US data at this speed, which will be discussed in the following sections, data was also collected at a flow rate of 50 μl/min for comparison.

Choice of pulse amplitude

The US pulse amplitude appropriate for imaging a flow rate of 15 μl/min was investigated using the optical setup. 50 optical frames were collected before the US pulse, and 50 optical frames collected during the contrast imaging sequence described previously. The average number of MBs per frame were counted using the algorithm described previously, based on the "imfindcircles()" MATLAB function. Whether there was a significant level of MB destruction was assessed by performing a two-sample t-test using the MATLAB "ttest2()" function. The alternative hypothesis tested was, whether the mean number of MBs detected before the US sequences was greater than the mean number of MBs detected after the US sequence. The null hypothesis was rejected at a significance level of 5 %. It was not assumed that the two distributions would have equal variances. This was repeated over the full range of ULA-OP pulse amplitude settings by adjusting the amplitude of each pulse in the contrast sequence from 0 to 1 in 0.1 steps. See Appendix C for the relationship between the ULA-OP amplitude setting and the peak negative pressure in MPa and/or MI.

An ULA-OP pulse amplitude of 0.2 was chosen as one which did not destroy the MBs but still generated adequate contrast signal at a flow rate of 15 μl/min. Simultaneous optical and acoustic data were collected at this amplitude.

Choice of receive gain

Due to concerns over saturation of the tube signal at the receive gains required to capture weak MB signals, the pulse sequence was adapted to acquire data at different gains over successive pulses. In this chapter, low gain data collected at a gain of 30 dB and at a high gain of 46 dB using a MB flow rate of 50 μl/min and without MBs are presented. The motivation for this will be covered more thoroughly in the discussion section 3.5.4 and the following chapter.

Calculation of MB sizes

When required, the radii of MBs were calculated by binarising the image such that the pixel values greater than the mean plus three standard deviations of the background signal were set to 1. All pixels under this threshold were set to 0. Then a region containing the MB to be measured was extracted and "imfindcircles" function was used to determine the MB radius.

3.4 Results

3.4.1 Effect of adjustable aperture.

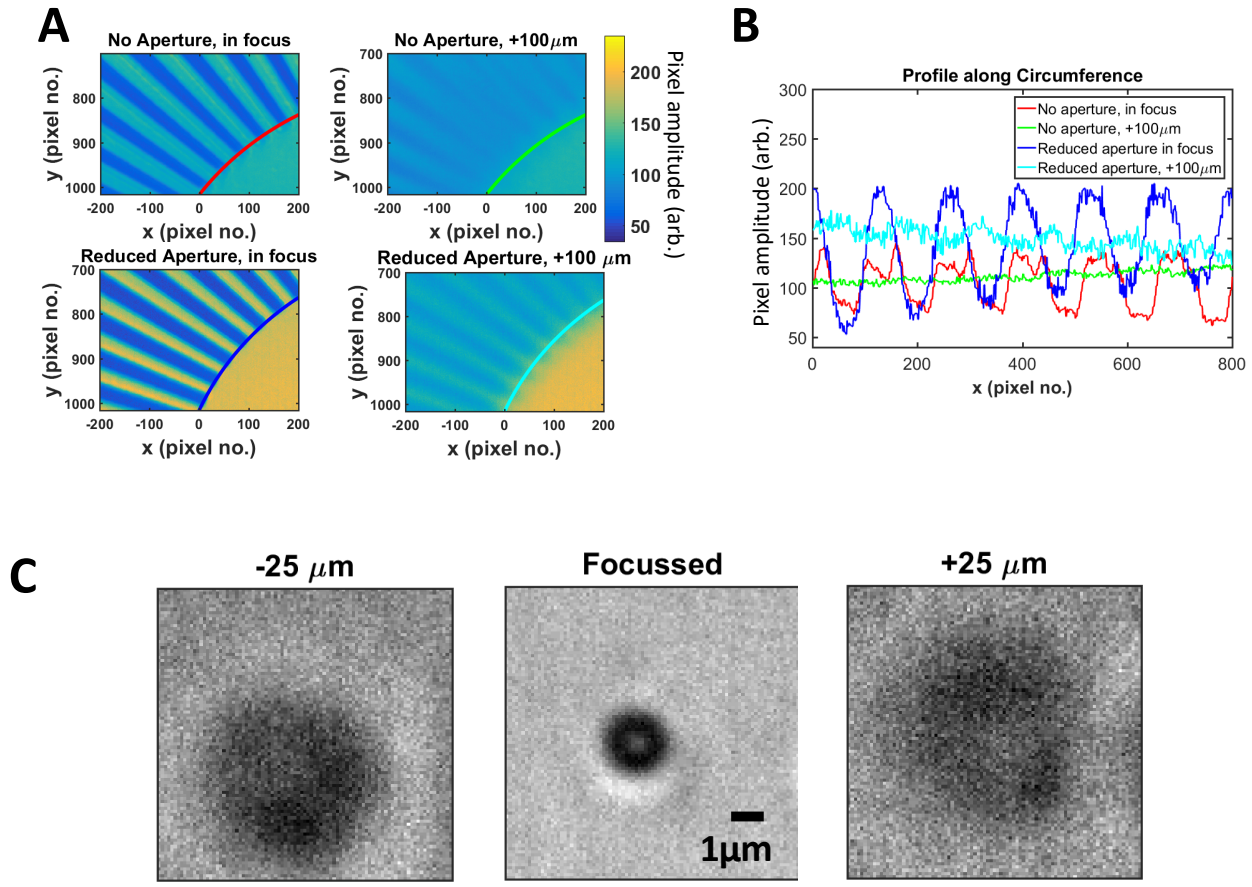

Figure 3-7: Contrast quantification using a lens with focal length of 20 cm. (A) Images of the star sector resolution target at the optical focus and 100 µm from the focus. Reduced aperture images correspond to an aperture size of 4 mm. (B) Profiles were taken at the same radii to visualise the resolution variation. (C) Example image of microbubble detected over a field of view of 50 µm using the 4 mm aperture.

Figure 3-7(A) shows how the introduction of the aperture enabled the smallest structure in the resolution target, 4.4 µm, to be resolved at a distance of 100 µm from the optical focus when using the tube lens of focal length 20 cm. An aperture 4 mm in diameter was used as it was the smallest possible to avoid obscuring the image. Figure 3-7(B) shows the profiles taken at the smallest possible radii. At 100 µm from

the focus, without any aperture, the image is blurred such that the amplitude plot (green) is flat. When the aperture is reduced (cyan), more variation in amplitude can be observed at 100 µm from the focus. An example MB image of a MB resting at the top surface of the cellulose tubing is shown in Figure 3-7(C) over a DOF of 50 µm.

A more detailed characterisation was done with the lens of focal length 12.5 cm because this had the most suitable magnification to allow the full tube to be visualised in a single frame. Thus the 12.5 mm lens was used for all the following results figures. The contrast at three positions are shown over the full range of modulation periods in Figure 3-8(A). Figure 3-8(B) shows that the most improvement in contrast could be achieved over the range 10 - 50 µm from the optical focus. Overall Figure 3-8 shows that the restricted aperture caused a negligible improvement in contrast at the focus and far from the focus, but was most beneficial in between.

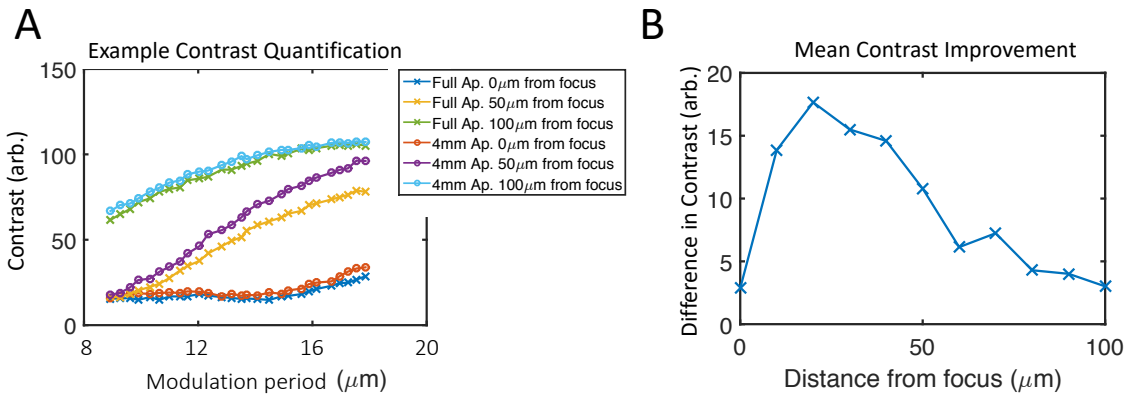

Figure 3-8: Characterisation of optical DOF and resolution with a lens of focal length 12.5 cm. (A) Plotting contrast over resolution at 100 µm, 50 µm and 0 µm from the focus for the full aperture and 4 mm aperture. (B) The average difference in contrast between the full aperture and 4mm aperture, calculated as an average over all periods of modulation measured and at 10 µm increments away from the focus is shown.

Figure 3-9 shows the results of the imaging MBs at varying apertures and distances from the focus. Figure 3-9(A) shows the effect of decreasing the aperture size down to 2 mm, where the FOV began to be obstructed. Figure 3-9(B) shows how decreasing the aperture size did allow an improvement in the number of MBs which could be detected at 25 µm and 50 µm away from the focus. The white ROIs in Figure 3-

9(B-C) show MBs which would not have been detected if the full aperture (12 mm) was used. More distinct regions of MBs are also observed when using the reduced aperture compared to the full aperture, showing improved resolution at a distance from the focus.

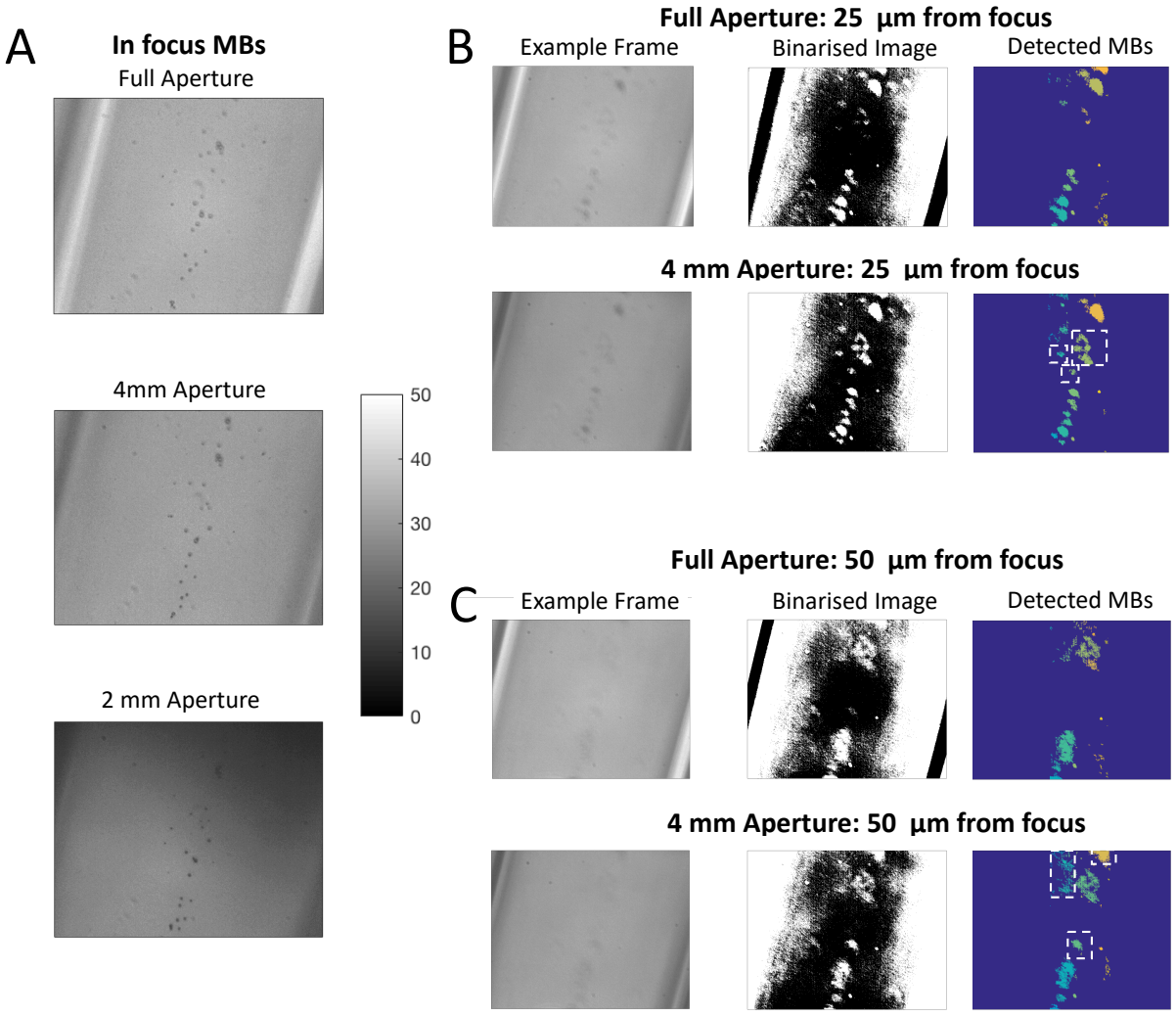

Figure 3-9: Effect of reduced aperture on MB imaging. (A) shows in focus images of MBs resting on the top of the cellulose tube using the full 12 mm aperture (top), a 4 mm aperture (middle) and 2 mm aperture (bottom). (B) shows images 25 µm from the focus (left), which were binarised (middle) and then regions of 8-connected components identified. The white square indicates regions where better separation of the MBs and background was achieved using a smaller aperture. (C) shows the results of repeating the process in (B) at 50 µm from the focus.

3.4.2 *In silico* characterisation of MB flow in tube

Modelling of the MB flow considering drag, gravity, buoyancy and parabolic flow showed that buoyancy would be expected to have a significant effect over a range of MB flow speeds. The tube position which is optically observed in experiments is generally around 4-5 cm from the needle junction. Figure 3-10 shows that only the smallest MBs (of radius < 1 μm) will be found in the upper 50 μm of the tube after flowing a distance of 5 cm with a maximum speed, of 1 mm/s. As the speed increases to match one of the experimentally used flow rates of 5 μl/min MBs of radius ≤ 2 μm are predicted to flow in the imaged tube region. For a flow rate of 15 μl/min MBs ≤ 4 μm are expected to enter the FOV. At a flow rate of 50 μl/min the full range of MB sizes considered are expected to contribute to the acoustic imaging.

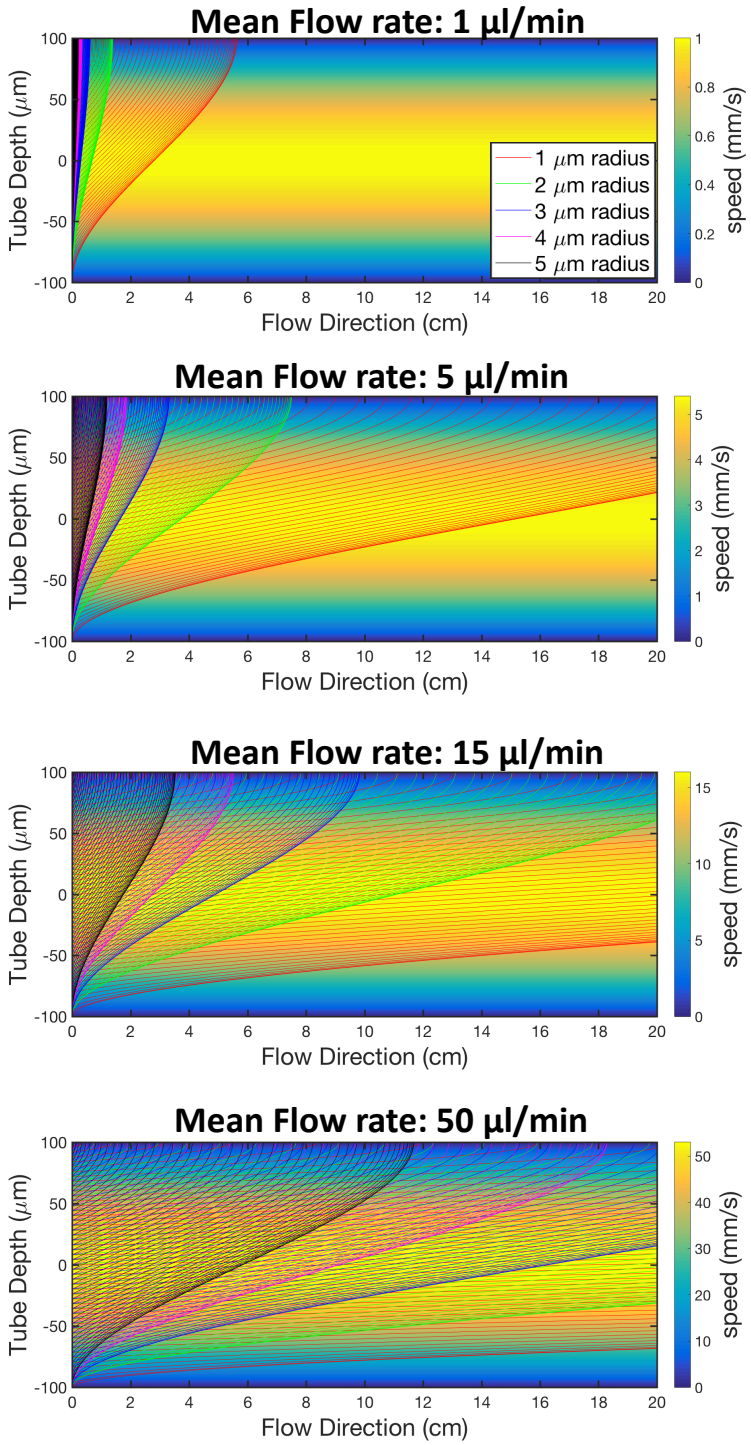

Figure 3-10: Modelling the MB trajectories. The paths of MBs, of 5 radii, are plotted for flow rates of 1 µl/min (corresponding to max. speed of 1 mm/s), 5 µl/min, 15 µl/min and 50 µl/min where the colormap is in terms of (mm/s) for easier interpretation.

3.4.3 *In vitro* characterisation of MB flow in tube

Figure 3-11(A) provides a qualitative example of any image taken at a flow rate of 50 µl/min, where streaks are observed instead of well resolved MB images. This illustrates why higher flow speeds are more challenging to capture with the optical camera.

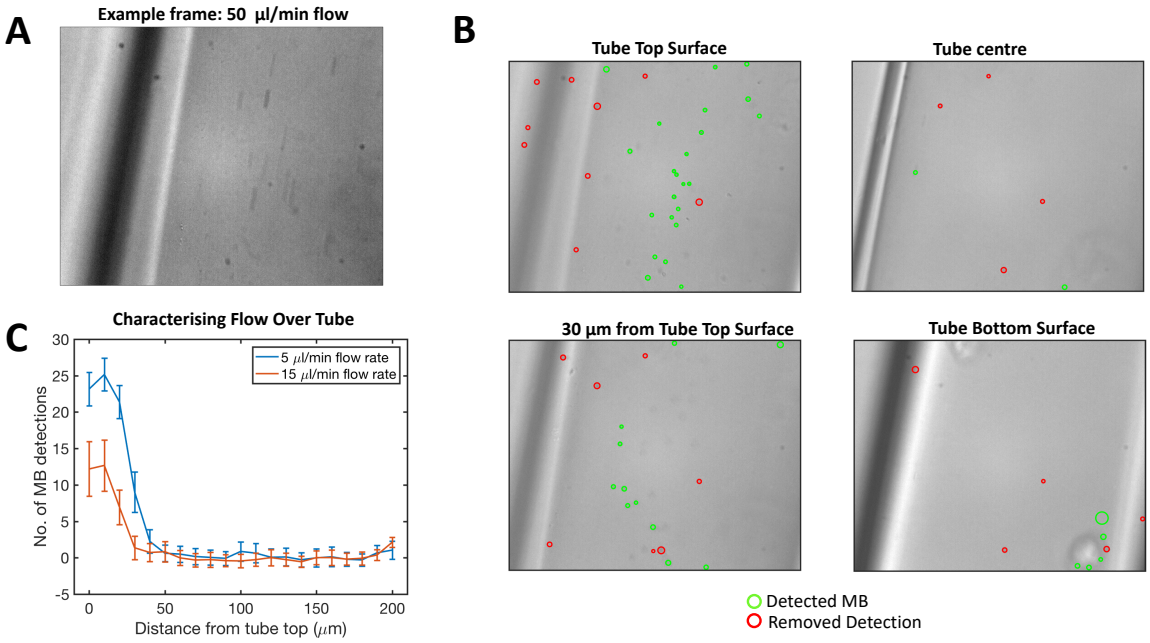

Figure 3-11: *In vitro* measurements of MB flow in the tube. (A) shows the challenge of optically imaging MBs flowing at 50 µl/min. (B) shows example images at different axial positions in the tube, at a flow rate of 15 µl/min. The green circles show the signals the algorithm has identified as MBs and the red circles are those detections which have been filtered out due to being at locations where there is a dust on the lens or locations outside the tube walls. (C) collates the results of the MB counting algorithm at different positions in the tube at a flow rate of 5 µl/min (blue) and 15 µl/min (red).

As presented in the example frames in Figure 3-11(B) the MBs were qualitatively observed to be concentrated in the upper portion of the tube for these slow flows. The green circles show the signals the algorithm has identified as MBs. The red circles are those detections which have been filtered out due to being at locations where there is dust on the lens or locations outside the tube walls. The curves in Figure 3-11(C) show this result quantitively. Here the mean is plotted, with error bars corresponding

to the standard deviation over 100 frames. MBs were most likely to be found in the top $\approx$ 30 μm and $\approx$ 40 μm of the tube for 5 μl/min and 15 μl/min flow rates respectively.

The image 200 μm from the tube top in Figure 3-11(B) shows how debris which has sunk to the tube bottom can erroneously be detected as MBs - this explains the slight increase in the curves in this region. The error of the MB detection code was determined to be an average of 1.15 false detections per frame by performing the experiment on an empty tube. This was subtracted from the curves shown in Figure 3-11(C).

3.4.4 Challenges of imaging at slow flows

Figure 3-12 shows some of the challenges of imaging a flowing MB population at low flow speeds. Using a ULA-OP amplitude of 0.8 and a flow rate of 50 μl/min, a sparse distribution of MBs appropriate for SRUS can be acoustically imaged, as shown in Figure 3-12(A). The relatively high pulse amplitude generates a high SNR for individual MB signals. However, given that the flow is from left to right, MB destruction can be observed after the MBs have spent more time in the FOV. When imaging a flow rate of 15 μl/min the MB signal is initially strong, however all MBs are rapidly destroyed over $<$ 100 frames and the flow rate is too slow to replenish the FOV.

Figure 3-12(B) shows the simultaneous optical imaging alongside the acoustic measurements at 15 μl/min presented in (A). Immediately before the US imaging four MBs can be observed flowing in the optical FOV, these are seen more clearly in the difference image (top right panel of Figure 3-12(B)). After the US is initiated, the MBs, labelled 3 and 4 (2.0 μm and 2.1 μm in radius), were observed to rapidly decelerate and float to the top of the tube. Only very small MBs (1.2 μm and 1.1 μm in radius), labelled 5 and 6 continued to flow.

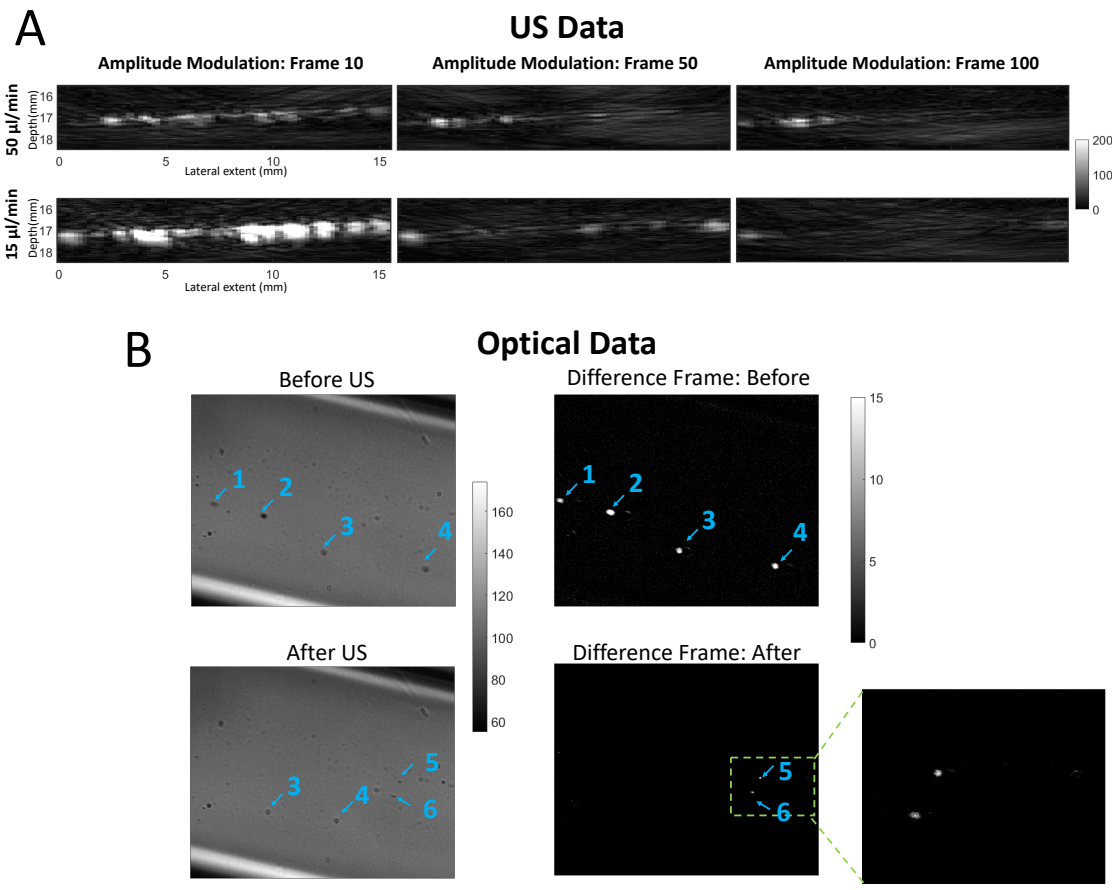

Figure 3-12: Challenge of US imaging at slow flow rate of 15 µl/min. (A) shows example amplitude modulation frames collected using the sample concentration of MBs and US pulse sequence for MBs flowing at 50 µl/min (top) and 15 µl/min (bottom). (B) shows optical data collected immediately before US (top) and immediately after the US acquisition started (bottom). An example optical frame is shown on the left, and the difference image between successive frames is presented on the right to show the movement of the MBs between frames

Figure 3-13 shows at which ULA-OP pulse amplitudes the MB destruction is significant. ULA-OP pulse amplitudes settings of ≥ 0.5 showed significant destruction to a 5% significance level. See Appendix C for the relationship between the ULA-OP pulse amplitude setting and peak negative pressure in MPa. For quick reference, an ULA-OP amplitude setting of 0.5 corresponds to a peak negative pressure of -0.14 MPa. The number of MBs before the US pulse decreased with respect to pulse amplitude because MBs which had floated to the tube top were destroyed.

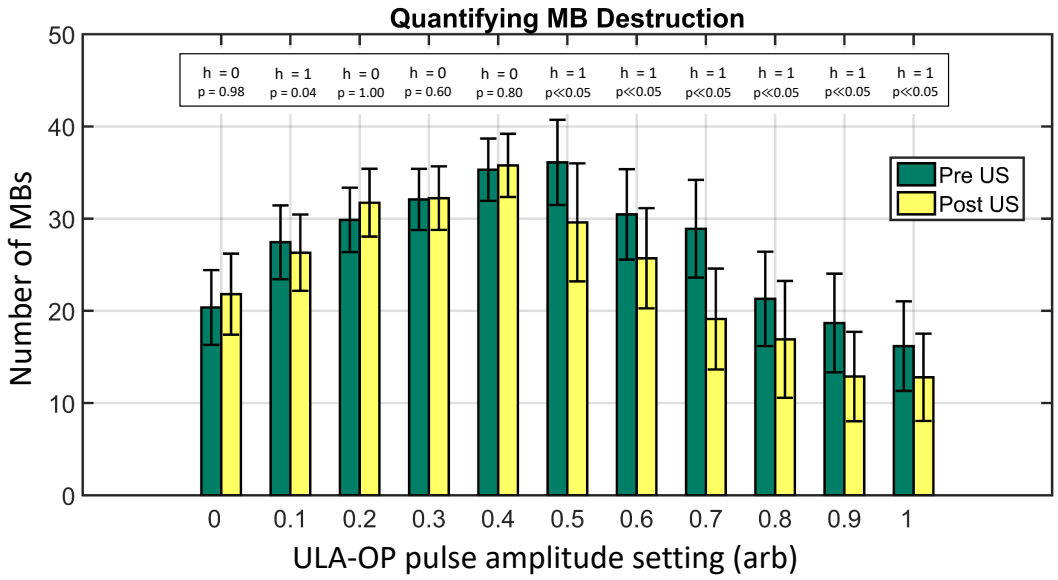

Figure 3-13: Destruction of MBs at various ULA-OP pulse amplitude settings. See Appendix C for the relationship between the ULA-OP pulse amplitude setting and peak negative pressure in MPa. The plot compares the mean number of MBs per frame before the US (green) compared to after the US (yellow). The value of h is 1 if a significant number of MBs have been destroyed by the US sequence (significance level of 5%).

3.4.5 Simultaneous acquisition at slow flows

Figure 3-14(A) and Figure 3-14(B) show corresponding acoustic and optical frames shortly after the acoustic insonation was triggered.

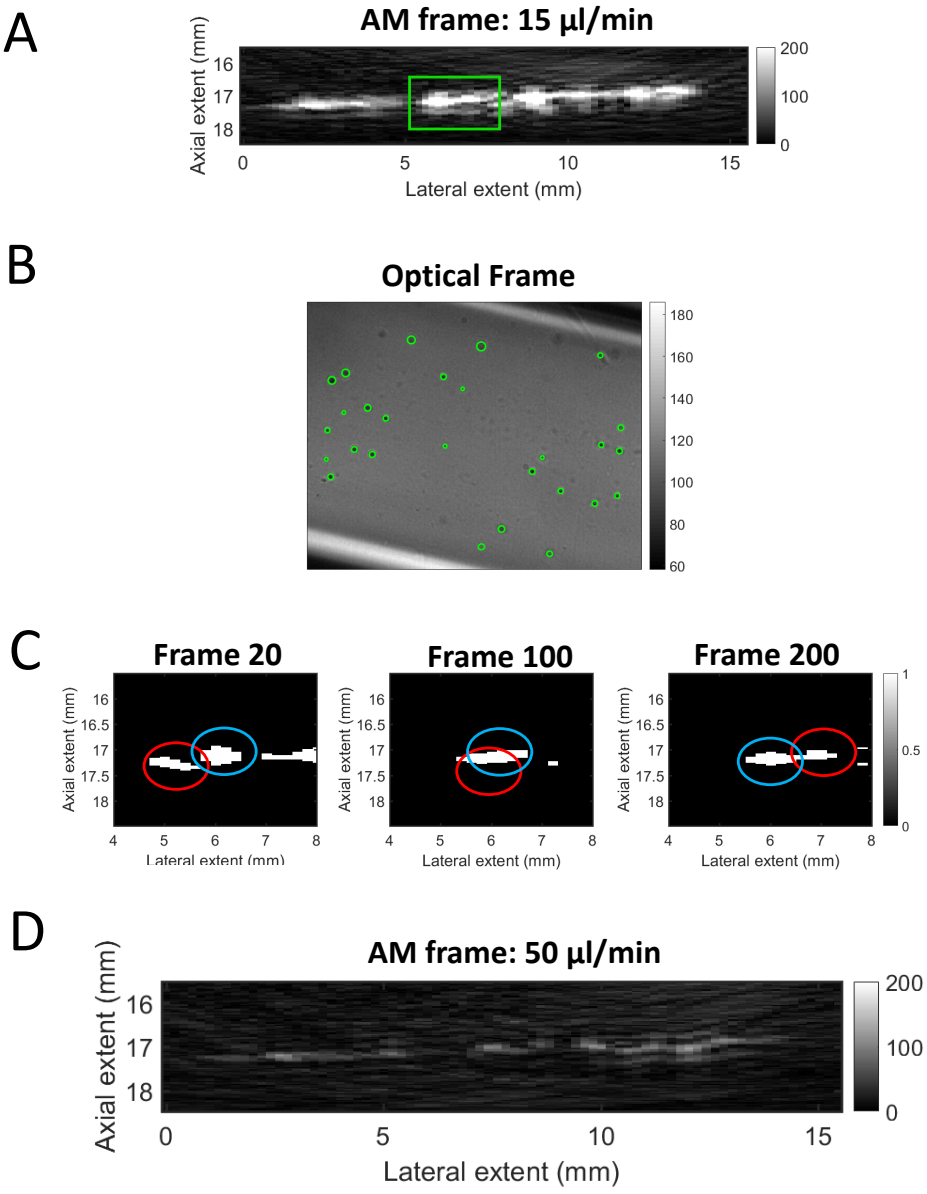

Figure 3-14: Simultaneous US and optical imaging at an ULA-OP amplitude of 0.2. (A) shows an example acoustic amplitude modulation frame with MB flow at 15 µl/min and (B) shows the corresponding optical frame. (C) shows how the MB signals, highlighted by the green box of (A), appear to show two MBs (highlighted using red and blue circles) passing each other when the images are binarised. (D) shows the amplitude of using the same concentration of MBs, at a higher flow rate of 50 µl/min.

Initially the results of Figure 3-14 seemed to show that there were fewer bubbles

observed acoustically (A) than optically (B). When the US frames were thresholded as shown in Figure 3-14(C) they appeared to show two MBs passing each other. Figure 3-14(D) shows that individual MB signals collected at a higher flow rate of 50 μl/min, acquired using the same pulse amplitude, showed that the signal amplitude from MBs spatially separated sufficiently to be acceptable for SR imaging processing was much less than that observed in (A). Thus, perhaps there is not an expected mismatch between Figure 3-14(A) and Figure 3-14 (B). Just that the MBs are more concentrated in some tube regions than others, giving rise to stronger regions of signals which correspond to more than one MB.

Another, more practical, factor that made SRUS at lower flow speeds more challenging was simply the lack of movement between frames. When MBs are flowing it is easier to judge whether a region of contrast is due to two nearby MBs or an isolated MB as the signals will move relative to each other. However, without significant movement of the MBs during the experiment, with respect to the resolution of the US image, it was difficult to assess the suitability of the concentration and whether single MBs were present.

3.5 Discussion

The aim of this work was to develop an optical ground truth of the SRUS process. When the MB concentration has been tuned to enable the detection of isolated MBs in the acoustic FOV the distribution of acoustically active MBs is sparse in the US image, especially compared to the in-plane FOV of the optical imaging (≈ 200 μm). Perhaps naively, it was expected that if the DOF of the optical system was increased over the tube extent it would be fairly straightforward to identify individual MBs in the optical image and match them with their acoustic signal. This would have enabled the influence of the MB surroundings, size and flow characteristics on the localisations to be better understood. This work has developed and implemented a simple optical set-up to investigate the SRUS process. Although the set-up developed in this chapter did not allow the effect of the MB environment on SRUS to be optically

validated, it did provide insight into the SRUS process which could have implications for future directions of SR. This section will discuss the findings of the existing set-up, implications for SRUS and limitations.

3.5.1 Summary of findings

Expanding the DOF

This work has shown that introduction of an adjustable aperture is a cheap and flexible way of increasing the likelihood of MB detection approximately 50 μm about the optical focus. Although individual MBs may not be well resolved 50 μm from the focus, an increase in contrast will increase the likelihood that those frames where more than one MB exists in the tube can be identified. Expanding the aperture over the full extent of the 200 μm tube was not achieved in this work. However, *in vitro* and *in silico* studies both showed that the required DOF was reduced due to buoyancy, with MBs most likely to be observed in the top half of the tube.

Simultaneous optical and acoustic measurements

It was challenging to experimentally achieve acoustic signals appropriate for SRUS at flow rates of $\leq$ 15 μl/min (mean speed of 8.0 mm/s) compared to the faster flow rates of 50 μl/min (mean speed of 26.5 mm/s). However, using faster flow, the optical set-up did not have a high enough frame rate to capture the flowing MBs without blurring. Regardless, if SRUS is to be useful for imaging microvasculature flow it will be necessary to image acoustically at speeds « 15 μl/min (a mean speed of 1mm/s $\approx$ 2 μl/min). Thus, the optical framerate was suitable for the investigation of relevant flow speeds and accordingly the acoustic parameters were adjusted. The simultaneous optical imaging alongside the US imaging was used as a tool to test pulse amplitudes which would not destroy MBs at a flow rate of 15 μl/min. This allowed an amplitude which would not significantly destroy MBs during imaging to be used in the following experiments. Figure 3-14 showed results using a lower amplitude, chosen not to destroy the MBs. At a flow rate of 15 μl/min stronger signals than those expected of

isolated MB appeared to move together. Instead of visualising single MBs it is more likely that, at these low speeds, acoustically active MBs are more concentrated in some tube regions than others, giving rise to stronger regions of signals. As the same concentration was used for the flow at 50 μl/min which gave a spatial separation of MBs feasible to perform SR on, it was uncertain what might be causing these more concentrated regions. In the small FOV observed optically, there were tens of MBs detected. This meant that it was not possible to determine which MBs were contributing to the acoustic signal.

3.5.2 Implication of Findings

MB size tuning

The *in silico* results showed that imaging faster flow rates may allow a greater range of MB sizes to contribute to the image when using a phantom such as the 200 μm tubes. The simulation showed that, at a mean flow rate of 5 μl/min, only MBs of radius $\leq$ 2 μm are predicted to flow in the imaged tube region. Comparatively, at a flow rate of 50 μl/min, the full range of MB sizes are expected to enter the imaged region. Perhaps the larger MBs are responsible for the stronger MB signal using these imaging parameters. This would agree with the previous studies on the optimum MB size for SR imaging which have suggested that larger MB diameters are more suitable for SRUS under certain conditions [122, 196]. More generally, Gorce et al. (2000) has shown how total MB gas volume can be a better predictor of echogenicity than MB number [191]. The authors showed that although MBs smaller than 2 μm in diameter make up 60% of the Sonovue polydisperse population, they are responsible for less that 5% of the total contrast signal for transmit frequencies up to 7 MHz. It was predicted that MBs imaged at frequencies below their resonance frequency will not contribute significantly to the image. However, the response of MBs of different sizes is affected by imaging parameters such as frequency, bandwidth and detection method, as shown in the previous chapter. Thus, the most efficient MB size is too sensitive to imaging parameters to definitively say that larger MBs should be used

for SRUS. However, this will be discussed further in the final chapter and suggestions for future work outlined.

Figure 3-12 showed that larger MBs also may have very different trajectories following the US insonation than smaller MBs. Larger MBs of radii ≈ 2.1 μm were observed to travel rapidly to the top of the tube immediately after insonation and remain stationary during the imaging procedure. Conversely, smaller MB of radii ≈ 1.2 μm continued to flow. The Bjerkes force is dependent on the MB radius, as the amplitude is proportional to $1/(Ro^4)$ and the direction depends on whether the MB is above or below resonance [203]. However, the direction of gravity was aligned to be approximately perpendicular to the acoustic radiation, thus this was not the direction that MBs were expected to be pushed by the radiation force. This is an observation which could be investigated further in future work.

Influence of US amplitude

One factor which makes it easier to obtain acoustic data with strong isolated signals at high flow rates of 50 μl/min is because it is possible to use a higher pulse amplitude without destruction of the MBs. In previous SR work where the maximum ULA-OP amplitude was used successfully with a flow rate of 50 μl/min in a 200 μm cellulose tube. The relative ease of imaging fast flow due to the potential of using higher amplitudes is something that will also likely be true *in vivo*.

If the cellulose tubing is a reasonable mimic, then the results of this chapter could have important implications for the imaging microvasculature flow. If the slow moving MBs are easily destroyed by the pulse strength required to give high SNR then perhaps this will decrease the efficacy of SRUS for imaging the smallest vessels. One possible area of investigation could be the use of an imaging sequence less likely to destroy MBs but still using pulse strengths sufficient to generate a high SNR. For example, brief periods of high frame rate imaging could be interspersed with pauses to retain the benefits of ultrafast imaging without significant MB destruction [138].

Nonetheless, previous *in vivo* investigations have shown that MBs flowing at speeds < 2mm/s can be imaged [118, 124]. Foiret et al. (2017) showed that MBs

travelling in the kidney microvasculature can withstand hundreds of pulses whilst still generating a strong enough response to be detected. This *in vivo* environment differs from the *in vitro* environment in that the slowest flowing MBs are likely to be in vessels « 200 μm. Previous literature has shown that the MB response is damped, and fragmentation is reduced in smaller tubes [205]. Whether this protective effect can compensate for the damped response and benefit SRUS of microvasculature is a possible direction for future work.

Alternatively, other authors have shown, also using simultaneous optical and acoustic imaging, that stationary MBs can be easily destroyed at routinely used imaging parameters [221]. Thus perhaps the MB concentrations in these vessels are just higher than expected when SRUS is performed, and destruction of a subset of the imaged MBs is required for sufficient SNR .

Influence of MB buoyancy

Figure 3-12 showed how, using the same concentration, the MB contrast was much stronger at 15 μl/min compared to 50 μl/min at the start of the acoustic acquisition. This may be due to the increased number of MBs that float to the top of the tube due to buoyancy. Destroying these MBs before imaging with CEUS sequence is not feasible, because on the timescale required to replenish the MB flow in the tube more MBs will have floated to the tube surface. Thus, it was not possible in this work to achieve an appropriate concentration of flowing MBs in the FOV without multiple MBs being optically observed resting on the tube top. Dayton et al., (1999) performed a very similar set up of acoustically and optically measuring signal from single flowing MBs. The authors did not report the same problem, although did mention that the effect of buoyancy may make it harder to maintain a constant MB concentration in the FOV [76]. For the work shown in this chapter, this effect was problematic *in vitro* but it is unknown how buoyancy would affect the SRUS process *in vivo*. Future work could use a branching phantom with channels of varying diameters down to capillary dimensions to more realistically model the MB trajectories.

General benefits of an optical window into the SRUS process

Figure 3-13 shows a simple example of the benefits of having such a setup. Earlier *in vivo* research in SRUS has aimed to use a pulse amplitude which would not destroy MBs by using a suitable MI value [116]. The optical set-up was useful for providing a ground truth of where destruction was significant at the specific imaging parameters and geometry used in this work.

Another useful, practical, insight from implementing the optical set-up with the tube phantom was the observation of the tube vibration as described in subsection 3.3.1. This may seem trivial, but movement even on a micron scale is important for SRUS. After this observation the necessity of improving the set-up, for example by using damped rods, was recognised. This is a simple adjustment, but something that may otherwise have been neglected in future experiments.

Being able to optically quantify the distribution of MBs across the tube meant that the trajectories of the MBs could be better understood at specific flow rates. Thus, it was found that MB concentration was not constant over the tube. This work has shown that this can be predicted using modelling, this has not been previously discussed in the literature.

During this work, optically visualising the phantom during the acoustic acquisition also helped make a more informed interpretation of the results. For example, using the acoustic data in Figure 3-14 from MBs flowing at 15 μl/min, regions could be thresholded such that the data could be interpreted as single MBs moving in the tube. However, the relatively large amplitude of the signals (compared to flow at 50 μl/min) and the optical ground truth showing many MBs in the FOV meant that this dataset should not necessarily be appropriate for localisation of isolated MBs. If the moving signals were isolated MBs then the optical data would show that a low percentage of MBs are acoustically active. It is possible that the higher amplitude observed for 15 μl/min is simply due to the AM imaging mode performing better at lower speeds due to improved overlap of MB signals between the frames in the multi-pulse sequence. An alternative hypothesis is that these signals were not isolated (acoustically active) MBs

and the stronger regions of contrast were due to an inhomogeneous concentration over the tube phantom which was moving in bulk. Another possible explanation is that these regions of signals were caused by MB coalescence. The secondary radiation force causes MBs of a similar size to cluster together, coalescence can be defined as the fusion of two or more of these MBs [222]. Alternatively, MBs may cluster together without actually coalescing but still act as a single entity in the acoustic field [223]. Generally, studies observing coalescence have not considered flowing MBs [222, 223, 224]. Investigating any relationship between flow rate and coalescence is a topic for future work and would be especially interesting using concentrations of MBs suitable for SRUS.

3.5.3 Limitations:

There were some limitations and areas of future improvement regarding the detailed experiments which should be highlighted.

One limitation of the quantification of the enhanced DOF using the optical target was that the contrast between bars of the resolution target may not be representative of the contrast difference between a MB and the surrounding water. A similar experiment to that performed with the target was repeated using MBs resting at the top of the cellulose tube. However due to the time taken to complete the full set of experiments the MBs were liable to dissolve or change position in the FOV, thus performing a well-controlled experiment was difficult. Perhaps a future measurement could be done by adapting the target to better mimic the contrast difference of a MB in the tube centre. It should be noted that the results may also be sensitive to changes in the set-up such as the illumination source. For a fairer comparison between aperture sizes, the exposure could be adjusted to ensure that the same quantity of light reaches the CMOS sensor. However, for this work, the frame rate could not be sacrificed. The minimum possible exposure time to enable a good SNR had already been identified, thus this parameter was not varied. Perhaps future work could try introducing a brighter light source to allow the exposure time to be further reduced.

Although not essential for investigating low flows, a camera with a higher fram-

erate may allow some of the unanswered questions raised in this chapter to be investigated. For example, it would allow validation of how the size distribution of MBs over the tube depended on flow speed.

The simulation was simplistic, although it did agree with the experimental measurements. The model did not include the mass of any added palmitic acid (used to stabilise the shell) because no literature values for fraction of palmitic acid to phospholipids in the shell could be determined. Thus, the mass may have been underestimated. Likewise, the additional terms due to the radiation force were not considered since US pulses are only incident on the MB for a negligible time compared to the overall flow through the phantom.

It was challenging to design a simple optical tracking algorithm so that it was general enough to work for a range of flow speeds and positions in the tube. For example, the contrast was affected by non-uniformity of the illumination. A main concern was that the "imfindcircles()" algorithm may miss quickly moving MBs which would have more of a streak appearance. In particular, the smallest MBs are most likely to be moving fastest due to being swept along by the lateral parabolic flow but are the hardest to optically observe. Manual observation showed that a small number of MBs were present over a wider DOF than the algorithm. Thus, the quantitative results may be slightly skewed to underestimate the number of faster MBs near the tube centre. More importantly this means that limited DOF, despite the modest improvement made by using the aperture, is still problematic for imaging flowing MBs. This is something was has not been discussed in previous similar set-ups using the 200 μm tubes [76, 82]. Nonetheless, the results still demonstrate that the MBs are concentrated in the upper half of the tube. If the flow speed limited the optical detection then the plots shown in Figure 3-11(C) should be approximately symmetrical about 100 μm to account for the slower moving MBs in the bottom half of the tube, assuming parabolic horizontal flow.

3.5.4 Observations for future directions

Processing improvements

During this work strong scattering from the tube was observed. The previous non-linear results had the background subtracted by initially acquiring a tube image without MBs, and only water. This could then be subtracted from the MB images. Both of these images were acquired using the maximum system gain. This is simple in this stationary *in vitro* situation, but less useful for more imaging where there is some movement of the probe or tube, or when taking the image without MBs is not possible.

There was a relatively strong linear reflection from the cellulose tubing, which could be saturated when imaging with the set-up described in this chapter. Linear signal from the tube filled with water was saturated after a ULA-OP setting of 0.5 when using the full gain. Using a high gain is needed for capturing the weak non-linear MB signal as shown in Figure 3-15(A) by comparing the single RF frame in the right-hand column collected at high gain compared to the left column collected at low gain. The parabola tails from the MBs are more visible in the high gain image, although the peak of the parabola inside the tube region is not visible due to saturation of the cellulose signal.

Figure 3-15(B) shows a single line of the received RF plane wave data for each pulse of the contrast sequence. The saturation shown for the +1 and -1 pulses would be particularly problematic when combining for non-linear imaging modes, such as AM, as now the linear signal from the tube will not cancel.

It was hypothesised that, using the ultrafast imaging rates, data could be collected at low and high gains and then combined together to extract the MB signal without the tube saturation. This will be explored in the following chapter.

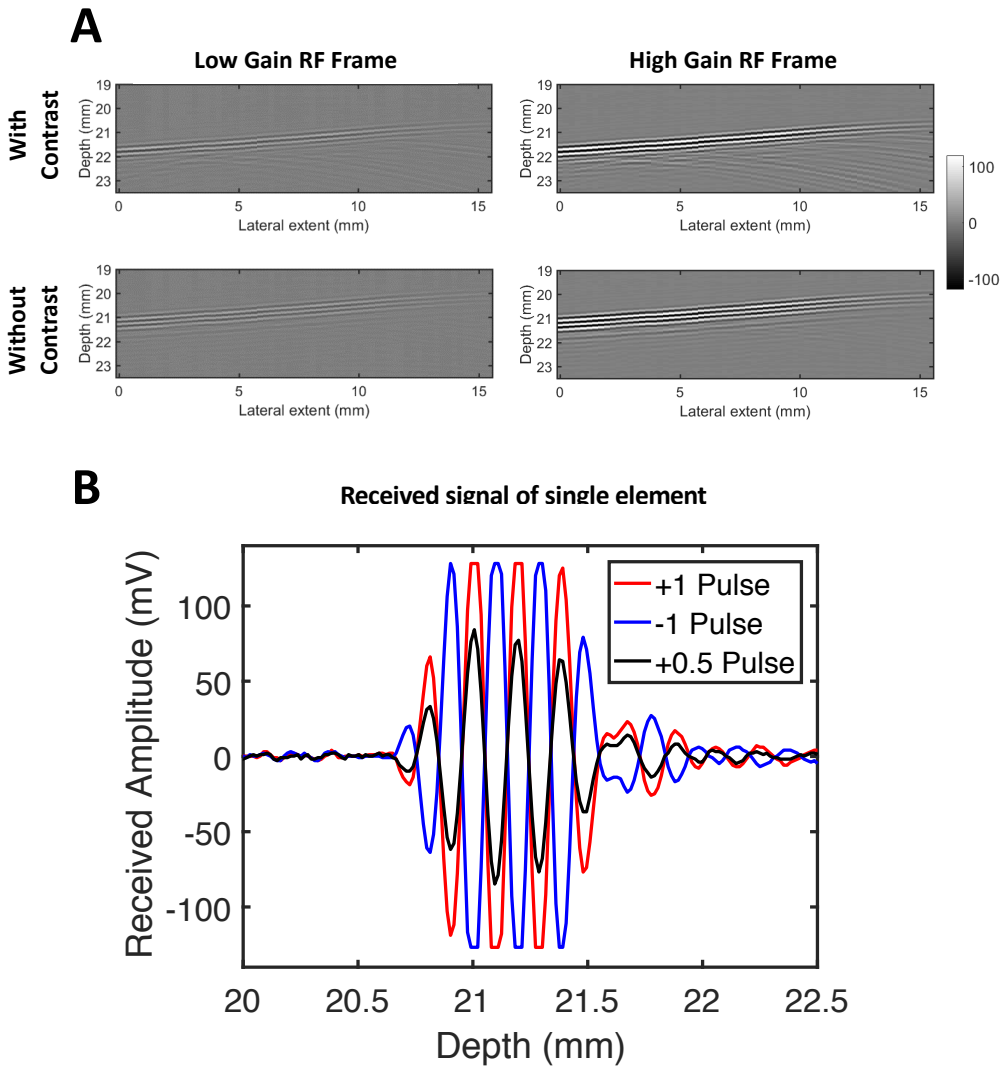

Figure 3-15: Acquiring data at various gains. (A) Example RF frames acquired at a low gain of 30 dB (left) and at a high gain of 46 dB (right), with MB contrast (top) and without MB contrast (bottom). (B) shows the RF signal received at a single element when a cellulose tube is imaged using a CEUS sequence.

Phantom development

Another direction to prioritise should be development of more appropriate microvasculature phantoms. MBs can be detected over 50 µm. Even if flowing MBs are more likely to be in the upper tube portion, ideally the full phantom extent should be in

the optical view. If phantoms with channels < 50 μm were used then a tube lens of longer focal length (such as the 20 cm lens used in Figure 3-7) could be used to provide greater magnification. This would mean that the DOF and in-plane FOV would cover the full phantom extent. Working at a higher magnification would be particularly beneficial for imaging the smallest MBs which are also likely to move the fastest, assuming parabolic lateral flow and buoyancy, and thus most difficult to capture without blurring using the optical camera.

In subsection 3.4.5 it was not possible to match acoustic signals to corresponding optical images. An alternative approach could involve imaging an extremely low concentration of MBs flowing through the cellulose tubes so that only a single MB enters the optical and acoustic FOV [76]. However, during preliminary trials, it was not possible to achieve an optically dilute flowing solution without MBs which have floated to the top of the tube also being in the acoustic FOV. Using a vessel of diameter close to capillary scale should avoid this problem. Moreover, this will allow some the questions raised in subsection 3.4.4 regarding the pulse amplitude required for appropriate SNR of single MBs in small tubes to be answered.

Overall, a common theme during the interpretation of the results of this chapter was that simultaneous optical and acoustic validation of SRUS was made unnecessarily more challenging by using a tube diameter an order of magnitude larger than capillaries. Thus, the penultimate chapter in this thesis will focus on developing more suitable microvasculature phantoms.

3.6 Conclusions

Overall this work has developed and implemented an optical set-up to investigate the SRUS process. The introduction of an adjustable aperture can marginally improve optical MB detection up to a distance 50 μm from the focus. Acoustic imaging MB flow rates relevant to microvasculature is challenging *in vitro* due to MB destruction. *in silico* and *in vitro* results have shown that the MB distribution is not uniform over the tube extent, due to buoyancy. Instead, MBs are most likely to be found

in the top half of the tube. The results also suggest that, for these parameters, the larger MBs ($\approx$ 2 μm in radius) contributed more to the signal and their trajectories are more significantly altered by US insonation compared to smaller MBs ($\approx$ 1 μm in radius). However, more work is required to confirm this. Although the set-up developed in this chapter did not allow the effect of the MB environment on SRUS to be optically validated as intended, this work draws out new insights and challenges for its development of an optical ground truth, and to SRUS itself. Future work should focus on improving imaging sequences to enhance SNR without destroying MBs, developing phantoms with smaller channels, and characterising the signal from isolated flowing MBs. Channels $<$ 50 μm in diameter would enable optical MB detection over the full channel extent.

Chapter 4

High Dynamic Range Non-linear Ultrasound Imaging

4.1 Abstract

The non-linear response of MBs provides the opportunity to extract the MB signal from surrounding tissue using non-linear processing techniques. However, capturing the non-linear MB signal often requires a high receive gain. This can cause strong tissue signal to be saturated and appear as an artifact. This chapter proposes a high dynamic range (HDR) acquisition strategy for non-linear imaging inspired from the previous chapter, section 3.5.4. The HDR non-linear ultrasound imaging was tested *in silico* and *in vitro*. The *in silico* results showed that HDR non-linear ultrasound generated a 4.6 dB improvement in CTR over high gain saturated data and a 9.8% increase in contrast to acoustic noise ratio (CANR) over low gain unsaturated images. The *in vitro* data showed a 13.3 dB and 44% improvement in CTR and CANR respectively for HDR non-linear imaging. Overall, this method can significantly improve image quality whilst being easily implemented on existing systems.

4.2 Introduction

As discussed in the introductory chapter section 1.3.10, in some instances MBs have a non-linear response to US which enables them to be extracted from the surrounding, mainly linearly scattering, tissue using non-linear image processing techniques [200]. Since the non-linear components of the MB signals are much weaker than the linear, the receive gain of the US system must be high to capture this non-linear response. However, this can cause the signal from strong tissue scattering to become saturated and then breakthrough the filtering process. This is a common problem in commercial ultrasound systems, with the saturated signal appearing as bright structures in the contrast enhanced image [225]. The work in this chapter was motivated from the previous chapter which showed how the cellulose tube signal could be saturated when imaging at a gain which enabled better visualisation of the MB signal. In response to this observation I invented an imaging acquisition and signal processing technique to combine information received at different gains. This technique would be useful for CEUS imaging beyond SRUS, thus it is presented more generally in this chapter. This work has been submitted to the UK patent office and is pending examination.

In ultrasound acquisition the received signal undergoes analogue amplification before being digitised [226]. There is a finite range over which the analogue amplifier can ensure linear amplification of the input voltage with respect to the output voltage [227]. That is, input voltages over a specific amplitude will become saturated following amplification. However, if the gain is decreased to prevent this saturation the weak non-linear MB contributions may give low contrast due to decreased contrast to acoustic noise ratio (CANR). Thus, for non-linear imaging, saturated signal from otherwise linearly scattering tissue will not be cancelled. Figure 4-1 illustrates this problem using amplitude modulation (AM) where two pulses, one of amplitude A (full amplitude) and a second of amplitude $A/2$ (half amplitude), are transmitted successively. Non-linear signal is extracted by subtracting double the response of the half pulse from the full pulse response.

This problem is not unique to ultrasound. For example, the pixel intensity in

an optical image is a function of the brightness of the object being imaged and the exposure time [228]. A relatively short exposure time allows visualisation of bright objects at the expense of darker objects. If exposure time is increased, the darker objects will be visible but the brighter objects saturated. Tone mapping techniques involve combining images acquired using high and low exposures to visualise both bright and dark features [229]. Previous authors have applied analogous techniques to ultrasound imaging without contrast agents [228, 230]. These involved combining images acquired at different pulse amplitudes. However, they require the assumption that the scattering properties of the imaged medium vary linearly with amplitude. For non-linear imaging techniques, this is no longer valid. MB responses depend on pulse amplitude and they will be destroyed/damaged if the amplitude increases over a certain threshold [231].

Conventional HDR approaches combine multiple images taken over several amplitude settings [228]. The HDR image is calculated using a response function which describes the relationship between the scattered pressure and pixel intensity. Following the image computation, the pixels can then be rescaled using a process such as tone-mapping to display the image on dynamic range suitable for human visualisation (dynamic range of 30 dB). The work in this chapter is different from the conventional approach in that it only corrects the artifact generated at one gain by predicting the missing information using a second image acquired at a different gain. Contrary to the conventional approach, most of the information in the image has originated from a single acquired image. Only the saturated pixels have been replaced. This work is considered a form of high dynamic range imaging in this chapter because it corrects for an artifact caused by the limited dynamic range of the US probe.

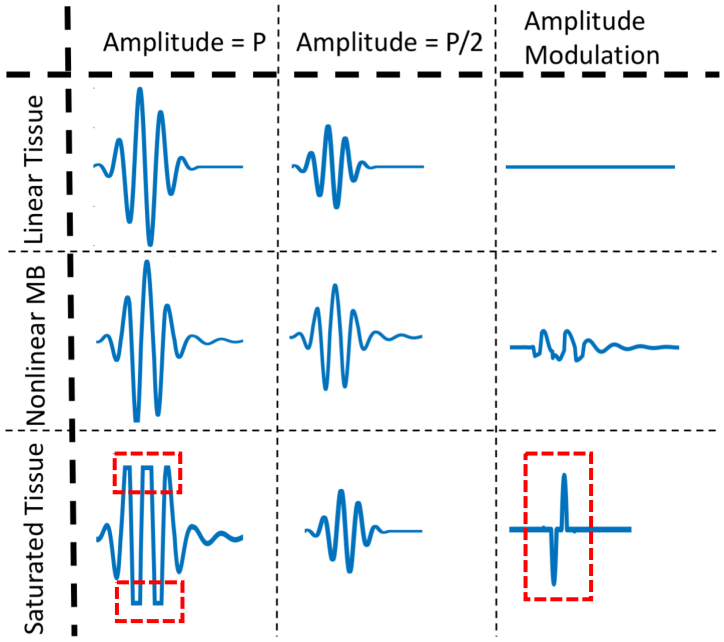

Figure 4-1: Schematic describing need for high dynamic range nonlinear ultrasound for amplitude modulation. For non-saturated data, the top row shows how linear tissue signals will be completely cancelled using amplitude modulation and the middle row shows that microbubble signals will be extracted. The bottom row shows how the saturated signal will result in an artifact.

Ishihara et al. (2015), describe a system which also looks at the effect of saturation specifically for amplitude modulated data [227]. If the highest amplitude pulse is flagged as being saturated, the gain applied to subsequent pulses of lower transmit amplitude is increased prior to the digitisation. For example, if the signal from the pulse of amplitude A has been saturated at gain G, the signal from the pulse of amplitude $A/2$ will be received using gain $2G$. This attempts to recreate the saturation artifact for the lower amplitude pulse. The two received signals can be subtracted to generate an image equivalent to that normally acquired with AM. This patent is the closest work related to this innovation. However, the patent suggests this is a hardware change - in that it must be possible for the user to manipulate how the system gain changes in response to the amplitude of the initial pulse. Thus this innovation may be challenging to incorporate into existing experimental systems and is only applicable to AM imaging.

Overall, the problem of visualising MB non-linear signal, without saturation of strong linearly scattering structure, has not be sufficiently addressed for contrast enhanced ultrasound imaging. This work will outline a novel technique with potential for filling this gap

4.3 Methods

4.3.1 The HDR non-linear method

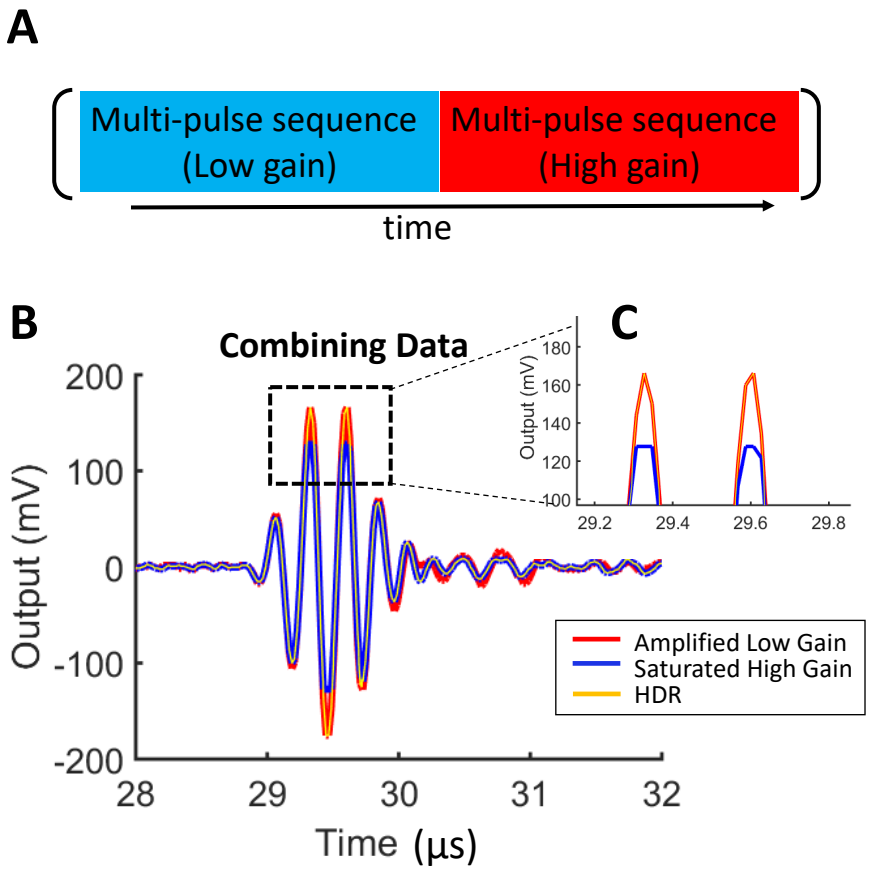

Figure 4-2: The new HDR non-linear method. (A) shows a schematic of the pulse sequence performed first at low gain and then high gain. (B) shows a single line of saturated high gain data (blue) with the amplified low gain data (red) and reconstructed HDR data (thin yellow). The inset (C) shows the regions where the correction is made.

Using plane wave ultrafast imaging, frame rates are primarily limited by the depth being imaged [51]. For example, when imaging at depths of 30 cm, frames rates on the order of 1 kHz can be achieved. This means that imaging transmit or receive parameters can be changed on a very fast timescale. The proposed method uses ultrafast imaging to acquire data at different gains before being combined. Figure 4-2(A) shows an example acquisition sequence and Figure 4-2(B) how the received data is combined.

1. Data is acquired using a non-linear multi-pulse sequence at the highest gain before saturation occurs (low gain), and the gain required to capture non-linear signal (high gain).

2. The received low gain signal is amplified during post processing according to the known relationship between gains.

3. The data lost due to saturation of the high gain pulse is replaced with that from the amplified low gain acquisition. This is achieved by replacing the data points above the known saturation threshold with the corresponding data points from the amplified low gain pulse. The result can then be low pass filtered to remove any discontinuities, if necessary.

4. A multi-pulse sequence is then applied to the reconstructed HDR data.

This means that the MB information contained in the high gain data is conserved, but the saturated portions are replaced by data which should better represent the linear tissue contribution.

4.3.2 *In silico*

k-Wave, a simulation package used to model acoustic wave propagation in tissue [161] was combined with the Marmottant model [80] as detailed in Chapter 2. This was used to simulate 2D plane wave contrast enhanced ultrasound images received with different gains. Simulation geometry with layers of fat and muscle to generate strong

reflections was designed as shown in Figure 4-3. A circular region of contrast was defined with a random distribution of MB radii between 0.5 µm and 5 µm. The received data was scaled to have a 7 dB difference between low gain and high gain to match the experimental data. A constant level of noise was calculated so that the low gain, maximum amplitude, pulse had an SNR of 26.4. The results were quantified using contrast to tissue (CTR):

$$\mathrm{CTR} = 20\log_{10}\left(\frac{\mu_{\mathrm{contrast}}}{\mu_{\mathrm{tissue}}}\right) \tag{4.1}$$

and contrast to acoustic noise ratio (CANR):

$$\mathrm{CANR} = \frac{|\mu_{\mathrm{contrast}} - \mu_{\mathrm{noise}}|}{\sqrt{\sigma^2{}_{\mathrm{contrast}} + \sigma^2{}_{\mathrm{noise}}}} \tag{4.2}$$

where µ is the signal mean and σ is the standard deviation. For the method to be useful, the HDR image should have better CANR compared to the low gain image and better CTR compared to the high gain image.

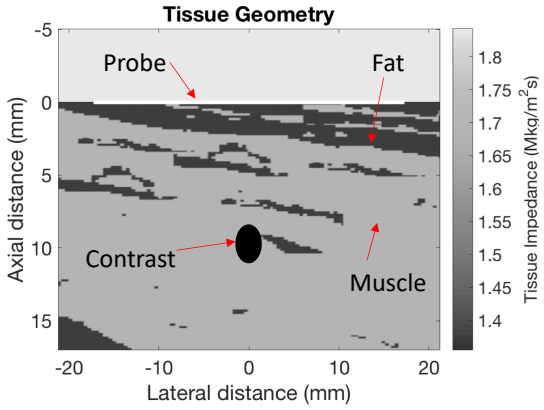

Figure 4-3: Simulation geometry. The colour map provides the tissue impedance values, probe position is shown in white, and region of microbubble contrast is shown in black.

4.3.3 *In vitro*

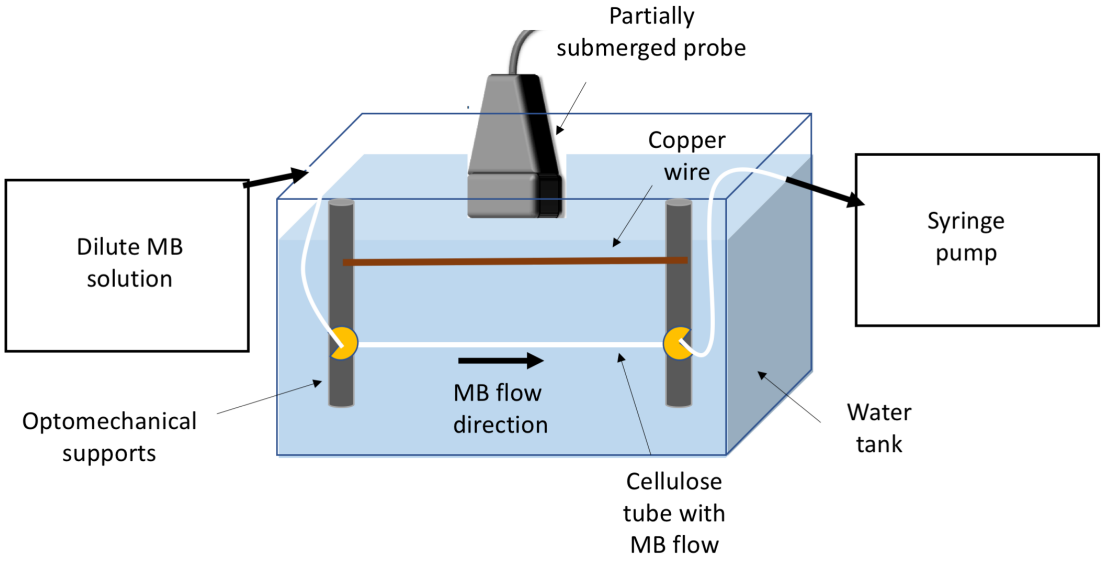

Figure 4-4: Set-up for *in vitro* experiments. A schematic of the experimental set-up used to test the non-linear HDR method

A 200 μm copper wire was used as a strong linear scatterer and a diluted solution of Sonuvue^{TM} (Bracco Imaging SpA, Milan, Italy) MBs was drawn through a 200 μm cellulose tube (Hemophan®, Membrana) at 30 μm/min to generate a region of contrast, as shown in Figure 4-4. Plane wave ultrasound data, was acquired at a pulse repetition frequency of 4 kHz, using the programmable ULA-OP system (MSD Lab, University of Florence, Italy) and pulse sequence [A_{low_gain}, -A_{low_gain}, $(A/2)_{low\_gain}$, A_{high_gain}, -A_{high_gain}, $(A/2)_{high\_gain}$] where A is the amplitude. However, it should be noted that for the following quantifications only the A_{low_gain}, A_{high_gain} and $(A/2)_{high\_gain}$ pulses were used. The maximum possible gain before saturation was found to be 22 dB. A gain of 29 dB was chosen as the high gain setting because it was the highest gain setting before the half amplitude pulse was also saturated. The mean and standard deviation of the CANR and CTR were calculated over 100 frames.

4.4 Results

4.4.1 *In silico*

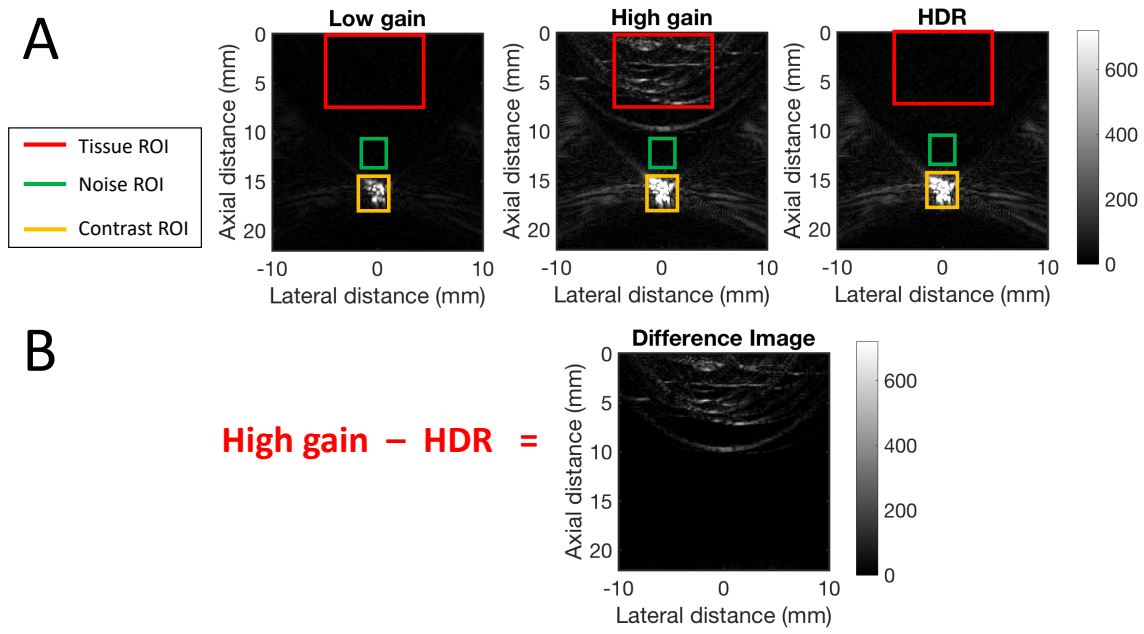

Figure 4-5: *In silico* demonstration. (A) Beamformed images following amplitude modulation at low gain (left), high gain (middle) and following the high dynamic range technique (right). (B) Difference between high gain image and HDR image showing the saturated tissue signal removed.

As shown in Figure 4-5, HDR imaging can clearly conserve strong MB signal from the high gain image, whilst removing the saturation artifact. The difference image shows the result of subtracting the HDR image from the high gain image. With these gain settings, HDR imaging achieved an improvement in CTR of 4.6 dB over high gain data and an improvement in CANR of 9.8% over the low gain image.

4.4.2 *In vitro*

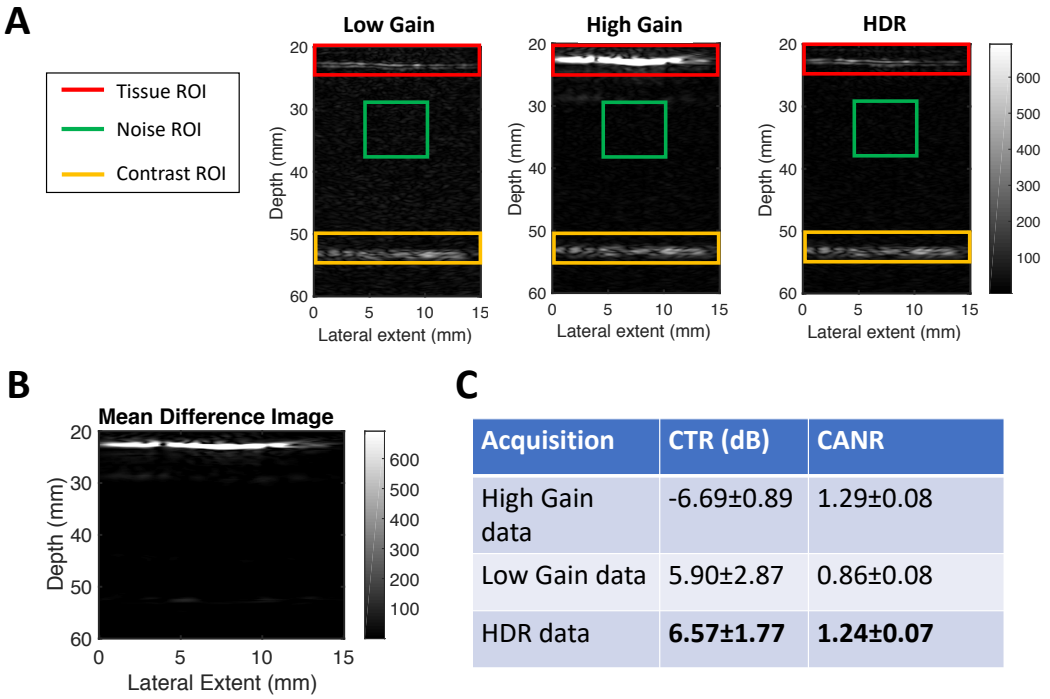

Acquisition	CTR (dB)	CANR
High Gain data	-6.69±0.89	1.29±0.08
Low Gain data	5.90±2.87	0.86±0.08
HDR data	**6.57±1.77**	**1.24±0.07**

Figure 4-6: Experimental demonstration. (A) Beamformed images following amplitude modulation at low gain (left), high gain (middle) and following the high dynamic range technique (right). (B) Difference between high gain image and HDR image showing the saturated tissue signal removed. (C) Quantification of the images using contrast to tissue ratio (CTR) and contrast to acoustic noise ratio (CANR).

Figure 4-6 shows how the MB contrast can be captured without the saturation artifact *in vitro*. In the tissue ROI for the HDR image in Figure 4-6 some signal from the wire can still be observed. This is breakthrough due to non-linear propagation. It should be noted that this method can not correct for any unwanted non-linear behaviour.

4.5 Discussion

Artifacts due to saturation when performing non-linear pulse sequences can be distracting and lead to misinterpretation of clinical data. By combining ultrafast data received at high and low gains, the strong contrast signals possible at high gains can be visualised without the saturation of strong linear signals. The *in vitro* data

provided a example of removing the saturation from a strong linear scatterer. The simulation used realistic tissue properties and geometry to show how the method would be useful in a clinical environment.

Due to the transmit amplitudes of incident pulses being unchanged, the MB scattering properties should be unaffected. This makes this method more appropriate for imaging of non-linear contrast agents compared to the HDR method used by Degirmenci et al. (2018) and Xiao et al. (2018).

The primary limitation of this method is the reduction in frame rate required. That is, when receiving data at two gain settings the maximum possible framerate has halved. However, with the growing availability of ultrafast plane wave imaging, this increase in pulse sequence time is likely to be insignificant for most applications. Moreover synthetic aperture imaging, an established technique where subsets of transducer elements are used independently [232], could potentially be applied to this HDR technique to receive at different gains simultaneously.

This method is only necessary if sufficient contrast cannot be visualised without increasing the gain until saturation occurs. In practice, a test sequence over a possible range of receiver gain levels can be performed on the imaging target to determine where saturation occurs and whether gains above this threshold are necessary. An additional point to underline is that this method will also require calibration of the system if the relationship between gain settings is not already well characterised. One benefit of retaining these regions of saturation is that they can be used by clinicians as landmarks to navigate the anatomical structure within the field of view [225]. Thus, perhaps the saturated data and HDR non-linear data could be visualised side-by-side on a dual display to provide complementary information. Otherwise, this method can be easily implemented on existing clinical and research ultrasound systems.

It is important to note that this technique will only correct for artifacts due to saturation. Clutter in non-linear images caused by non-linear propagation or mismatch between the transmitted waves will remain.

This technique is sufficiently general to have potential for other modes of non-linear imaging. Changing the order of the pulses within the sequence is not foreseen

to have consequences on the final reconstructed data. Moreover, this work considered only when the maximum amplitude pulse was saturated and not the half amplitude pulse. It would be possible to use a higher gain and apply the HDR reconstruction to the half amplitude pulse too. Future work is required to investigate application to other multi-pulse techniques and second harmonic tissue imaging where saturation may also be problematic.

4.6 Conclusions

Overall, this work has shown how this novel HDR non-linear imaging method can provide superior CTR and CANR compared to imaging conventionally with a single gain level. This approach can be easily implemented on existing systems whilst minimising changes to non-linear behaviour of MBs as transmit pulse amplitudes are unchanged.

Chapter 5

Development of Microvascular Phantoms

5.1 Abstract

There is a need for microvascular phantoms across many scientific disciplines. This chapter draws on inspiration from other fields such as 3D printing and tissue engineering to investigate the feasibility of a range of microvascular phantom options for SRUS. Four potential SRUS phantoms; 3D printed channels, wire extrusion phantoms, sacrificial sugar structures and decellularised leaves are considered in this chapter.

The simplest option, wall-less 50 μm channels fabricated in low melt agar, were the most successful phantom trialled during this work. SR images of the tubing were generated alongside optical validation. The results from this chapter showed that the sacrificial sugar scaffolds could also be utilised as microvascular phantoms for SRUS. Channels with diameters < 50 μm were achieved. These structures also had the most tortuosity which may be useful for the application of SRUS to tumour vasculature. Three-dimensional printing of Agilus30 using polyjetting technology achieved channels with diameters 290-360 μm. Smaller channels < 200 μm were fabricated using Layfomm-40, however the channels printed using Layfomm were less able to accommodate flow compared to Agilus30. The results showed that Agilus30 had reasonable acoustic properties compared to soft tissue of 1425.1 ± 5.2 m/s and

1140 -1150 (kg/m^3 for sound speed and density respectively. The attenuation was significantly higher than ideal 21.9 ± 4.1 dB/(cmMHz). However, imaging of MB flow was still possible. Optical imaging of MBs flowing in the decellularised leaf phantoms did show that perfusion of a range of vessel diameters (as low as 20 μm) was possible. However, the protocol did not work well enough to allow all vessels to be perfused, and it was difficult to determine which vessels could accommodate flow. Therefore, the decellularised leaves were the least successful as SRUS phantoms.

In future work the ground truth available from these phantoms (particularly the wire extrusion and sugar scaffolds) could be used to test and compare the various acquisition and processing choices for SRUS.

5.2 Introduction

The key criteria for a realistic phantom for *in vitro* validation of SRUS are:

- microvascular structures,
- can accommodate flow,
- acoustically similar properties to soft tissue and,
- be able to withstand the probe pressure during imaging.

It would also be desirable for the vessels to:

- have a degree of complexity in the 3rd dimension,
- be resistant to any degradation over time (i.e., a new phantom not required for each experiment) and,
- be optically transparent.

This is a challenging set of requirements which has not previously been met for SR imaging phantoms.

5.2.1 *In vitro* vessel phantoms

Previous *in vitro* work demonstrating SRUS has used 200 μm ± 15 μm cellulose tubing with a wall thickness of 8 μm ±1 μm as *in vitro* vessel models, either as a single tube [115], two tubes positioned diagonally [145] or two tubes parallel to each other [115]. Cellulose is not the only available material for microtubing; Lin et al., (2017) used thin walled polycarbonate microtubing to test their SRUS method *in vitro* [196]. In the field of perfusion US imaging more generally, a variety of tube materials have been used. For example, Caskey et al., (2006) has used polymethacrylate (PMMA/acrylic) tubing to investigate how MBs behave in tubes similarly sized to capillaries [205]. These mimetric vessels are generally less compliant than real capillaries and, although available at small diameters, the PMMA tubing used in literature generally have unrealistically large wall thicknesses which may affect the received MB response. For example, the 12 μm inner diameter tubing used in Caskey et al. 2006 had an outer diameter of 50 μm. Related work has shown that proximity to the tube wall boundaries [77, 206], vessel size [205, 213], and compliance [148] all significantly affect the MB response.

The literature described above performed measurements on these tubes suspended in water. Another option is to fabricate them within larger block of material, ideally a material which has similar properties to biological soft tissue. Early work in SRUS by Desailly et al., (2013) printed channels were between 40-100 μm in width and 80 μm in polydimethylsiloxane (PDMS) using lithography [134]. However, PDMS has an unrealistically low sound speed and high attenuation to be appropriate as a tissue mimicking material (TMM) [233]. There is a wealth of literature on tissue mimicking materials. Culjat et al., (2010) provides a review of the materials conventionally used [1] and Browne et al., (2003) provides a comparison of material used commercially such as Zerdine, condensed milk-based gel and Urethane rubber [234]. For reference, Table 5.1 gives some typical tissue impedances and Table 5.2 details those currently achieved using phantom materials.

Table 5.1: Typical Acoustic Properties of Soft Tissue (adapted from Culjat et al., (2010)[1] with permission from Elsevier under the License no. 4687810135301.)

Material	Velocity (m/s)	Density (kg/m^3)	Attenuation (dB/cm MHz)	Acoustic Impedence (MRayl)	Source
Brain	1560	1040	0.6	1.62	ICRU 1998
Breast	1510	1020	0.75	1.54	ICRU 1998
Fat	1478	950	0.48	1.40	Mast 2000
Liver	1595	1060	0.5	1.69	ICRU 1998
Muscle	1547	1050	1.09	1.62	Mast 2000
Soft tissue (Average)	1561	1043	0.54	1.63	Mast 2000

Table 5.2: Acoustic Properties of Soft Tissue Mimics (adapted from Culjat et al., (2010) [1] with permission from Elsevier under the License no. 4687810135301.)

Material	Velocity (m/s)	Density (kg/m^3)	Attenuation (dB/cm MHz)	Impedence (MRayl)	Source
Agarose-based	1498–1600+	1016–1100	0.04–1.40	1.52–1.76+	Burlew et al. 1980; Madsen et al. 1998; D'souza et al. 2000; Ramnarine et al. 2000
Gelatin-based	1520–1650	1050	0.12–1.5	1.60–1.73	Madsen 1978; Bush and Hill 1983
Magnesium Silicate-based	1458–1520	–	0.85	–	Sheppard and Duck 1982
Oil Gel-based	1480–1580	1040–1060	0.4–1.8	1.54–1.67	Kondo, Kitatuji 2005
Open Cell Foam-based	1540	–	0.46 dB/cm MHz	–	Ophir 1981, Ophir 1984
Polyacrylimide Gel-based	1540	1103	0.7 dB/cm @ 5 MHz	1.7	Zell et al. 2007
Polyuerethane	1468	1130	0.13	1.66	Kondo, Kitatuji 2005
Polyvinyl Alcohol-based	1520–1610	–	0.07 – 0.35	1.60–1.77	Kharine, Manohar 2003
Tofu	1520	1059	0.75	1.61	Wojcik, Szabo 1999
Water–based	1518–1574	1000+	–	1.48–1.60	Giacomini 1947; Sonotech 2006
Condensed Milk-based	1540	–	0.5	–	Browne et al. 2003
Urethane Rubber	1460	900	0.5–0.7	1.31	Browne et al. 2003
Zerdine	1540	–	0.5–0.7	–	Browne et al. 2003

5.2.2 Validation using *in vivo* models

The lack of a realistic *in vitro* option makes it challenging to replace the use of *in vivo* models (in accordance with the 3R aims for animal protection [235]). Obtaining a ground truth from *in vivo* studies is not trivial. One option is preclinical micro-CT where the reported resolutions are around 4-10 μm [236]. However, increasing the time that the animal is under anaesthetic and moving the animal between modalities is practically difficult and may not be ethically possible for all studies. For some studies, performing the microCT *ex vivo* following the SRUS procedure could be an option. However, if imaging the exact same FOV with both modalities is important, this may still be a significant challenge. Another option to provide a ground truth is

ex vivo optical microscopy of a sample. However, this can still be subject to errors - the need to slice into thin samples can distort the vessel structures and it can be unfeasible to reconstruct a continuous 3D structure from finite slices [169]. A possible alternative for representing 3D structures is vasculature corrosion casting. Vasculature corrosion casting create a model of the vasculature *ex vivo* by infusing Mercox resin into the vasculature. The resin then polymerises and the surrounding tissue can be removed. Zhu et al., 2019 performed SRUS on rabbit lymph nodes and a corrosion cast of an example lymph node was imaged using microCT [120]. The size distribution of vessels within the corrosion cast was compared with that obtained using SRUS. A limitation of this work was that the same lymph node imaged with US was not used to provide a ground truth due to practical reasons. Moreover, other authors have cautioned that the resin may not necessarily perfuse all vessels and may not accurately represent the vessel diameters [237]. These *in vivo* challenges are common to several fields thus inspiration for the avenues in this chapter have been taken from a range of disciplines.

5.2.3 Commercially available phantoms

Commercial ultrasound phantoms for quality assurance can be purchased to test the performance of an imaging system or technique. The subset of these test objects of most relevance to this work are those assessing Doppler flow imaging and those assessing image resolution. The Doppler test phantoms generally consist of a series of channels embedded within a TMM, for example Urethane rubber [238, 239] with flow controlled using a pump. These phantoms are designed to test sensitivity to flow and the accuracy that flow velocity at varying flow positions and depths can be measured. However, they have not been designed with assessing microvascular flow in mind. Resolution phantoms typically use nylon pins/wires at varying axial and lateral separations to test spatial resolution at varying depth within a TMM [240]. Figure 5-1(A) provides an example of how these pins could be used to measure the axial cross section, where pins are only resolved if there is no overlap between the upper and lower boundaries of adjacent PSFs. An analogous method can be used

for lateral resolution. Alternatively, the PSF dimensions can be measured at isolated nylon pins throughout the FOV to allow system resolution to be characterised, as shown in Figure 5-1(B).

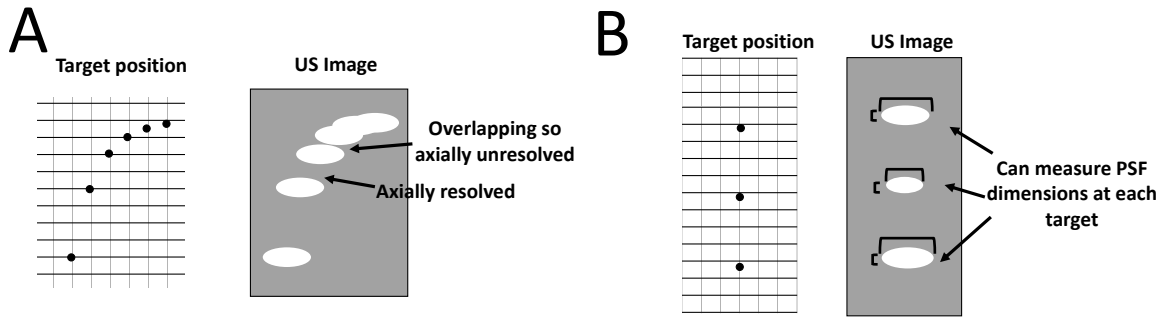

Figure 5-1: Example nylon pin resolution targets used in commercially available US phantoms. The resolution target arrangement shown in (A) can be used to quantify axial resolution by determining the minimum pin separation for which there is no axial overlap of adjacent PSFs. Alternatively the dimensions of the PSFs imaged at individual pins can be characterised (B).

No commercially available phantoms were found that could be useful for testing SRUS. Nonetheless, the approach used to quantify resolution and various materials used may be valuable to consider when designing super-resolution test objects. The following sections will outline the motivation for the four approaches considered in this work.

5.2.4 3D printed phantoms

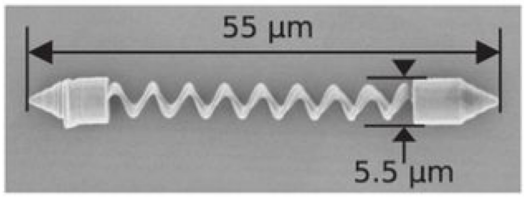

Figure 5-2: Helical microrobot printed using Nanoscribe. Adapted from (Barbot et al., 2016) [241]. This work is licensed under a Creative Commons Attribution 4.0 International License.

Three-dimensional printing is a natural consideration during the development of a three-dimensional phantom and printing at the microscale or nanoscale is now possible. For example, the Nanoscribe Professional GT is a laser lithography system which polymerises photosensitive resins through a two photon polymerisation process and has been applied to a number of applications [241, 242, 243]. One example of a microscale print is given in Figure 5-2. However, typically the thermosetting materials used are often brittle [244] and so unsuitable for US phantom material. The hardness of 3D printing flexible filaments is generally quantified in terms of Shore hardness.

$$E = \frac{1-\mu^2}{2 \cdot R \cdot C_3} \cdot \frac{C_1 + C_2 + Sh_{\mathrm{A}}}{100 - Sh_{\mathrm{A}}} \tag{5.1}$$

where E is the Young's modulus, Sh_{A} is the shore hardness, μ is Poisson's ratio, R is the width of the indenter used to make the measurement and C_1, C_2 and C_3 are constants.

Previous literature has also shown the possibility of 3D printing of the paraffin wax material discussed earlier in this section, however the gel nature limits the printing resolution [245]. The trade-off between printing resolution and flexibility is

problematic for several fields in bioengineering, thus there is a steady growth in the development of novel materials for 3D printing which may have the potential to address the need for softer materials with high resolutions [246]. Poro-Lay is a composite blend of a thermoplastic polymer and PVA. The stiff Polyvinyl acetate (PVA) makes the material easy to print, but the PVA can later dissolve in water leaving behind a microporous, flexible structure [247]. The softest material in the series is Lay-fomm 40 which has a Shore A of 40. Lay-fomm is printed using Fused Deposition Modelling (FDM). This involves the material in filament form being melted through a heated nozzle and deposited layer by layer to build up the 3D structure [248]. The nozzle is computer operated using computer aided design (CAD) drawing to determine the translation. Another particularly soft material, Agilus30, was assessed. Agilus30 is printed using Material Jetting, where droplets of photosensitive material is solidified using UV light and layered to form a 3D structure [244]. Agilus30 has been used previously by the co-developers of the material to print realistic vasculature phantoms for characterisation of blood pressure [249].

5.2.5 Wire extrusion phantoms

Maneas et al. (2018) fabricated realistic vessel phantoms made using moulding of paraffin gel wax based on a placenta model. Moulding a vessel phantom refers to setting two halves of the phantom separately and then sealing together. For this work, the authors primarily aimed to demonstrate that acoustically realistic phantoms could be fabricated using paraffin wax - as opposed specifically fabricating microvascular phantoms. Thus the smallest vessel fabricated was 2 mm in diameter [250]. It was hypothesised that fabricating micro-channels using moulding is challenging due to the need to seal two half channels together, so this was not tested during this chapter. An alternative approach to moulding is the extrusion of a tube from a tissue mimicking gel. Nikitichev et al., (2016) fabricated vessel phantoms instead by the removal of polytetrafluoroethylene tubes from set agar gel, the smallest tube diameter demonstrated was 4 mm [251]. A similar technique enabled the construction of flow phantoms of diameter 1 mm [252]. To our knowledge, the smallest micro vessel flow

phantoms using this extrusion technique have been fabricated by Grand-Perret et al., 2018 with straight channels between 147-436 μm made within a silicone based material [253]. However, previous work focusing on therapeutic ultrasound have shown that smaller channels are possible. By withdrawing 10 μm Tungsten wire from acrylamide gel a microvascular phantom was used to study how MB oscillation under incident US could affect the vessel wall [254].

5.2.6 Sacrificial phantoms

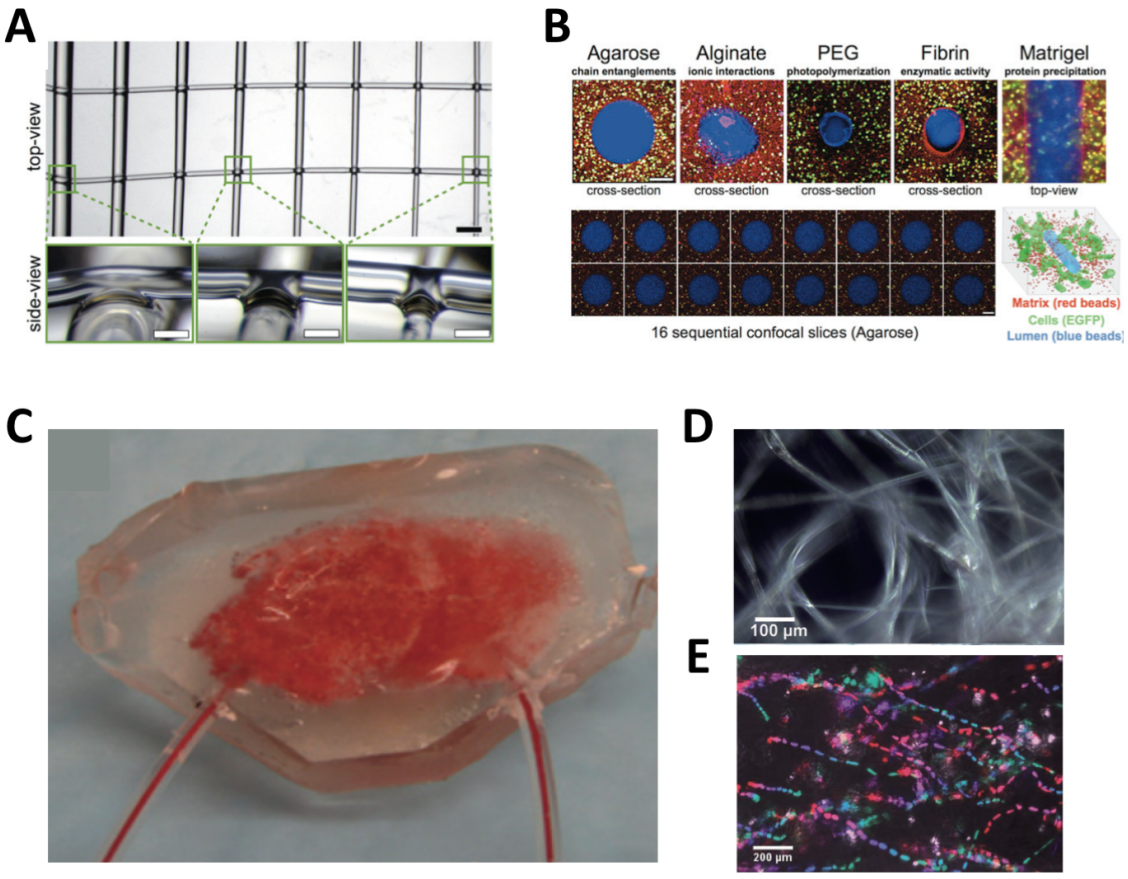

Figure 5-3: Example of using sugar for sacrificial structures. (A) The top view shows 3D printed scaffolds with channels ranging in diameter from 150 µm - 750 µm (scale bar = 1 mm). The side view shows the junctions magnified (scale bar = 200 µm). (B) shows the channels embedded in various medium and seeded with cells (scale bars = 200 µm). Blue beads are used to highlight the lumen for easier visualisation. The images, (A) and (B), were replicated from Miller et al., (2012) [255] with permission from Springer Nature under license no. 4687800084760. (C) shows the channels left when sugar structures made in a modified cotton candy machine are embedded in PDMS before being dissolved. An example of the micron structures are shown in (D) using dark field microscopy. (E) shows the tracking of fluorescent particles to demonstrate flow. The images, (C-E), were replicated from Bellan et al., (2009) [256] with permission from ROYAL SOCIETY OF CHEMISTRY under license no. 4687801283875.

Another option is the possibility of developing sacrificial structures which can be made using a dissolvable material. A tissue mimicking material can then be set around this

structure before it is later dissolved to leave behind channels. One particularly novel material is carbohydrate glass [255], shown in Figure 5-3(A-B). Miller et al., (2012) demonstrated 3D printing of this sacrificial vasculature architecture for 3D tissue culture. The authors developed a recipe of combining easily accessible carbohydrates which can be vitrified to give structures which are both mechanically stiff and easily dissolved. A custom-made printer then printed perfusable channels of diameters down to 150 μm. Earlier work demonstrated the same idea to fabricate less ordered structures. Bellan et al., (2009) used modified cotton candy machine to fabricate spun sugar fibre networks, as shown in Figure 5-3(C-E) [256]. Polydimethylsiloxane (PDMS) was then set around these structures and the sugar later dissolved to leave channels with diameters reported on the order of 1-100 μm. Flow was introduced by welding the cotton candy to sugar sticks with diameters on the order of 1 mm. Although few details are provided, the authors suggested that materials more appropriate to biomedical applications than PDMS could be used to surround the sugar. Using sugar spinning techniques rather than 3D printing will be used for this work to first check the viability of fabricating a microvascular phantom using sacrificial sugar structures before investing in purchasing and modifying a 3D printer. Ordered structures are not necessary for a SRUS phantom as long as the channel structures can be characterised to provide a ground truth. Imaging of sacrificial sugar phantoms is not an option which has been previously pursued for US imaging.

5.2.7 Decellularising tissue

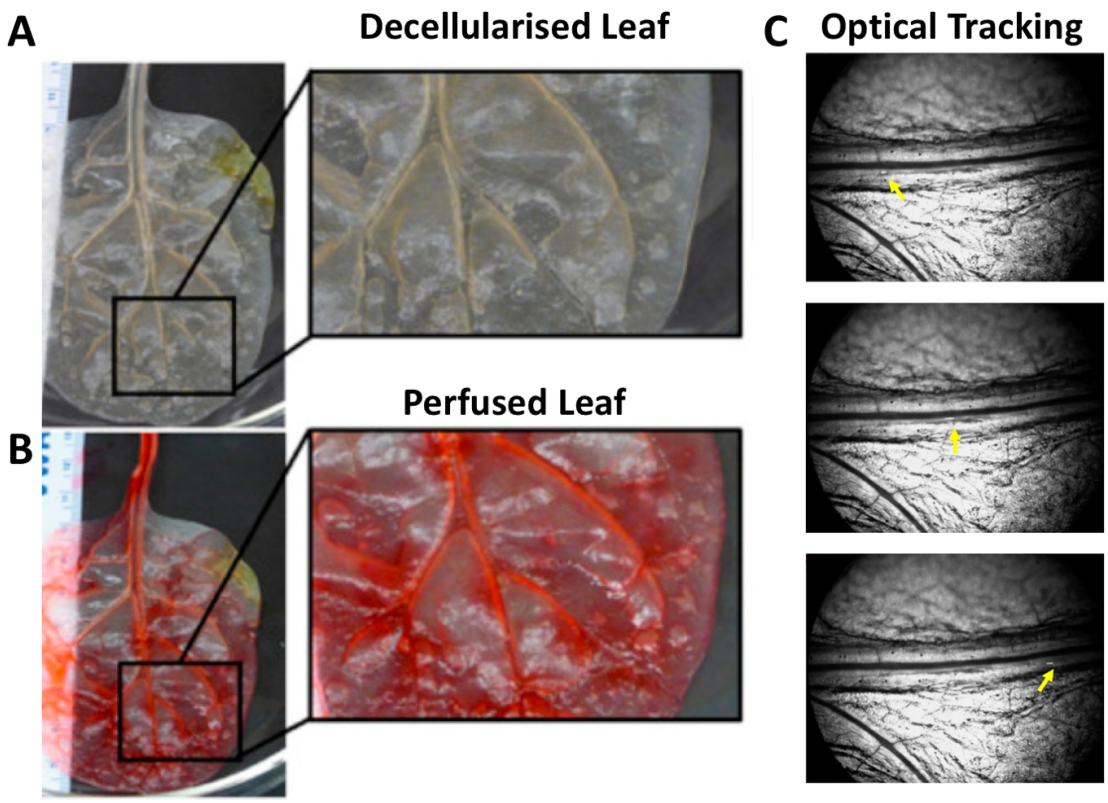

Figure 5-4: Perfusion of decellularised leaf scaffold. (A) shows a decellularised leaf sample (top) which could be perfused using red dye (bottom). (B) shows how microspheres could be tracked along vessels, where the yellow arrow highlights the microsphere. These images were adapted with permission from Gershlak et al., (2017) [257] under the Creative Commons Attribution-NonCommercial-No Derivatives License (CC BY NC ND).

Authors in the field of tissue engineering have considered decellularising plant material to use as a tissue scaffold [257]. Decellularisation is the process of removing cellular material whilst leaving behind the tissue structures such as the extracellular matrix and vasculature. Gershlak et al., (2017) decellularised plant material with the aim of engineering an immunogenic scaffold with a viable vasculature. These scaffolds could then potentially be recellularised with a patient's own cells for organ transplantation applications. SRUS phantoms do not need to satisfy the immunogenic requirements of this literature, however the mechanical changes to the leaf are

of interest. Following decellularisation the leaf becomes more pliable and flow can be easily pumped through the existing vasculature structure. This was demonstrated by perfusing red dye through the decellularised leaves as shown in Figure 5-4(A-B). Gershlak et al., (2017) demonstrated how individual 50 μm microspheres could be optically tracked flowing through the vasculature channels - not unlike how MBs are tracked during SRUS. An example of one such particle being tracked along the petiole is provided in Figure 5-4(C). There are a number of physical, chemical and enzymatic methods for achieving decellularisation and commonly a protocol will use a combination of these [258]. Gershlak et al., (2017) use a mainly chemical approach where ionic and non-ionic detergents are perfused using a gravity flow. The ionic detergents sodium dodecyl sulfate (SDS) was used to break up cellular membranes and denature proteins. The non-ionic solvent Triton X-100 was then used to disrupt lipid-lipid and lipid-protein interaction [258]. Although this is a relatively lengthy procedure, with at least 9 days of perfusion, this phantom has the potential to generate the most realistic vasculature structure compared to the other options considered in this chapter. This is also not an option which has been previously pursued for US imaging.

5.2.8 Chapter outline

This chapter builds on these ideas in the literature to investigate four potential SRUS microvascular phantoms.

1. Firstly, the suitability of novel 3D printing materials, particularly Layfomm-40 and Agilus30, will be assessed using a custom designed resolution test object.

2. Secondly, the withdrawal of wires from TMMs to fabricate flow channels with smaller dimensions (three-fold smaller) than previously reported will be demonstrated and imaged with SRUS.

3. Thirdly, sacrificial structures made from carbohydrate glass using conventional sugar spinning techniques, instead of a 3D printing, will be explored to assess the feasibility of fabricating 3D structures on a microscale.

4. Finally, the protocol for decellularisation of spinach leaves will then be performed and the resulting structure tested for SRUS imaging.

Previous SRUS literature has generally used vessel phantoms on the scale of 200 μm [115]. Smaller polycarbonate tubing (50 μm in diameter) have been used [121], but it is unclear how acoustically transparent these are. Likewise, vessels on the scale of 100 μm have been printed using non tissue mimicking material [134]. Moreover, until now, SRUS images been of simple linear structures which are not representative of tortuous 3D vasculature. The development of realistic microvascular phantoms is important for the refinement of SRUS, and would also have implications more generally in the field of US perfusion imaging. This chapter is structured such that the methods and results of each phantom are presented together, before a single discussion comparing the potential SR phantoms.

5.3 3D printing

This section investigates the feasibility of using 3D printing for microvascular US phantoms. A resolution phantom was designed and used to test the smallest possible channel dimension which could be 3D printed for various materials. Two promising material Layfomm-40 and Agilus30 were acoustically characterised, and tested for the feasibility of establishing MB flow in channels.

There are several other researchers who should be acknowledged for their contribution to this section.

Three GCSE students; Sabah Ally, Nimah Ashraf and Senthooran Ramesh visited our lab once a week for 10 weeks as part of a school outreach programme. They contributed by helping with designing the resolution phantom and researching potentially useful materials. They also learned how to use TinkerCad and built the 3D computer aided design of the phantom.

This section hugely benefitted from the help of fellow PhD student S. Wang. She approached me for help in acoustically characterising novel materials she had identified as useful for a multi-modal (including US) imaging phantom. She then offered

access to her lab's 3D printers and organised a print of the Agilus30 phantom with her collaborators. Her interest in helping with the challenging task of identifying materials which were both flexible and could be printed at high resolution was invaluable.

5.3.1 Methods

Resolution Phantom

The resolution phantom shown in Figure 5-5 was designed using TinkerCad. This had 100% infill and hollow channels ranging in diameter from 2mm to 0.01mm (2 mm, 1.5 mm, 1 mm, 0.8 mm, 0.6 mm, 0.4 mm, 0.2 mm, 0.1 mm, 0.05 mm, 0.01 mm).

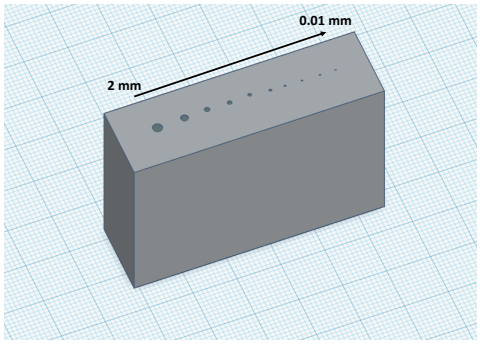

Figure 5-5: Resolution phantom in TinkerCad software.

Preliminary 3D printing investigations:

Early in the research process Formlabs Flexible Resin was selected as a potential candidate (Shore A 80-90) to test the efficacy of stereolithography (SLA) printing. Using the Form 2 printer the resolution phantom in Figure 5-5 was printed. This printer can achieve a layer resolution of 25 microns and has a laser spot size (FWHM) of 140 microns. Both orientations of printing channels were trialled (either parallel or perpendicular to the channels). A commonly used flexible FDM material NinjaFlex (NinjaTek) was also trialled (Shore A 85) using a BQ Wiltbox 2 printer. However, for both the materials, only channels diameters of approximately 1 mm were successfully printed. There were two main challenges with this work. Without access to

a dedicated printer there was limited possibility to make multiple iterations whilst adjusting printing speed/temperature/nozzle speed. Thus it was challenging to rule out commercial materials. Secondly, from discussions with the 3D printer technicians it became evident that there was an empirically observed trade-off between resolution and hardness. This makes it challenging to print a material for high resolution ultrasound phantoms. To tackle this challenge collaboration was established with S. Wang.

Identification and printing of novel materials

The Poro-Lay series had been identified as a potential TMM in previous work (Wang et al., (In Review)). For this work, the Lay-fomm 40 material, which has a Shore A of 40 was trialled. Poro-Lay is a composite blend of a thermoplastic polymer and PVA. The stiff PVA makes the material easy to print, but the PVA can later dissolve in water leaving behind a microporous, flexible structure. Due to access to an onsite printer (DeltaWASP Turbo 2040 printer (WASP, Italy)), this collaboration allowed us more opportunity to iterate through various printing parameters to more fully assess the possible printing resolution. To print the phantoms, the speed was set to 40 mm/s and temperature was set to 230 ^{o}C. No support media was required. The layer height resolution was set to be 100 µm. This the approximate height of each layer. The phantom was then immersed in ultrapure water for 48 hours.

Agilus30^{TM} was the softest of those trialled, with a shore hardness of 30-40 scale A. This material can be printed using material Jetting, where droplets of photosensitive material is solidified using UV light and layered to form a 3D structure [244]. The resolution of this printer is dependent on the laser spot size. This material has been used previously by the co-developers of the material to print realistic vasculature phantoms for characterisation of blood pressure [249].

Characterisation of acoustic properties:

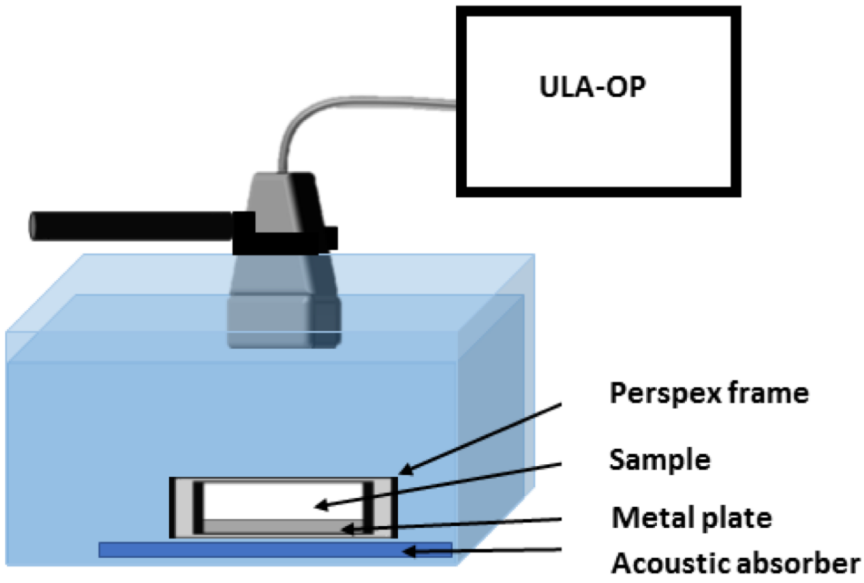

Figure 5-6: Experimental set-up for measuring acoustic properties.

Attenuation, speed of sound and density were determined for both materials using the set-up shown in Figure 5-14. The pulse echo method was used to determine the acoustic sound speed and attenuation [234]. An aluminium plate was chosen to generate strong reflections and a uniform slab of each sample material held adjacent to the plate using a simple Perspex holder (if necessary). The data was collected using a LA332 probe (Esaote, Genoa, Italy) operating at 3 MHz and ULA-OP system (Univ. degli Studi di Firenze, Florence, Italy)[192] and analysed using MATLAB. The velocity and attenuation values were the mean values from 100 replications over the 64 elements.

The acoustic velocity can be calculated from equation 5.3.1, where c_s is acoustic velocity in sample, c_w is acoustic velocity of water which is 1486 m/s, d is the sample thickness measured using a calliper, ΔT is the time shift upon displacement of water with the sample in place.

$$\frac{1}{c_s} = \frac{1}{c_w} - \frac{\Delta T}{2d}$$

(5.2)

The attenuation calculation is from the log difference between the acquired two spectra, where α is the attenuation coefficient, $A(x, f)$ is the magnitude of the spectrum with the sample in place and $A_0(x, f)$ is the magnitude of the spectrum with no sample in place:

$$\alpha = -\frac{20}{2d}\log_{10}\frac{A(x, f)}{A_0(x, f)}[\text{dB/cm}] \tag{5.3}$$

The x dependence refers to the calculation being made including all 64 elements, and the frequency (f) range included was 2 MHz - 4 MHz.

It should be noted that the same set-up was used to determine the acoustic properties of the low melt agar (2%) phantom used in other areas of this chapter.

5.3.2 Results

Layfomm-40 optical characterisation

Figure 5-7 shows the result of printing the resolution phantom using Layfomm-40. Poor layer adhesion meant individual polymer strands could be identified (A) and that the material was liable to separate along the layers as shown in (B) after soaking. As shown by Figure 5-7(C), the material was easily deformable by hand. Comparing (D) and (E) is evident that swelling of the material after soaking helped to make the phantom more uniform. Based on the optical observations, the smallest hole printed was the fifth largest channel (designed to be 600 μm in diameter). After soaking this hole had a diameter ranging between 0.11-0.2 mm. This range comes from the maximum and minimum diameters measured for each hole since the channels did not print uniformly. Sacrificing of the phantom, after all experiments had been completed, confirmed that the presence of these 5 channels was consistent throughout the phantom extent.

A

B

C

D

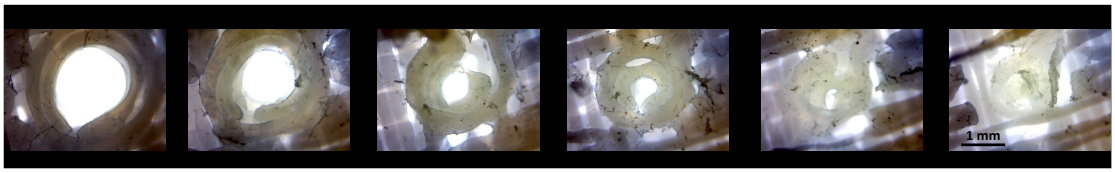

E

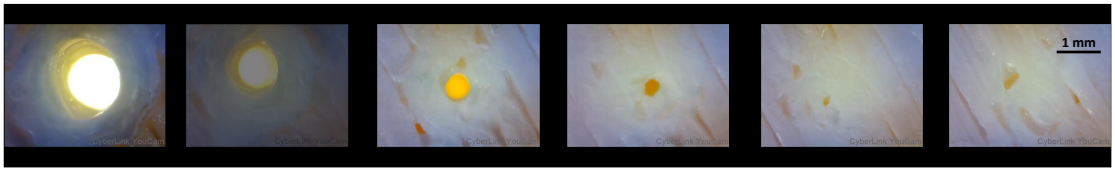

F

Optical measurements of hole diameters

Designed Diameter (mm)	2	1.5	1	0.8	0.6	0.4
Unsoaked Diameter (mm)	1.70-2.00	1.28-1.52	0.62-0.76	0.53-0.64	0.23-0.43	NA
Soaked Diameter (mm)	1.61-1.89	1.18-1.35	0.48-0.65	0.27-0.40	0.11-0.20	NA

Figure 5-7: Optical characterisation of Lay-fomm 40 phantom. (A) shows the resolution phantom immediately after printing. After soaking the phantom is liable to breakages along the layers (B) but gentle pressure by hand confirms that the material is easily deformable (C). Optical images of the channels before (D) and after (E) soaking are shown and the range of channel diameters reported (F).

Layfomm-40 US characterisation

Figure 5-8 shows US imaging of the Layfomm-40 phantom. Using US only the largest three channels could be identified, as shown in (A). In (B) the probe is orientated so that the channel is parallel to the lateral direction to show how MB flow could be established alone a channel. The sum of 129 difference images for the largest channel are shown in part (B). The green arrows indicate where MB flow is leaving the channel through the gap between layers. As shown in (C), there is a relatively high background signal which means that the introduction of MBs do not significantly increase signal without the use of a contrast mode.

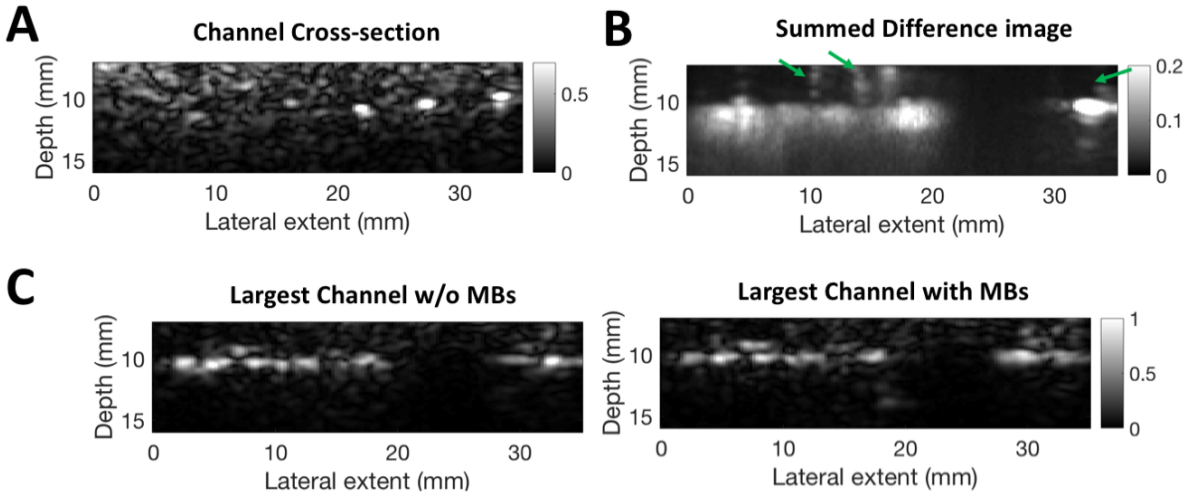

Figure 5-8: Acoustic imaging of Lay-fomm 40 phantom. (A) shows the optical cross-section of the phantom with air only in the channels after soaking. The sum of 129 difference images is provided in (B) of a high concentration of MBs flowing through the largest channel. The green arrows indicate MB flow flowing between layers. (C) shows the acoustic image of the largest channel without MBs (left) and with flowing MBs (right)

Agilus30 optical characterisation

Figure 5-9 shows the result of printing the resolution phantom using Agilus30. The material has a reported value of 220-270% for elongation at break and (B) shows that the phantom is easily deformable by hand. The largest 6 channels could be printed

with less variation between the maximum and minimum diameter for each channel (56 µm on average) compared to Layfomm-40. Based on the optical observations, the smallest hole printed was the sixth largest channel (designed to be 400 µm in diameter). In practice, this channel has a diameter between 290 - 360 µm.

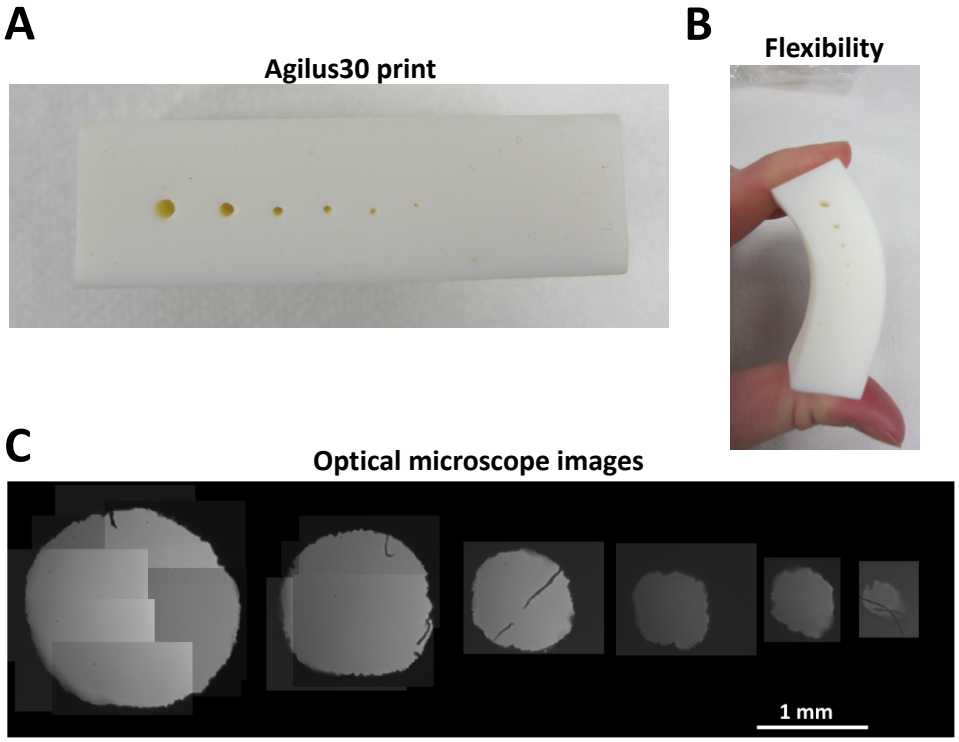

Designed Diameter (mm)	2	1.5	1	0.8	0.6	0.4
Diameter (mm)	1.79-1.82	1.29-1.35	0.91-0.96	0.61-0.69	0.55-0.62	0.29-0.36

Figure 5-9: Optical imaging of Agilus30 phantom. (A) shows the resolution phantom immediately after printing. Again the phantom is easily deformable as shown in (B). Optical images of the channels before and quantification of each diameter is provided in (C) and (D) respectively.

Agilus30 US characterisation

Figure 5-10 shows US imaging of the Agilus30. (A) shows the cross section of the largest 6 channels. When imaging parallel to the channel (B) shows that the seventh channel could just be visualised, although this could not be measured optically. MB flow was established in the sixth largest channel as shown in (C).

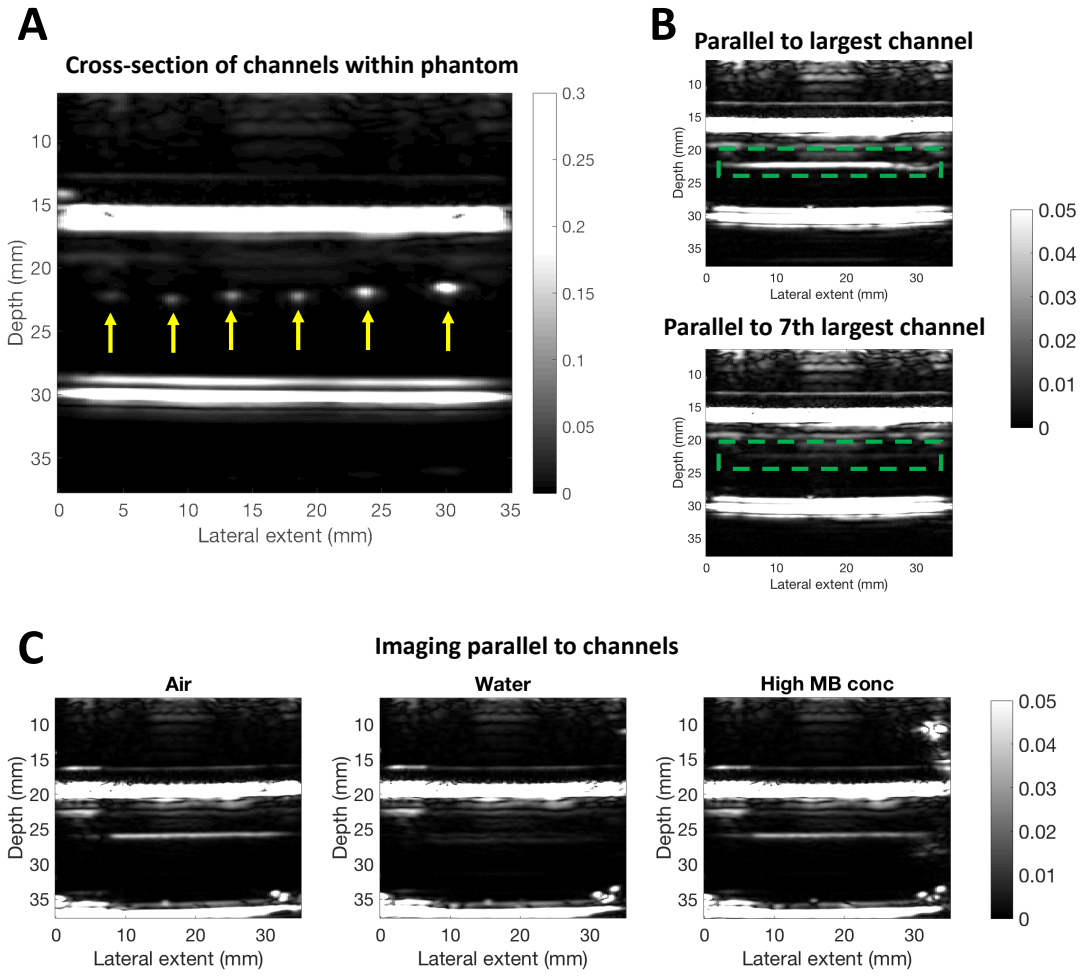

Figure 5-10: Acoustic imaging of Agilus30 phantom. (A) shows the optical cross-section of the phantom with air only in the channels, where the yellow arrows are used to highlight the channel signal. (B) shows the lateral image of the largest channel (top) and seventh largest channel (bottom), where the green box indicates the channel position. (C) shows the sixth largest channel with air (left), water (centre) and MB flow (right).

Acoustic properties

Table 5.3 shows the acoustic properties of Layfomm-40 and Agilus30.

	Agilus30	**Layfomm-40**
Speed of sound (m/s)	1425.1 ± 5.2	1628.9 ± 6.9
Attenuation (dB/(cm MHz))	21.9 ± 4.1	17.6 ± 1.6
Density (kg/m^3)	1140 -1150*	989 -1271

Table 5.3: Acoustic Properties of 3D printed materials. * indicates a literature value.

5.4 Wire extrusion phantoms

This section details the fabrication of channels within an optically transparent agar block by the extrusion of 50 μm wires. The SRUS image processing protocol, i.e. the method of identification of isolated MB signals, will be described here and used throughout this chapter. For full disclosure of other group members' contributions, the SRUS image processing code was based on that written by Dr Kirsten Christensen Jeffries and Dr Sevan Harput.

5.4.1 Methods

For the first iteration of this phantom, branching wall-less phantoms were made within silicon baking moulds as shown in Figure 5-11 (A -B). Windows were cut out of the silicon mould to accommodate an acoustic window and integration of a light source. A 25G butterfly needle (Terumo) was supported in the mould and threaded with three or four lengths of 50 μm co-polymer mono hooklength line (Preston Innovations). The lengths of the line were secured together in a fan shape, so that the wires are held together to form a single channel at the needle tip and gradually spread to form 50 μm channels.

3D printed holder

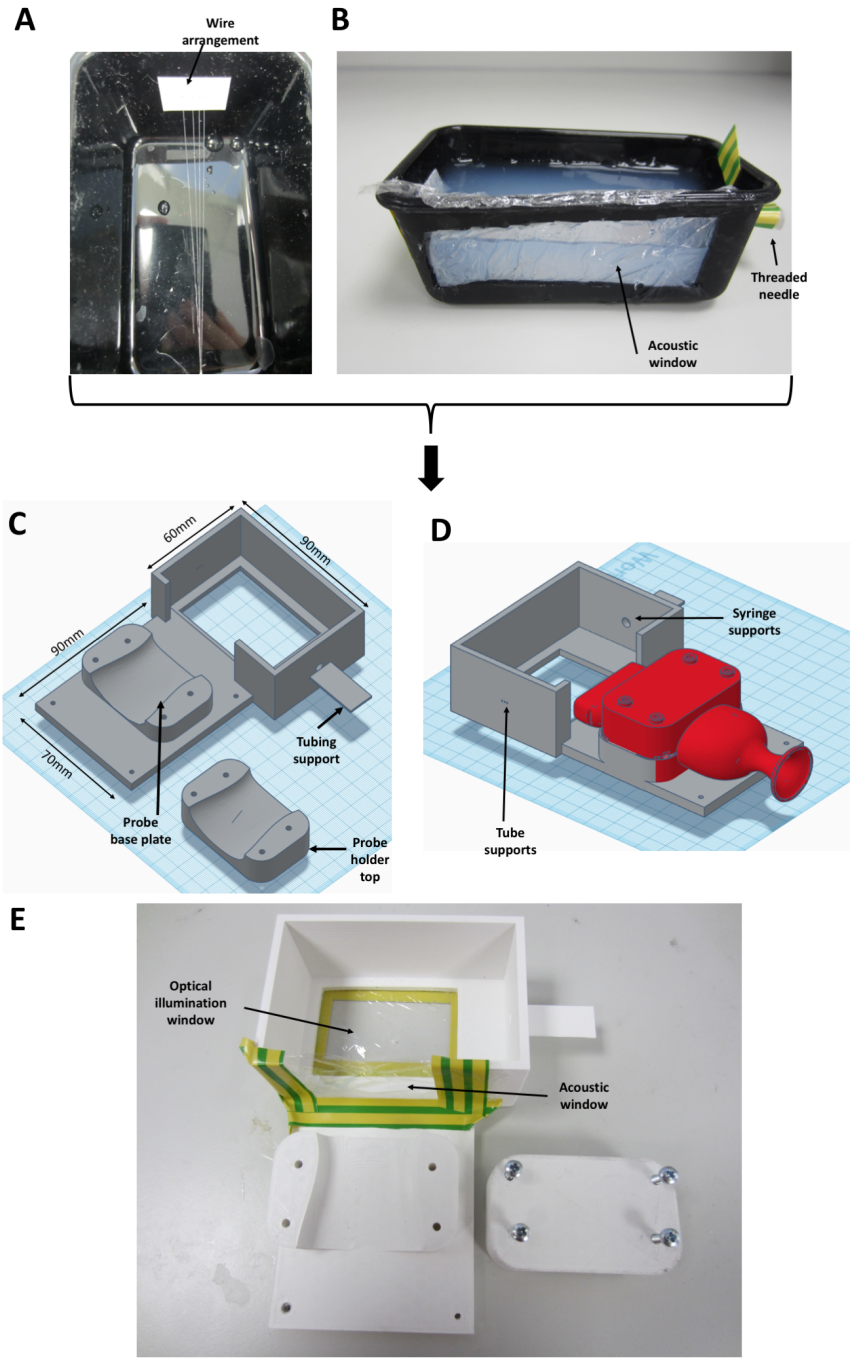

Figure 5-11: Tube extrusion experimental set-up. (A) shows the fan shaped wire arrangement, and (B) shows the position of the acoustic window relative to the needle connection. (C) show the different parts designed on TinkerCad software and (D) how the probe was secured in the holder. (E) shows the finished printed product.

To ensure a constant probe position and enable easier alignment with the channels, a custom probe holder was designed using TinkerCad as shown in Figure 5-11 (C -D). The holder was designed to hold a rectangular cuboid of gel, with a window on one side and the base for the acoustic probe coupling and optical light source respectively. A channel of diameter 5 mm to hold the needle was aligned with three smaller channels with diameters 0.8 mm to hold the polymer line in a fan shape. Beneath the channel for the needle was a small plate to support any tubing and associated connections. The centre line of the probe was aligned parallel to the channels using the base plate of a custom-made probe holder. The holder was printed using standard polylactic acid filament (PLA) and the finished product is shown in Figure 5-11 (E).

Low-melt agar

A 2 % (w/vol) solutions of low melt agar gel was made by measuring 2 g of low melt agar (Fisher Scientific, New Hampshire, United States) and adding to 100 ml of ultrapure water. The agar was melted in a microwave at high power. The solution was brought to the boil and allowed to boil for approximately 1 minute or until the particles were visibly dissolved. The flask was gently swirled to mix and allowed to cool to < 45 ^{o}C before use.

Phantom construction

Three lengths of 50 µm co-polymer mono hooklength line (Preston Innovations, Telford, UK) were threaded through a 25G needle (Terumo Corporation, Tokyo, Japan) glued into the holder. Each line was then threaded through a hole in the holder wall. Standard Clingfilm was attached over the open windows to contain the unset gel. The low melt agar solution was then set around the wires. The gel set within an hour, however, empirically it was found that the gel was more durable to handling and probe pressure after at least 3 hours in the refrigerator. Air bubbles in the mixture rose to the surface during the cooling and could be removed by slicing the top layer after setting. When set, the wire could then be extruded from the gel leaving behind wall-less channels.

Ultrasound imaging protocol

B-mode IQ data of 144 lines was acquired using the ULA-OP system (MSD Lab, University of Florence, Italy) and LA332 probe (Esaote, Genoa, Italy) operating at 3 MHz centre frequency. This was done at an amplitude setting of 0.1 on the ULA-OP. This amplitude setting, when measured using a 0.2 mm hydrophone needle (Precision Acoustics, Dorchester, UK) at 30 mm depth in ultrapure water, corresponded to a PNP of approximately -0.09 MPa. The PRF was set to 1000 Hz. The B-mode data was interleaved with RF plane wave acquisition using the contrast sequence [A, -A, A/2]. This was also done using a centre frequency of 3 MHz. A higher amplitude setting of 0.8 on the ULA-OP was used for better SNR, which corresponded to a PNP of approximately -0.22 MPa. A dilute MB solution using 0.3 ml of Sonovue^{TM} (Bracco Imaging SpA, Milan, Italy) MBs mixed in 600 ml of ultrapure water using a magnetic stirrer was injected at 200 µl/min, using a syringe pump (SP210 IWZ syringe pump, World Precision Instruments, Stevenage, UK). Due to rupture of the agar gel around the needle, some solution escaped without passing through the channels, thus the actual flow rate within the tubes was less than 200 µl/min. The targets were most easily imaged when the holder was turned on its side and the flow ran parallel with gravity.

Motion correction

The imaging set-up was largely without motion. However, compression was periodically applied to the set agar to stimulate stalled flow and it was possible that this could result in some shift of the channels. A rigid, sub-pixel, motion correction algorithm "Efficient_subpixel_registration()" was used. This code uses cross-correlation on upsampled data, where selective upsampling is achieved using a multiplication of a discrete Fourier transform matrix about the neighbourhood of the cross-correlation peak. More details can be found in [259] where the algorithm is referred to as the single-step DFT algorithm. The overall motion correction algorithm is shown in Figure 5-12. Initially high concentration frames were rejected by determining the mean

value of the frame and empirically setting a threshold corresponding to too high a concentration for detection of isolated MBs. A region of interest was chosen around one of the channels to use as an input to the image registration algorithm. When the local mean value of that region of interest suggested there was a MB in the ROI, the frame was rejected so as not to affect the motion correction. Finally, any frames with significant movement (corresponding to the compression of the agar) were rejected, due to this movement likely being highly non-rigid and so not possible to correct using this algorithm. Finally, the remaining frames were corrected for motion using the output of the registration algorithm.

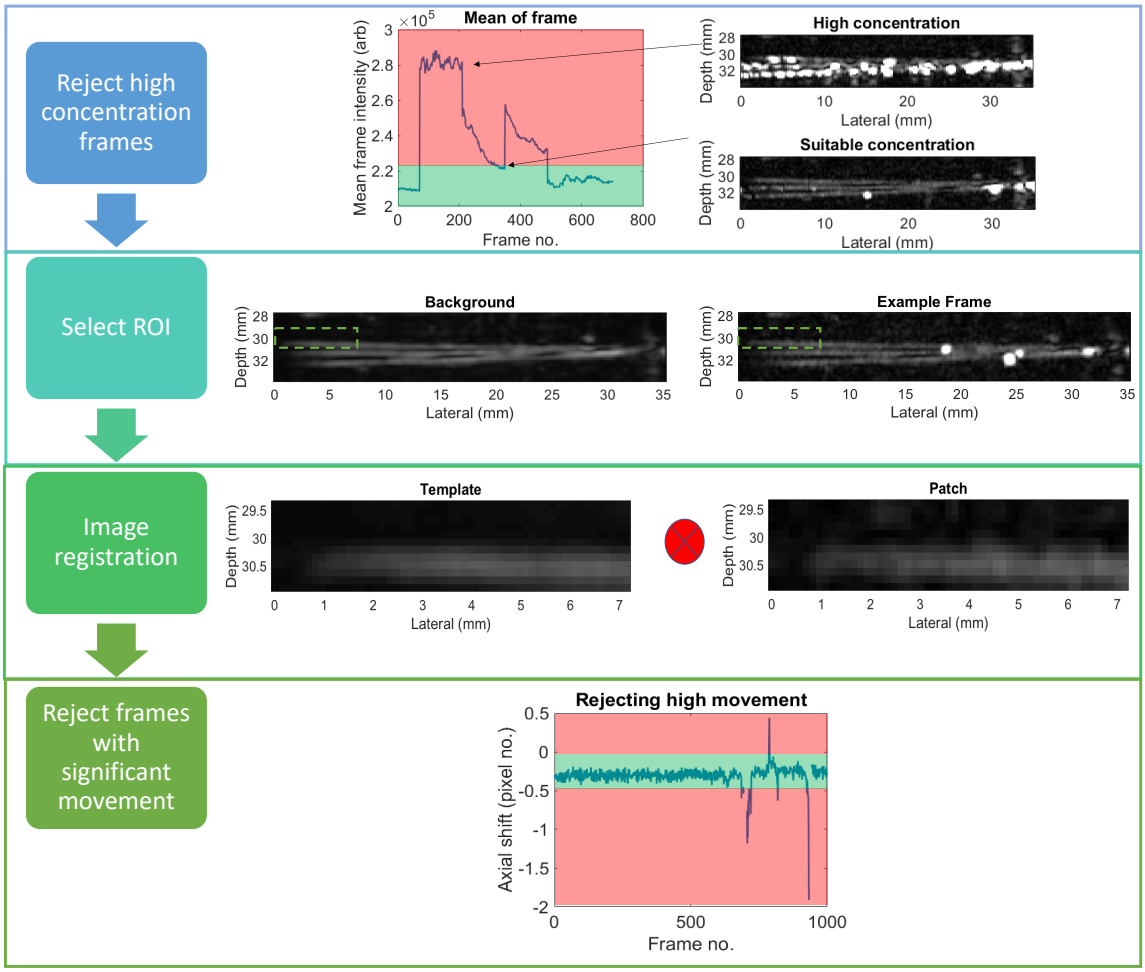

Figure 5-12: Motion correction protocol.

Data processing

After the motion correction procedure, the data was processed to generate a SR image. For this dataset, the pixels were interpolated to square pixels of dimensions $\lambda/4$. Background subtraction was achieved using a rolling background subtraction of 60 frames either side of each frame. MB properties were determined by manual classification of the potential MB regions detected in a random selection of 200 intensity thresholded frames. The intensity threshold was set to be three standard deviations over the mean of all frames. The regions were classified into either isolated MBs, multiple MBs or false detections. Due to the relatively low number of multiple MB detection, a further random set of 200 frames was used to collect the characteristics of only multiply MBs. Histograms corresponding to signal area, power, major axis length and eccentricity were generated and thresholds to characterise the signals determined.

Estimating localisation precision

A 200 μm copper wire was embedded in the low melt agar solution perpendicular to the transducer and at the imaging focus. The cross-section of the wire was estimated to approximate a point scatterer. 500 frames of BMode IQ data were collected and the same pixel interpolation and intensity thresholding applied as to the MB data. Localisation was repeated 500 times and the standard deviation of the axial and lateral positions reported as the SR precisions.

Optical imaging protocol

Following the acoustic acquisition, ground truth images of the underlying structure were acquired optically. The channels were examined under x10, x20 and x40 magnification using a table-top microscope (Apex Practitioner Digital, Apex Microscopes, UK). Food dye injected into the syringe to provide more optical contrast. In early tests, to ensure that MB flow could be established, a concentrated solution of MBs was also injected and imaged.

5.4.2 Results

Sizing of hollow channels

Using the initial phantom set-up of the silicon mould, the channel diameters were measured following wire removal. The red colour of the tubes, corresponding to the injected food dye, and the presence of MBs in Figure 5-13 (B) show that the channels could accommodate flow. The measured portion of the right hand tube, highlighted with the red bar, was determined to be 51.6 μm ± 1.5 μm. And the extent of two tubes (blue bar) were within 123.0 μm ± 1.2 μm.

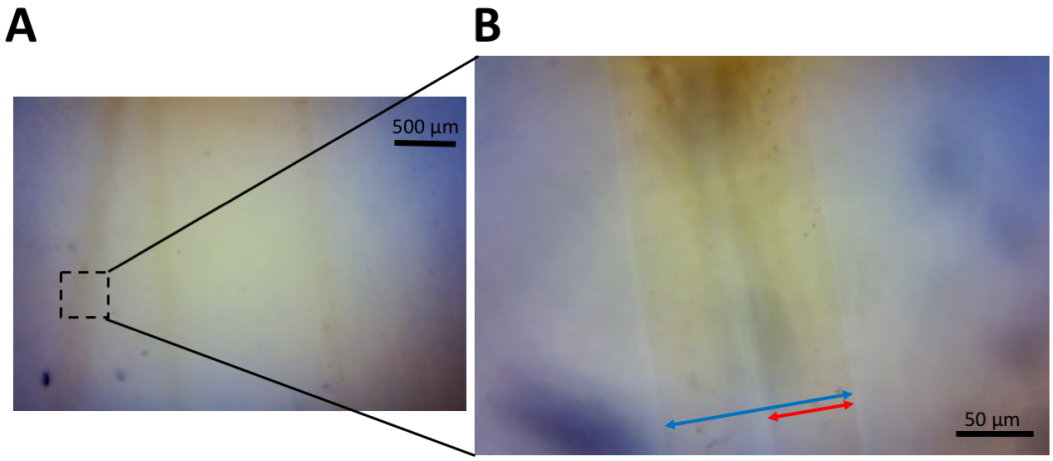

Figure 5-13: Optical measurements of agar tubing. Optical images at a magnification x4 (A) and at magnification x40 (B) The red bar shows the position where the tube width was measured, and the blue bar shows where the extent of two tubes was measured.

Estimating US imaging precision

An example of the point target localisation is shown in Figure 5-14. The lateral precision was determined to be 8.9 μm and the axial precision was 2.7 μm. Figure 5-14 and more specifically the clusters of points will be explained further in the discussion subsection 5.7.2.

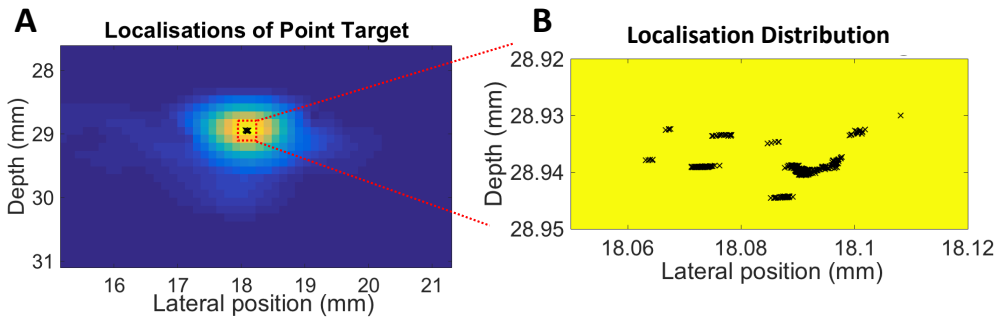

Figure 5-14: Localisation precision. (A) shows the point target localisation and (B) shows the localisations over 500 repeats.

Isolated MB properties

In total, 214 single MBs, 19 multiple MBs and 149 false signals were detected. False signals refer to those which may be mistaken for isolated MBs but are manually classified as being noise or artefacts due to reflection from a region of stronger signal. The characteristics of each classification were compared using the histograms shown in Figure 5-15. It should be noted that these classifications are manually predicted by the user based on how signals present over time. The green regions represent the properties associated with isolated MBs and the red regions represent the characteristics which lead to the region localisation not being included in the final SR image.

Table 5.4 shows the appropriateness of the thresholds in terms of false positives (FP), true positives (TP), false negatives (FN) and true negatives (TN). Sensitivity, provided in Equation 5.4 for reference, was chosen as a metric to quantify how well the threshold choices use the potential of the data to provide a high SNR. Sensitivity for this data was 69.2%.

$$\text{Sensitivity} = \frac{\text{TP}}{(\text{TP} + \text{FN})} \tag{5.4}$$

Table 5.4: Description of localisations determined as individual MBs following filtering in terms of false positives (FP), true positives (TP), false negatives (FN) and true negatives (TN).

	Predicted: NO LOCALISATION	**Predicted: LOCALISATION**	
Actual: NO LOCALISATION	**TN = 133**	**FP = 34**	**167**
Actual: LOCALISATION	**FN = 66**	**TP = 148**	**214**
	199	**182**	

False positives are likely to blur the image. There were 34 false positives recorded which corresponds to a false discovery rate (or 1-Precision) of 18.7%. Equation 5.5 provides the false discover rate.

$$\text{False Discovery Rate} = \frac{\text{FP}}{(\text{TP} + \text{FP})} \tag{5.5}$$

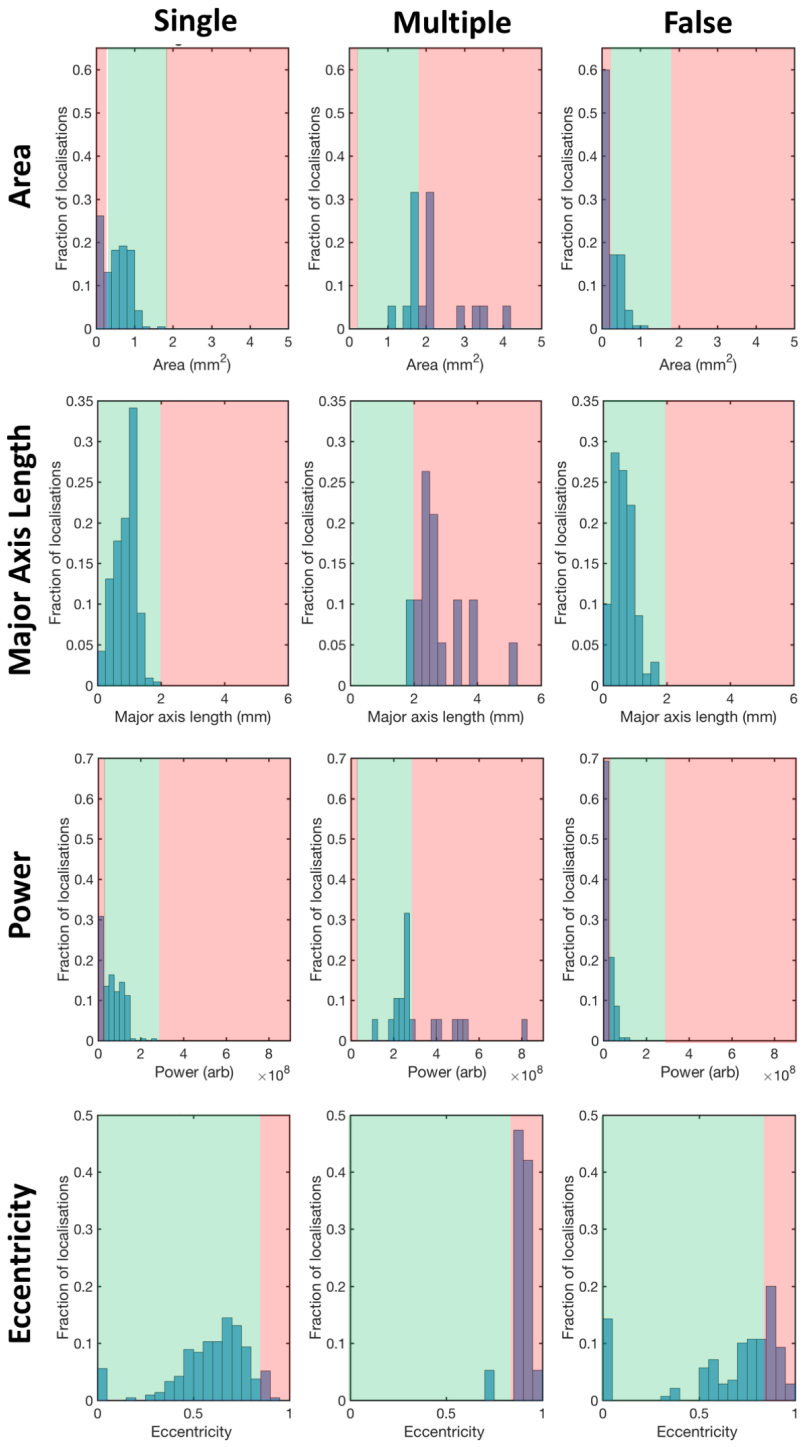

Figure 5-15: Single MB properties. Histograms showing the distribution of signal area, power, major axis length and eccentricity for isolated MBs, mutiple MBs and erroneous/false localisations. The red regions contain values which cause a MB to be rejected and the green regions contain those values considered consistent with single MB properties.

SR imaging protocol

Figure 5-16 shows the example US images of the phantom. The final two images (D-E) show that, for this phantom, only the bottom two channels could be well perfused.

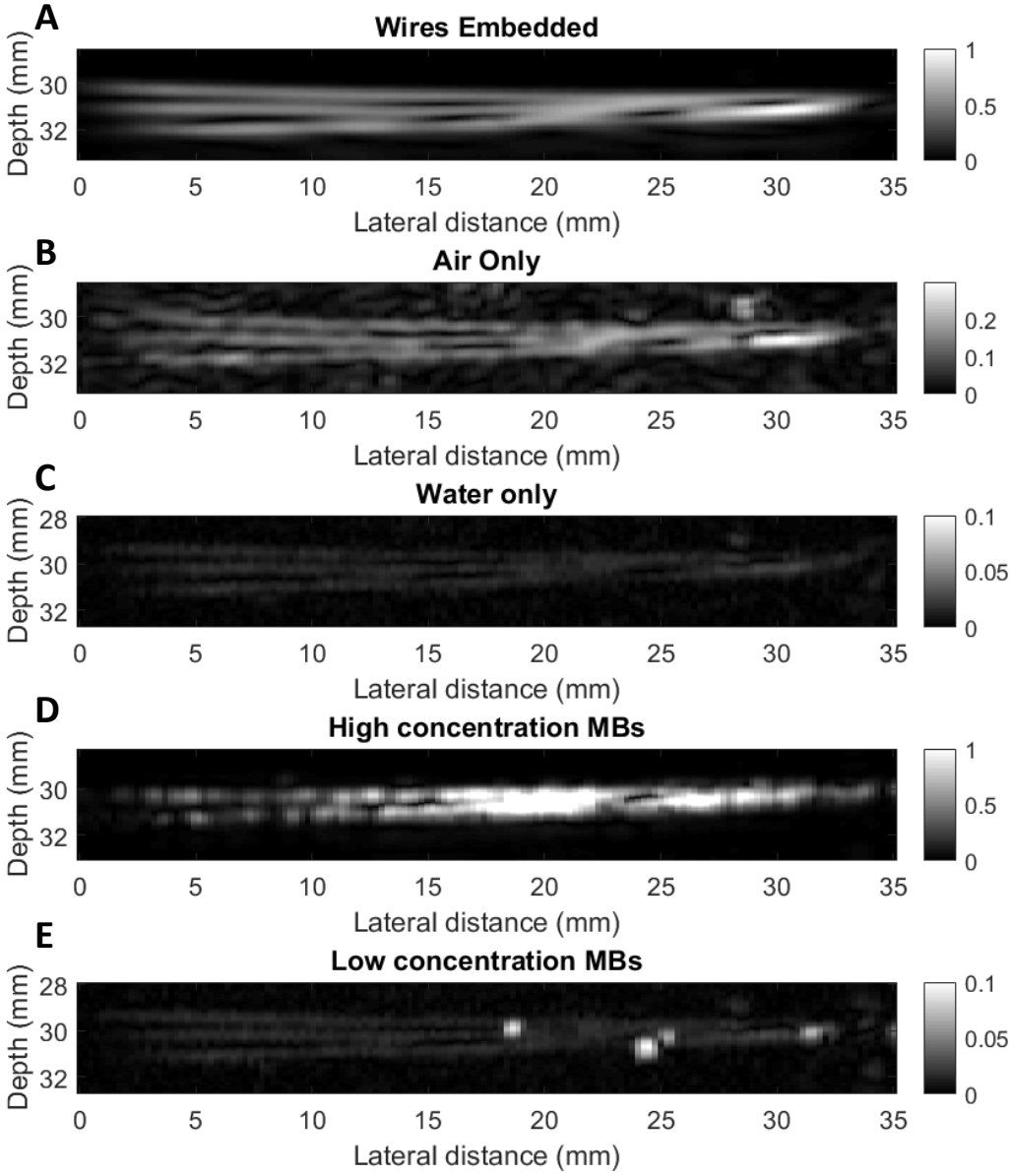

Figure 5-16: Example US frames of the channels. Before the wires have been removed (A), with air only (B), after the perfusion of water (C), a high concentration of MBs (D) and a low concentration of MBs suitable for SR (E).

After motion correction there were 14409 frames which could be used for super-

localisation. 17029 potential MB signal were detected and after filtering, based on the single MB characteristics, 10645 single MBs were localised. The pixel size of the SR images is 2.7 µm x 2.7 µm.

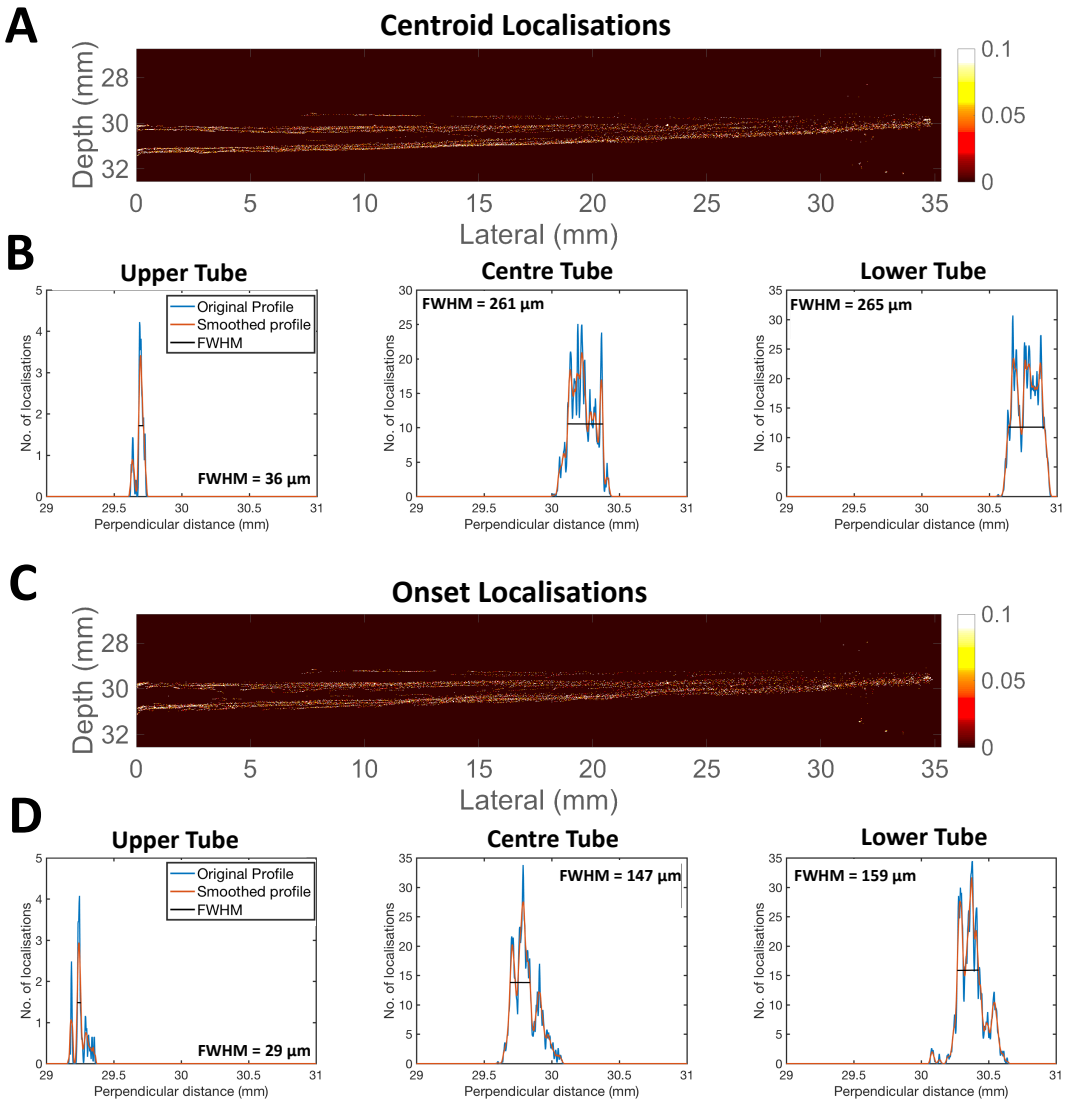

Figure 5-17: SR imaging of agar channels. The SR images of the channels using the centroid method and onset method are shown in (A) and (C) respectively. (B) and (D) show the profile perpendicular to each tube and averaged over the first 10 mm (blue line) for the centroid and onset method respectively. The FWHM of the smoothed profile (red line) was calculated and shown on each plot.

Figure 5-17 shows the SR images using centroid localisation (A) and onset localisation (C). The images were rotated such as each channel was parallel to the x axis and the profiles perpendicular to the channels shown in Figure 5-17 (B and D)

determined. For the two well perfused channels the average FWHM was 263 µm and 153 µm for the centroid and onset method respectively.

Figure 5-18(A) shows the three ROIs centred at 3 mm (ROI 1), 23.5 mm (ROI 2) and 30.5 mm (ROI 3). Figure 5-18 (B) shows the SR profiles overlayed with the conventional profile (averaged frames containing MBs). Each of the SR profiles are normalised with respect to the onset profile in ROI 1. ROI 1 is an example of where the three channels can be resolved with conventional US imaging. ROI 2 is an example of where the SR imaging enabling visualisation beyond the dimensions of the PSF. ROI 3 shows the profiles at the point at which the channels are no longer resolvable using SR.

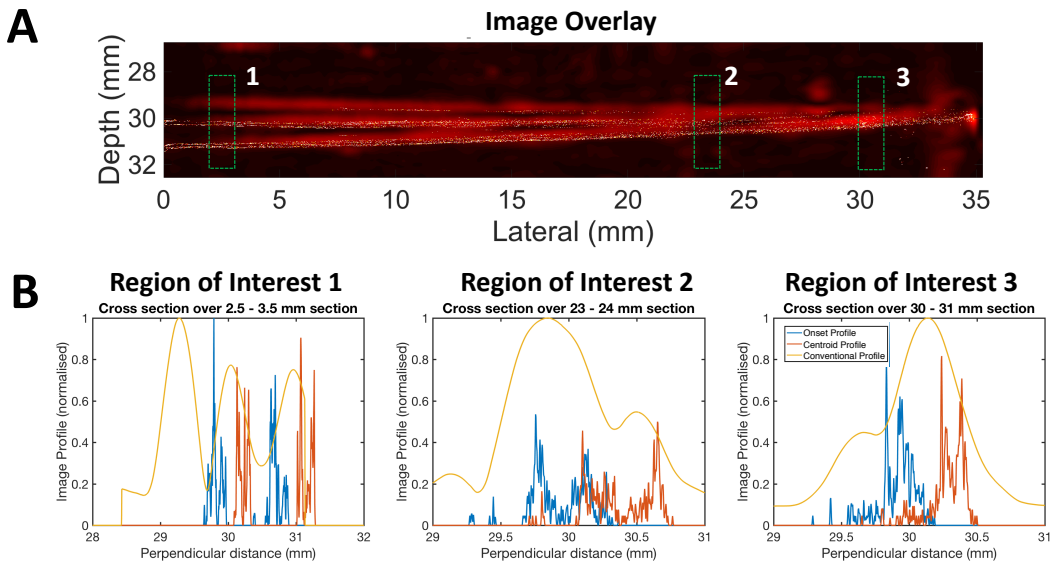

Figure 5-18: Testing the SR resolution. (A) shows an overlay of an average conventional imaging frame and the localisations in white. (B) shows the profile perpendicular to the centre tube and averaged over 1 mm for centroid localisation at different lateral positions with the conventional resolution (yellow), the SR onset image profiles (blue) and centroid SR image profiles (red).

Figure 5-19 shows the SR image alongside the optical ground truth. The optical images shown in Figure 5-19 (B) were acquired using a x4 microscope. Several frames were aligned together to represent the full extent of the phantom imaged optically. Unfortunately, the uneven lighting meant that this introduced the diagonal line arte-

facts. Figure 5-19 (C) is an approximate alignment of the optical and US images to show the relative scales and overlapping FOV.

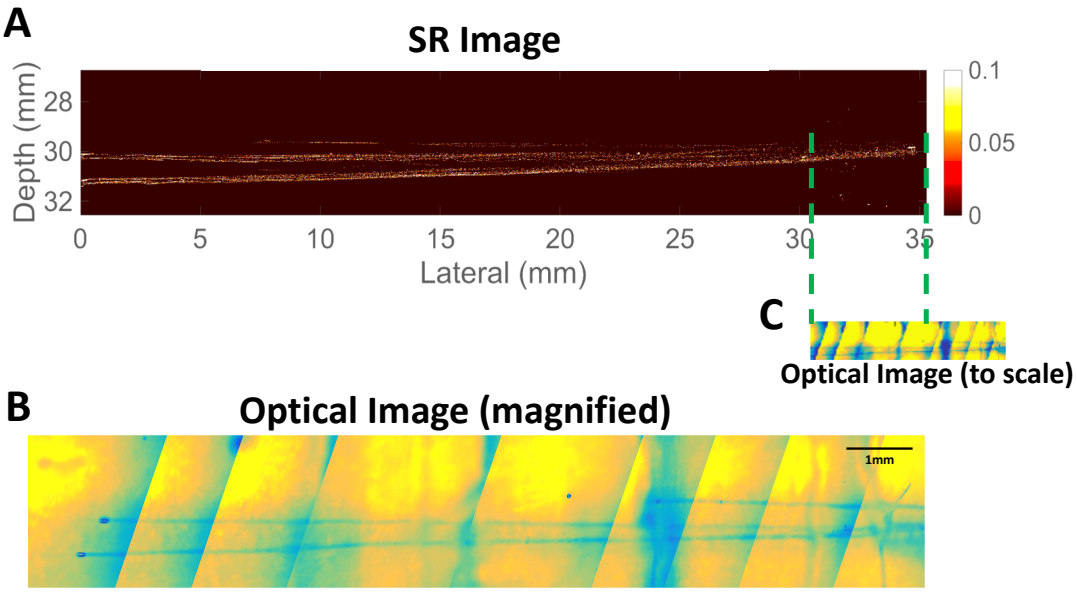

Figure 5-19: Optical ground truth data. (A) shows the SR image for reference and (B) the corresponding optical images of the three channels. (C) shows the relative scale of the images and where in the US FOV the optical measurements correspond to.

5.5 Sacrificial sugar structures

This section details the fabrication of sugar structures which could be immersed within a low melt agar block and, after setting of the agar, dissolved to leave behind channels. These structures were optically characterised, and MB flow established in the channels. SRUS images were generated using background subtracted B-mode imaging and PW AM imaging. This is a novel method of manufacturing a microvascular phantom.

5.5.1 Methods

Sugar structure

The sugar composition from Miller et al. (2012) was replicated [255]. A mixture of 25 g glucose (Alfa Aesar, Massachusetts, United States), 53 g sucrose (Alfa Aesar, Massachusetts, United States), 10 g dextran (86 kDa) (Alfa Aesar, Massachusetts, United States), and 50 ml ultrapure water was gradually heated to 165 ^{o}C whilst continually stirring. Instead of 3D printing, a range of 2D and 3D structures were made simply by using sugar spinning techniques common in cookery - this mainly involved the rapid movement of a metal dining fork coated in the mixture above a wooden spoon. The structures were then vitrified in a laboratory convection oven (APT.line^{TM} FD (E2),Binder,Tuttlingen, Germany) at 50 ^{o}C, and then stored at 45 ^{o}C to avoid ambient moisture absorption until used.

Polymer coating

The original protocol immersed the structures in a 25 mg ml solution of Poly DL-lactide-co-glycolide (PDLGA) in chloroform to provide a polymer coating on the glass structures. This allowed the dissolved structures to be easily flowed out of the channels leaving behind smooth vessels. However, due to the expense of PDLGA and the toxicity of chloroform, two alternative plastic coatings, nail polish (Rimmel, London, UK) and hairspray (Ultimate hold hairspray, Vo5, Alberto-Culver, Illinois, United States), were trialled. The main chemical difference between the two is that hairspray has an alcohol base and is water soluble, whereas nail polish has an acetate base and is non-water soluble. After investigation into which method preserved the structures best, as described in the following results section, clear nail varnish coating was used as an alternative polymer coating.

Surrounding mediums

Paraffin phantoms were made by melting paraffin gel wax (medium density gel wax, the candle making shop, London, UK) in a silicon dish in a laboratory oven at 115^{o}C

for 3 hours. The paraffin quickly sets once removed from the oven, so had to be poured as quickly as possible. The paraffin could be set at room temperature within 1 hour. Low melt agar was prepared as per the protocol provided previously and set around the structures in a 4^oC fridge for at least 3 hours.

Dissolution and perfusion of vessels

When the phantoms were ready for use, ultrapure water was used to dissolve out the carbohydrate glass. A 25g butterfly needle was inserted into a thick portion of the channel and glued in place using epoxy-resin glue (Araldite). The block was cut along a line containing vessels with a razor blade to enable an output for the flow.

Optical imaging

The structures were examined under x10 and x20 magnification using a table-top microscope (Apex Practitioner Digital, Apex Microscopes, UK) or, for larger structures, a standard digital camera (Canon Powershot SX240 HS, Canon, Tokyo, Japan) was used. Food dye/MB solution was used to provide more optical contrast and to test whether MB flow could be established.

5.5.2 Results

Sugar structures

Figure 5-20 shows the scale and geometries of sugar structures that could be formed. It was possible to form structures with dimensions < 50 μm.

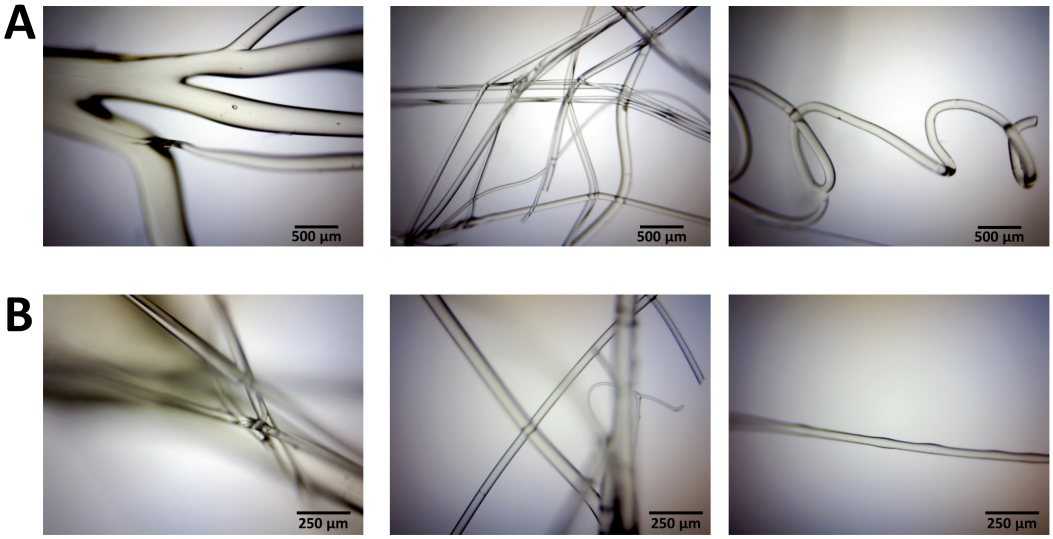

Figure 5-20: Fabricated micron scale structures. Optical images of structures collected at a magnification of x 4 (A) and at x 10 (B).

Figure 5-21 shows an example of a complex structure embedded in low melt agar and taken with a standard digital camera (Canon Powershot SX240 HS, Canon, Tokyo, Japan). This was an example of a structure without any polymer coating. At this point it became evident that many of the smaller vessels were not being preserved once embedded in the agar gel, despite the gel temperature being less that the scaffold melting point. The sugar structures were also dissolving during the setting process, instead of being flushed out with water before use. Moreover, the channel edges were uneven and air bubbles could be formed along the channel surfaces. However, what this figure does clearly show is the potential for flow through the channels left by the dissolution of the sugar structures.

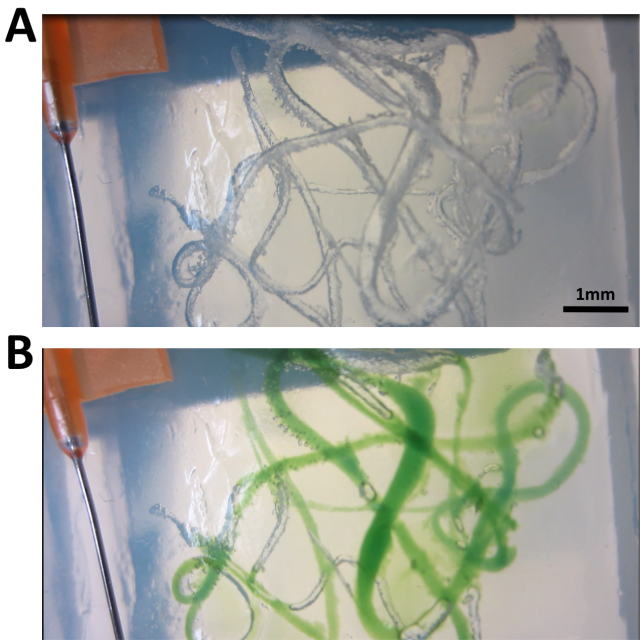

Figure 5-21: Perfusion of sacrificial channels. (A) shows the channels within a layer of low melt agar and (B) shows the perfusion of the majority of the vessels using food dye.

Polymer coating choice

Table 5.5 qualitatively describes the effect of TMM and coating choice on the sugar structures. With paraffin it was easier to preserve structures compared to agar, however due to the high working temperature of paraffin, many more air bubbles were incorporated into the phantom. The results show that a combination of nail varnish and low melt agar was the best option due to the preservation of structures without the formation of bubbles. Figure 5-22 provides examples of each of the scenarios when a polymer coating was used. Due to the non-uniformity of the sugar structures, these experiments were not controlled with respect to vessel size.

Surrounding Media	**No coating**	**Hairspray**	**Nail polish**
Low melt agar	Low success: dissolution of most structures.	Low success: dissolution of most structures.	High success: structures apparently preserved.
Paraffin	Low success: dissolution of most structures.	Low success: few large structures preserved, but many trapped air bubbles.	Moderate success: structures apparently preserved, many trapped air bubbles.

Table 5.5: Qualitative effect of different polymer coatings.

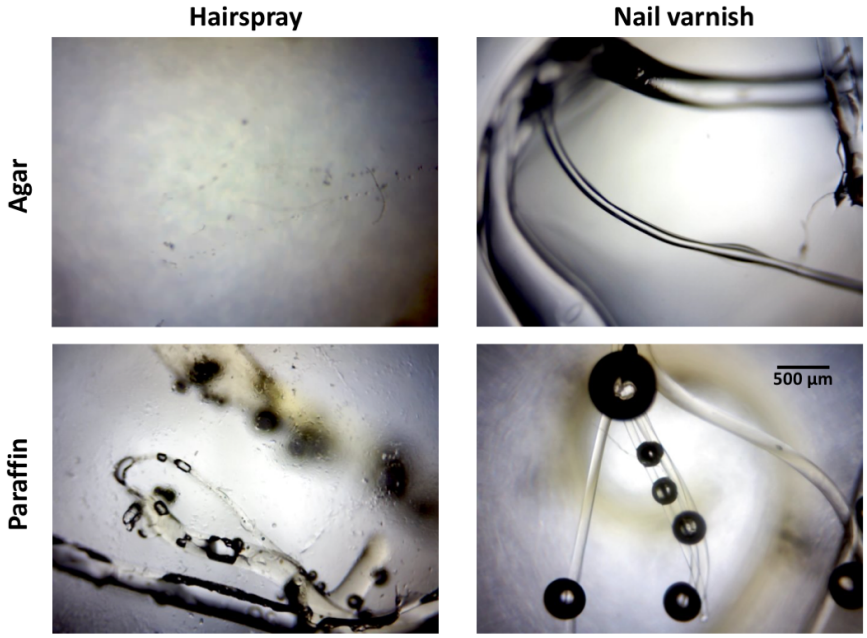

Figure 5-22: Effect of different polymer coatings (nail varnish vs paraffin) and surrounding medium (low melt agar vs paraffin).

Ideally, it would be possible to optically document the shape of these structures before embedding in the TMM. This would allow the dimensions and geometry of the structures to be measured without any distortion from surrounding medium. However, this would require the structures to remain constant before and after setting

of the surrounding media. Figure 5-23 (A) shows some example shapes before (red) and after (blue) encasing in a thin layer of agar. The smallest vessel identified and preserved is shown in the green box and found to be 41 µm ± 5.7 µm. No measurable change in shape was observed. It should be noted that care should be taken to avoid any non-uniform application of the polymer coating. This is demonstrated in Figure 5-23 (B-C) where the arrows indicate where a non-uniform coating of nail varnish could potentially affect the shape of the channel.

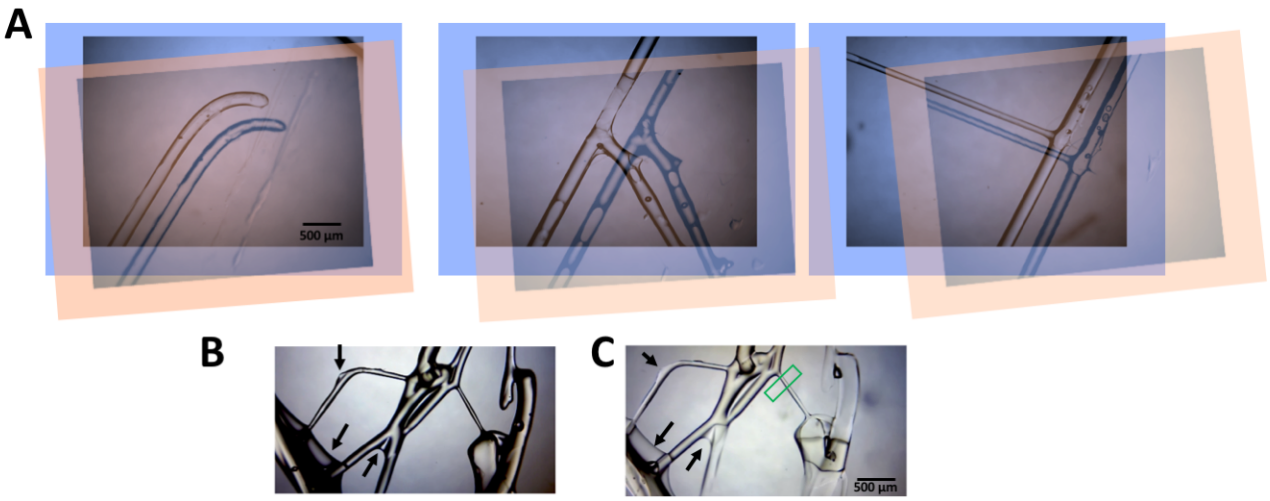

Figure 5-23: Vessel shape change following coating in nail varnish and embedding in low melt agar. Three examples are shown of structures before being embedded (red) and after (blue). (B) shows a structure before being embedded and (C) shows the same structure after. The black arrows indicate areas of non-uniform nail varnish coating which may affect the size of the channels. And the green region was where the smallest vessel size was measured.

Optically observed flow

Figure 5-24 shows optical microscopy images which demonstrate the feasibility of MB flow in these tortuous phantoms. The red dye highlights the channels and the difference images show how MBs can be circulated through these structures.

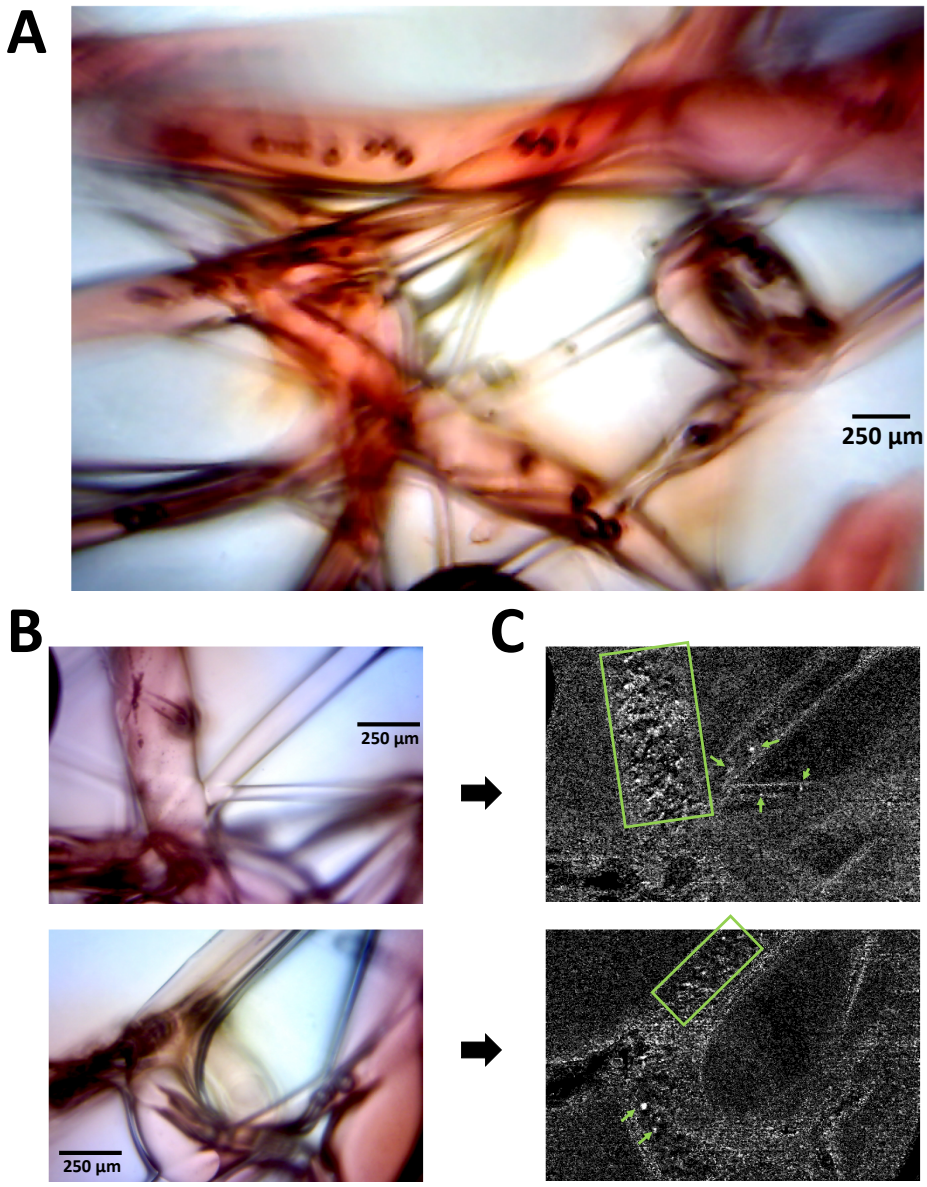

Figure 5-24: Perfusion of channels with MBs and food colouring. (A) shows optical images of a tortuous structure collected at a magnification of x4 and (B) shows two sections imaged at a magnification of x10. (C) shows difference images over time for the structures in (B) when MB flow is introduced. The green boxes and arrows indicate regions where the MB contrast was easily visualised.

SR imaging

Figure 5-25 show an example of one sugar phantom when imaged with US and MBs. Figure 5-25(B) demonstrates the issue that it can be challenging to perfuse the smaller vessels due to less resistance to flow through the larger channels.

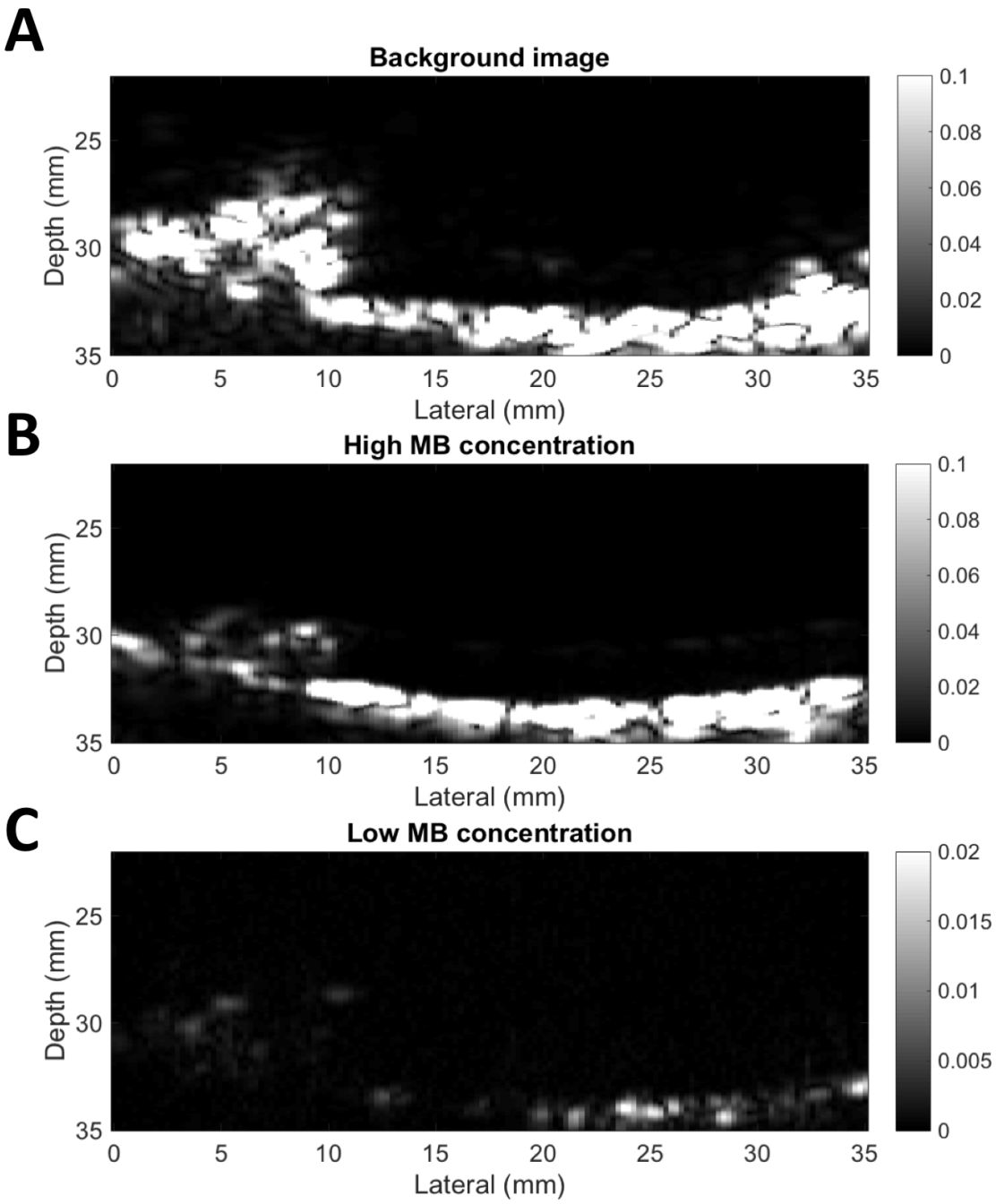

Figure 5-25: US imaging of sugar phantom. (A) shows the mean background image over 500 frames of low concentration MB flow. (B) shows a background subtracted image of the phantom when a high concentration of MBs is introduced and (C) is an example of using a concentration of MBs better suited to SRUS, where the background has again been subtracted using a rolling average.

Figure 5-26(A) shows the SR image for centroid and onset localisation, using IQ and PW data. The structures visualised can be compared to the optical ground truth shown in Figure 5-26(B) which was generated by stitching multiple frames taken using the optical microscope at a magnification of x4. Panoramic image software introduced distortion of the frames so was avoided.

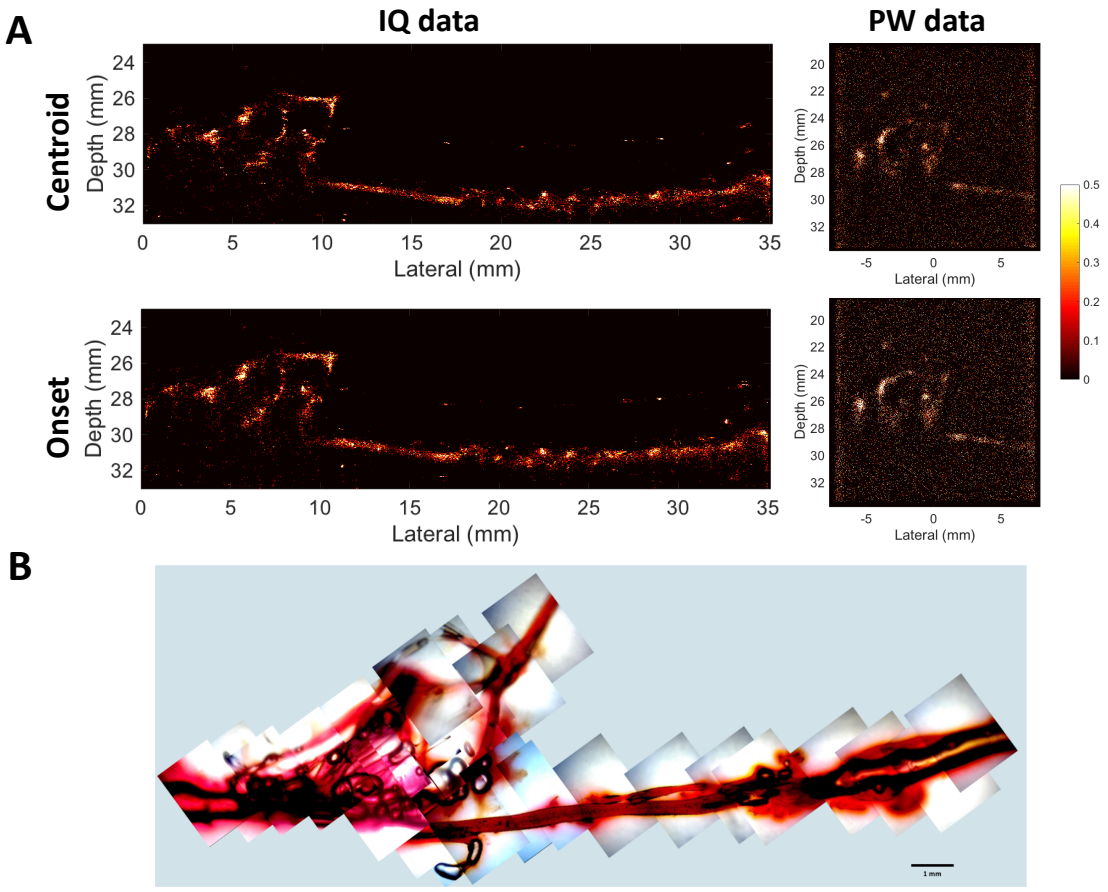

Figure 5-26: SRUS imaging of sugar phantom. (A) shows the SRUS image using IQ data (left) and PW data (right) with either centroid (top) or onset (bottom) localisation. (B) shows the optical ground truth image.

Two channels that were easily identified in the SRUS image were chosen to quantify their widths, as shown in Figure 5-27. Channel 1 and channel 2 had optically determined widths of 284 µm ± 24 µm and 487 µm ± 16 µm respectively. On the SRUS image, the FWHM of these channels were measured to be 164 µm and 276 µm respectively.

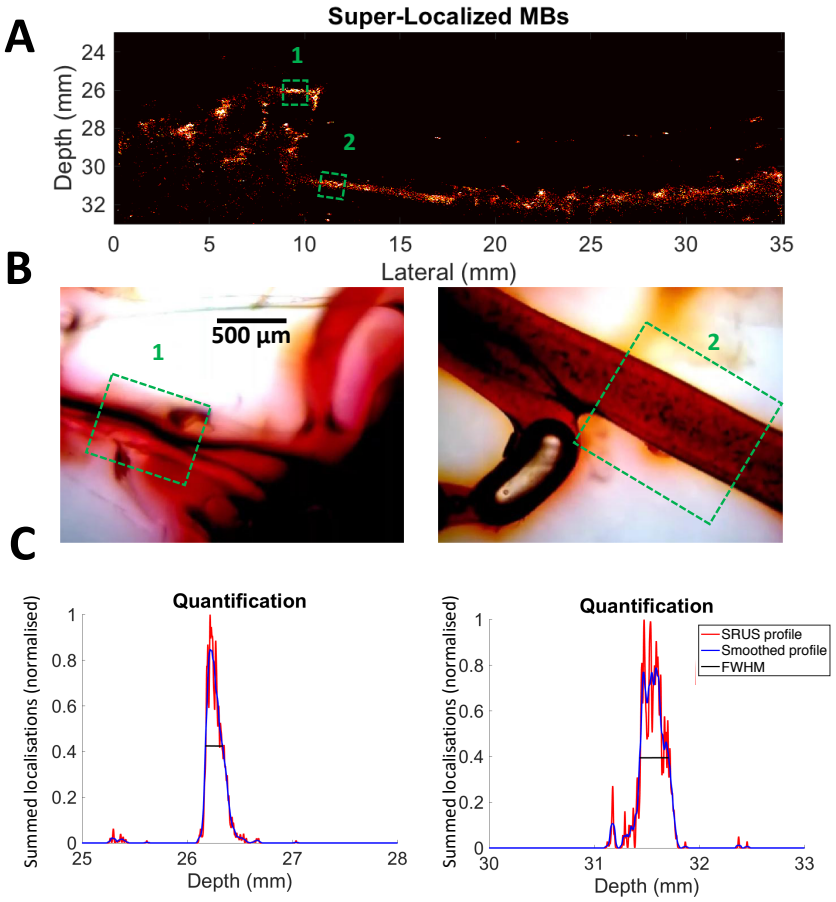

Figure 5-27: Measuring vessel sizes. (A) shows the SRUS image with two channels highlighted in green. (B) shows the optical ground truth image for each of these channels and (C) shows the intensity profile averaged over 800 µm for each of these channels (red) and a smoothed profile (blue) that was used to calculate the FWHM (black).

5.6 Perfusable leaves

This section tests the suitability of decellularised leaves, originally developed for tissue engineering purposed, as microvascular phantoms for SRUS. The research in this section benefitted from work of A. Skondras who I co-supervised for his BEng project. His contribution was invaluable help in trialling the perfusion protocol. Together we also benefitted from the expertise of Professor Gaudette, who generously shared his expertise to help improve the set-up.

5.6.1 Methods

Decellularisation protocol

The decellularisation process from Gershlak et al., (2017) was followed [257]. The waxy leaf cuticles were removed by submerging in hexane (98%, Mixed Isomers, Alfa Aesar, Massachusetts, United States) for 30 minutes and then washed in 1x PBS (Alfa Aesar) for 2 minutes, with the wash repeated twice. This was performed in a fume hood (ChemcapTM Ductless Fumes Cabinet, Bigneat, Waterlooville, UK). Spinach leaves were cannulated through the petiole. They were held in place using epoxy resin glue (Araldite) and taped to the sides of a container in such a way to allow gravity to aid the perfusion. The cannula was attached to air infusion set (Medisave, Weymouth, UK) which controlled the flow of the various agents. The set-up is shown in Figure 5-28. A 10% sodium dodecyl sulfate (SDS)(Alfa Aesar) was perfused for 5 days. Crystallised salt formed on the leaf surface and had to be removed at regular intervals. A 0.1% Triton-X-100 in a chlorine dioxide water purification solution made from 60 ml of sodium dioxide water purification drops (Lifesystems, Berkshire, UK) diluted in 750 ml of ultrapure water. Ultrapure water was then perfused for a further 48 hours. The scaffolds were then stored in ultrapure water in the fridge until required. This set-up required large volumes of the solvents to maintain perfusion over several days. Blockages and breakage at the leaf junctions were common, leading to unsuccessful phantom materials. Thus, a meeting was arranged with Professor Glen Gaudetter, the principle investigator of Gershlak et al. (2017).

Professor Gaudette very kindly shared further details on the protocol and improvements which had been made following publication. More details were provided for the hexane wash; the leaves were now washed in hexanes for 2 minutes (repeated 3 times) and then washed in 1x PBS for 2 minutes. Instead of the sodium dioxide water purification tables, a 10% solution of domestic bleach could be used. The following results used Domestos, Original, which was 4.5% (w/w) sodiumhypochlorite. The leaves could also be sutured to the needle using Low-Density Polyethylene (LDPE) tubing of inner diameter of 0.58 mm (Smiths Medical Portex^{tm} Fine Bore LDPE Tub-

ing, Fisher Scientific, New Hampshire, United States) to strengthen the junction. It was advised to secure the junction with thread. However in practice, securing using epoxy resin glue was found to be more practical. Finally, a simpler alternative to the perfusion set-up was the use of a tube roller (SciQuip Tube Roller BASIC, SciQuip, Newtown, UK) to submerge the leaves in the solvents and gently rotate.

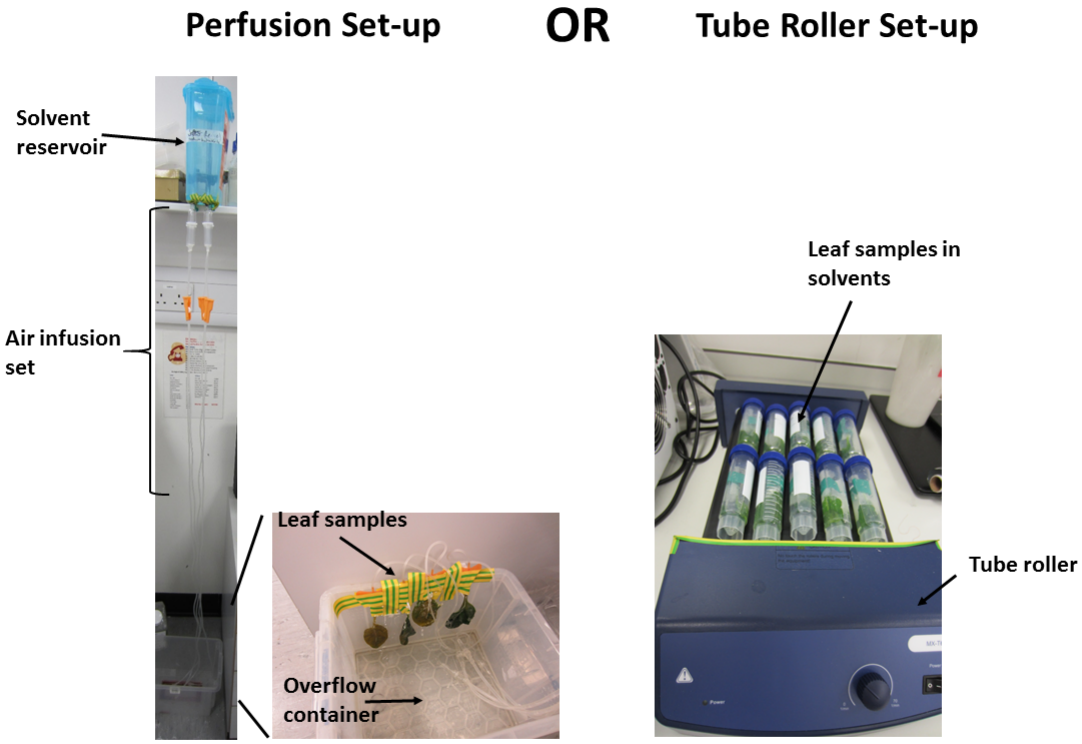

Figure 5-28: Decellularisation set-up. The leaves could either be prepared using the perfusion set up (left) or more simply with a tube roller (right).

The new protocol was as follows:

1. The spinach leaves were cannulated via the petiole. A 27G syringe was sheathed in the LDPE tubing and threaded within the spinach petiole. The tubing, leaf and needle were secured by tightly tying 100% polyester thread.

2. Once leaves are cannulated, the leaves were submerged in hexanes and washed

vigorously for 2 minutes. This was repeated 3 times. The phantoms were then rinsed in 1 x PBS for 2 minutes.

3. The leaves were placed in 50 ml conical tubes (Consumable Direct, Amazon.co.uk) and the tubes filled with 1 x SDS.

4. The tubes were gently rotated on the tube roller until the leaves became more transparent (48 hours).

5. The SDS was then removed and replaced with the 0.1% Triton-X-100 in a 10% solution of bleach.

6. The tubes were again rotated until the leaves were transparent and had no remaining green coloration (48 hours).

7. The leaves were then washed in ultrapure water for 24 hours.

8. The phantoms could then be stored in the 4^{o}C fridge until use (for up to a week).

Acoustic set-up

It was relatively challenging to image the leaf structures as they were so fragile. Small spots of superglue were used to secure the leaf to standard clingfilm. This was stretched between two optical posts (Thorlabs, New Jersey, United States). The LA332 linear array transducer was clamped above the phantoms, as shown in Figure 5-29. IQ and PW data was collected at a centre frequency of 3 MHz. A moderate concentration, based on 0.3 ml of Sonovue in 600 ml of ultrapure water but empirically adjusted, of MBs was injected using a syringe pump.

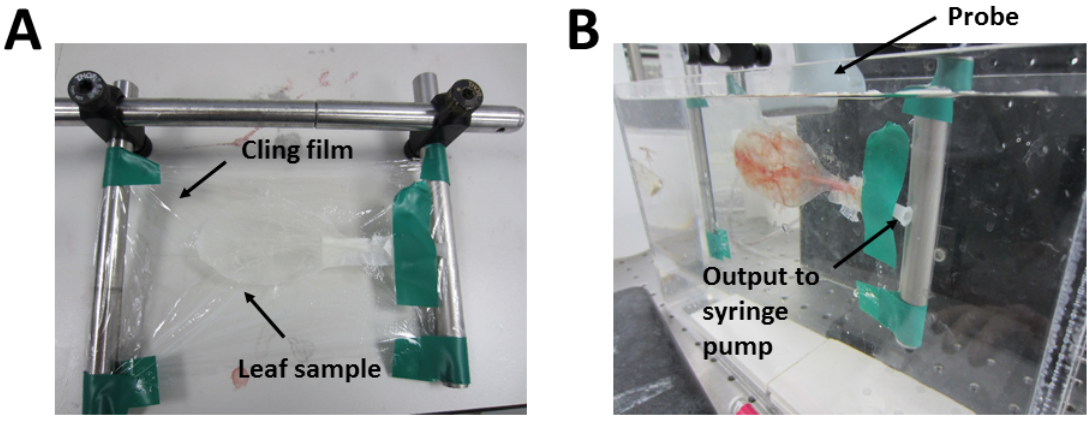

Figure 5-29: Acoustic imaging of leaf. The leaves were glued to clingfilm stretched over optical poles (A) and imaged in a water tank (B).

5.6.2 Results

Decellularisation outcomes

Figure 5-30 shows the progression of the decellularisation process, beginning with the initial leaf shown in (A). The cannulation is shown in (B) and the securing of the junction with glue shown in (C). A very early initial test, of forcing flow into the initial leaf (D), was simply to demonstrate that the decellularisation protocol was necessary to make a perfusion phantom. The dye does not travel through the vasculature, but instead leaks through the leaf surface. The result of the hexane wash is shown in part (E) and the increase in transparency/decolouration following 48 hours of immersion in SDS, and a further 48 hours in Triton-X/bleach solution are shown in (F) and (G) respectively.

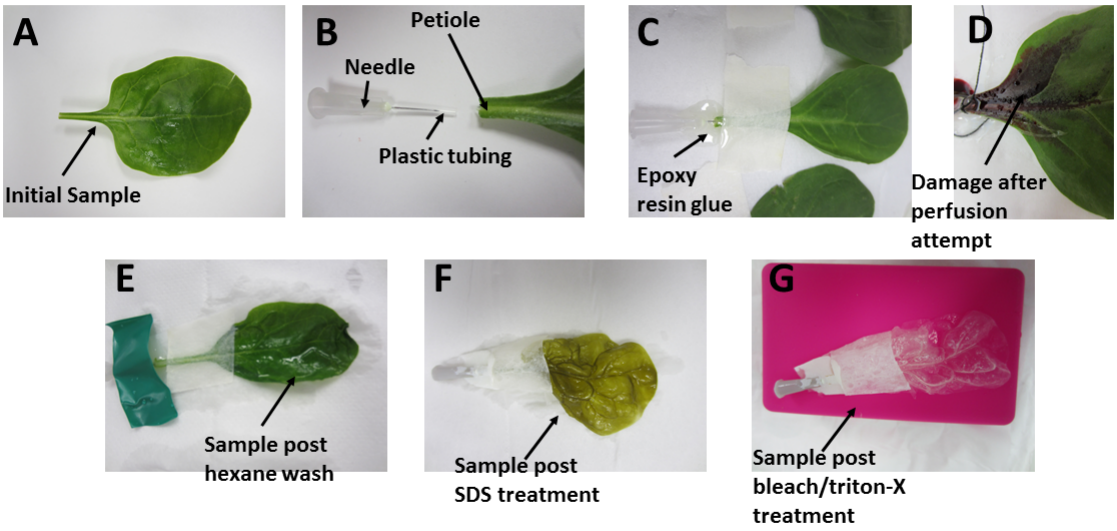

Figure 5-30: Decellularisation of leaves. (A) shows the initial leaf which could then be cannulated (B) and secured using glue (C). Forcing flow before decellularisation is shown in (D). The leaves were then underwent a hexane wash (E), SDS treatment (F) and bleaching (G).

Optical quantification

One of the methods used to confirm perfusion in Gershlak et al., (2017) was the visualisation of perfused dye. However, when this was trialled, it was found that dye leakage often naturally followed the raised vasculature as flowed over the surface. Figure 5-31 shows how the perfusion was tested alongside a control where the leaf was dipped in dye instead of being internally perfused. Figure 5-31 (A) does appear to show more convincingly that the main petiole was perfused and some of the smaller branches than the control (B) which is more uniformly coated in dye. However, for a SRUS phantom, a ground truth collected using an optical microscope was desirable. Figure 5-31 (C) shows how, after resting on the slide for a few minutes, both the vasculature of the perfused sample and control were stained red. Microscope images did not show a marked difference in the staining of either the main branches or microvasculature for the control leaf compared to the perfused sample. Thus it was not

possible to assess which channels had been successfully perfused using this method.

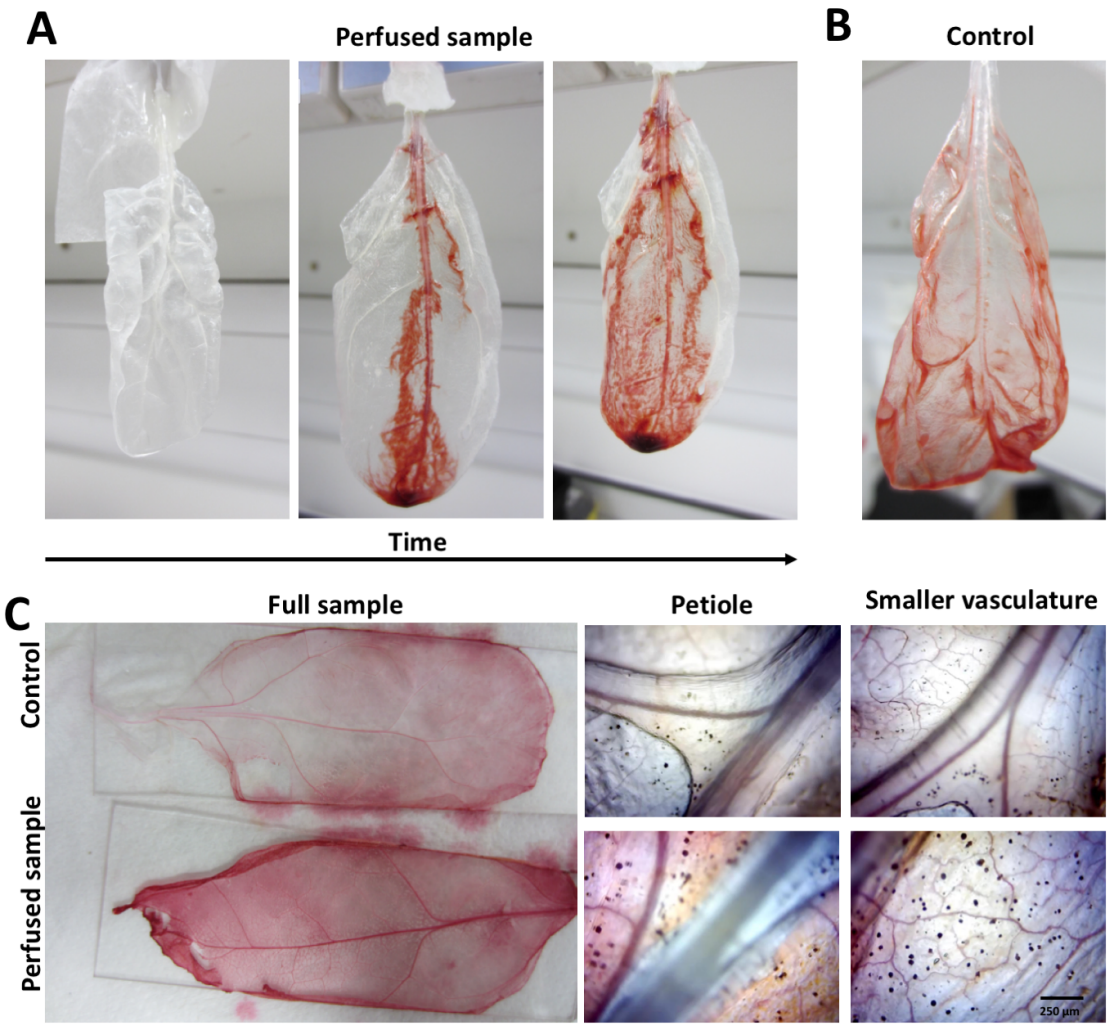

Figure 5-31: Testing the perfusion of the samples using dye. (A) shows the treated leaf being slowly perfused with red food dye compared to a control (B) which was only dipped in dye. (C) shows the final staining of the perfused sample and the control using a conventional camera (left) and a x10 microscope objective (right).

Introducing MB flow made it easier to assess perfusion. Adjusting the focusing depth meant that it possible to focus within the vessel either side of the bubble flow - which made it more convincing that internal perfusion had been achieved. It was consistently more challenging to achieve perfusion in the smaller vessels. The smallest vessel where perfusion was convincingly shown in Figure 5-32 was approximately 20 µm. Taking difference images over time, meant that the signal due to MB movement

could be extracted. Figure 5-32 (A - B) show that this movement was within the channel for the perfused leaf and following the outside channel wall for the control (C).

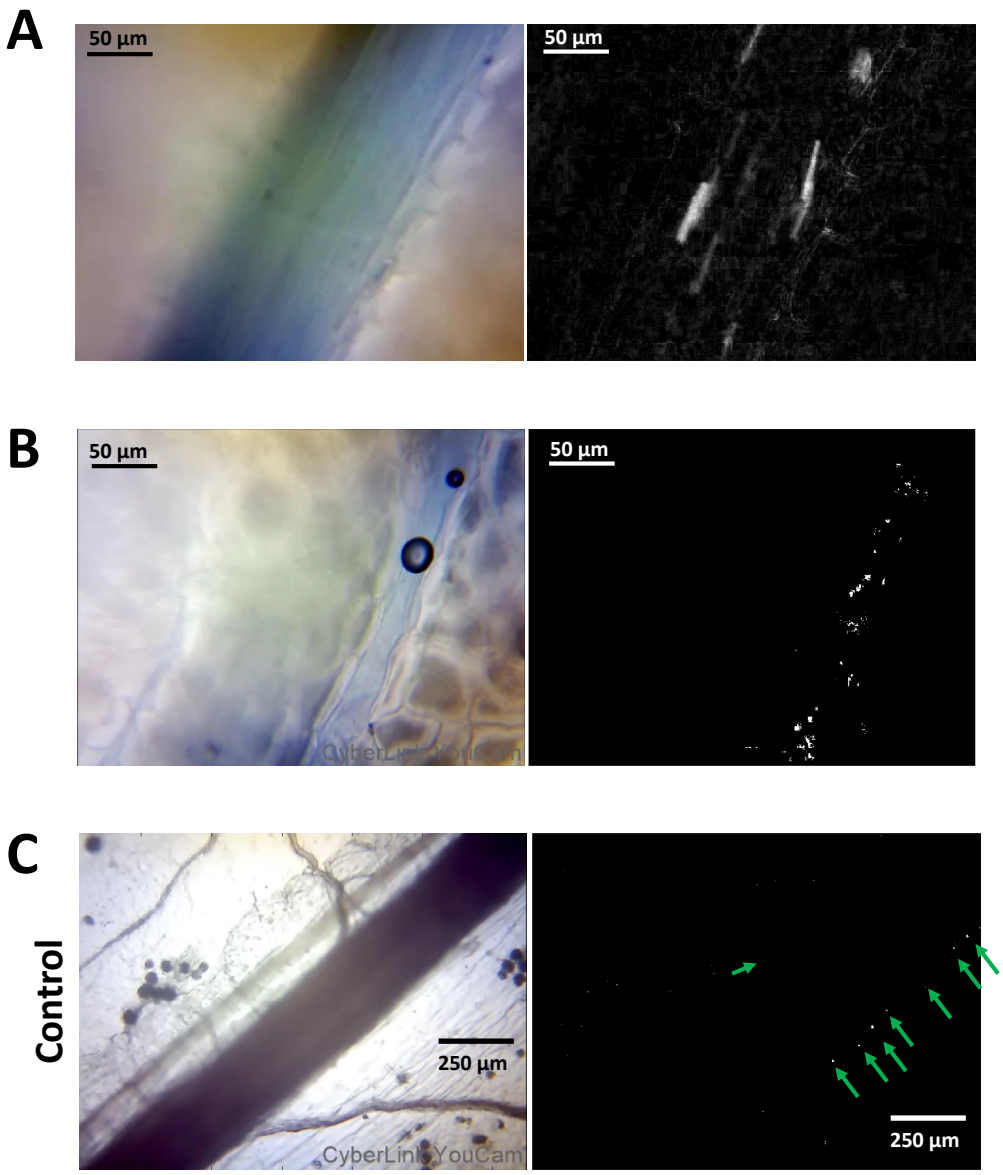

Figure 5-32: Testing the perfusion of the samples with MBs. (A) shows the treated leaf being slowing perfused with MBs and imaged using the x40 objective. The right image is the summed difference images over time to show MB flow. (B) shows the smallest vessel where perfusion could be confirmed alonside a single difference image (right). (C) shows MBs introduced onto the surface of the control leaf. Here they appear to follow the channel edge. MBs in the single difference image (right) are highlighted using the green arrows.

Preliminary SR imaging

Figure 5-33 (A) shows BMode differential images of the vasculature acquired. The majority of the MB signals are within the main petiole. However, several MBs also appear to be travelling along branches. Figure 5-33 (B) shows the SR image generated using only 258 frames of data with 3585 localisations. For easier visualisation, the localisations were convolved with a symmetrical gaussian with a standard deviation of 50 µm.

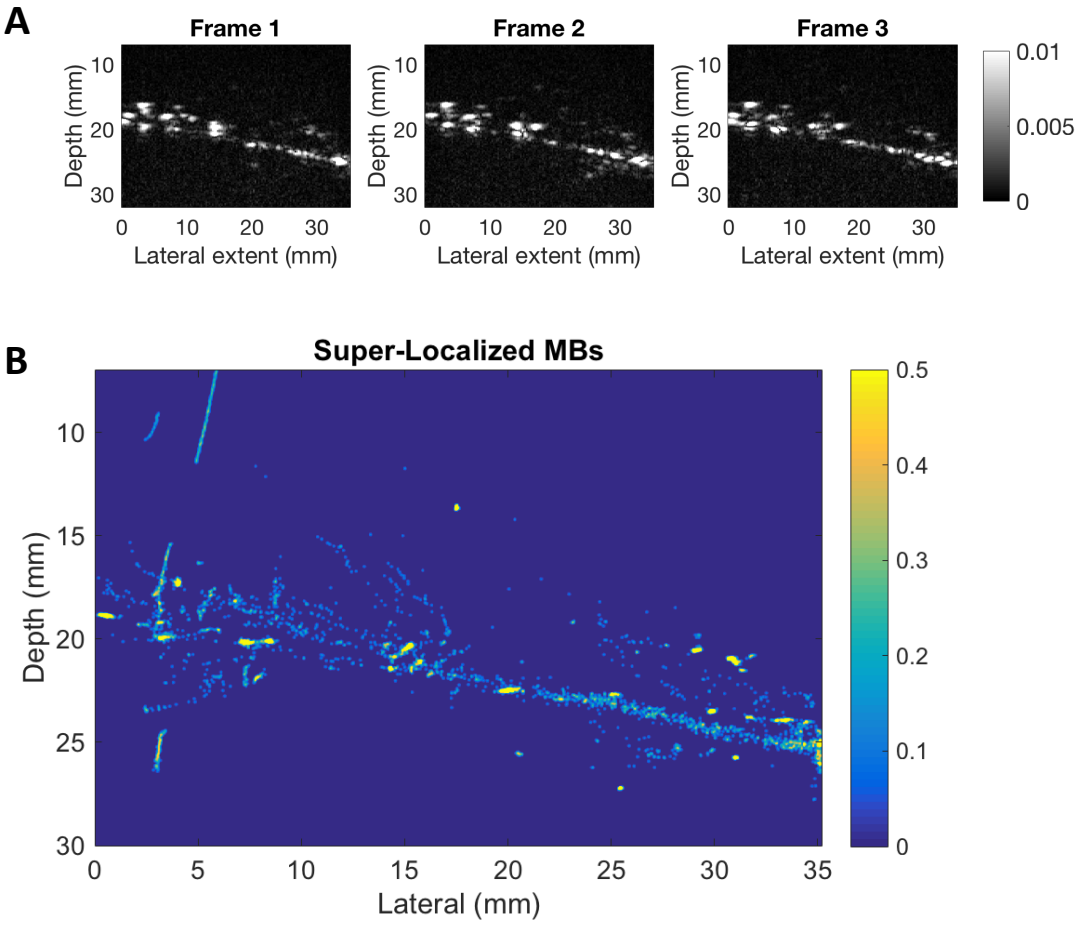

Figure 5-33: SR image of leaf. (A) shows three successive differential images of the BMode data and (B) shows the SR image obtained from this phantom.

5.7 Discussion

In this chapter, four novel microvascular phantoms for testing SRUS were considered. This discussion section will be used to assess how successful each phantom type was based on the results presented previously and the desired criteria of a SRUS phantom. The results are summarised in Table 5.6 with reference to the criteria defined in the introduction of this chapter. One addition criterion (which was not stated in the introduction but is interesting to compare here) is the ease of fabrication.

	Phantom Type			
Desirable Property	**3D Printing (Agilus30)**	**Wire Extrusion**	**Sacrificial Sugar Structures**	**Perfusable Leaves**
Appropriate diameter	Limited (confirmed channels on the order of 300 µm)	Yes	Yes	Yes
Can accommodate flow	Yes	Yes	Yes	Partially
Acoustically realistic TMM	Limited (relatively high attenuation)	Yes	Yes	Imaged suspended in water/medium
Withstand probe pressure	Yes	Yes (relatively fragile and care required)	Yes (relatively fragile and care required)	Imaged suspended in water/medium
Structure in 3 dimensions	To be tested	Yes (depends on tube arrangement)	Yes (Could be achieved using more than one sugar structure)	Yes (only if folded)
Resistant to degradation over time	Yes	Limited	Limited	No, too fragile to be suitable for reuse.
Optically transparent	Not tested, but transparent version available for future work.	Yes	Yes	Yes (some obstruction due to tissue structures)
Easy to fabricate	Yes	Yes	Relatively easy but multiple steps required.	Challenging to fabricate and at least five days required.

Meets requirements

Meets requirements with conditions

Partially meets requirements/not fully tested

Does not meet requirements

Table 5.6: Assessment of microvascular phantoms.

Although not considered in this chapter, in future work it may also be important to consider other criteria such as production cost and repeatability.

None of the consumables used in this chapter were prohibitively expensive. However, it is noted that the overall cost depends on the availability of equipment such as 3D printers.

Being able to repeatably fabricate the same microvascular structure could be highly valuable when testing and improving various parts of a SRUS protocol over a long period of time. The methods for perfusable leaves and sacrificial sugar structures are not useful for fabricating repeatable phantoms. The extruded wire phantoms and especially the 3D printed phantoms would appear to have more potential to provide repeatable phantoms. However, even 3D printing of the same design multiple times will likely be associated with some variation between the printed structures when printing at these resolutions. Quantifying the repeatability of phantom fabrication would be an interesting addition to future comparisons.

5.7.1 3D printed phantoms

It quickly became evident over the course of this work that 3D printing at microscale resolution using ultrasound compatible materials was at the leading edge of commercially available technology. This meant that it was useful to engage with researchers in the 3D printing field to identify potential materials and printing technologies. Layfomm-40 and Agilus30 were investigated using a simple resolution phantom to determine the smallest channel that could be printed. Layfomm-40 printed the smallest diameter channels < 200 μm. However, these channels were highly non-uniform. Poor adhesion between the layers of this material meant that MB flow was not necessarily contained within the intended channels and could instead leak through the phantom bulk. The inhomogeneity of this phantom also meant that there was strong signal from the phantom material surrounding the channel relative to the MB contrast signal within the channel. This meant that only the three largest air filled channels ($>$ 480 μm in diameter) could be visualised using linear US imaging. Overall, this material was determined to be a poor choice for microvascular phantoms. Perhaps this material would be more useful as a layer of TMM where the generation of background signal from tissue inhomogeneity is desirable.

Agilus30 was more successful that Layfomm-40. Agilus material was more durable to manipulation than Layfomm-30 during imaging, despite having a lower Shore A number. Due to the use of material jetting technology rather than FDM printing, the

Agilus30 phantom was also more homogenous and the tubes measured optically could also be identified acoustically. The smallest tube measured optically had a diameter ranging between 290-360 μm. However, the ultrasound imaging suggested that the next smallest channel (designed to be 200 μm) had also been printed. Failure to identify this optically suggested that the channel may have a blockage obstructing the light. The phantom was 40 mm in the direction parallel to the channels. In future work a smaller phantom could be printed to more easily optically assess the resolution limits of printing with this material.

Testing of the acoustic properties suggested that the Agilus30 had an appropriate sound speed and density to be a tissue mimic (1425.1 ± 5.2 m/s and 1140 -1150 kg/m^3 respectively). The speed of sound of Agilus30 is 9% less than the average sound speed for soft tissue presented in Table 5.1. The density of Agilus30 is less than 10% more that the average density for soft tissue presented in Table 5.1. However, the attenuation was potentially unfeasibly high (21.9 ± 4.1 dB/(cmMHz)) compared to literature values for average soft tissue of 0.54 dB/(cm MHz). Nonetheless, MB flow (high concentration) could be visualised in the smallest diameter channel optically identified using linear US imaging.

The channels printed were relatively uniform in diameter compared to Layfomm-30, and there was no MB leakage. The fabrication of perfusable channels ($<$ 300 μm) in an US compatible and durable material was positive. This meant that Agilus30 channels with diameters $< \lambda/2$ could be used as sub diffraction channels for US imaging at frequencies $<$ 2.4 MHz. Due to not being able to generate a ground truth for straight channels $<$ 200 μm in diameter this phantom was not pursued further since there is existing availability of 200 μm cellulose tubing. However, if this work was to be continued with SRUS as the application, it would be interesting to test the potential to fabricate more complicated structures such as branching and tortuosity. This structural complexity would have benefits over the cellulose tubing currently used.

As shown in Table 5.6 one major benefit of the Agilus30 phantom was the resistance to changes over time and the ability to withstand probe pressure during

imaging. This would allow for measurements to be repeated over several days in a way that is currently not possible using any other SRUS phantom. There are also significant practical advantages to being able to fabricate phantoms in advance and easily transport between laboratories. The Layfomm-30 is less suitable for long term storage and repeated measurements. The material must be stored in water. It was observed to increase in flexibility and decrease in size over the course of several days. Thus, the acoustic properties are also likely to vary with time.

5.7.2 Agar tubing

This very simple idea was the most successful. Withdrawal of the wire from low melt agar generated perfusable, uniform, channels of 50 μm. The optical transparency of the low melt agar means that this phantoms also has the potential for use with the simultaneous optical and acoustic set-up.

A benefit of the agar tubing and sacrificial sugar structures was that the material used to form the microscale structure did not need to be ultrasound compatible. Low melt agar was used for the sacrificial phantoms as it was the gel which gave the most uniform channels in Miller et al., (2012). Additionally, agar is a commonly used TMM [1]. Using the same characterisation apparatus and method used for the 3D printing material, the sound speed and attenuation was measured to be 1485.4 ± 1.2 m/s and 0.29 ± 0.63 dB/cm respectively which is very similar to that of water. As the agar set, larger bubbles could be observed to rise to the top of the phantom. Any smaller bubbles remaining in the gel may generate a strong signal in the US image. For the SRUS experiments this will generally be subtracted using background subtraction. However, in future, perhaps the agar solution could be prepared in a low-pressure environment to limit the formation of any bubbles in the medium.

There are many possible adaptations to the arrangement/sizes of the tubes used in this phantom which could be investigated in future work. The branching structure chosen in this work, of three tubes from a common junction, enabled the resolution of the SR imaging to be tested. High resolution imaging is often desirable to distinguish

between multiple structures which are closer than the diffraction limit, as opposed to simply accurately determining the dimensions of a single structure. Moreover, true testing of resolution ability requires the separation of two nearby objects. Thus, this wall-less phantom may be preferable over the cellulose tubing due to the potential to place channels adjacent to each other without the effect of the finite tube wall width. The normalisation of Figure 5-18 relative to one SR profile shows how the density of SR localisations can change over the length of the phantom. If all MBs are passing through without destruction this should remain constant. The difference could be accounted for by the possibility of detecting isolated MBs decreasing as the vasculature becomes more dense. This arrangement of branches is sensitive to the axial extent of the MB signals in adjacent tubes overlapping. The resolution achievable using SRUS is likely to be affected by the orientation of these channels relative to the transducer.

Obtaining an optical ground truth for this phantom was made more difficult by the 3D printed holder used to make the US imaging easier. Removal of the phantom for optical imaging required that the flow junction was broken. This meant that a ground truth was not collected for the full extent of the phantom. In the future, the holder could be designed to ensure easier removal where the flow connection can be maintained. Alternatively, optical characterisation could be avoided by allowing less variation in the tubing position. Instead of relying on the 3D printed holes in the support to hold the wires in place, a holder could be precision machined to more closely match the wire diameter and hold the wire in place so that the position is more precisely known.

One challenge was that flow of the MBs was observed to stop during the perfusion. Indeed, one of the three channels within this phantom had very little flow at all, so could not be successfully imaged. Some gentle pressure on the phantom surface was enough to reinitiate flow on the two well perfused tubes, however the possibility for this pressure to change the phantom position relative to the probe was a concern. This could be due to the possibility of the agar gel rupturing near the needle junction as this could provide a route of less resistance for flow than through the channels.

This was problematic when this phantom was initially trialled using paraffin wax gel instead of agar in early attempts at this work. Future work would involve investigating the reasons why flow could be restricted and how to mitigate them.

Another challenge of using these phantoms is their limited ability to withstand probe pressure and resistance to degradation over time. It was possible for splits to appear if too much pressure was applied, especially near the delicate needle junction region. Over a period of days the low melt agar was observe to shrink slightly, thus it is not resistance to changes over time.

Very recently, Heiles et al. (2019) have used a similar approach to fabricate a wall-less agar phantom for SRUS in 3D [137]. This phantom had a branching architecture by gluing a 400 µm diameter wire with two 200 µm diameter wires that could be pulled from set agar. The phantoms was then imaged in 3D using a 2D matrix array probe. Future work could involve using the wire extrusion method to make different 3D structures within the medium with the smaller 50 µm wires used in this chapter. For example, the wires could be separated from each other in two dimensions by securing the loose end of one wire deeper than the other two before encasing in agar. Thus this phantom is also appropriate for 3D SRUS imaging.

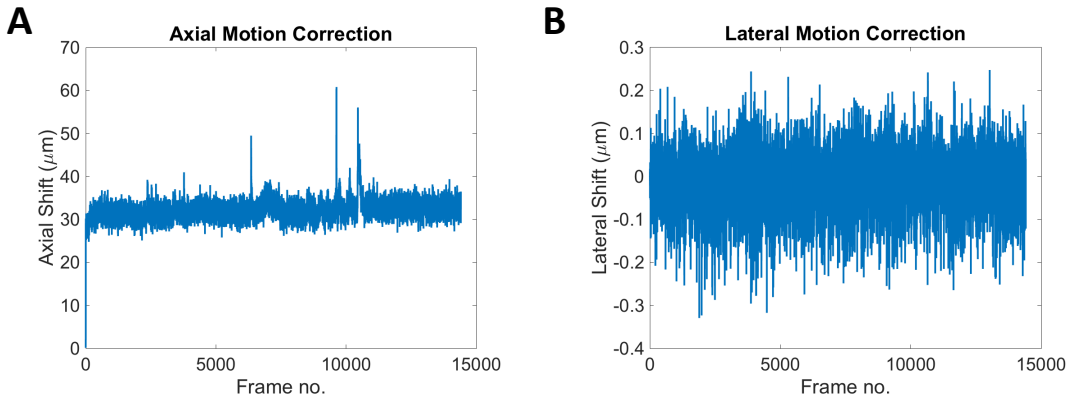

Figure 5-34: Motion correction shifts calculated on the data processed with SR algorithm after frames with significant motion were rejected. The axial shift calculated using the motion correction (A) and the lateral shift calculated using the motion correction (B).

As shown in Figure 5-17 the tube width measured using SRUS for the well perfused

channels were significantly wider than the expected 50 μm. A rigid motion correction algorithm was trialled to test whether the pressure used to reinitiate flow could have shifted the channels. However, as shown in Figure 5-34 the influence of the motion correction on the tube widths was negligible. There was axial shift of approximately 30 μm regardless of the starting frame used to correlate subsequent frames with, suggesting a systematic error associated with the motion correction algorithm. Less than 1% of frames were calculated to have a shift in position over 10 μm in magnitude about the systematic 30 μm axial shift. Thus any shifts accounted for using the motion correction algorithm were not sufficient to account for the FWHM being at least three-fold larger than the expected 50 μm. Moreover, it was expected that the more closely spaced channels near the junction, and recorded using the optical microscopy, would be resolvable using SRUS. Imaging of this phantom had shown that the SRUS protocol used had generated lower resolutions than expected.

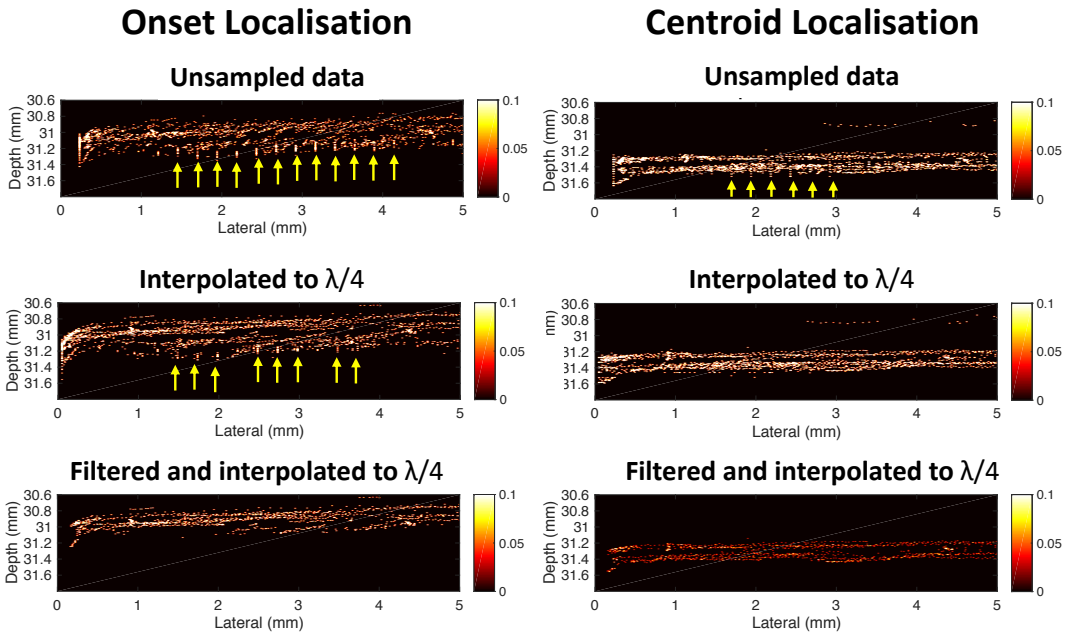

Figure 5-35: Gridding artifact due to interpolation. The artifact, highlighted by the yellow arrows, is most evident for SR data processed without additional interpolation from the data acquired directly from the scanner (top). Interpolations to pixel dimensions of $\lambda/4$ decreases the artifact (centre) and filtering to extract only isolated MB signals decreases it further (bottom). This data is presented with SR pixel size of 2 μm x 2 μm.

This phantom also highlighted the incidence of a gridding artefact shown in Figure 5-35. Gridding artifacts have been investigated in earlier literature. Song et al. (2018) investigated how a gridding artefact can occur when the data is insufficiently sampled upon acquisition [260]. The authors showed that sampling data to obtain a beamforming resolution of 0.5λ laterally and 0.25λ axially should avoid quantisation error. They also showed that, in that case of undersampling, localisation using Gaussian fitting and centroiding was more robust than peak detection. The data used in this chapter exceeded the sampling criteria, however a gridding artefact was still present. It was hypothesised that the extent of interpolation performed on the data may affect this artefact. Figure 5-35 shows the gridding artefact that could be observed in the beamformed data without any interpolation (unsampled data). Upon performing linear interpolation of each frame to square pixels of $\lambda/4$ prior to intensity thresholding, the gridding artefact was reduced (more successfully in the case of centroid localisation). Upon filtering out signals from noise and multiple MBs the gridding artefact had been removed from both localisation methods. This suggested that interpolation was related to the gridding artefact, onset localisation was more susceptible than centroiding, and weaker signals (attributed to noise) were also more susceptible.

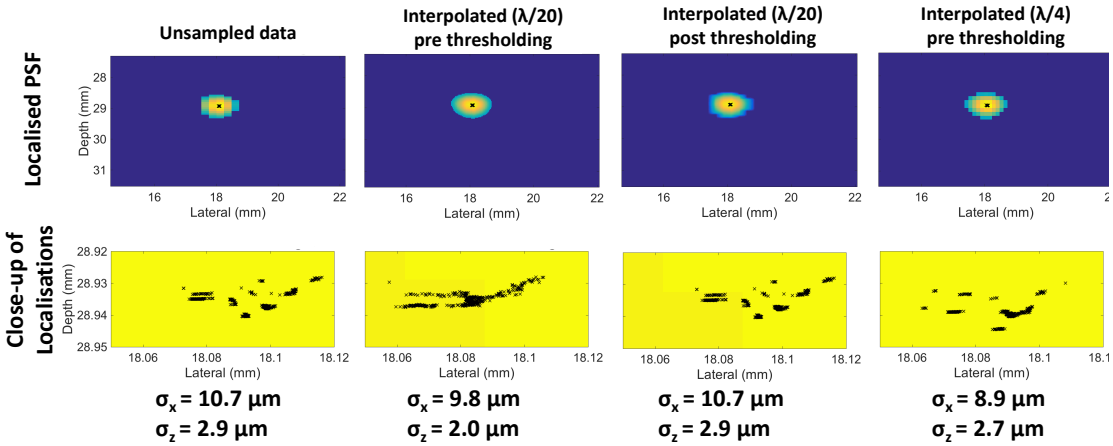

Figure 5-36: How centroid localisations are affected by interpolation choices. The choice of the level of interpolation and whether thresholding is done before or after interpolation will change the appearance of the PSF (top). The discretion of signal to pixel values also changes the variation in localisations due to noise as shown by the spread of individual localisations (bottom) over 500 repeats.

This artifact was also seen earlier in Figure 5-14 where repeated localisations of the linear point target resulted in groups of localisation points. Figure 5-36 explores this further. Without interpolation the distribution of the localisations does not look as random as expected if the localisation precision was primarily determined by noise. Interpolation to square pixels of $\lambda/20$ prior to intensity thresholding, results in a much smoother distribution. It is important to note that this should be performed before intensity thresholding, as otherwise the gridding artefact will persist due to the thresholding of large pixels having a significant impact on the shape of the PSF. Centroid localisation may be less affected than onset localisation because centroiding uses all the PSF pixels whereas the axial position of the signal onset is determined only by two columns about the lateral centroid location. Following interpolation, these adjacent columns are likely to be more similar than if they also included information from the edges of the PSF. This could also be why small PSFs in the case of noise/weaker signals were also more affected.

Overall, this phantom was the easiest to use and manufacture out of the four options tested in this chapter. This meant that it could already by used to investigate interesting research questions related to SRUS such as the degree of interpolation.

5.7.3 Sacrificial sugar structures

This method was a novel application of a technique originally designed to fabricate a 3D tissue culture scaffold to fabricating a microvascular US phantom. There are many materials which could be considered for use as sacrificial structures. The benefit of this approach was that the carbohydrate recipe had been previously shown to quickly and easily dissolve within a material (low melt agar) suitable as a TMM. This dissolution of the structure could be performed using water within a few minutes. The integrity of the surrounding low melt agar was not affected - as it might have been if a harsher solvent was required. Moreover, Miller et al., (2012) had intentionally designed and iterated the recipe to enable easy dissolution. The results showed that not all US TMMs will be suitable for use with the sugar scaffolds. For example, paraffin wax was more likely to cause the structures to dissolve than the low melt agar. Thus the surrounding material of low melt agar, as trialled in Miller et al., (2012) was also used in this chapter.

The results showed that the sugar spinning method could fabricate channels with diameters < 50 μm. Figure 5-26 shows that the channels left by these structures could accommodate MB flow and SRUS was possible. Out of the four phantoms tested, this example enabled the most tortuous perfusable vessels to be fabricated. In future work, it would be interesting to use these phantoms to assess the efficacy of using SRUS to make structural measures of tortuosity and distance which previous literature has suggested is useful for the diagnosis of malignancy [121].

Of particular interest is that, Figure 5-26 shows that, the SRUS protocol used has not detected all of the perfused vessels. Having this ground truth allows such issues to be identified, and the reasons/solutions investigated in the future. In contrast to the agar-tubing, the FWHM of the SRUS image of two example vessels was less than expected based on the widths measured using the optical microscope. This could suggest that the MB distribution was not uniform across the channels generated. Another point to note is that most of the images of the phantoms in this chapter were generated using the IQ data. Figure 5-26 shows that the PW data provided a

poor visualisation of the structures due to increased noise, compared to when IQ data was used. Other authors have noted the need to develop methods to counter the low SNR of PW imaging [119]. This is a topic for future work.

Initially it was hoped that the structures could be optically characterised before embedding in the TMM. This would prevent any distortion of the optical image due to uneven surrounding medium causing refraction, or changes to the structure during the process of extracting it from the US set-up and moving it to the optical microscope. However, by making the structures using a sugar spinning technique, it was not possible to ensure that the strands would be connected such that they could all be perfused. Thus, it was necessary to optically characterise the phantom after perfusion with dye. Future work could involve following a 3D printing approach of the scaffolds as in Miller et al., (2012). This would allow the structures to be designed to ensure perfusion.

One limitation of this method is that it may not be as suitable for fabricating 3D phantoms as expected. Although 3D structures were made during the sugar spinning process, they collapsed into a single plane during vitrification in the oven. This does make 2D imaging easier since the full phantom can be aligned with the imaging plane, but as research in SRUS moves in the direction of 3D imaging this could be a disadvantage. In future, several structures could placed in a 3D arrangement prior to pouring of the low melt agar.

For the phantom imaged using SRUS, some vessel leakage was observed during the optical imaging. Leakage is not ideal as it makes it more difficult to accurately measure the width of the channel over which MBs may exist. This was not observed in previous phantoms which had been stored in the 45^{o}C oven for a several days instead of being used straight away. In future, perhaps the scaffolds should be left to dry out for several days in order to reduce the possibility of any dampness affecting the efficacy of the coating.

Overall, referring to Table 5.6 the sacrificial sugar phantoms performed similarly to the extracted agar tubing (largely due to the use of the same TMM). Although they were more difficult and time consuming to fabricate, this phantom may be a

good option when more complex structures are required.

5.7.4 Leaf decellularisation

This method was motivated by the potential to take advantage of the natural vasculature branching structure of leaves. It was also desirable that the transparent, thin, vessel boundaries could enable this phantom to be visualised simultaneously optically and acoustically. However, this was judged the least successful phantom for SRUS which was investigated.

Optical imaging of MBs did show that perfusion of a range of vessel diameters (as low as 20 μm). However, difficulty in distinguishing the dye perfused leaf from the control sample meant that obtaining a ground truth of those vessels that could be perfused was challenging - a crucial criteria for a phantom. Instead, flowing particles were required to assess if the vessels were perfused. The phantoms were very delicate and the prolonged manipulation of the samples on the optical microscope set-up whilst perfusing MBs easily resulted in damage. Perhaps, in future work, this could be avoided by extracting a fraction of the leaf, with only a few perfusable vessels, which could be characterised optically and then easily registered to the SRUS image.

The preliminary SRUS image of a sample did hint at some potential as a vasculature phantom despite only 258 frames being processed. The petiole could be easily perfused and identified. Moreover, there was evidence of MBs flowing along smaller vessel branching from the petiole. Future work would be required to assess whether the decellularised vasculature had realistic acoustic properties compared to human vasculature. If so, perhaps the easily perfusable petiole would have applications for other flow applications where microvessels are not necessary.

5.8 Conclusion

Overall, this chapter has shown that the agar tube phantoms were the simplest for testing SRUS. Since this phantom has a reliable ground truth, there is potential to use the phantom to help investigate potential choices that have to be made in SRUS. For

example, the data collected using the agar tubing allowed investigation of the effect of interpolation choices, something that has not been previously characterised in the literature. SRUS images were also generated using the sacrificial sugar phantoms and future work could develop the methodology to make the fabrication of these more reliable. The 3D printed phantoms and leaf phantoms both showed more promise as US phantoms than perhaps expected, however the results from this work suggest that SRUS is unlikely to be the most appropriate application for these phantoms.

Chapter 6

Conclusion

The primary aim of this thesis was to develop validation tools for SRUS. This was motivated by the challenge of exploring the multitude of factors that affect SRUS *in vivo*, and the lack of existing realistic *in vitro* and *in silico* techniques suitable to provide a ground truth. SRUS is a rapidly emerging field with numerous groups proposing new strategies and improvements to the SRUS process. However, without a well-known and physiologically realistic ground truth it is challenging to compare and validate these techniques.

6.1 Main findings and contributions

The first contribution of this thesis was the introduction of a new simulation platform developed in order to simulate SRUS. This simulation is novel over the previous *in silico* investigations in the literature in that it incorporates the non-linear MB response, using an established MB model, with the nonlinear acoustic wave modelling of k-Wave. The simulation can incorporate different transducer models, MB sizes and MB/tissue movement.

The first application of this simulation platform was the comparison of MB detection techniques. Overall, this work has highlighted that the choice of detection technique is not inconsequential. Different detection techniques will be more appropriate for use with different acquisition parameters and different physiological conditions. In

particular, the velocity dependence of DI and SVD mean that they are less suitable for visualisation of tumour microvasculature than non-linear techniques such as PI.

A further application of the simulation was the identification and investigation of artifacts due to application of the SVD filter. Within a collaboration with other colleagues, the "smearing", "flashing" and "splitting" artifacts were investigated *in silico*, *in vitro* and in clinical data. The simulation allowed the factors which affected the artifacts to be more reliably controlled and fully investigated. This work elucidated the origin of the SVD artifacts and measures which could be taken to avoid them.

A further contribution of this thesis was the design of a simultaneous acoustic and optical rig to study SRUS of flowing MBs in a 200 μm cellulose tube. During this work the limitation of the relative DOFs of the optical and acoustic FOVs was highlighted, something that has not been discussed in previous literature. The improvement achievable from introducing an adjustable aperture into the optical microscope was quantified. However, the results showed that this idea was insufficient for extending the DOF over the full tube. Despite this set-up not allowing the effect of the MB environment on SRUS to be optically validated as intended, this work did provide insight into performing SRUS at low flow speeds in this *in vitro* environment. *In silico* and *in vitro* results have shown that the MB distribution is not uniform over the tube extent due to buoyancy. This raises an interesting question for future research about whether buoyancy might also affect the SRUS profiles obtained during *in vivo* imaging. The results of this chapter could also be used by future researchers to guide their choice of tube diameter in similar set-ups. The effect of buoyancy at slow flows makes it challenging to achieve a constant dilute MB concentration due to MBs floating to rest at the top of the tube. It is suggested that vessels of diameters closer to the capillary scale be used to avoid this problem. Achieving a constant flowing concentration of MBs would also be useful when investigating how to achieve strong MB signal without MB destruction - a key challenge identified during this work. Furthermore, using vessels of smaller diameters will also avoid problems associated with the limited optical DOF by making it easier to optically detect MBs over the full

phantom extent.

An observation from acoustic images obtained during the work of Chapter 3, led to the contribution of a new signal processing strategy to avoid the saturation artefact commonly observed when operating at gains suitable for contrast imaging. High dynamic range non-linear imaging has the potential for use with SRUS and the field of CEUS more widely.

The final contribution of this thesis was the fabrication and comparison of four potential microvasculature phantoms for SRUS. The two most successful phantoms considered were the wire extrusion phantoms and the sacrificial sugar phantoms. The agar channels fabricated in this thesis are the smallest wire extrusions channels that have been shown to sustain flow and generate a SRUS image. The sacrificial sugar structures are a novel SRUS phantom option that have the potential to mimic tortuous vessels.

6.2 Future work

The results of this thesis also have implications for potential directions of future work. In particular, there are some key research questions which the tools developed during this work are well posed to investigate.

6.2.1 Application of simulation to investigate effect of aberration

Aberration is distortion of the wavefront due to inhomogeneous acoustic properties of the medium [261]. When different sections of the wavefront propagate through regions with different sound speeds, the different wavefront sections experience different non-geometric path lengths. This changes the shape of the wavefront. When the image is beamformed, assuming a constant sound speed, resolution will be degraded. Understanding the degree to which SRUS will be affected by aberration is an important step in assessing the depth capabilities of SRUS.

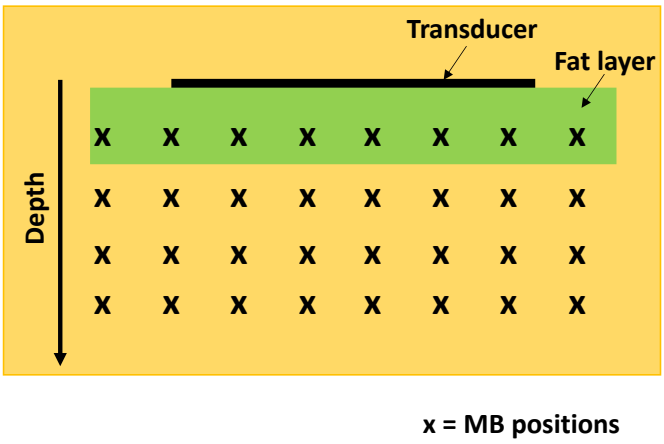

Figure 6-1: Simulation geometry to investigate aberration.

This work has been started with the help of project student C. Salib. A possible means of investigating the effect of aberration using the simulation was developed. The proposed simulation would involve a grid of MBs relative to layers/or other clinically relevant distributions of fat. One embodiment of this investigation, wherein aberration due to a layer of fat is modelled, is shown in Figure 6-1. The grid formulation would allow the effects of aberration on resolution and position of beamformed MB signals over the FOV to be quantified. The simulation would be particularly useful for investigating any change in localisation position of the scatterers caused by aberration because the true MB positions are well known.

Previous authors have discussed how a point scatterer in the FOV can be used to correct for aberration [262]. Unfortunately, this is generally unfeasible *in vivo*. However, assuming that MBs can be well approximated as spherical scatterers, perhaps such correction methods would be relatively straight forward to adapt for aberration correction of SRUS. This is an exciting area for future study.

6.2.2 Application of simulation to compare statistical and localisation methods

There is clear motivation to increase the acquisition speed of SRUS. Bar Zion et al. (2017), suggest that their technique, given that images can be generated at a temporal

resolution of <1s which is appropriate for imaging flow dynamics [129]. As discussed in Chapter 1, this technique is one of several [129, 130, 131, 132] that operate at higher MB concentrations than suitable for localisation microscopy.

It can be very difficult to fully compare these techniques *in vivo*, or even *in vitro*, settings as they perform best over different time scales and MB concentrations. Moreover, it will require investigators which have an interest in both approaches such as the optimum acquisition parameters for both methods can be applied. A topic for future work is the use of the simulation presented in Chapter 2 to compare these approaches. Ultimately, it may be possible to use both techniques complementarily. For example, consistently low concentration of MBs can be challenging to achieve *in vivo* and consequently it could be beneficial to use both techniques so that data could be used more efficiently.

6.2.3 Combination of agar tubing and optical set-up

The results of Chapter 3 showed that 200 μm tubes may have too large a diameter due to the effects of buoyancy and limited optical DOF. MBs could however be detected over 50 μm, therefore it would be interesting to use the wire extrusion phantoms developed in Chapter 5 with the optical set-up. The low melt agar is already optically transparent. The next step would be careful design of the 3D printed holder to enable incorporation with the optical set-up. Using the smaller tubing could make the investigation of how MB environment affects localisation easier.

One of the challenges encountered during the work of Chapter 3 was obtaining a sufficiently high SNR of a low concentration of slowly flowing MBs. SNR limitations of PW imaging also motivated the use of a focused mode when testing the phantom options in Chapter 5. The need to counter the relatively poor SNR of PW relative to focused mode for SRUS has already been raised in the literature [119]. However, this is topic where significant future research could be useful. Using this proposed set-up could allow the effect of potential approaches such as; varying amplitude and/or framerate, introducing compounding, or signal processing/tracking approaches on flowing MBs to be investigated.

Investigation of monodisperse MBs for SRUS

There is motivation to develop monodisperse agents for applications beyond SRUS because they can be tailored to improve imaging sensitivity [263, 264] and ensure more consistent drug delivery [265]. For SRUS in particular, there is motivation to develop monodisperse MBs both to increase agent sensitivity and ensure less variation between MB signals.

Both the optical and simulation results have shown motivation for tuning MBs size for SRUS. MBs of radii 1 μm and 0.5 μm generally contributed the least to the signal using both the linear and non-linear techniques during the work of Chapter 2. This relates well to the work by Gorce et al. (2000) where MBs of radii < 1 μm were found to not significantly contribute to the overall echogenicity [191]. Previous work considering the application of monodisperse MBs for SRUS has also suggested that larger MBs are preferred [122, 196]. However, as shown in the simulation, the most appropriate MB size depends on the transmit frequency, probe bandwidth and detection method. For example, referring to Figure 2.5.2 when PI was performed at a transmit frequency of (2 MHz), the smaller MBS (of radii 2 μm and 3 μm) generated a higher CTR than the larger MBs (of radii 4 μm and 5 μm). Using the optical set-up it was shown that flow rate may have an impact on the size of MBs in the optical FOV. The effects of buoyancy meant that the larger MBs were more likely to float to the top of the tube than the smaller MBs which could more easily move through the FOV. This size selection may also contribute to why less acoustic signal can be observed at slower flow rates. In future work it will be important to understand how practical factors which unintentionally affect the size distribution such as lung filtration [266], flow rate [267], and needle gauge [267, 268] all influence SRUS images.

Overall, future work is required to investigate the influence of using a polydisperse agent for SRUS and the potential of monodisperse MBs to improve images.

6.2.4 Application of sacrificial sugar phantoms to assess SRUS quantification of tortuosity

One potential clinical application of SRUS is the extraction of parameters such as tortuosity and distance between vessels which can be used to identify pathological tissue [20, 121]. Previously, the structural measures have been extracted without a ground truth of individual vessels - instead relying on bulk measurements of the overall sample. Thus, it is not possible to assess how accurately the SRUS protocol is capturing the complex vessel shapes. Aside from the relatively large spiral phantoms used in [114] the sugar scaffolds are the first microvascular phantoms which can be used to generate complex structures. Future work could involve assessing how accurately SRUS images these channels and how long data needs to be acquired to identify pathology.

Appendix A

Convergence testing for simulation toolbox.

A.1 Motivation

The spatial discretisation and temporal discretisation may introduce numerical error which affects the phase and amplitude of measured pressures. Thus convergence tests, which mimic the following experiments as closely as possible, were required to ensure that any numerical error is at an acceptable level. As this work incorporates the highly non-linear MB signal, where it is important to resolve at least the 2nd harmonic, the wavelength is defined as twice the transmit frequency. Due to the limitations of defining the transducer geometry on the k-Wave grid, the lateral discretisation was set to be a constant 20 μm to match the probe pitch value. By varying the ppw (from 2 ppw to 10 ppw) and CFL value (from 0.005 to 0.5), see Equation 2.30, convergence tests were performed.

A.2 Methods

Propagation in homogeneous medium

This test was designed to be most relevent to step 1 of the MB simulation process. A k-Wave sensor was used to measure the signal at the centre of the transducer, 7 mm axially from the probe. Care was taken to ensure that any rounding errors in positioning the source on grid points did not change the distance travelled for varying ppw, and that the effect of the staggered grid was corrected for. To keep computational times manageable, base values of CFL and ppw were chosen to be 0.05 and 5 respectively. That is, for testing the effect of ppw the CFL value was set to 0.05. A transmit pulse frequency of 4 MHz was used here, and the LA332 probe modelled. Phase error was determined by calculating the shift between the signal peaks for each signal with respect to the simulation output performed at the finest discretisation. Using the phase error to shift the signal, the amplitude error was calculated by taking the root mean squared (RMS) error between each signal and that determined at the finest discretisation.

Propagation in heterogeneous medium

An identical procedure to that with homogenous medium was performed using the tissue distribution used for later experiments and provided in Figure 2-5. The grid sizes were slightly different for each ppw value as the dimensions were set to have low prime factors to increase the speed of the k-Wave simulation [182]. To keep the tissue geometry the same at the point where the signal was measured, the distribution was cropped to fit the smallest grid size. Random inhomogeneity was not included here as it would cause variation to the propagation medium for varying pixel dimensions which may affect the received signal.

Non-linear MB signal

It is necessary to investigate how the grid discretisation impacts the non-linear MB signal. The MB response for a 2 MHz transmit pulse was propagated back to the probe

position and the Fourier transform calculated. For this experiment no transducer bandwidth was modelled to ensure non-linear signal components were not removed. The fraction of linear signal was found by integrating the frequency spectrum between 1.6 MHz and 3.4 MHz and dividing by the total area under the frequency plot between 0 MHz and 12 MHz. Non-linear signal was considered to be contained between a transmit frequency of 3.4 MHz and 12 MHz. No sub-harmonics were observed for this set of parameters. The RMS error of the percentage of linear and non-linear signal was calculated relative to the finest discretisation investigated.

Resolving small movements

Any error in absolute position caused by numerical choices is less important than error that is not consistent and will cause relative errors when consider moving scatterers. The effect of ppw choice on relative movement was investigated by putting the sensor at the MB position and at 0.1 μm increments axially about the MB position. The delay between the signals received was found using the correlation-based MATLAB function "finddelay()". The RMS error between this value and the known step size was calculated.

A.3 Results

Figure A-1 shows the results of the convergence tests for homogeneous and heterogeneous media. There is no significant different between the discretisations required for heterogeneous media compared to homogeneous. Appropriate ppw choice is more important than CFL choice for limiting numerical error. Working at a grid spatially discretised to match the Nyquist limit of 2 ppw can introduce amplitude error up to 10 kPa compared to performing the simulation at 10 ppw. The results suggest that simulation performed at ≥ 6 ppw and CFL ≤ 0.05 will result in phase error $< 1^o$ and amplitude error < 1 kPa.

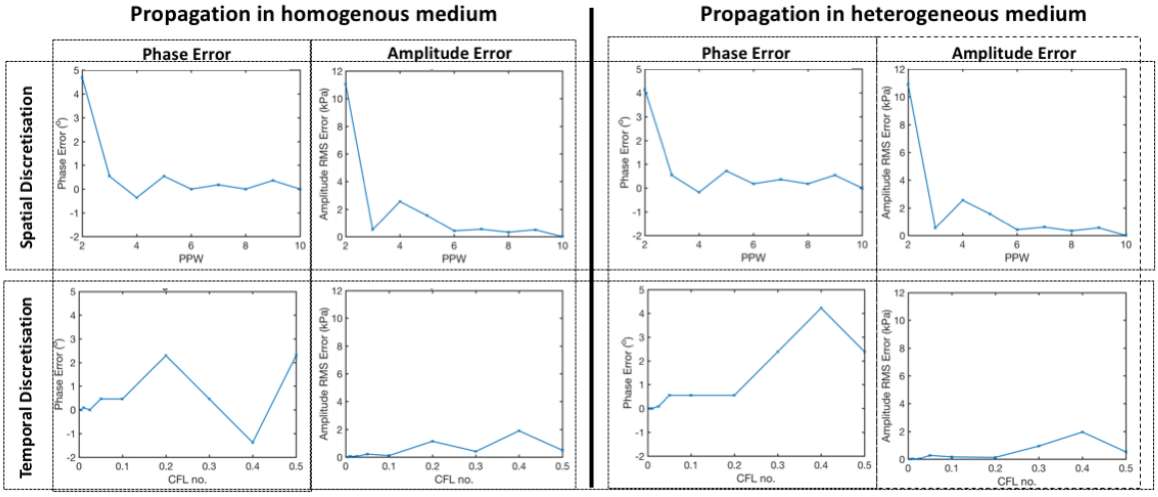

Figure A-1: Convergence testing for homogenous and heterogeneous media. Dependence of numerical error on ppw (top) and CFL (bottom) for propagation through homogenous (left) and heterogeneous media (right).

Figure A-2 shows that the fraction of the non-linear signal components has a small percentage error relative to simulations performed at the finest discretisations. Again a spatial discretisation of ≥ 6 ppw is recommended.

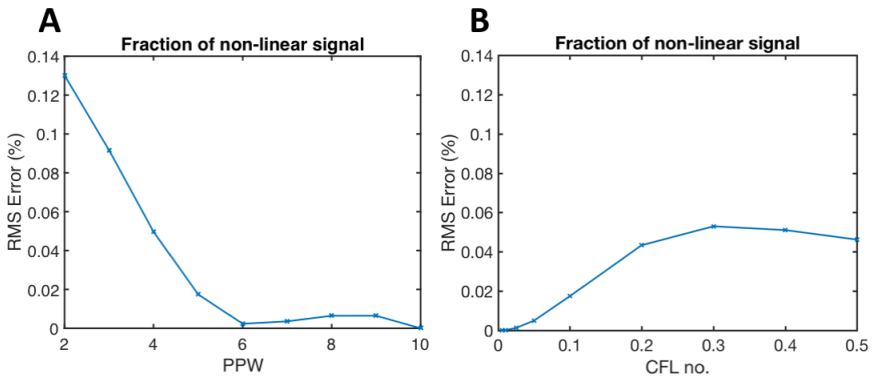

Figure A-2: Converging testing, considering MB non-linear signal. Dependence of preservation of non-linear MB signal components on ppw (A) and CFL (B).

Assuming a bulk sound speed of 1570 m/s, a frequency of 4 MHz, and a phase error on the order of 1^o (as expected from Figure A-1), there may be a error in the signal position of ≈ 2 µm. This may be problematic when investigating the lowest

MB speeds, as the MBs will move less than 2 µm between frames. Fortunately, Figure A-3 shows relative motion at each ppw has less error. For a MB speed of 1 mm/s and PRF of 1000 Hz, a ppw ≥ 4 will give an estimated percentage error of $< 5\%$.

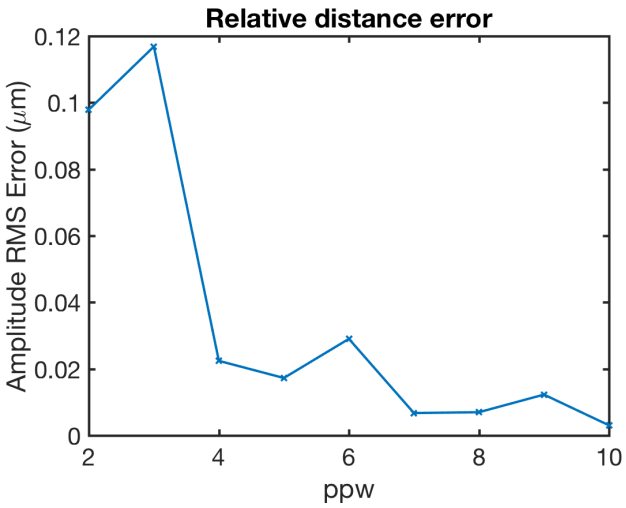

Figure A-3: Dependence of movement resolution on ppw.

A.4 Conclusion

The use of the Fourier Spectral method for solving the wave equations reduces computational time but is not without compromises. For example, inappropriate temporal and spatial discretisation of the grid may introduce inaccuracies and numerical instability. The results presented in Figures A-1, A-2 and A-3 have aimed to replicate the parameters used in simulations during this thesis. By using a ppw ≥ 6 and CFL ≤ 0.05, we can ensure a degree of phase error $< 1^o$ and amplitude error < 1 kPa.

Appendix B

Methodology of *in vitro* and clinical experiments within the SVD collaboration

Artifacts associated with SVD clutter filtering were more fully explored through collaboration. The methodology of the *in vitro* experiments (performed by J. Zhu) and clinical experiments (performed by F. Xu and P. Huang) are provided here for reference.

B.0.1 *In vitro*

In vitro experiments used a 300 μm tube embedded in a TMM [269]. MBs (made in-house) of concentration approximately equal to 2.5 x 10^7 MB/mL were injected into the tube using a programmable syringe pump (Harvard Apparatus Programmable PHD2000 pump, Harvard Apparatus UK, Cambridge, United Kingdom) which controlled the mean flow velocities at 4, 10 and 80 mm/s. Plane wave data was collected using a linear probe L12-3v and research system (Verasonics Vantage 128). A sequence with 5-angle compounding plane wave (angle range of 20^o) at centre frequency of 4 MHz, MI of 0.11 and frame rate of 1000 Hz was used. Compounded and beamformed images were filtered using various stack sizes (1000, 500, 250, 100 and 50 frames).

CTR was measured by taking a MB ROI around the vessel phantom and a background ROI 3 mm above the MB ROI. The CTR was computed as the mean pixel intensity of the MB ROI over the mean pixel intensity over the tissue region.

B.0.2 Clinical

In vitro contrast data of a human cervical lymph node was collected using a clinical scanner (EPIQ 7, Philips,Bothell,WA,USA) using a L12-3 linear array transducer in penetration frequency mode. A 1.2 mL bolus of Sonovue MBs was injected, followed by a 5 ml saline flush. To achieve a concentration suitable for SR, destruction pulses with a MI of 0.75 were used. This was followed by imaging at an MI of 0.06 and framerate of 62 Hz using the penetration frequency mode. 471 frames were acquired for SVD processing.

Appendix C

Calibration Table for the ULA-OP Amplitude Setting

This ULA-OP amplitude setting at a centre frequency of 4 MHz was calibrated using a 0.2 mm hydrophone needle (Precision Acoustics, Dorchester, UK). The results are presented below in Table C.1 for the *in vitro* work in chapter 3.

ULA-OP Amplitude Setting	**Peak Negative Pressure (MPa)**	**MI**
0.1	-0.03	0.01
0.2	-0.06	0.03
0.3	-0.08	0.04
0.4	-0.11	0.05
0.5	-0.14	0.07
0.6	-0.17	0.09
0.7	-0.20	0.2
0.8	-0.22	0.11
0.9	-0.25	0.12
1.0	-0.27	0.14

Table C.1: Calibration of ULA-OP amplitude.

Bibliography

[1] M. O. Culjat, D. Goldenberg, P. Tewari, and R. S. Singh, "A review of tissue substitutes for ultrasound imaging," *Ultrasound in Medicine & Biology*, vol. 36, no. 6, pp. 861–873, 2010.

[2] B. M. Koeppen and B. A. Stanton, *Berne & Levy Physiology, Updated Edition E-Book*. Elsevier Health Sciences, 2009.

[3] J. E. Hall, *Guyton and Hall textbook of medical physiology*. Elsevier Health Sciences, 2015.

[4] InformedHealth.org [Internet], "How does the blood circulatory system work?," Jan 2019. `https://www.ncbi.nlm.nih.gov/books/NBK279250/` Last accessed on 2019-11-30.

[5] B. Alberts, A. Johnson, J. Lewis, M. Raff, K. Roberts, and P. Walter, *Blood Vessels and Endothelial Cells*. Garland Science, 2002.

[6] J. Tam, P. Tiruveedhula, and A. Roorda, "Characterization of single-file flow through human retinal parafoveal capillaries using an adaptive optics scanning laser ophthalmoscope," *Biomedical Optics Express*, vol. 2, no. 4, pp. 781–793, 2011.

[7] L. Weiss, F. W. Orr, and K. V. Honn, "Interactions of cancer cells with the microvasculature during metastasis," *The FASEB journal*, vol. 2, no. 1, pp. 12–21, 1988.

[8] L. Weiss, "Biomechanical interactions of cancer cells with the microvasculature during hematogenous metastasis," *Cancer and Metastasis Reviews*, vol. 11, no. 3-4, pp. 227–235, 1992.

[9] P. Carmeliet and R. K. Jain, "Angiogenesis in cancer and other diseases," *Nature*, vol. 407, no. 6801, pp. 249–257, 2000.

[10] W. V. Brown, "Microvascular complications of diabetes mellitus: renal protection accompanies cardiovascular protection," *The American Journal of Cardiology*, vol. 102, no. 12, pp. 10L–13L, 2008.

[11] Q. Gong, E. W. Gregg, J. Wang, Y. An, P. Zhang, W. Yang, H. Li, Y. Jiang, Y. Shuai, and B. Zhang, "Long-term effects of a randomised trial of a 6-year lifestyle intervention in impaired glucose tolerance on diabetes-related microvascular complications: the China Da Qing Diabetes Prevention Outcome Study," *Diabetologia*, vol. 54, no. 2, pp. 300–307, 2011.

[12] P. G. Camici and F. Crea, "Coronary microvascular dysfunction," *New England Journal of Medicine*, vol. 356, no. 8, pp. 830–840, 2007.

[13] A. R. Nelson, M. D. Sweeney, A. P. Sagare, and B. V. Zlokovic, "Neurovascular dysfunction and neurodegeneration in dementia and Alzheimer's disease," *Biochimica et Biophysica Acta (BBA)-Molecular Basis of Disease*, vol. 1862, no. 5, pp. 887–900, 2016.

[14] T. H. Adair and J.-P. Montani, "Angiogenesis," in *Colloquium Series on Integrated Systems Physiology: From Molecule to Function*, vol. 2, pp. 1–84, Morgan & Claypool Life Sciences, 2010.

[15] P. Carmeliet and R. K. Jain, "Principles and mechanisms of vessel normalization for cancer and other angiogenic diseases," *Nature Reviews Drug Discovery*, vol. 10, no. 6, pp. 417–427, 2011.

[16] R. K. Jain, "Cancer Cell Antiangiogenesis Strategies Revisited: From Starving Tumors to Alleviating Hypoxia," *Cancer Cell*, vol. 26, pp. 605–622, 2014.

[17] J. C. Miller, H. H. Pien, D. Sahani, A. G. Sorensen, and J. H. Thrall, "Imaging angiogenesis: Application and potential for drug development," *Journal of the National Cancer Institute*, vol. 97, pp. 172–187, feb 2005.

[18] M. Siepmann, G. Schmitz, J. Bzyl, M. Palmowski, and F. Kiessling, "Imaging tumor vascularity by tracing single microbubbles," in *Ultrasonics Symposium (IUS), 2011 IEEE International*, pp. 1906–1909, IEEE, 2011.

[19] S. Dencks, M. Piepenbrock, T. Opacic, B. Krauspe, E. Stickeler, F. Kiessling, and G. Schmitz, "Clinical pilot application of super-resolution US imaging in breast cancer," *IEEE Transactions on Ultrasonics, Ferroelectrics, and Frequency Control*, 2018.

[20] T. Opacic, S. Dencks, B. Theek, M. Piepenbrock, D. Ackermann, A. Rix, T. Lammers, E. Stickeler, S. Delorme, and G. Schmitz, "Motion model ultrasound localization microscopy for preclinical and clinical multiparametric tumor characterization," *Nature Communications*, vol. 9, no. 1, p. 1527, 2018.

[21] J. Fang, H. Nakamura, and H. Maeda, "The EPR effect: unique features of tumor blood vessels for drug delivery, factors involved, and limitations and augmentation of the effect," *Advanced Drug Delivery Reviews*, vol. 63, no. 3, pp. 136–151, 2011.

[22] J. T. Bushberg, *The essential physics of medical imaging*. Lippincott Williams & Wilkins, 2002.

[23] M. E. Ladd, P. Bachert, M. Meyerspeer, E. Moser, A. M. Nagel, D. G. Norris, S. Schmitter, O. Speck, S. Straub, and M. Zaiss, "Pros and cons of ultra-high-field MRI/MRS for human application," *Progress in Nuclear Magnetic Resonance Spectroscopy*, vol. 109, pp. 1–50, dec 2018.

[24] S. C. Kale, X. J. Chen, and R. M. Henkelman, "Trading off SNR and resolution in MR images," *NMR in Biomedicine*, vol. 22, no. 5, pp. 488–494, 2009.

[25] A. Nowogrodzki, "The world's strongest MRI machines are pushing human imaging to new limits," *Nature*, vol. 563, pp. 24–26, nov 2018.

[26] Siemens Healthineers, "Translate 7T research power into clinical care MAGNETOM Terra," 2019. `https://www.siemens-healthineers.com/en-uk/magnetic-resonance-imaging/7t-mri-scanner/magnetom-terra` Last accessed on 2019-09-23.

[27] D. Stucht, K. A. Danishad, P. Schulze, F. Godenschweger, M. Zaitsev, and O. Speck, "Highest resolution in vivo human brain MRI using prospective motion correction," *PLoS ONE*, vol. 10, jul 2015.

[28] L. Johansson, "Translational imaging research," in *Principles of Translational Science in Medicine*, pp. 189–194, Elsevier, 2015.

[29] E. Lin and A. Alessio, "What are the basic concepts of temporal, contrast, and spatial resolution in cardiac CT?," *Journal of Cardiovascular Computed Tomography*, vol. 3, pp. 403–408, nov 2009.

[30] H. Lusic and M. W. Grinstaff, "X-ray-computed tomography contrast agents," *Chemical Reviews*, vol. 113, pp. 1641–1666, mar 2013.

[31] E. Shefer, A. Altman, R. Behling, R. Goshen, L. Gregorian, Y. Roterman, I. Uman, N. Wainer, Y. Yagil, and O. Zarchin, "State of the art of CT detectors and sources: a literature review," *Current Radiology Reports*, vol. 1, no. 1, pp. 76–91, 2013.

[32] P. K. Upputuri, K. Sivasubramanian, C. S. K. Mark, and M. Pramanik, "Recent developments in vascular imaging techniques in tissue engineering and regenerative medicine," *BioMed Research International*, vol. 2015, 2015.

[33] C. M. Downey, A. K. Singla, M. L. Villemaire, H. R. Buie, S. K. Boyd, and F. R. Jirik, "Quantitative Ex-vivo micro-computed tomographic imaging of blood vessels and necrotic regions within tumors," *PLoS ONE*, vol. 7, jul 2012.

[34] I. Willekens, N. Buls, T. Lahoutte, L. Baeyens, C. Vanhove, V. Caveliers, R. Deklerck, A. Bossuyt, and J. De Mey, "Evaluation of the radiation dose in micro-CT with optimization of the scan protocol," *Contrast Media and Molecular Imaging*, vol. 5, pp. 201–207, jul 2010.

[35] T. E. Peterson and L. R. Furenlid, "SPECT detectors: The Anger Camera and beyond," *Physics in Medicine and Biology*, vol. 56, sep 2011.

[36] K. Van Audenhaege, R. Van Holen, S. Vandenberghe, C. Vanhove, S. D. Metzler, and S. C. Moore, "Review of SPECT collimator selection, optimization, and fabrication for clinical and preclinical imaging," *Medical Physics*, vol. 42, pp. 4796–4813, aug 2015.

[37] J. A. Sorenson, S. R. Cherry, and Phelps, "Chapter 14 - Gamma Camera Performance," in *Physics in Nuclear Medicine*, ch. 14, Elsevier, 2012.

[38] C. Bouckaert, S. Vandenberghe, and R. Van Holen, "Evaluation of a compact, high-resolution SPECT detector based on digital silicon photomultipliers," *Physics in Medicine and Biology*, vol. 59, pp. 7521–7539, dec 2014.

[39] A. Rahmim and H. Zaidi, "PET versus SPECT: strengths, limitations and challenges," *Nuclear Medicine Communication*, vol. 29, no. 3, pp. 193–207, 2008.

[40] W. W. Moses, "Fundamental limits of spatial resolution in PET," *Nuclear Instruments and Methods in Physics Research, Section A: Accelerators, Spectrometers, Detectors and Associated Equipment*, vol. 648, aug 2011.

[41] W. Cai, K. Chen, Z.-B. Li, S. S. Gambhir, and X. Chen, "Dual-function probe for PET and near-infrared fluorescence imaging of tumor vasculature," *Journal of Nuclear Medicine*, vol. 48, no. 11, pp. 1862–1870, 2007.

[42] S. Shi, K. Yang, H. Hong, H. F. Valdovinos, T. R. Nayak, Y. Zhang, C. P. Theuer, T. E. Barnhart, Z. Liu, and W. Cai, "Tumor vasculature targeting and imaging in living mice with reduced graphene oxide," *Biomaterials*, vol. 34, no. 12, pp. 3002–3009, 2013.

[43] "DiffractionLimit | Scientific Volume Imaging." https://svi.nl/DiffractionLimit, Last accessed on 2019-09-23.

[44] G. Huszka and M. A. Gijs, "Super-resolution optical imaging: A comparison," *Micro and Nano Engineering*, vol. 2, pp. 7–28, mar 2019.

[45] "The diffraction barrier in optical microscopy | microscopyu." https://www.microscopyu.com/techniques/super-resolution/the-diffraction-barrier-in-optical-microscopy Last accessed on 2019-09-19.

[46] J. Allen and K. Howell, "Microvascular imaging: techniques and opportunities for clinical physiological measurements.," *Physiological Measurement*, vol. 35, pp. R91–R141, jul 2014.

[47] J. L. Sandell and T. C. Zhu, "A review of in-vivo optical properties of human tissues and its impact on PDT.," *Journal of Biophotonics*, vol. 4, pp. 773–87, nov 2011.

[48] D. Huang, E. A. Swanson, C. P. Lin, J. S. Schuman, W. G. Stinson, W. Chang, M. R. Hee, T. Flotte, K. Gregory, and C. A. Puliafito, "Optical coherence tomography," *Science (New York, NY)*, vol. 254, no. 5035, p. 1178, 1991.

[49] P. N. T. Wells, "Ultrasound imaging," *Physics in Medicine and Biology*, vol. 51, no. 13, p. R83, 2006.

[50] P. R. Hoskins, K. Martin, and A. Thrush, *Diagnostic ultrasound: physics and equipment*. Cambridge University Press, 2010.

[51] G. Montaldo, M. Tanter, J. Bercoff, N. Benech, and M. Fink, "Coherent plane-wave compounding for very high frame rate ultrasonography and transient elastography," *IEEE Transactions on Ultrasonics, Ferroelectrics, and Frequency Control*, vol. 56, no. 3, pp. 489–506, 2009.

[52] O. Couture, S. Bannouf, G. Montaldo, J.-F. Aubry, M. Fink, and M. Tanter, "Ultrafast imaging of ultrasound contrast agents," *Ultrasound in Medicine & Biology*, vol. 35, no. 11, pp. 1908–1916, 2009.

[53] P. Y. Barthez, R. Léveillé, and P. V. Scrivani, "Side lobes and grating lobes artifacts in ultrasound imaging.," *Veterinary Radiology & Ultrasound : The Official Journal of the American College of Veterinary Radiology and the International Veterinary Radiology Association*, vol. 38, no. 5, pp. 387–93, 1997.

[54] T. L. Szabo, *Diagnostic Ultrasound Imaging: Inside Out: Second Edition*. Elsevier Inc., 2004.

[55] J. A. Jensen, "Ultrasound imaging and its modeling," in *Imaging of Complex Media with Acoustic and Seismic Waves*, pp. 135–166, Springer, 2002.

[56] D. R. Dance, S. Christofides, A. D. A. Maidment, and I. D. McLean, *Diagnostic radiology physics: A handbook for teachers and students Endorsed by: American Association of Physicists in Medicine, Asia-Oceania Federation of Organizations for Medical Physics, European Federation of Organisations for Medical Physics*. International Atomic Energy Agency (IAEA): IAEA, 2014.

[57] T. Ilovitsh, A. Ilovitsh, J. Foiret, B. Z. Fite, and K. W. Ferrara, "Acoustical structured illumination for super-resolution ultrasound imaging," *Communications Biology*, vol. 1, no. 1, p. 3, 2018.

[58] Z. Alomari, S. Harput, S. Hyder, and S. Freear, "The effect of the transducer parameters on spatial resolution in plane-wave imaging," in *Ultrasonics Symposium (IUS), 2015 IEEE International*, pp. 1–4, IEEE, 2015.

[59] G. ter Haar, "Ultrasonic imaging: Safety considerations," *Interface Focus*, vol. 1, no. 4, pp. 686–697, 2011.

[60] F. A. Duck, "Hazards, risks and safety of diagnostic ultrasound.," *Medical Engineering & Physics*, vol. 30, pp. 1338–48, dec 2008.

[61] G. ter Haar, "Safety and bio-effects of ultrasound contrast agents.," *Medical & Biological Engineering & Computing*, vol. 47, pp. 893–900, aug 2009.

[62] L. Bassi, E. Boni, A. Dallai, F. Guidi, S. Ricci, and P. Tortoli, "ULA-OP: A novel ultrasound advanced open platform for experimental research," in *Proceedings - IEEE Ultrasonics Symposium*, pp. 632–635, 2007.

[63] D. Cosgrove, "Ultrasound contrast agents: an overview," *European Journal of Radiology*, vol. 60, no. 3, pp. 324–330, 2006.

[64] C. Greis, "Ultrasound contrast agents as markers of vascularity and microcirculation," *Clinical Hemorheology and Microcirculation*, vol. 43, no. 1-2, pp. 1–9, 2009.

[65] R. Gramiak and P. Shah, "Echocardiography of the Aortic Root. : Investigative Radiology," *Investigative Radiology*, vol. 3, no. 5, pp. 356–366, 1968.

[66] S. Fan, T. Nagai, H. Luo, S. Atar, T. Naqvi, Y. Birnbaum, S. Lee, and R. J. Siegel, "Superiority of the combination of blood and agitated saline for routine contrast enhancement.," *Journal of the American Society of Echocardiography : Official Publication of the American Society of Echocardiography*, vol. 12, pp. 94–8, feb 1999.

[67] S. K. Gupta, S. S. Shetkar, S. Ramakrishnan, and S. S. Kothari, "Saline contrast echocardiography in the era of multimodality imaging - Importance of bubbling it right," *Echocardiography*, vol. 32, pp. 1707–1719, nov 2015.

[68] T. Faez, M. Emmer, K. Kooiman, M. Versluis, A. F. W. van der Steen, and N. de Jong, "20 years of ultrasound contrast agent modeling," *IEEE Transactions on Ultrasonics, Ferroelectrics, and Frequency Control*, vol. 60, no. 1, 2013.

[69] V. Paefgen, D. Doleschel, and F. Kiessling, "Evolution of contrast agents for ultrasound imaging and ultrasound-mediated drug delivery," *Frontiers in Pharmacology*, vol. 6, no. SEP, 2015.

[70] M. Blomley, M. Claudon, and D. Cosgrove, "WFUMB safety symposium on ultrasound contrast agents: Clinical applications and safety concerns," *Ultrasound in Medicine and Biology*, vol. 33, pp. 180–186, feb 2007.

[71] V. Rafailidis, A. Deganello, T. Watson, P. S. Sidhu, and M. E. Sellars, "Enhancing the role of paediatric ultrasound with microbubbles: a review of intravenous applications.," *The British Journal of Radiology*, vol. 90, p. 20160556, jan 2017.

[72] European Medicines Agency, "ANNEX I SUMMARY OF PRODUCT CHARACTERISTICS," tech. rep. `https://www.ema.europa.eu/en/documents/product-information/sonovue-epar-product-information_en.pdf` Last accessed on 2019-09-23.

[73] S. R. Sirsi and M. A. Borden, "Microbubble compositions, properties and biomedical applications," *Bubble Science, Engineering and Technology*, vol. 1, no. 1-2, pp. 3–17, 2009.

[74] T. Kokate and A. Laniyonu, "Review and Evaluation of Pharmacology and Toxicology Data Division of Medical Imaging and Radiopharmaceutical Drug Products," tech. rep., 2004.

[75] N. De Jong, A. Bouakaz, and P. Frinking, "Basic acoustic properties of microbubbles," *Echocardiography*, vol. 19, no. 3, pp. 229–240, 2002.

[76] P. A. Dayton, K. E. Morgan, A. L. Klibanov, G. H. Brandenburger, and K. W. Ferrara, "Optical and acoustical observations of the effects of ultrasound on contrast agents," *IEEE Transactions on Ultrasonics, Ferroelectrics, and Frequency Control*, vol. 46, no. 1, pp. 220–232, 1999.

[77] V. Garbin, D. Cojoc, E. Ferrari, E. Di Fabrizio, M. L. J. Overvelde, S. M. Van Der Meer, N. De Jong, D. Lohse, and M. Versluis, "Changes in microbubble dynamics near a boundary revealed by combined optical micromanipulation and high-speed imaging," *Applied Physics Letters*, vol. 90, no. 11, p. 114103, 2007.

[78] J. Sijl, H. J. Vos, T. Rozendal, N. de Jong, D. Lohse, and M. Versluis, "Combined optical and acoustical detection of single microbubble dynamics," *The Journal of the Acoustical Society of America*, vol. 130, no. 5, pp. 3271–3281, 2011.

[79] P. A. Dayton, K. E. Morgan, A. L. Klibanov, G. Brandenburger, K. R. Nightingale, and K. W. Ferrara, "A preliminary evaluation of the effects of primary and secondary radiation forces on acoustic contrast agents," *IEEE Transactions on Ultrasonics, Ferroelectrics, and Frequency Control*, vol. 44, no. 6, pp. 1264–1277, 1997.

[80] P. Marmottant, S. van der Meer, M. Emmer, M. Versluis, N. de Jong, S. Hilgenfeldt, and D. Lohse, "A model for large amplitude oscillations of coated bubbles accounting for buckling and rupture," *The Journal of the Acoustical Society of America*, vol. 118, no. 6, pp. 3499–3505, 2005.

[81] J. Tu, J. Guan, Y. Qiu, and T. J. Matula, "Estimating the shell parameters of SonoVue® microbubbles using light scattering," *The Journal of the Acoustical Society of America*, vol. 126, no. 6, pp. 2954–2962, 2009.

[82] P. Dayton, K. Morgan, M. Allietta, A. Klibanov, G. Brandenburger, and K. Ferrara, "Simultaneous optical and acoustical observations of contrast agents," in *Ultrasonics Symposium, 1997. Proceedings., 1997 IEEE*, vol. 2, pp. 1583–1591, IEEE, 1997.

[83] I. Beekers, K. R. Lattwein, J. J. P. Kouijzer, S. A. G. Langeveld, M. Vegter, R. Beurskens, F. Mastik, R. V. Lunel, E. Verver, and A. F. W. van der Steen, "Combined Confocal Microscope and Brandaris 128 Ultra-High-Speed Camera," *Ultrasound in Medicine & Biology*, 2019.

[84] G. A. Brock-Fisher, M. D. Poland, and P. G. Rafter, "Means for increasing sensitivity in non-linear ultrasound imaging systems," U.S. Patent US5577505A, 1996.

[85] D. H. Simpson, C. T. Chin, and P. N. Burns, "Pulse inversion Doppler: a new method for detecting nonlinear echoes from microbubble contrast agents," *IEEE Transactions on Ultrasonics, Ferroelectrics, and Frequency Control*, vol. 46, no. 2, pp. 372–382, 1999.

[86] J.-J. Hwang and D. H. Simpson, "Two pulse technique for ultrasonic harmonic imaging," US Patent: US5951478A, 1999.

[87] R. J. Eckersley, C. T. Chin, and P. N. Burns, "Optimising phase and amplitude modulation schemes for imaging microbubble contrast agents at low acoustic power," *Ultrasound in Medicine & Biology*, vol. 31, no. 2, pp. 213–219, 2005.

[88] M.-X. Tang, N. Kamiyama, and R. J. Eckersley, "Effects of nonlinear propagation in ultrasound contrast agent imaging," *Ultrasound in Medicine and Biology*, vol. 36, no. 3, pp. 459–466, 2010.

[89] "SonoVue 8 microlitres/ml, powder and solvent for dispersion for injection - Summary of Product Characteristics (SmPC) - (emc)," 2019. `https://www.medicines.org.uk/emc/product/1539{#}CONTRAINDICATIONS`, Last accessed on 2019-09-19.

[90] T. M. Khumri and M. L. Main, "Safety and Risk—Benefit Profile of Microbubble Contrast Agents in Echocardiography," *Asia Pacific Cardiology*, vol. 2, no. 1, p. 47, 2008.

[91] D. E. Goertz, D. A. Christopher, L. Y. Joanne, R. S. Kerbel, P. N. Burns, and F. S. Foster, "High-frequency color flow imaging of the microcirculation," *Ultrasound in Medicine & Biology*, vol. 26, no. 1, pp. 63–71, 2000.

[92] S. M. Van der Meer, M. Versluis, D. Lohse, C. T. Chin, A. Bouakaz, and N. De Jong, "The resonance frequency of SonoVue$^{\mathrm{TM}}$ as observed by high-speed optical imaging," in *Ultrasonics Symposium, 2004 IEEE*, vol. 1, pp. 343–345, IEEE, 2004.

[93] C. R. Hill, J. C. Bamber, G. R. ter Haar, G. M. Baxter, P. L. P. Allan, P. Morley, and P. Fish, *Doppler ultrasound: physics, instrumentation and signal processing*. Wiley, 2000.

[94] D. S. Babcock, H. Patriquin, M. LaFortune, and M. Dauzat, "Power Doppler sonography: basic principles and clinical applications in children," *Pediatric Radiology*, vol. 26, no. 2, pp. 109–115, 1996.

[95] C. Errico, B.-f. Osmanski, S. Pezet, O. Couture, Z. Lenkei, and M. Tanter, "NeuroImage Transcranial functional ultrasound imaging of the brain using microbubble-enhanced ultrasensitive Doppler," *NeuroImage*, vol. 124, pp. 752–761, 2016.

[96] A. Stanziola, C. H. Leow, E. Bazigou, P. D. Weinberg, and M.-X. Tang, "ASAP: Super-Contrast Vasculature Imaging Using Coherence Analysis and High Frame-Rate Contrast Enhanced Ultrasound.," *IEEE Transactions on Medical Imaging*, vol. 37, no. 8, pp. 1847–1856, 2018.

[97] R. C. Gessner, C. B. Frederick, F. S. Foster, and P. A. Dayton, "Acoustic angiography: a new imaging modality for assessing microvasculature architecture," *Journal of Biomedical Imaging*, vol. 2013, p. 14, 2013.

[98] P. A. Dayton, R. C. Gessner, L. Phillips, S. E. Shelton, K. Heath Martin, M. Lee, and F. S. Foster, "The implementation of acoustic angiography for microvascular and angiogenesis imaging," *Conference proceedings : ..*, vol. Annual Int, pp. 4283–4285, 2014.

[99] S. E. Shelton, Y. Z. Lee, M. Lee, E. Cherin, F. S. Foster, S. R. Aylward, and P. A. Dayton, "Quantification of microvascular tortuosity during tumor evolution using acoustic angiography," *Ultrasound in Medicine and Biology*, vol. 41, no. 7, pp. 1896–1904, 2015.

[100] L. V. Wang and S. Hu, "Photoacoustic tomography: In vivo imaging from organelles to organs," *Science*, vol. 335, pp. 1458–1462, mar 2012.

[101] M. Erfanzadeh and Q. Zhu, "Photoacoustic imaging with low-cost sources; A review," *Photoacoustics*, vol. 14, pp. 1–11, jun 2019.

[102] P. Beard, "Biomedical photoacoustic imaging," *Interface Focus*, vol. 1, no. 4, pp. 602–631, 2011.

[103] G. Ku and L. V. Wang, "Deeply penetrating photoacoustic tomography in biological tissues enhanced with an optical contrast agent," *Optics Letters*, vol. 30, p. 507, mar 2005.

[104] C. Kim, T. N. Erpelding, L. Jankovic, M. D. Pashley, and L. V. Wang, "Deeply penetrating in vivo photoacoustic imaging using a clinical ultrasound array system," *Biomedical Optics Express*, vol. 1, p. 278, aug 2010.

[105] K. Maslov, H. F. Zhang, S. Hu, and L. V. Wang, "Optical-resolution photoacoustic microscopy for in vivo imaging of single capillaries," *Optics Letters*, vol. 33, p. 929, may 2008.

[106] K. Wei, A. R. Jayaweera, S. Firoozan, A. Linka, D. M. Skyba, and S. Kaul, "Quantification of Myocardial Blood Flow With Ultrasound-Induced Destruction of Microbubbles Administered as a Constant Venous Infusion," *Circulation*, vol. 97, no. 5, pp. 473–483, 1998.

[107] J. Vangindertael, R. Camacho, W. Sempels, H. Mizuno, P. Dedecker, and K. P. F. Janssen, "An introduction to optical super-resolution microscopy for the adventurous biologist," *Methods and Applications in Fluorescence*, vol. 6, no. 2, p. 22003, 2018.

[108] W. Godbey, "Fluorescence," in *An Introduction to Biotechnology*, pp. 173–186, Elsevier, 2014.

[109] R. M. Dickson, A. B. Cubittt, R. Y. Tsient, and W. E. Moerner, "On/off blinking and switching behaviour of single molecules of green fluorescent protein," *Nature*, vol. 388, no. 6640, pp. 355–358, 1997.

[110] J. Lippincott-Schwartz and G. H. Patterson, "Development and use of fluorescent protein markers in living cells," *Science*, vol. 300, pp. 87–91, apr 2003.

[111] E. Betzig, G. H. Patterson, R. Sougrat, O. W. Lindwasser, S. Olenych, J. S. Bonifacino, M. W. Davidson, J. Lippincott-Schwartz, and H. F. Hess, "Imaging intracellular fluorescent proteins at nanometer resolution," *Science*, vol. 313, pp. 1642–1645, sep 2006.

[112] S. T. Hess, T. P. Girirajan, and M. D. Mason, "Ultra-high resolution imaging by fluorescence photoactivation localization microscopy," *Biophysical Journal*, vol. 91, no. 11, pp. 4258–4272, 2006.

[113] O. Couture, B. Besson, G. Montaldo, M. Fink, and M. Tanter, "Microbubble ultrasound super-localization imaging (MUSLI)," in *Ultrasonics Symposium (IUS), 2011 IEEE International*, pp. 1285–1287, IEEE, 2011.

[114] M. A. O'Reilly and K. Hynynen, "A super-resolution ultrasound method for brain vascular mapping," *Medical Physics*, vol. 40, no. 11, p. 110701, 2013.

[115] O. M. Viessmann, R. J. Eckersley, K. Christensen-Jeffries, M. X. Tang, and C. Dunsby, "Acoustic super-resolution with ultrasound and microbubbles," *Physics in Medicine and Biology*, vol. 58, no. 18, p. 6447, 2013.

[116] C. Errico, J. Pierre, S. Pezet, Y. Desailly, Z. Lenkei, O. Couture, and M. Tanter, "Ultrafast ultrasound localization microscopy for deep super-resolution vascular imaging," *Nature*, vol. 527, no. 7579, pp. 499–502, 2015.

[117] J. Foiret, H. Zhang, L. Mahakian, S. Tam, and K. W. Ferrara, "Super-localization of contrast agents in moving organs, first experiments in a rat kidney," in *IEEE International Ultrasonics Symposium*, 2016.

[118] J. Foiret, H. Zhang, T. Ilovitsh, L. Mahakian, S. Tam, and K. W. Ferrara, "Ultrasound localization microscopy to image and assess microvasculature in a rat kidney," *Scientific Reports*, vol. 7, no. 1, p. 13662, 2017.

[119] P. Song, J. D. Trzasko, A. Manduca, R. Huang, R. Kadirvel, D. F. Kallmes, and S. Chen, "Improved Super-Resolution Ultrasound Microvessel Imaging With Spatiotemporal Nonlocal Means Filtering and Bipartite Graph-Based Microbubble Tracking," *IEEE Transactions on Ultrasonics, Ferroelectrics, and Frequency Control*, vol. 65, no. 2, pp. 149–167, 2018.

[120] J. Zhu, E. M. Rowland, S. Harput, K. Riemer, C. H. Leow, B. Clark, K. Cox, A. Lim, K. Christensen-Jeffries, and G. Zhang, "3D Super-Resolution US Imaging of Rabbit Lymph Node Vasculature in Vivo by Using Microbubbles," *Radiology*, vol. 291, no. 3, pp. 642–650, 2019.

[121] F. Lin, S. E. Shelton, D. Espíndola, J. D. Rojas, G. Pinton, and P. A. Dayton, "3-D ultrasound localization microscopy for identifying microvascular morphology features of tumor angiogenesis at a resolution beyond the diffraction limit of conventional ultrasound," *Theranostics*, vol. 7, no. 1, p. 196, 2017.

[122] D. Ghosh, F. Xiong, S. R. Sirsi, R. Mattrey, R. Brekken, J.-W. Kim, and K. Hoyt, "Monitoring early tumor response to vascular targeted therapy using super-resolution ultrasound imaging," in *2017 IEEE International Ultrasonics Symposium (IUS)*, pp. 1–4, IEEE, 2017.

[123] M. Schneider, "Characteristics of SonoVuetrade mark," *Echocardiography*, vol. 16, no. 7, Pt 2, pp. 743–746, 1999.

[124] K. Christensen-Jeffries, R. J. Browning, M.-X. Tang, C. Dunsby, and R. J. Eckersley, "In vivo acoustic super-resolution and super-resolved velocity mapping using microbubbles," *Medical Imaging, IEEE Transactions on*, vol. 34, no. 2, pp. 433–440, 2015.

[125] S. Dencks, M. Piepenbrock, G. Schmitz, T. Opacic, and F. Kiessling, "Determination of adequate measurement times for super-resolution characterization of tumor vascularization," in *Ultrasonics Symposium (IUS), 2017 IEEE International*, pp. 1–4, IEEE, 2017.

[126] K. Christensen-Jeffries, J. Brown, S. Harput, G. Zhang, J. Zhu, M.-X. Tang, C. Dunsby, and R. J. Eckersley, "Poisson Statistical Model of Ultrasound Super-Resolution Imaging Acquisition Time.," *IEEE Transactions on Ultrasonics, Ferroelectrics, and Frequency Control*, vol. 66, pp. 1246–1254, jul 2019.

[127] V. Hingot, C. Errico, B. Heiles, L. Rahal, M. Tanter, and O. Couture, "Microvascular flow dictates the compromise between spatial resolution and acquisition time in Ultrasound Localization Microscopy," *Scientific Reports*, vol. 9, no. 1, p. 2456, 2019.

[128] T. Dertinger, R. Colyer, G. Iyer, S. Weiss, and J. Enderlein, "Fast, background-free, 3D super-resolution optical fluctuation imaging (SOFI)," *Proceedings of the National Academy of Sciences*, vol. 106, no. 52, pp. 22287–22292, 2009.

[129] A. Bar-Zion, C. Tremblay-Darveau, O. Solomon, D. Adam, and Y. C. Eldar, "Fast vascular ultrasound imaging with enhanced spatial resolution and background rejection," *IEEE Transactions on Medical Imaging*, vol. 36, no. 1, pp. 169–180, 2017.

[130] A. Bar-Zion, O. Solomon, C. Tremblay-Darveau, D. Adam, and Y. C. Eldar, "SUSHI: Sparsity-based Ultrasound Super-resolution Hemodynamic Imaging," *IEEE Transactions on Ultrasonics, Ferroelectrics, and Frequency Control*, 2018.

[131] R. J. G. van Sloun, O. Solomon, Y. C. Eldar, H. Wijkstra, and M. Mischi, "Sparsity-driven super-resolution in clinical contrast-enhanced ultrasound," in *Ultrasonics Symposium (IUS), 2017 IEEE International*, pp. 1–4, IEEE, 2017.

[132] O. Solomon, R. J. G. van Sloun, H. Wijkstra, M. Mischi, and Y. C. Eldar, "Exploiting flow dynamics for super-resolution in contrast-enhanced ultrasound," *IEEE Transactions on Ultrasonics, Ferroelectrics, and Frequency Control*, 2019.

[133] J. Brown, K. Christensen-Jeffries, S. Harput, G. Zhang, J. Zhu, C. Dunsby, M. X. Tang, and R. J. Eckersley, "Investigation of Microbubble Detection Methods for Super-Resolution Imaging of Microvasculature," *IEEE Transactions on*

Ultrasonics, Ferroelectrics, and Frequency Control, vol. 66, pp. 676–691, apr 2019.

[134] Y. Desailly, O. Couture, M. Fink, and M. Tanter, "Sono-activated ultrasound localization microscopy," *Applied Physics Letters*, vol. 103, no. 17, p. 174107, 2013.

[135] F. Lin, C. Cachard, R. Mori, F. Varray, F. Guidi, and O. Basset, "Ultrasound contrast imaging: influence of scatterer motion in multi-pulse techniques.," *IEEE Transactions on Ultrasonics, Ferroelectrics, and Frequency Control*, vol. 60, pp. 2065–78, oct 2013.

[136] S. Harput, K. Christensen-Jeffries, J. Brown, Y. Li, K. J. Williams, A. H. Davies, R. J. Eckersley, C. Dunsby, and M.-X. Tang, "Two-Stage Motion Correction for Super-Resolution Ultrasound Imaging in Human Lower Limb," *IEEE Transactions on Ultrasonics, Ferroelectrics, and Frequency Control*, vol. 65, no. 5, pp. 803–814, 2018.

[137] B. Heiles, M. Correia, V. Hingot, M. Pernot, J. Provost, M. Tanter, and O. Couture, "Ultrafast 3D Ultrasound Localization Microscopy using a 32x32 Matrix Array," *IEEE Transactions on Medical Imaging*, 2019.

[138] S. Harput, K. Christensen-Jeffries, A. Ramalli, J. Brown, J. Zhu, G. Zhang, C. H. Leow, M. Toulemonde, E. Boni, and P. Tortoli, "3-D Super-Resolution Ultrasound (SR-US) Imaging with a 2-D Sparse Array," *arXiv preprint arXiv:1902.01608*, 2019.

[139] K. B. Hansen, C. A. Villagómez-Hoyos, J. C. Brasen, K. Diamantis, V. Sboros, C. M. Sørensen, and J. A. Jensen, "Robust microbubble tracking for super resolution imaging in ultrasound," in *2016 IEEE International Ultrasonics Symposium (IUS)*, pp. 1–4, IEEE, 2016.

[140] D. Ackermann and G. Schmitz, "Detection and Tracking of Multiple Microbub-

bles in Ultrasound B-Mode Images," *Ultrasonics, Ferroelectrics, and Frequency Control, IEEE Transactions on*, vol. 63, no. 1, pp. 72–82, 2016.

[141] S. Dencks, D. Ackermann, and G. Schmitz, "Evaluation of bubble tracking algorithms for super-resolution imaging of microvessels," in *2016 IEEE International Ultrasonics Symposium (IUS)*, pp. 1–4, IEEE, 2016.

[142] C. Demené, T. Deffieux, M. Pernot, B.-F. Osmanski, V. Biran, J.-L. Gennisson, L.-A. Sieu, A. Bergel, S. Franqui, and J.-M. Correas, "Spatiotemporal clutter filtering of ultrafast ultrasound data highly increases Doppler and fUltrasound sensitivity," *IEEE Transactions on Medical Imaging*, vol. 34, no. 11, pp. 2271–2285, 2015.

[143] S. Harput, K. Christensen-Jeffries, J. Brown, J. Zhu, G. Zhang, R. J. Eckersly, C. Dunsby, and M.-X. Tang, "3-D Motion Correction for Volumetric Super-Resolution Ultrasound Imaging," in *2018 IEEE International Ultrasonics Symposium (IUS)*, pp. 1–9, IEEE, 2018.

[144] V. Hingot, C. Errico, M. Tanter, and O. Couture, "Subwavelength motion-correction for ultrafast ultrasound localization microscopy," *Ultrasonics*, vol. 77, pp. 17–21, 2017.

[145] K. Christensen-Jeffries, S. Harput, J. Brown, P. N. T. Wells, P. Aljabar, C. Dunsby, M.-X. Tang, and R. J. Eckersley, "Microbubble Axial Localization Errors in Ultrasound Super-Resolution Imaging," *IEEE Transactions on Ultrasonics, Ferroelectrics, and Frequency Control*, vol. 64, no. 11, pp. 1644–1654, 2017.

[146] F. Foroozan, M. A. O'Reilly, and K. Hynynen, "Microbubble Localization for Three-Dimensional Superresolution Ultrasound Imaging Using Curve Fitting and Deconvolution Methods," *IEEE Transactions on Biomedical Engineering*, vol. 65, no. 12, pp. 2692–2703, 2018.

[147] K. Christensen-Jeffries, J. Brown, P. Aljabar, M. Tang, C. Dunsby, and R. J. Eckersley, "3-D In Vitro Acoustic Super-Resolution and Super-Resolved Velocity Mapping Using Microbubbles," *IEEE Transactions on Ultrasonics, Ferroelectrics, and Frequency Control*, vol. 64, no. 10, pp. 1478–1486, 2017.

[148] S. Qin and K. W. Ferrara, "Acoustic response of compliable microvessels containing ultrasound contrast agents," *Physics in Medicine & Biology*, vol. 51, no. 20, p. 5065, 2006.

[149] S. Lin, A. Shah, J. Hernández-Gil, A. Stanziola, B. I. Harriss, T. O. Matsunaga, N. Long, J. Bamber, and M. X. Tang, "Optically and acoustically triggerable sub-micron phase-change contrast agents for enhanced photoacoustic and ultrasound imaging," *Photoacoustics*, vol. 6, pp. 26–36, jun 2017.

[150] G. P. Luke, A. S. Hannah, and S. Y. Emelianov, "Super-resolution ultrasound imaging in vivo with transient laser-activated nanodroplets," *Nano Letters*, vol. 16, no. 4, pp. 2556–2559, 2016.

[151] G. Zhang, S. Harput, S. Lin, K. Christensen-Jeffries, C. H. Leow, J. Brown, C. Dunsby, R. J. Eckersley, and M.-X. Tang, "Acoustic wave sparsely activated localization microscopy (AWSALM): Super-resolution ultrasound imaging using acoustic activation and deactivation of nanodroplets," *Applied Physics Letters*, vol. 113, no. 1, p. 14101, 2018.

[152] H. Yoon, K. A. Hallam, C. Yoon, and S. Y. Emelianov, "Super-resolution imaging with ultrafast ultrasound imaging of optically triggered perfluorohexane nanodroplets," *IEEE Transactions on Ultrasonics, Ferroelectrics, and Frequency Control*, vol. 65, no. 12, pp. 2277–2285, 2018.

[153] G. Zhang, S. Harput, H. Hu, K. Christensen-Jeffries, J. Zhu, J. Brown, C. H. Leow, C. Dunsby, R. J. Eckersley, and M.-X. Tang, "Fast Acoustic Wave Sparsely Activated Localization Microscopy (Fast-AWSALM) Using Octafluoropropane N Anodroplets," in *2018 IEEE International Ultrasonics Symposium (IUS)*, pp. 1–9, IEEE, 2018.

[154] M. X. Tang, H. Mulvana, T. Gauthier, A. K. Lim, D. O. Cosgrove, R. J. Eckersley, and E. Stride, "Quantitative contrast-enhanced ultrasound imaging: A review of sources of variability," *Interface Focus*, vol. 1, no. 4, pp. 520–539, 2011.

[155] "k-Wave: A MATLAB toolbox for the time domain simulation of acoustic wave fields." `http://www.k-wave.org/acousticsoftware.php` Last accessed on 2019-11-25.

[156] T. X. Misaridis, K. Gammelmark, C. H. Jørgensen, N. Lindberg, A. H. Thomsen, M. H. Pedersen, and J. A. Jensen, "Potential of coded excitation in medical ultrasound imaging," *Ultrasonics*, vol. 38, no. 1, pp. 183–189, 2000.

[157] J. A. Jensen, "Users' guide for the Field II program," *Technical University of Denmark*, vol. 2800, 2001.

[158] M. J. Ledesma-Carbayo, J. Kybic, M. Desco, A. Santos, M. Suhling, P. Hunziker, and M. Unser, "Spatio-temporal nonrigid registration for ultrasound cardiac motion estimation," *IEEE Transactions on Medical Imaging*, vol. 24, no. 9, pp. 1113–1126, 2005.

[159] T. Gehrke and H. M. Overhoff, "Simulation of Contrast Agent Enhanced Ultrasound Imaging Based on Field II," in *Bildverarbeitung für die Medizin 2008*, pp. 62–66, Springer, 2008.

[160] M. Piepenbrock, S. Dencks, and G. Schmitz, "Performance of Foreground-Background Separation Algorithms for the Detection of Microbubbles in Super-Resolution Imaging," in *2018 IEEE International Ultrasonics Symposium (IUS)*, pp. 1–9, IEEE, 2018.

[161] B. E. Treeby, J. Jaros, A. P. Rendell, and B. T. Cox, "Modeling nonlinear ultrasound propagation in heterogeneous media with power law absorption using a k-space pseudospectral method," *The Journal of the Acoustical Society of America*, vol. 131, no. 6, pp. 4324–4336, 2012.

[162] B. T. Cox, J. G. Laufer, K. P. Kostli, and P. C. Beard, "Experimental validation of photoacoustic k-space propagation models," in *Biomedical Optics 2004*, pp. 238–248, International Society for Optics and Photonics, 2004.

[163] A. A. Doinikov and A. Bouakaz, "Review of shell models for contrast agent microbubbles," *IEEE Transactions on Ultrasonics, Ferroelectrics, and Frequency Control*, vol. 58, no. 5, pp. 981–993, 2011.

[164] Y. Desailly, J. Pierre, O. Couture, and M. Tanter, "Resolution limits of ultrafast ultrasound localization microscopy," *Physics in Medicine and Biology*, vol. 60, no. 22, p. 8723, 2015.

[165] R. J. G. van Sloun, O. Solomon, M. Bruce, Z. Z. Khaing, Y. C. Eldar, and M. Mischi, "Deep Learning for Super-resolution Vascular Ultrasound Imaging," in *ICASSP 2019-2019 IEEE International Conference on Acoustics, Speech and Signal Processing (ICASSP)*, pp. 1055–1059, IEEE, 2019.

[166] G. R. Lockwood, D. H. Turnball, D. A. Christopher, and F. S. Foster, "Beyond 30 MHz [applications of high-frequency ultrasound imaging]," *IEEE Engineering in Medicine and Biology Magazine*, vol. 15, no. 6, pp. 60–71, 1996.

[167] F. Lin, J. D. Rojas, and P. A. Dayton, "Super resolution contrast ultrasound imaging: Analysis of imaging resolution and application to imaging tumor angiogenesis," in *Ultrasonics Symposium (IUS), 2016 IEEE International*, pp. 1–4, IEEE, 2016.

[168] F. Yuan, H. A. Salehi, Y. Boucher, U. S. Vasthare, R. F. Tuma, and R. K. Jain, "Vascular permeability and microcirculation of gliomas and mammary carcinomas transplanted in rat and mouse cranial windows," *Cancer Research*, vol. 54, no. 17, pp. 4564–4568, 1994.

[169] D. M. McDonald and P. L. Choyke, "Imaging of angiogenesis: from microscope to clinic," *Nature Medicine*, vol. 9, no. 6, pp. 713–725, 2003.

[170] D. A. I. Fukumura, D. G. Duda, L. L. Munn, and R. K. Jain, "Tumor Microvasculature and Microenvironment: Novel Insights Through Intravital Imaging in Pre-Clinical Models," *Microcirculation*, vol. 17, no. 3, pp. 206–225, 2010.

[171] C. Korn and H. G. Augustin, "Review Mechanisms of Vessel Pruning and Regression," *Developmental Cell*, vol. 34, no. 1, pp. 5–17, 2015.

[172] P. Song, A. Manduca, J. D. Trzasko, and S. Chen, "Ultrasound Small Vessel Imaging With Block-Wise Adaptive Local Clutter Filtering," *IEEE Transactions on Medical Imaging*, vol. 36, no. 1, pp. 251–262, 2017.

[173] Y. Desailly, A.-M. Tissier, J.-M. Correas, F. Wintzenrieth, M. Tanter, and O. Couture, "Contrast enhanced ultrasound by real-time spatiotemporal filtering of ultrafast images," *Physics in Medicine and Biology*, vol. 62, no. 1, p. 31, 2016.

[174] J. Baranger, B. Arnal, F. Perren, O. Baud, M. Tanter, and C. Demené, "Adaptive spatiotemporal SVD clutter filtering for Ultrafast Doppler Imaging using similarity of spatial singular vectors," *IEEE Transactions on Medical Imaging*, 2018.

[175] E. Stride and N. Saffari, "Microbubble ultrasound contrast agents: a review," *Proceedings of the Institution of Mechanical Engineers, Part H: Journal of Engineering in Medicine*, vol. 217, no. 6, pp. 429–447, 2003.

[176] T. G. Leighton, *The Acoustic Bubble*. Academic Press, 2012.

[177] H. Poritsky, "The collapse or growth of a spherical bubble or cavity in a viscous fluid," *Journal of Applied Mechanics-Transactions of the ASME*, vol. 18, no. 3, pp. 332–333, 1951.

[178] S. M. van der Meer, B. Dollet, M. M. Voormolen, C. T. Chin, A. Bouakaz, N. de Jong, M. Versluis, and D. Lohse, "Microbubble spectroscopy of ultrasound contrast agents," *The Journal of the Acoustical Society of America*, vol. 121, no. 1, pp. 648–656, 2007.

[179] M. P. Brenner, S. Hilgenfeldt, and D. Lohse, "Single-bubble sonoluminescence," *Reviews of Modern Physics*, vol. 74, no. 2, p. 425, 2002.

[180] D. Chatterjee and K. Sarkar, "A Newtonian rheological model for the interface of microbubble contrast agents," *Ultrasound in Medicine & Biology*, vol. 29, no. 12, pp. 1749–1757, 2003.

[181] L. Bjørnø, "Introduction to nonlinear acoustics," *Physics Procedia*, vol. 3, no. 1, pp. 5–16, 2010.

[182] B. Treeby, B. Cox, and J. Jaros, *k-Wave: A MATLAB toolbox for the time domain simulation of acoustic wave fields*. 2012.

[183] H. Chen, "Staggered-grid pseudospectral viscoacoustic wave field simulation in two-dimensional media," *The Journal of the Acoustical Society of America*, vol. 100, no. 1, pp. 120–131, 1996.

[184] M. Tabei, T. D. Mast, and R. C. Waag, " A k -space method for coupled first-order acoustic propagation equations ," *The Journal of the Acoustical Society of America*, vol. 111, pp. 53–63, jan 2002.

[185] C. H. Alfred and L. Lovstakken, "Eigen-based clutter filter design for ultrasound color flow imaging: a review," *IEEE Transactions on Ultrasonics, Ferroelectrics, and Frequency Control*, vol. 57, no. 5, pp. 1096–1111, 2010.

[186] F. W. Mauldin Jr., D. Lin, and J. A. Hossack, "The singular value filter: a general filter design strategy for PCA-based signal separation in medical ultrasound imaging," *IEEE Transactions on Medical Imaging*, vol. 30, no. 11, pp. 1951–1964, 2011.

[187] G. Park, S. Yeo, J. J. Lee, C. Yoon, H. W. Koh, H. Lim, Y. Kim, H. Shim, and Y. Yoo, "New adaptive clutter rejection based on spectral analysis for ultrasound color doppler imaging: Phantom and in vivo abdominal study," *IEEE Transactions on Biomedical Engineering*, vol. 61, pp. 55–63, jan 2014.

[188] H. Azhari, *Basics of biomedical ultrasound for engineers*. John Wiley & Sons, 2010.

[189] J. Mamou and M. L. Oelze, *Quantitative ultrasound in soft tissues*. Springer, 2013.

[190] I. C. A. Organization, "Manual of the ICAO Standard Atmosphere, Doc 7488-CD," 1993.

[191] J.-M. Gorce, M. Arditi, and M. Schneider, "Influence of bubble size distribution on the echogenicity of ultrasound contrast agents: a study of Sonovue^{TM}," *Investigative Radiology*, vol. 35, no. 11, pp. 661–671, 2000.

[192] P. Tortoli, L. Bassi, E. Boni, A. Dallai, F. Guidi, and S. Ricci, "ULA-OP: An advanced open platform for ultrasound research," *IEEE Transactions on Ultrasonics, Ferroelectrics, and Frequency Control*, vol. 56, no. 10, pp. 2207–2216, 2009.

[193] S. Sudha, G. R. Suresh, and R. Sukanesh, "Speckle noise reduction in ultrasound images by wavelet thresholding based on weighted variance," *International Journal of Computer Theory and Engineering*, vol. 1, no. 1, p. 7, 2009.

[194] J. L. Mateo and A. Fernández-Caballero, "Finding out general tendencies in speckle noise reduction in ultrasound images," *Expert Systems with Applications*, vol. 36, no. 4, pp. 7786–7797, 2009.

[195] B. D. Lindsey, S. E. Shelton, and P. A. Dayton, "Optimization of contrast-to-tissue ratio through pulse windowing in dual-frequency "acoustic angiography" imaging," *Ultrasound in Medicine & Biology*, vol. 41, no. 7, pp. 1884–1895, 2015.

[196] F. Lin, J. K. Tsuruta, J. D. Rojas, and P. A. Dayton, "Optimizing Sensitivity of Ultrasound Contrast-Enhanced Super-Resolution Imaging by Tailoring Size Distribution of Microbubble Contrast Agent," *Ultrasound in Medicine and Biology*, vol. 43, no. 10, pp. 2488–2493, 2017.

[197] M. A. Lediju, M. J. Pihl, S. J. Hsu, J. J. Dahl, C. M. Gallippi, and G. E. Trahey, "A motion-based approach to abdominal clutter reduction," *IEEE Transactions on Ultrasonics, Ferroelectrics, and Frequency Control*, vol. 56, no. 11, pp. 2437–2449, 2009.

[198] W. T. Shi and F. Forsberg, "Ultrasonic characterization of the nonlinear properties of contrast microbubbles," *Ultrasound in Medicine & Biology*, vol. 26, no. 1, pp. 93–104, 2000.

[199] T. R. Porter and F. Xie, "Myocardial perfusion imaging with contrast ultrasound," *JACC: Cardiovascular Imaging*, vol. 3, no. 2, pp. 176–187, 2010.

[200] P. J. Phillips, "Contrast pulse sequences (CPS): imaging nonlinear microbubbles," in *Ultrasonics Symposium, 2001 IEEE*, vol. 2, pp. 1739–1745, IEEE, 2001.

[201] W. Kong, W. Wang, B. Huang, H. Ding, and F. Mao, "Value of wash-in and wash-out time in the diagnosis between hepatocellular carcinoma and other hepatic nodules with similar vascular pattern on contrast-enhanced ultrasound," *Journal of Gastroenterology and Hepatology*, vol. 29, no. 3, pp. 576–580, 2014.

[202] K. Christensen-Jeffries, *Super-resolution ultrasound imaging with microbubbles* . PhD thesis, King's College London, London, 2016.

[203] T. G. Leighton, A. J. Walton, and M. J. W. Pickworth, "Primary bjerknes forces," *European Journal of Physics*, vol. 11, no. 1, p. 47, 1990.

[204] K. E. Morgan, J. S. Allen, P. A. Dayton, J. E. Chomas, A. L. Klibaov, and K. W. Ferrara, "Experimental and theoretical evaluation of microbubble behavior: Effect of transmitted phase and bubble size," *IEEE Transactions on Ultrasonics, Ferroelectrics, and Frequency Control*, vol. 47, no. 6, pp. 1494–1509, 2000.

[205] C. F. Caskey, D. E. Kruse, P. A. Dayton, T. K. Kitano, and K. W. Ferrara, "Microbubble oscillation in tubes with diameters of 12, 25, and 195 microns," *Applied Physics Letters*, vol. 88, no. 3, p. 33902, 2006.

[206] H. J. Vos, B. Dollet, J. G. Bosch, M. Versluis, and N. De Jong, "Nonspherical vibrations of microbubbles in contact with a wall—a pilot study at low mechanical index," *Ultrasound in Medicine & Biology*, vol. 34, no. 4, pp. 685–688, 2008.

[207] E. C. Gelderblom, H. J. Vos, F. Mastik, T. Faez, Y. Luan, T. J. A. Kokhuis, A. F. W. van der Steen, D. Lohse, N. de Jong, and M. Versluis, "Brandaris 128 ultra-high-speed imaging facility: 10 years of operation, updates, and enhanced features," *Review of Scientific Instruments*, vol. 83, no. 10, p. 103706, 2012.

[208] M. Postema, A. Bouakaz, C. T. Chin, and N. de Jong, "Simulations and measurements of optical images of insonified ultrasound contrast microbubbles," *IEEE Transactions on Ultrasonics, Ferroelectrics, and Frequency Control*, vol. 50, no. 5, pp. 523–536, 2003.

[209] A. L. Klibanov, K. W. Ferrara, M. S. Hughes, J. H. Wible Jr, J. K. Wojdyla, P. A. Dayton, K. E. Morgan, and G. H. Brandenburger, "Direct videomicroscopic observation of the dynamic effects of medical ultrasound on ultrasound contrast microspheres," *Investigative Radiology*, vol. 33, no. 12, pp. 863–870, 1998.

[210] B. L. Helfield, E. Cherin, F. S. Foster, and D. E. Goertz, "Investigating the Subharmonic Response of Individual Phospholipid Encapsulated Microbubbles at High Frequencies: A Comparative Study of Five Agents," *Ultrasound in Medicine and Biology.*, 2012.

[211] S. H. Bloch, M. Wan, P. A. Dayton, and K. W. Ferrara, "Optical observation of lipid-and polymer-shelled ultrasound microbubble contrast agents," *Applied Physics Letters*, vol. 84, no. 4, pp. 631–633, 2004.

[212] H. Chen, A. A. Brayman, and T. J. Matula, "Microbubble dynamics in microvessels: Observations of microvessel dilation, invagination and rupture," in *Ultrasonics Symposium, 2008. IUS 2008. IEEE*, pp. 1163–1166, IEEE, 2008.

[213] H. Zheng, P. A. Dayton, C. Caskey, S. Zhao, S. Qin, and K. W. Ferrara, "Ultrasound-driven microbubble oscillation and translation within small phantom vessels," *Ultrasound in Medicine & Biology*, vol. 33, no. 12, pp. 1978–1987, 2007.

[214] C. T. Chin, C. Lancée, J. Borsboom, F. Mastik, M. E. Frijlink, N. de Jong, M. Versluis, and D. Lohse, "Brandaris 128: A digital 25 million frames per second camera with 128 highly sensitive frames," *Review of Scientific Instruments*, vol. 74, no. 12, pp. 5026–5034, 2003.

[215] X. Chen, J. Wang, M. Versluis, N. de Jong, and F. S. Villanueva, "Ultrafast bright field and fluorescence imaging of the dynamics of micrometer-sized objects," *Review of Scientific Instruments*, vol. 84, no. 6, p. 63701, 2013.

[216] P. L. Marston, S. C. Billette, and C. E. Dean, "Scattering of light by a coated bubble in water near the critical and Brewster scattering angles," in *Ocean Optics IX*, vol. 925, pp. 308–316, International Society for Optics and Photonics, 1988.

[217] P. Rademeyer, D. Carugo, J. Y. Lee, and E. Stride, "Microfluidic system for high throughput characterisation of echogenic particles," *Lab on a Chip*, vol. 15, no. 2, pp. 417–428, 2015.

[218] V. Garbin, *Optical tweezers for the study of microbubble dynamics in ultrasound*. PhD thesis, University of Trieste, 2006.

[219] C. F. Caskey, S. M. Stieger, S. Qin, P. A. Dayton, and K. W. Ferrara, "Direct observations of ultrasound microbubble contrast agent interaction with the microvessel wall," *The Journal of the Acoustical Society of America*, vol. 122, no. 2, pp. 1191–1200, 2007.

[220] J. C. Pickup, *Chronic complications of diabetes*. Blackwell Scientific Publ., 1994.

[221] K. E. Morgan, P. A. Dayton, D. E. Kruse, A. L. Klibanov, G. H. Brandenburger, and K. W. Ferrara, "Changes in the echoes from ultrasonic contrast agents with

imaging parameters," *IEEE Transactions on Ultrasonics, Ferroelectrics, and Frequency Control*, vol. 45, no. 6, pp. 1537–1548, 1998.

[222] M. Postema, P. Marmottant, C. T. Lancée, S. Hilgenfeldt, and N. D. Jong, "Ultrasound-induced microbubble coalescence," *Ultrasound in Medicine and Biology*, vol. 30, pp. 1337–1344, oct 2004.

[223] S. Kotopoulis and M. Postema, "Microfoam formation in a capillary," *Ultrasonics*, vol. 50, pp. 260–268, feb 2010.

[224] J. Zhu, S. Lin, C. H. Leow, E. M. Rowland, K. Riemer, S. Harput, P. D. Weinberg, and M.-X. Tang, "High Frame Rate Contrast-Enhanced Ultrasound Imaging for Slow Lymphatic Flow: Influence of Ultrasound Pressure and Flow Rate on Bubble Disruption and Image Persistence," *Ultrasound in Medicine & Biology*, vol. 45, no. 9, pp. 2456–2470, 2019.

[225] D. T. Fetzer, V. Rafailidis, C. Peterson, E. G. Grant, P. Sidhu, and R. G. Barr, "Artifacts in contrast-enhanced ultrasound: a pictorial essay," *Abdominal Radiology*, vol. 43, no. 4, pp. 977–997, 2018.

[226] M. A. Haidekker, *Medical imaging technology.* Springer, 2013.

[227] C. Ishihara, H. Tanaka, K. Hashiba, and H. Kuribara, "Ultrasound imaging device and ultrasound imaging method," Patent publication no.: WO2014119746, 2015.

[228] A. Degirmenci, D. P. Perrin, and R. D. Howe, "High dynamic range ultrasound imaging," *International Journal of Computer Assisted Radiology and Surgery*, vol. 13, no. 5, pp. 721–729, 2018.

[229] A. Artusi, T. Richter, T. Ebrahimi, and R. K. Mantiu, "High Dynamic Range Imaging Technology [Lecture Notes]," *IEEE Signal Processing Magazine*, vol. 34, no. 5, pp. 165–172, 2017.

[230] Y. Xiao, M. Boily, H. S. Hashemi, and H. Rivaz, "High-Dynamic-Range Ultrasound: Application for Imaging Tendon Pathology," *Ultrasound in Medicine and Biology*, vol. 44, no. 7, pp. 1525–1532, 2018.

[231] S. Qin, C. F. Caskey, and K. W. Ferrara, "Ultrasound contrast microbubbles in imaging and therapy: physical principles and engineering," *Physics in Medicine & Biology*, vol. 54, no. 6, p. R27, 2009.

[232] S. I. Nikolov, J. Kortbek, and J. A. Jensen, "Practical applications of synthetic aperture imaging," in *2010 IEEE International Ultrasonics Symposium*, pp. 350–358, IEEE, 2010.

[233] J. K. Tsou, J. Liu, A. I. Barakat, and M. F. Insana, "Role of ultrasonic shear rate estimation errors in assessing inflammatory response and vascular risk," *Ultrasound in Medicine & Biology*, vol. 34, no. 6, pp. 963–972, 2008.

[234] J. E. Browne, K. V. Ramnarine, A. J. Watson, and P. R. Hoskins, "Assessment of the acoustic properties of common tissue-mimicking test phantoms," *Ultrasound in Medicine & Biology*, vol. 29, no. 7, pp. 1053–1060, 2003.

[235] W. M. S. Russell, R. L. Burch, and C. W. Hume, *The principles of humane experimental technique*, vol. 238. Methuen London, 1959.

[236] A. Du Plessis, C. Broeckhoven, A. Guelpa, and S. G. Le Roux, "Laboratory x-ray micro-computed tomography: a user guideline for biological samples," *GigaScience*, vol. 6, no. 6, p. gix027, 2017.

[237] F. E. Hossler and J. E. Douglas, "Vascular corrosion casting: review of advantages and limitations in the application of some simple quantitative methods," *Microscopy and Microanalysis*, vol. 7, no. 3, pp. 253–264, 2001.

[238] "Peripheral vascular doppler flow phantom - cirs." `https://www.cirsinc.com/products/ultrasound/ats-urethane/peripheral-vascular-doppler-flow-phantom/` Last accessed on 2019-11-30.

[239] "Doppler flow directional discrimination phantom - cirs." https://www.cirsinc.com/products/ultrasound/ats-urethane/doppler-flow-directional-discrimination-phantom/ Last accessed on 2019-11-30.

[240] "General purpose ultrasound phantom - cirs." https://www.cirsinc.com/products/ultrasound/zerdine-hydrogel/general-purpose-ultrasound-phantom/ Last accessed on 2019-11-30.

[241] A. Barbot, D. Decanini, and G. Hwang, "On-chip microfluidic multimodal swimmer toward 3D navigation," *Scientific Reports*, vol. 6, p. 19041, 2016.

[242] W. C. Lee, Y. J. Heo, and S. Takeuchi, "Wall-less liquid pathways formed with three-dimensional microring arrays," *Applied Physics Letters*, vol. 101, no. 11, p. 114108, 2012.

[243] R. Di Giacomo, S. Krödel, B. Maresca, P. Benzoni, R. Rusconi, R. Stocker, and C. Daraio, "Deployable micro-traps to sequester motile bacteria," *Scientific Reports*, vol. 7, p. 45897, 2017.

[244] "Introduction to material jetting 3d printing | 3d hubs." https://www.3dhubs.com/knowledge-base/introduction-material-jetting-3d-printing/ Last accessed on: 2019-11-30.

[245] E. Dong, Z. Zhao, M. Wang, Y. Xie, S. Li, P. Shao, L. Cheng, and R. X. Xu, "Three-dimensional fuse deposition modeling of tissue-simulating phantom for biomedical optical imaging," *Journal of Biomedical Optics*, vol. 20, no. 12, p. 121311, 2015.

[246] J.-Y. Lee, J. An, and C. K. Chua, "Fundamentals and applications of 3D printing for novel materials," *Applied Materials Today*, vol. 7, pp. 120–133, 2017.

[247] "Porolay-serie overview." https://www.3dhubs.com/s3fs-public/talk/attachments/porolay-overview-3dhub-a.pdf Last accessed on 2019-11-30.

[248] S. S. Crump, "Apparatus and method for creating three-dimensional objects," U.S. Patent US5121329A, 1992.

[249] A. B. Allman, L. M. Shepard, A. R. Podgorsak, R. A. Rava, and C. N. Ionita, "Controlled compliancy of 3D printed vascular patient specific phantoms," in *Medical Imaging 2019: Imaging Informatics for Healthcare, Research, and Applications*, vol. 10954, p. 109540C, International Society for Optics and Photonics, 2019.

[250] E. Maneas, W. Xia, D. I. Nikitichev, B. Daher, M. Manimaran, R. Y. J. Wong, C.-W. Chang, B. Rahmani, C. Capelli, and S. Schievano, "Anatomically realistic ultrasound phantoms using gel wax with 3D printed moulds," *Physics in Medicine & Biology*, vol. 63, no. 1, p. 15033, 2018.

[251] D. I. Nikitichev, A. Barburas, K. McPherson, J.-M. Mari, S. J. West, and A. E. Desjardins, "Construction of 3-dimensional printed ultrasound phantoms with wall-less vessels," *Journal of Ultrasound in Medicine*, vol. 35, no. 6, pp. 1333–1339, 2016.

[252] X. Zhou, D. A. Kenwright, S. Wang, J. A. Hossack, and P. R. Hoskins, "Fabrication of two flow phantoms for Doppler ultrasound imaging," *IEEE Transactions on Ultrasonics, Ferroelectrics, and Frequency Control*, vol. 64, no. 1, pp. 53–65, 2017.

[253] V. Grand-Perret, J.-R. Jacquet, I. Leguerney, B. Benatsou, J.-M. Grégoire, G. Willoquet, A. Bouakaz, N. Lassau, and S. Pitre-Champagnat, "A novel microflow phantom dedicated to ultrasound microvascular measurements," *Ultrasonic Imaging*, vol. 40, no. 5, pp. 325–338, 2018.

[254] S. Imai and N. Kudo, "Development of a Microvascular Phantom for Studies on Microbubble Dynamics and Bubble-Cell Interaction Inside a Capillary," in *2018 IEEE International Ultrasonics Symposium (IUS)*, pp. 1–4, IEEE, 2018.

[255] J. S. Miller, K. R. Stevens, M. T. Yang, B. M. Baker, D.-H. T. Nguyen, D. M. Cohen, E. Toro, A. A. Chen, P. A. Galie, and X. Yu, "Rapid casting of patterned vascular networks for perfusable engineered three-dimensional tissues," *Nature Materials*, vol. 11, no. 9, p. 768, 2012.

[256] L. M. Bellan, S. P. Singh, P. W. Henderson, T. J. Porri, H. G. Craighead, and J. A. Spector, "Fabrication of an artificial 3-dimensional vascular network using sacrificial sugar structures," *Soft Matter*, vol. 5, no. 7, pp. 1354–1357, 2009.

[257] J. R. Gershlak, S. Hernandez, G. Fontana, L. R. Perreault, K. J. Hansen, S. A. Larson, B. Y. K. Binder, D. M. Dolivo, T. Yang, and T. Dominko, "Crossing kingdoms: Using decellularized plants as perfusable tissue engineering scaffolds," *Biomaterials*, vol. 125, pp. 13–22, 2017.

[258] T. W. Gilbert, T. L. Sellaro, and S. F. Badylak, "Decellularization of tissues and organs," *Biomaterials*, vol. 27, no. 19, pp. 3675–3683, 2006.

[259] M. Guizar-Sicairos, S. T. Thurman, and J. R. Fienup, "Efficient subpixel image registration algorithms," *Optics Letters*, vol. 33, p. 156, jan 2008.

[260] P. Song, A. Manduca, J. D. Trzasko, R. E. Daigle, and S. Chen, "On the effects of spatial sampling quantization in super-resolution ultrasound microvessel imaging," *IEEE Transactions on Ultrasonics, Ferroelectrics, and Frequency Control*, vol. 65, no. 12, pp. 2264–2276, 2018.

[261] R. C. Waag, "Measurements of ultrasonic pulse arrival time differences produced by abdominal wall specimens," *Journal of the Acoustical Society of America*, vol. 90, no. 6, pp. 2924–2930, 1991.

[262] S. W. Flax and M. O'Donnell, "Phase-Aberration Correction Using Signals From Point Reflectors and Diffuse Scatterers: Basic Principles," *IEEE Transactions on Ultrasonics, Ferroelectrics, and Frequency Control*, vol. 35, no. 6, pp. 758–767, 1988.

[263] E. Talu, K. Hettiarachchi, S. Zhao, R. L. Powell, A. P. Lee, M. L. Longo, and P. A. Dayton, "Tailoring the size distribution of ultrasound contrast agents: possible method for improving sensitivity in molecular imaging," *Molecular Imaging*, vol. 6, no. 6, p. 7290.2007. 00034, 2007.

[264] T. Segers, P. Kruizinga, M. P. Kok, G. Lajoinie, N. de Jong, and M. Versluis, "Monodisperse Versus Polydisperse Ultrasound Contrast Agents: Non-Linear Response, Sensitivity, and Deep Tissue Imaging Potential," *Ultrasound in Medicine and Biology*, vol. 44, pp. 1482–1492, jul 2018.

[265] R. Shih, D. Bardin, T. D. Martz, P. S. Sheeran, P. A. Dayton, and A. P. Lee, "Flow-focusing regimes for accelerated production of monodisperse drug-loadable microbubbles toward clinical-scale applications," *Lab on a Chip*, vol. 13, pp. 4816–4826, dec 2013.

[266] N. de Jong, F. J. Ten Cate, W. B. Vletter, and J. R. Roelandt, "Quantification of transpulmonary echocontrast effects," *Ultrasound in Medicine and Biology*, vol. 19, no. 4, pp. 279–288, 1993.

[267] E. Talu, R. L. Powell, M. L. Longo, and P. A. Dayton, "Needle Size and Injection Rate Impact Microbubble Contrast Agent Population," *Ultrasound in Medicine and Biology*, vol. 34, pp. 1182–1185, jul 2008.

[268] R. J. Browning, H. Mulvana, M. Tang, J. V. Hajnal, D. J. Wells, and R. J. Eckersley, "Influence of needle gauge on in vivo ultrasound and microbubble-mediated gene transfection.," *Ultrasound in Medicine & Biology*, vol. 37, pp. 1531–7, sep 2011.

[269] E. L. Madsen, G. R. Frank, and F. Dong, "Liquid or solid ultrasonically tissue-mimicking materials with very low scatter," *Ultrasound in Medicine & Biology*, vol. 24, no. 4, pp. 535–542, 1998.

Publications and Other Research Outputs

Publications relevant to the work in this thesis:

Brown, J., Christensen-Jeffries, K., Harput, S., Zhang, G., Zhu, J., Dunsby, C., Tang, M. X., Eckersley, R. J., (2019) Investigation of Microbubble Detection Methods for Super-resolution Imaging of Microvasculature, IEEE Transactions on Ultrasonics, Ferroelectrics, and Frequency Control, p. 1. doi: 10.1109/TUFFC.2019.2894755.

Brown, J., Christensen-Jeffries, K., Harput, S., Zhang, G., Zhu, J., Dunsby, C., Tang, M. X., Eckersley, R. J., Development of Simultaneous Optical Imaging and Super-Resolution Ultrasound to Improve Microbubble Localization Accuracy, in IEEE International Ultrasonics Symposium, IUS. IEEE Computer Society. doi: 10.1109/ULTSYM.2018.8580212.

Brown, J., Christensen-Jeffries, K., Harput, S., Dunsby, C., Tang, M. X., Eckersley, R. J. (2017). Investigation of microbubble detection methods for super-resolution imaging of microvasculature. In 2017 IEEE International Ultrasonics Symposium, IUS 2017 [8092177] IEEE Computer Society. DOI: 10.1109/ULTSYM.2017.8092177

Brown, J.*, Zhu, J. *, Riemer, K*, Stanziola, A., Harput, S., Christensen-Jeffries, K., Xu, F., Huang, P., Dunsby, C., Eckersley, R. J., Weinberg P.D., and Tang, M.X. Ultrasound Imaging Artefacts due to Singular Value Decomposition Clutter Filtering. (in review) *Authors contributed equally.

Wang, S., Noh, Y., **Brown, J.**, Roujol, S., Li, Y., Wang, S., Housden, R., Casajuana Ester, M., Al-Hamadani, M., Rajani, R. and Rhode, K. Development and Testing of an Ultrasound-Compatible Cardiac Phantom for Interventional Procedure Simulation Using Direct 3D Printing, Journal of 3D Printing and Additive Manufacturing (Accepted/in press).

Patent Pending:

Brown, J., Eckersley, R.J., High Dynamic Range Non-linear Ultrasound Imaging, WO2020128482 (A1).

Conference Presentations:

Jan 2019: Poster competition: 'High Dynamic Range Non-linear Ultrasound Imaging.", The 24th European Symposium on Ultrasound Contrast Imaging, Rotterdam.

Oct. 2018: IEEE International Ultrasonics Symposium, Kobe, Japan.

- **Oral presentation:** "Understanding the Origin of Flashing Artefacts due to Singular Value Decomposition Clutter Filter",
- **Poster presentation:** "Development of Simultaneous Optical Imaging and Super-Resolution Ultrasound to Improve Microbubble Localisation Accuracy"
- **Poster presentation:** "Investigation of microbubble detection methods for super-resolution imaging of microvasculature".

Sept. 2018: Poster presentation: "Development of Simultaneous Optical Imaging and Super-Resolution Ultrasound to Improve Microbubble Localisation Accuracy" at UK Biomedical Imaging CDT Summer School, Nottingham University. Poster prize

Jul. 2018: Poster presentation "Development of Simultaneous Optical Imaging and Super-Resolution Ultrasound to Improve Microbubble Localisation Accuracy", Leeds Microbubble Symposium, Leeds University.

Feb. 2018: Poster presentation: "Investigation of microbubble detection methods for super-resolution imaging of microvasculature", at OxFEST Annual Conference, Oxford University, Feb. 2018. Poster prize

Sept 2017: Oral presentation: "Investigation of Microbubble Detection Methods for Super-Resolution Imaging of Microvasculature", IEEE International Ultrasonics

Symposium, Washington D.C.

Jan 2017: Poster competition: "Questions in Super-Resolution Ultrasound Imaging with Microbubbles", The 22nd European Symposium on Ultrasound Contrast Imaging, Rotterdam.

Nov 2016: Poster presentation: "Modelling Two Methods for Super-Resolution Imaging". Imaging sciences and Biomedical Sciences Divisional Symposium, London.